IMPERIAL COLLEGE LONDON

Land–Boundary Layer–Sea Interactions in the Middle East

Evangelia Maria Giannakopoulou

A THESIS SUBMITTED FOR THE DEGREE OF
DOCTOR OF PHILOSOPHY OF IMPERIAL COLLEGE LONDON

in the

Department of Physics, Space and Atmospheric Physics Group,
Imperial College, London SW7 2BW

October 2012

Declaration of Originality

I, *Evangelia Maria Giannakopoulou*, declare that this thesis titled *Land–Boundary Layer–Sea Interactions in the Middle East* and the work presented in it are my own. I confirm that:

- This work was done wholly or mainly while in candidature for a research degree at Imperial College London.
- Where any part of this thesis has previously been submitted for a degree or any other qualification at Imperial College London or any other institution, this has been clearly stated.
- Where I have consulted the published work of others, this is always clearly attributed.
- Where I have quoted from the work of others, the source is always given. With the exception of such quotations, this thesis is entirely my own work.
- I have acknowledged all main sources of help.
- Where the thesis is based on work done by myself jointly with others, I have made clear exactly what was done by others and what I have contributed myself.

Signed: ____

Date: ____

Abstract

Understanding the land–boundary layer–sea interactions is a primary target both in the context of low-level jet (LLJ) development and landscape alterations. This thesis attempts to address and study these interactions in the Middle East.

The thesis investigates the summertime LLJ over the Persian Gulf, known as the Shamal. Terrain height, land-sea and novel mountain slope sensitivity experiments were conducted and compared with a control run. It was found that the Weather Research and Forecasting (WRF) model accurately simulates the LLJ's vertical structure, nocturnal features and strong diurnal oscillation of the wind, and that orography, mountain slope and land/sea breezes determine the Shamal diurnal variation of wind speed and wind direction. The Iranian mountain range not only channels the northwesterly winds but also provides a barrier for the easterly monsoon airflow. The steep slopes cause increased wind speeds; however, the shallow slopes reveal a stronger diurnally varying wind direction due to larger diurnal heating of the sloping terrain. The land breeze and the lower friction over the sea increase the intensity of the nocturnal jet over the Gulf.

To determine the effects of the Nile Delta man-induced greening on local climate, the WRF model was used to compare control simulations, which employ the present-day Nile Delta landscape, with desertification experiments in which the Nile Delta is replaced by desert. It was found that the low surface albedo of the present-day agricultural Nile Delta increases net radiation, which in turn raises potential evapotranspiration (PET). This suggests that agricultural use increases the water demand by enhancing PET. Non-local effects were also examined. It was found that a frontal system over the eastern Mediterranean Sea, associated with a storm event, is shifted farther away from the coast. This shift is attributed to a stronger land breeze in the present-day land-cover.

Acknowledgements

Clearly, this thesis would not have been possible without the academic supervision of Professor Ralf Toumi. I am humbly grateful for all his dedicated guidance and encouragement throughout my doctorate. I greatly appreciated his support, the freedom I got to conduct my research and the nice working environment he cultivated. I also wish to particularly thank Andrew Singleton for helping me in the early steps of my work and giving me the first guide in the application to the Weather Research and Forecasting (WRF) model. I am very grateful to him for always supporting my work and helping me through the many complex stages of my doctorate. Their kindness, help and guidance are deeply appreciated. Further thanks go to Hilary Glasman-Deal, Masoud Hassani and Veronica Valderrama for their helpful advices.

I also wish to express my sincere thanks to the people from the office, institute and beyond that made my working environment such an insightful and fun place.

A special thank you also goes to my Mum Lila Tsilikouna, Dad Giorgos Giannakopoulos, my brother Ioannis Giannakopoulos and my grandparents (Stavros Tsilikounas and Maria Tsilikouna) for their enduring love and support all these years. They have always given me strength to strive my goals, to be independent and never settle for less. I would also like to thank Christo Sakellariou and Adri Alekou for being there and making each day a great lot of fun.

I wish to acknowledge the OPAL for the financial support that made this work possible.

Contents

List of Figures

List of Tables

List of Abbreviations

ABL	Atmospheric Boundary Layer
ACM2	Asymmetrical Convective Model Version 2
AET	Actual Evapotranspiration
AFWA	Air Force Weather Agency
AGCM	Atmospheric General Circulation Model
AGL	Above Ground Level
ARW	Advanced Research WRF
ASL	Above Sea Level
AVHRR	Advanced Very High Resolution Radiometer
BADC	British Atmospheric Data Centre
BEM	Building Energy Model
BEP	Building Environment Parameterisation
BL	Boundary Layer
BMJ	Betts-Miller-Janjic
BouLac	Bougeault-Lacarrère
Bu	Burger number
CAM	Community Atmosphere Model
CAPE	Convective Available Potential Energy
CIN	Convective Inhibition
CTRL	Control run
DALR	Dry adiabatic lapse rate
DES	Desertification experiment
DEW	Dewpoint temperature

DFI	Digital Filtering Initialisation
DJF	December-January-February
ECMWF	European Centre for Medium-Range Weather Forecasts
FDDA	Four-Dimensional Data Assimilation
FGGE	First GARP Global Experiment
Fr	Froude number
G3	Grell 3D
GCM	General Circulation Model
GD	Grell-Devenyi
GFDL	Geophysical Fluid Dynamics Laboratory
GFS	Global Forecast System
GRIB	General Regularly-distributed Information
IFS	Integrated Forecasting System
IGBP	International Geosphere-Biosphere Programme
INS	Inertial Navigation Systems
ITCZ	Inter-Tropical-Convergence-Zone
JJA	June-July-August
KF	Kain-Fritsch
LAI	Leaf Area Index
LES	Large Eddy Simulation
LH	Latent Heat
LLJ	Low-Level Jet
LS	Land-Sea sensitivity experiment
LSM	Land Surface Model
LT	Local Time
MM5	Fifth-Generation Penn State/NCAR Mesoscale Model
MODIS	MODerate resolution Imaging Spectroradiometer
MRF	Medium Range Forecast

MS	Mediterranean Sea
MYJ	Mellor-Yamada-Janjic
MYNN	Mellor-Yamada Nakanishi and Niino
NCAR	National Center for Atmospheric Research
NCEP	National Centers for Environmental Prediction
NDVI	Normalized Difference Vegetation Index
NMM	Nonhydrostatic Mesoscale Model
NOAA	National Oceanic and Atmospheric Administration
NSAS	New Simplified Arakawa-Schubert
NWP	Numerical Weather Prediction model
PBL	Planetary Boundary Layer
PE	Potential Evaporation
PET	Potential Evapotranspiration
PX	Pleim-Xiu
QNSE	Quasi-Normal Scale Elimination
RCM	Regional Climate Model
Ri	Richardson number
RK3	Third-order Runge-Kutta
Ro	Rossby number
RRTM	Rapid Radiative Transfer Model
RRTMG	Rapid Radiative Transfer Model for GCMs
RUC	Rapid Update Cycle
SAS	Simplified Arakawa-Schubert
SBU	Stony Brook University
SH	Sensible Heat
SLP	Sea Level Pressure
SLR	Sea-Level Rise
SST	Sea-Surface Temperature

TE	Turbulent Energy
TEMF	Total Energy-Mass Flux
TKE	Turbulent Kinetic Energy
TOVS	Tiros Operational Vertical Sounder
TRMM	Tropical Rainfall Measuring Mission
UAE	United Arab Emirates
UCM	Urban Canopy Model
USGS	United States Geological Survey
UTC	Coordinated Universal Time
UW	University of Washington
WMO	World Meteorological Organization
WPS	WRF Preprocessing System
WRF	Weather Research and Forecasting model
WSM	WRF Single-Moment
YSU	Yonsei University scheme
ZM	Zhang-McFarlane
Zshallow	Mountain shallow slopes sensitivity experiment
Zsteep	Mountain steep slopes sensitivity experiment
Zzero	Zero terrain height sensitivity experiment

List of Symbols

A	Height of mountain peak
a	Surface albedo; inverse density
c_E	Stability dependent bulk transfer coefficient for moisture
c_h	Stability dependent transfer coefficient for heat
c_p	Specific heat of dry air at constant pressure
E_a	Parameter for the drying power of the air, wind speed and saturation deficit
e_{sat}	Mean saturation vapor pressure
F_L	Latent heat flux
F_S	Sensible heat flux
f	Coriolis parameter
G	Ground heat flux
g	The gravity at the Earth's surface
H	Average scale height
H_{day}	Number of daylight hours
K	Thermal conductivity
K_h	Horizontal eddy viscosity
K_v	Vertical eddy viscosity
k	Von Karman constant; a unit conversion for PET
L	Characteristic length scale
$L\uparrow$	Upward longwave radiation
$L\downarrow$	Downward longwave radiation
N	Brunt-Vaisala frequency
PET	Potential evapotranspiration

p	Pressure
q	Specific humidity
q_{sat}	Specific humidity at saturation
Ri	Richardson number
R_N	Net radiation
RRD	Rossby radius of deformation
r_a	Aerodynamic resistance
r_c	Canopy resistance
$S\uparrow$	Outgoing shortwave radiation
$S\downarrow$	Incoming shortwave radiation
T	Period of an inertial oscillation
$\overline{T}$	Layer-mean temperature
T_{air}	Mean air temperature
T_s	Surface skin temperature
U	Westerly wind component; wind speed
$u*$	Friction velocity
u_{ageo}	Zonal ageostrophic wind
u_{geo}	Zonal geostrophic wind
V	Southerly wind component; wind speed
V_g	Geostrophic wind
VPD	Vapour pressure deficit
v_{ageo}	Meridional ageostrophic wind
v_{geo}	Meridional geostrophic wind
W	Velocity in vertical direction
z	Vertical height; soil depth
z_0	Aerodynamic roughness length
z_i	Height of the capping inversion

Greek Symbols

β	Unit-less constant for PET
Γ	Lapse rate
γ	Psychometric constant
Δ	Slope of the saturation vapour pressure curve
θ	Potential temperature
λ	Latent heat of vaporization
μ	Column mass per unit area
ρ_0	Air density
ρ_p	Density of an air parcel
ρ_{water}	Water density
σ	Sigma vertical levels
σ_x	Spread of mountain range in the x direction
σ_y	Spread of mountain range in the y direction
τ_s	Surface stress
ϕ	Geopotential; latitude
Ω	Earth's rotation rate

Chapter 1

Introduction

1.1 General Introduction

Over the last century, there has been an increasing interest in the study of low-level jets (LLJs) because of their significant impact on weather (e.g. Blackadar, 1957; Bonner and Paegle, 1970; Burk and Thompson, 1996; Parish and Oolman, 2010). It is well known that the LLJs are responsible for severe weather in many geographic locations, and that extreme LLJs have a profound impact on the dynamics and the structure of stably stratified atmospheric boundary layers (ABLs) (e.g. Whiteman *et al.*, 1997; Rao *et al.*, 2003; Ting and Wang, 2006; Jiang *et al.*, 2007; Thoppil and Hogan, 2010; Shapiro and Fedorovich, 2010). However, deeper understanding of the fundamental ABL processes which control the development of the LLJs is needed (Stensrud, 1996). Over the past five decades, there has also been an increased awareness of the impact of anthropogenic land-use/land-cover changes on local, regional and global climate (e.g. Charney, 1975; Zheng and Eltahir, 1997; Gates and Liess, 2001; Wichansky, 2008). Understanding these effects is important for a wide range of fields including meteorology, climatology and hydrology (e.g. Gates and Liess, 2001; Angelini *et al.*, 2011). The extensive man-induced land-cover change has a significant influence on the Earth's surface energy budget, ABL processes, hydrological cycle, circulation patterns and large-scale weather systems (e.g. Gates and Liess, 2001; Wichansky *et al.*, 2008; Angelini *et al.*, 2011). The effects of such LLJs and land-use changes can be tested in numerical simulations which describe the physical interaction between the atmosphere, land surface and sea components. It is essential that we detect the LLJs and land-cover changes accurately, in a timely manner and at appropriate scales so as to better understand and model their impacts on climate and weather. Currently, the numerical modelling of the LLJs and the land–boundary layer coupling remain challenging tasks (Chen and Dudhia, 2001; Storm *et al.*, 2009; Angelini *et al.*, 2011). However, a next-generation numerical weather prediction (NWP) model, the Weather Research and Forecasting (WRF) model (Skamarock *et al.*, 2008) has the potential to capture the LLJs' characteristics and to predict the effects of man-made land-cover changes on climate and weather (e.g. Storm *et al.*, 2009; Bollasina and Nigam, 2011).

Theoretical, observational and numerical studies for LLJs occurring across the globe are generally available (e.g. Blackadar, 1957; Bonner, 1968; Parish *et al.*, 1988; Burk and Thompson, 1996; Renfrew *et al.*, 2008; Parish and Oolman, 2010). The LLJs can form in response to a variety of atmospheric processes. Physical mechanisms dependent on ABL processes have been proposed in the literature to explain the nocturnal jet features, the diurnal oscillation in LLJ intensity, and the nature of LLJs as a response to the diurnal heating and cooling of sloping terrain (e.g. Blackadar, 1957; Holton, 1967). Prior research has documented the need to numerically capture the basic characteristics of LLJs, which are generally observed in nocturnal stable ABLs (e.g. McNider and Pielke, 1981; Zhong *et al.*, 1996; Storm *et al.*, 2009). However, atmospheric models have problems in accurately forecasting the development, intensity, direction, location and diurnal cycle of LLJs (e.g. Jiang *et al.*, 2007; Storm *et al.*, 2009). According to Storm *et al.* (2009), this could be attributed to some extent to our limited understanding and modelling capability of nighttime stable ABLs. The stable ABL is very complex and its structure is more complicated and variable than the structure of the daytime ABL. The fact that the nocturnal ABL is driven by two distinct processes: turbulence and radiative cooling, makes it difficult to describe and to model (Stull, 1988).

Membery (1983) was one of the first researchers to study and explain the nocturnal features of the summertime LLJ over the Persian Gulf, known as the summer Shamal. The winter and summer Shamal wind events are of significant meteorological importance (i.e. raise desert surface material, reduce visibility, change the sea level, create sand and dust storms) and are mostly documented through theoretical and observational studies (e.g. Perrone, 1979; Membery, 1983; Ali, 1994; Brooks *et al.*, 1999; Rao *et al.*, 2003; Mostafaeipour, 2010; Vishkaee *et al.*, 2012). There are only few numerical studies that acknowledged the Shamal wind characteristics (e.g. Shi *et al.*, 2004; Atkinson and Zhu, 2005; Thoppil and Hogan, 2010). Most of these studies have not systematically simulated the summertime LLJ and the diurnal oscillation in the Shamal wind direction, using high-resolution atmospheric models. In this thesis, a summer Shamal wind event is studied by means of novel sensitivity experiments with the WRF model, which result in enhanced understanding of the diurnal variation in both the Shamal wind speed and wind direction. We discuss and analyse the relationship between the Shamal formation and the Persian Gulf topography, the land/sea breezes and the mountain heights and slopes. The implication of these relationships is essential to understand the ability of the WRF model to accurately simulate the horizontal and vertical structure, intensity, direction and diurnal oscillation of strong Shamal wind events and explain the physical mechanisms underlying these LLJs.

Several studies have documented the effects of the Earth's land-cover changes on global, regional and local climate through processes that modify ABL properties, energy and radiation budgets, circulation patterns and large-scale atmospheric systems (e.g. Charney, 1975; Xue and Shukla, 1996; Wichansky *et al.*, 2008). In particular, the physical landscape modification (e.g. vegetation removal or addition) is associated with changes in land surface parameters (e.g. shifts in surface albedo, roughness length and leaf area index), which in turn alter the key land-cover processes (energy, radiation and moisture budgets) that modulate the heat and moisture transfer to the atmosphere (e.g. Wichansky *et al.*, 2008; Anderson *et al.*, 2011). These changes can affect surface temperature and wind speed, ABL structure, convective clouds and precipitation, soil moisture, and mesoscale and large-scale circulations (e.g. Pielke *et al.*, 1998; Wichansky *et al.*, 2008). Land-cover changes also have a profound impact on hydrology and potential evapotranspiration (PET) changes (e.g. Zhang *et al.*, 2001; Han *et al.*, 2009; Yang *et al.*, 2009).

PET is an important index in studies related to water availability for agriculture (Shaw and Riha, 2011). The analysis of PET trends in different seasons over different land types (e.g. mountainous, oasis, forest and urban regions) has been a subject of numerous studies (e.g. Adebayo, 1991; Han *et al.*, 2009; Shaw and Riha, 2011). Most of these studies have been conducted in global scale, or in regions with high human activity, such as China and India (e.g. Chattopadhyay and Hulme, 1997; Gao *et al.*, 2006). However, in water-limited environments (e.g. the Nile Delta in Egypt), where agriculture mainly depends on water availability, the net influence of greening/farming on climate is still uncertain. The aim of this thesis is to fill in some gaps in our knowledge and understanding of the landscape–ABL–water interactions in the Nile Delta region of Egypt. The landscape of the Nile Delta has been extensively transformed to the present-day land-cover by increasing agriculture and urbanisation. In this thesis, the WRF model is used to investigate the sensitivity of the Nile Delta's local climate to the man-made greening. The changes in PET because of the man-induced land-cover modifications and the ABL interaction with the underlying surface are studied by conducting desertification experiments in the Nile Delta region for comparison with the control runs. Emphasis is also placed on understanding the non-local effects of the agricultural Nile Delta on a storm event observed over the eastern Mediterranean Sea.

1.2 Research Objectives

This thesis has the following main objectives related to the study of a summertime Shamal wind event in the Persian Gulf:

- Assess the work done in the related areas (e.g. LLJs occurring worldwide, Shamal wind events).
- Show the ability of the WRF model to accurately simulate the vertical structure, wind speed and wind direction of the Shamal winds.
- Examine the factors that determine the Shamal wind formation, development, strength, duration and direction.
- Investigate the orographic effects on the LLJ development.
- Identify the physical mechanisms that explain the diurnal oscillation of the Shamal winds.

The thesis has the following aims related to the investigation of the present-day Nile Delta man-made greening effects on the local climate:

- Assess the work done in the related areas (e.g. studies of land-cover changes, PET and Nile Delta studies).
- Determine the impacts of the man-made greening on the local climate.
- Investigate the Nile Delta land-use effects on the surface energy budget, circulation patterns and a storm event.
- Explore the changes in PET and the relationship of these changes to other meteorological parameters such as wind speed, temperature, and net radiation.

1.3 Thesis Organization

This thesis comprises seven chapters, four lists (including lists of tables, figures, abbreviations and symbols) and an extensive reference list. Chapter 2 briefly reviews some of the principles of atmospheric physics, focusing on the ABL and surface energy balance. Chapter 2 also explores the literature of related fields necessary for a critical analysis and assessment of the work presented in the thesis. In particular, the background related to more specific fields involves a review of the most known theories for LLJs' development and an overview of land-use change and PET studies. Chapter 3 describes the principal components of the WRF model, the atmospheric re-analyses and the topographic data that are used as input datasets with the WRF model. The methodology used for the study areas is discussed in the relevant chapters. Chapter 4 examines the sensitivity of the performance of the WRF model to the use of different PBL parameterisations. In particular, the work presented in chapter 4 is a series of WRF simulations used to explore the differences between the local and non-local approach to PBL modelling. Evidence of validation of the WRF model against surface and boundary layer observations and discussion of the choice of the PBL scheme for stable environments is provided. Chapter 5 proceeds with a section about the general climatic and weather conditions of the Persian Gulf. Emphasis is placed on the wind meteorology of this region. The work presented in chapter 5 relies on a numerical study of a summertime Shamal wind event over the Persian Gulf. The WRF model is used to examine the topographic effects on the Shamal development, and the physical mechanisms underlying the diurnal cycle of the Shamal wind speed and wind direction. To determine and understand the mountainous height and sloping terrain effects on the Shamal development, mountain height and novel mountain slope sensitivity experiments, in addition to a land–sea sensitivity run, are presented. Chapter 5 also provides a detailed investigation of previously proposed theories of LLJs' development. Chapter 6 briefly describes the climate of the eastern Mediterranean region and northern Egypt. Following this description, information about the Nile Delta in Egypt, which is an example of anthropogenic impact on land-cover, is provided too. In the rest of chapter 6, the present-day Nile Delta greening effects on the local climate are investigated. The WRF model is used to compare control runs, which employ the present-day Nile Delta landscape, with desertification experiments. Non-local effects are also examined. Finally, chapter 7 summarises the main achievements and contributions of this thesis, revisits the objectives, and discusses future research topics.

Chapter 2

Background to Atmospheric Physics

In order to provide a background to the forthcoming material that is discussed, this chapter reviews some of the principles of atmospheric physics, focusing on the atmospheric boundary layer (ABL) and surface energy balance.

At present, numerical weather prediction (NWP) models face a challenge in forecasting with accuracy the development, intensity, location and frequency of low-level jets (LLJs), which are mostly observed in nighttime stable ABLs. This might be because of the fact that our understanding and modelling capability of stable boundary layers are limited (e.g. Cuxart *et al.*, 2006; Storm *et al.*, 2009). This chapter reviews a number of previous LLJ studies, and briefly presents the LLJs' characteristics and physical mechanisms that have been investigated and proposed to explain many aspects of the LLJs' development.

Nowadays, the modelling of the vegetation and boundary layer coupling is also a challenging task (Angelini *et al.*, 2011). Although humans have been continually modifying the Earth's landscape for centuries, it has only been within the past four decades that land-cover/land-use change has been widely recognized as an important driving force for changing the climate in local, regional and global scale (Wichansky *et al.*, 2008). This chapter provides an overview of published research on the impact of land-use/land-cover changes on the climate and highlights knowledge gaps in modelling studies of the land surface–atmosphere–water interaction. The specific focus of this study on potential evapotranspiration is motivated by the importance of this variable for meteorology, hydrology and for studies related to water availability for agriculture.

2.1 The Atmospheric Boundary Layer (ABL)

This section presents a definition of the ABL, followed by a description of the ABL structure, static stability and diurnal cycle. A brief description of the basic ABL components including temperature, moisture and wind also is provided. Further information on the

ABL may be found in Stull (1988), Garratt (1992), Kaimal and Finnigan (1994) and Wallace and Hobbs (2006).

2.1.1 ABL definition

The portion of the atmosphere in the lowest 1 or 2 km that is mostly affected by the presence of the Earth's surface is defined as the ABL, whose thickness depends on daytime, season of year, space, strength of turbulent eddies, wind and temperature vertical profiles (e.g. Stull, 1988; Wallace and Hobbs, 2006). The ABL responds to surface forcings, such as evapotranspiration, frictional drag, latent and sensible heat transfer, terrain-induced flow changes and pollutant emission, with a timescale of approximately an hour or less. The primary source of energy for the whole atmosphere including the ABL is the solar (shortwave) radiation. Most of the shortwave radiation is absorbed by the ground and transmitted to the rest of the atmosphere via ABL processes (Stull, 1988).

2.1.2 ABL depth and structure

According to Kaimal and Finnigan (1994), the ABL is divided into two regions. The first and lower region is the surface layer (50–100 m in depth), where the shearing stress is nearly constant with height and the winds are not so sensitive to the Earth's rotation but are instead mostly influenced by the drag at the ground and the temperature vertical gradients. The second region (500–1000 m in depth) has variable shearing stress and the winds are determined by the frictional drag, Earth's rotation and temperature gradients (Kaimal and Finnigan, 1994). As seen in Figure 2.1, above these two layers there is a capping inversion (or entrainment zone) which is a layer characterised by high static stability. Turbulence, heat, moisture and pollutants are trapped within the ABL by the capping inversion. Above this inversion layer is the rest of the troposphere, called the free atmosphere, in which the winds are nearly geostrophic and the flow is insensitive to surface friction (e.g. Kaimal and Finnigan, 1994; Wallace and Hobbs, 2006).

According to Stull (1988), over land the ABL has a well-defined structure that evolves with a diurnal cycle. Figure 2.1 shows a typical evolution of the ABL with time in high-pressure regions over land. Note that the ABL is thinner in high-pressure regions than in low-pressure regions mainly due to descending motions that push the top of the ABL down. As seen in Figure 2.1, at and shortly after sunrise, the ABL consists of two parts: the thin surface layer and a mixed layer, whose depth reaches a maximum in mid-afternoon. The mixed layer can further sub-divided into a cloud layer and a sub-cloud layer. Turbulence in the mixed layer is primarily generated by convective sources, which include surface heating and radiative cooling from the top of the cloud layer. Strong

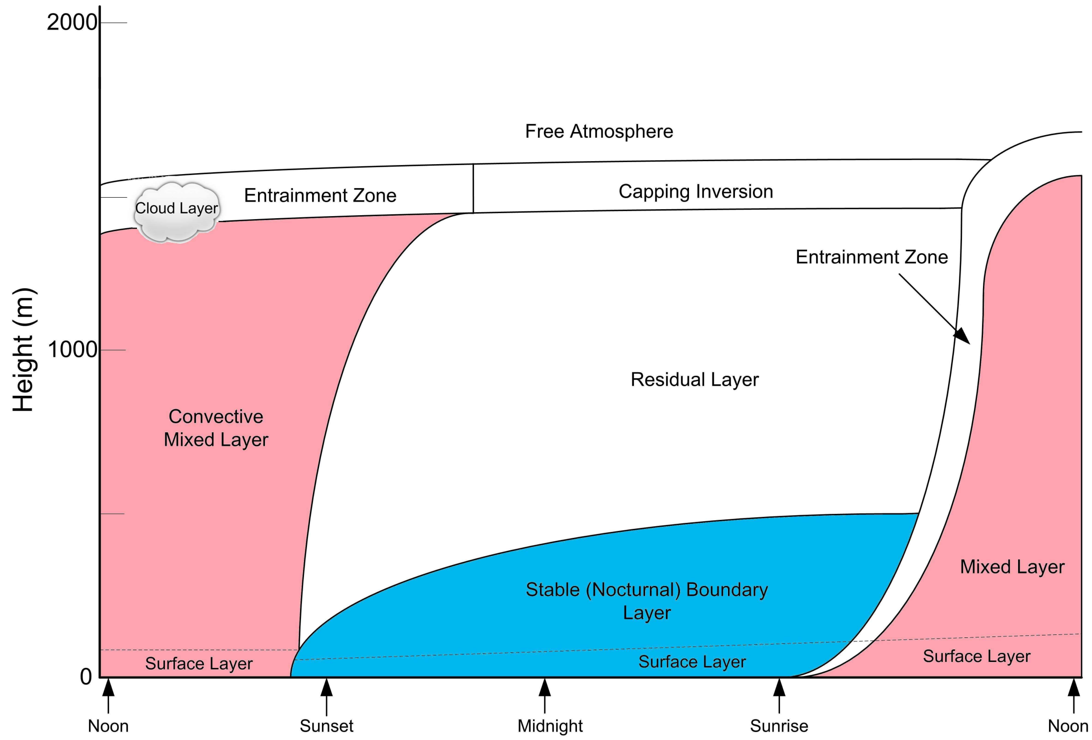

FIGURE 2.1: Diurnal evolution of the ABL in high-pressure regions over land. The x axis represents the hour in local time (LT). Redrawn after Stull (1988).

wind shear can also contribute to this turbulence generation. When buoyant turbulence generation dominates the ABL, the mixed layer is called a convective boundary layer. From sunset to sunrise, the ABL consists of three parts: the surface layer, a stable boundary layer and a residual layer (see Figure 2.1). As the evening progresses and the surface cools via radiational cooling, the nocturnal stable boundary layer is mainly characterised by strong static stability and weak turbulence. At the night, the winds at ground level are characterised as light and calm; however, the winds aloft may reach supergeostrophic speeds. The statically stable air tends to suppress turbulence, while the developing of supergeostrophic winds enhances wind shears that tend to generate turbulence. As a result, turbulence sometimes occurs in short bursts that can cause mixing throughout the nocturnal ABL. The residual layer does not come in direct contact with the ground and can be thought of as a left-over convective mixed layer (Stull, 1988). This layer usually contains dying or zero turbulence (Wallace and Hobbs, 2006). In general, the flow within the stable boundary layer is characterised by small eddies, strong wind shear and sporadic wave activity (Kaimal and Finnigan, 1994).

2.1.3 Winds in the ABL

Winds that can coexist or exist separately in the ABL are divided into three categories: mean winds, waves and turbulence. In the ABL, the horizontal transport (or advection) is dominated by the mean wind, whereas the turbulence is responsible for the vertical transport (Stull, 1988). According to Wallace and Hobbs (2006), turbulence is a natural response and has the tendency to decrease instability within the ABL. Turbulent flow in the boundary layer can be generated thermally, mechanically and inertially. The heating of the Earth's surface by solar radiation causes buoyant plumes, known as thermals, of warm air to rise from the ground and cold air to sink, generating the thermal turbulence (or free convection). Also, mechanical turbulence usually can form in the ABL when there is a wind shear caused by the surface frictional drag, which in turn results in slower winds near the ground. A special form of the wind shear turbulence is the inertial turbulent flow that forms when some of the larger eddies' inertial energy is lost to the smaller eddies (Wallace and Hobbs, 2006). Waves are usually observed in the nocturnal (stable) boundary layer. These waves are often generated by mean flow over obstacles and by mean wind shears. They transport momentum and energy, as well as little moisture, heat and pollutants (Stull, 1988).

2.1.4 Stability of the ABL

Static stability (or vertical stability) is the ability of a fluid at rest to become laminar or turbulent due to buoyancy effects. Based on atmospheric stability (buoyancy effects) and the dominant mechanism of turbulence generation, the ABLs are usually classified into three types: stable (air tends to become or remain laminar), unstable (air tends to become or remain turbulent) and neutral (air might remain laminar or turbulent depending on its history). Therefore, the static stability can be defined as the stability of the atmosphere in hydrostatic equilibrium with respect to vertical displacements. These displacements are usually explained by using the parcel concept (Peppler, 1988). The air parcel can be thought as a small mass of air that is influenced by the environment, but we assume that allows only adiabatic transformations (Andrews, 2000). Therefore, the air parcel undergoes a change in its temperature, pressure or volume without any heat being added to it or withdrawn from it (Wallace and Hobbs, 2006). The parcel's stability is dependent upon the motion of the parcel after a forced displacement from an original position. As the parcel undergoes adiabatic change, its temperature is compared to that of the surrounding environment so as to relate differences in density (Peppler, 1988). Suppose that $(\frac{d\rho}{dz})_E$ is the environmental density gradient and that the buoyancy of the parcel depends on the difference between its density and that of its environment, the parcel will therefore be positively buoyant if $(\frac{d\rho}{dz})_E > 0$, neutrally buoyant if $(\frac{d\rho}{dz})_E = 0$ and negatively buoyant if $(\frac{d\rho}{dz})_E < 0$ (Marshall and Plumb, 2008).

The atmospheric stability can be also expressed in terms of temperature T. The quantity $\Gamma(z)$ is the lapse rate which is defined as the rate of temperature decrease with increasing height z:

$$\Gamma(z) = -\frac{dT}{dz}. \tag{2.1}$$

There are two types of lapse rate:

1. Environmental lapse rate (Γ_E), which is the rate of temperature decrease with height in the stationary atmosphere at a given location and time (e.g. temperature gradient).

2. The adiabatic lapse rates (Γ_a), which refer to the change in temperature of an air parcel as it moves upwards (or downwards) without exchanging heat with its surroundings. Γ_d is the dry adiabatic lapse rate (DALR) when applied to a mass of dry or unsaturated air rising under adiabatic conditions and Γ_s is the moist adiabatic lapse rate when the air is saturated with water vapor (Andrews, 2000).

The stability condition can be expressed in terms of temperature with respect to vertical displacements as: unstable if $(\frac{dT}{dz})_E < 0$, neutral if $(\frac{dT}{dz})_E = 0$ and stable if $(\frac{dT}{dz})_E > 0$. Therefore, a high lapse rate indicates a greater than normal change of temperature associated with a change in height and is a characteristic of an unstable atmosphere (Marshall and Plumb, 2008).

The neutral conditions are rare and are considered ideal (Alinot and Masson, 2005). Usually, during windy and cloudy conditions a neutral boundary layer is formed, where the temperature changes adiabatically as the air parcels displaced up and down remain at exactly the same density as the surrounding air. Therefore, if $\Gamma_E = \Gamma_d$ we have neutral stability (Andrews, 2000). Under such conditions, turbulence is mainly mechanical and arises from the forces of friction and wind shearing (Alinot and Masson, 2005). An ABL is said to be unstable (stable) when the surface is warmer (colder) than the air above, such as during a sunny day (a clear night) (Wallace and Hobbs, 2006). Therefore, the unstable conditions correspond to daytime weather conditions and the stable conditions to nighttime (Alinot and Masson, 2005). In the daytime convective mixed ABL, the environment temperature decreases more rapidly with height than the adiabatic lapse rate and displaced parcels accelerate in the vertical direction away from their original positions. Thus, the ABL is said to be statically unstable near height z if $\Gamma_E > \Gamma_d$. However, in the nighttime stable ABL, the environment temperature decreases less rapidly with height than the adiabatic lapse rate and displaced parcels accelerate in the vertical direction towards their original positions (e.g. Andrews, 2000; Wallace and Hobbs, 2006). Therefore, the ABL is said to be statically stable near height z if $\Gamma_E < \Gamma_d$ (Andrews, 2000). Schematic vertical profiles of temperature (T), showing the DALR and examples of stable and unstable environmental lapse rates are given in Figure 2.2. Under unstable

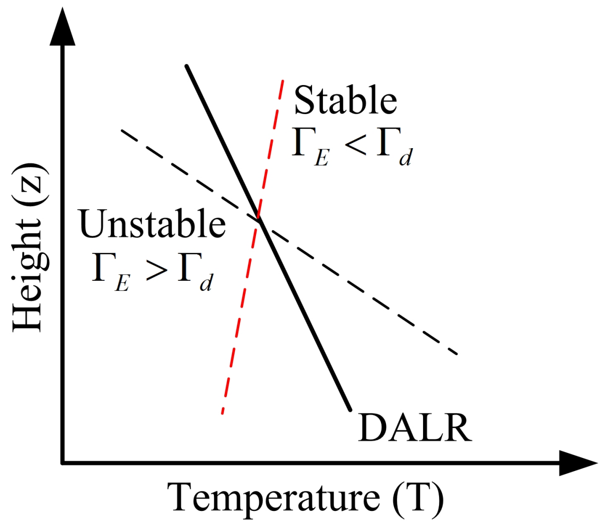

FIGURE 2.2: Schematic vertical profiles of temperature (T), showing the dry adiabatic lapse rate (DALR; black solid line) and examples of stable ($\Gamma_E < \Gamma_d$; red dashed line) and unstable ($\Gamma_E > \Gamma_d$; black dashed line) environmental lapse rates. Redrawn from Andrews (2000).

and stable conditions, turbulence results from the ground friction, the wind shearing and from thermal stratification of the air (Alinot and Masson, 2005).

The temperature of a saturated air parcel will decrease with increasing altitude at the saturated adiabatic lapse rate (Γ_s). It follows from the above arguments that the conditions $\Gamma_E < \Gamma_s$, $\Gamma_E = \Gamma_s$ and $\Gamma_E > \Gamma_s$ correspond to a stable, neutral and unstable stratification for saturated air parcels, respectively.

2.1.5 Buoyancy force

An expression for the upward buoyancy force on an unsaturated air parcel in terms of lapse rates Γ_E, Γ_d and acceleration g can be derived. The net upward force F acting on a unit volume of the air parcel is:

$$F = -(\rho - \rho_p)g, \tag{2.2}$$

where ρ is the density of the ambient air and ρ_p is the density of the air parcel. Then the upward acceleration of the air parcel is:

$$\frac{d^2 z_p}{dt^2} = \frac{F}{\rho_p} = (\frac{\rho - \rho_p}{\rho_p})g = (\frac{T_p - T}{T})g, \tag{2.3}$$

where z_p is the vertical displacement of the air parcel from its equilibrium level and the densities of the air parcel and the ambient air are inversely proportional to their temperatures. This last expression, using the lapse rate equation 2.1, will be:

$$\frac{d^2 z_p}{dt^2} = -\frac{g}{T}(\Gamma_d - \Gamma_E) z_p \tag{2.4}$$

and can be also written in the form:

$$\frac{d^2 z_p}{dt^2} + N^2 z_p = 0, \tag{2.5}$$

where

$$N = \left[\frac{g}{T}(\Gamma_d - \Gamma_E)\right]^{1/2} \tag{2.6}$$

is referred to as the Brunt–Vaisala (or buoyancy) frequency and the temperature T is that of the environment (e.g. Andrews, 2000; Wallace and Hobbs, 2006). The quantity N^2 is a useful measure of atmospheric stratification. For a stably stratified atmosphere ($\Gamma_E < \Gamma_d$), equation 2.6 indicates that the N^2 is positive and the solution of equation 2.5 is sinusoidal. For a statically unstable region of the atmosphere ($\Gamma_E > \Gamma_d$), equation 2.6 indicates that the N^2 is negative, which results to exponential solutions of equation 2.5. The Brunt-Vaisala frequency can be also related to the potential temperature of the environment as follows:

$$N^2 = \frac{g}{\theta}\frac{d\theta}{dz}. \tag{2.7}$$

Therefore, a region of the atmosphere is statically unstable if θ decreases with increasing height and is statically stable if θ increases with altitude (Andrews, 2000).

2.1.6 Logarithmic wind profile

The vertical wind profile in the surface layer also is influenced by static stability, as can be seen in Figure 2.3 where vertical wind speed profiles for different static stabilities are plotted on a logarithmic height scale. In general, one can derive the wind speed vertical profile in the surface layer as a logarithmic equation:

$$\overline{V}(z) = \frac{u*}{k}\ln(\frac{z}{z_0}), \tag{2.8}$$

where k is the von Karman constant with values ranging from 0.35 to 0.43, z is the vertical height, z_0 is the aerodynamic roughness length defined as the height where the

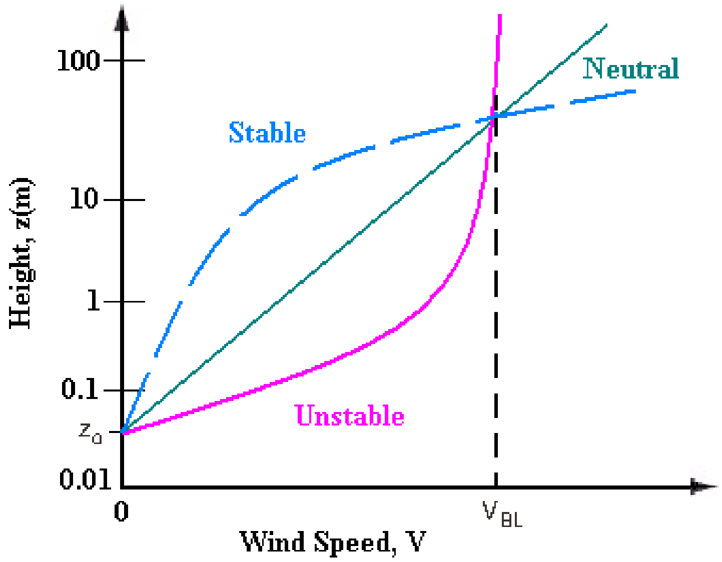

FIGURE 2.3: Semi-log graph of typical wind speed variations with height in the surface layer for stable, unstable and neutral profiles. Redrawn from Wallace and Hobbs (2006).

wind speed $\overline{V}$ tends to zero, and $u* = \left|\frac{\tau_s}{\rho}\right|^{1/2}$ is known as the friction velocity, where ρ is the density and τ_s is the surface stress (e.g. drag force per unit area). This logarithmic profile of the wind is strictly valid only for the neutral surface layers. As the surface layer becomes more unstable or stable, the vertical profile of wind speed departs from being logarithmic (see Figure 2.3). For unstable surface layers, due to vigorous turbulence, the wind gets stronger more rapidly with height than in the stable surface layers (e.g. Kaimal and Finnigan, 1994; Wallace and Hobbs, 2006).

2.1.7 Vertical structure of temperature, moisture and wind

The daytime heating and nighttime cooling over the Earth's surface result in diurnal variation of temperature, moisture and wind within the ABL. Turbulence generated near the ground by the aforementioned processes mixes the surface air. During the day, the resulting mixture creates a potential temperature (θ) vertical profile that is relatively uniform with height (i.e. homogenization within the ABL). As seen in Figure 2.4(a), potential temperature decreases gradually within the mixed layer. The highest potential temperature values are observed at the top of the ABL (z_i) and at the surface level owing to solar insolation that heats the ground and the air immediately above it. During the night, a stable boundary layer is formed and the turbulence is suppressed because of the radiative cooling that occurs on the Earth's surface. Consequently, the highest potential temperature values are at the top of the ABL marked by a capping inversion, and the lowest values are at the surface because of the radiational cooling (Wallace and Hobbs, 2006).

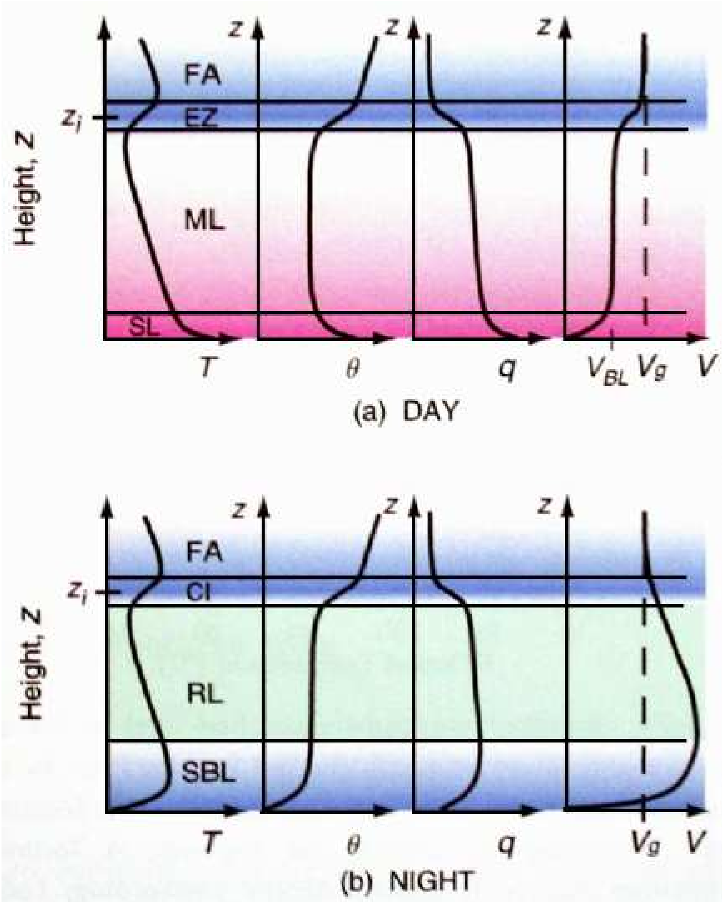

FIGURE 2.4: Typical (a) daily and (b) nightly vertical profiles of the temperature (T), potential temperature (θ), moisture (q), and wind speed (V) in the lower troposphere. In (a) SL is the surface layer, ML is the mixed layer, EZ is the entrainment zone and FA is the free atmosphere. In (b) SBL is the stable boundary layer, RL is the residual layer and CI is the capping inversion. z_i is the height of the capping inversion, which equals to the top of the ABL; V_g is the geostrophic wind. Taken from Wallace and Hobbs (2006).

Diurnal changes in temperature (T) and moisture (q) follow a similar cycle, as evident in Figure 2.4. During the day, the highest specific humidity is observed at the surface because of the evaporation from the ground. This moisture advects vertically, resulting in a gradual decrease of the specific humidity within the mixed layer and a rapid decrease in moisture at and above the entrainment zone. At night, the moisture is low at the surface levels because of the effects of dew or frost formation and it is relatively high between the nocturnal ABL and the capping inversion. Usually the specific humidity drops off sharply above the capping inversion where vertical moisture advection does not penetrate (Wallace and Hobbs, 2006).

During the day, the mixed surface air creates a wind speed (V) vertical profile that is also relatively uniform with height. The surface frictional effects dominate the wind profile in the surface and mixed layer, resulting in wind speeds that cease to exist at the surface and in winds that are relatively constant within the mixed layer. The frictional drag has minor effects on the free atmosphere, resulting in an increase of the winds above the capping inversion (see Figure 2.4). At night, between the stable ABL and the capping inversion, is the residual layer, which is characterised by frictionless air that undergoes an inertial oscillation due to the Coriolis force. A low-level wind speed maximum, called the nocturnal jet, is formed because the winds in the residual layer become supergeostrophic and the winds closer to the surface are calm due to friction (e.g. Blackadar, 1957; Wallace and Hobbs, 2006). A wind speed decrease immediately above the core of the low-level jet is marked; however the wind speed increases again or remains constant in the free atmosphere (Wallace and Hobbs, 2006).

2.2 Low-level Jets (LLJs)

The low-level jet (LLJ) is an ABL phenomenon that has been observed over many locations around the world including North and South America, Asia, Africa, Australia, Antarctica and China (e.g. Stensrud, 1996; Rife *et al.*, 2010). Among these geographic locations is the Great Plains region of the United States, in which one of the most famous LLJs, in terms of its effects on rainfall and severe weather, occurs. Consequently, the Great Plains LLJ has been studied extensively for over 50 years (e.g. Blackadar, 1957; Bonner, 1968; Stensrud, 1996; Ting and Wang, 2006; Parish and Oolman, 2010).

Perhaps, the most well-documented LLJs are those occurring at night and, as mentioned in section 2.1, usually form as a result of the inertial oscillation after late afternoon (Rife *et al.*, 2010). The formation of a nocturnal LLJ typically begins around sunset and may continue throughout evening. In the absence of clouds, and under strong radiational cooling, the LLJ generally reaches a maximum between midnight and sunrise at levels of less than 1 km above the ground (Shapiro and Fedorovich, 2010). According to Blackadar's (1957) study, these wind maxima are often supergeostrophic. Furthermore, a connection between the height of the maximum wind speed and the altitude of the temperature inversion exists (Blackadar, 1957; Bonner, 1968).

2.2.1 LLJ definition

There is no unique definition in the literature for the term LLJ, because this low-level wind speed maximum occurs in the ABL in a number of different temporal and spatial scales and depends on the forcing mechanisms, the type of investigation and modelling study (Stensrud, 1996). However, according to Stensrud (1996), the LLJ is commonly defined by examining the vertical profile of the horizontal winds to determine if a wind speed maximum occurs at the lower-tropospheric levels. This subsection includes a short synopsis of the LLJ characteristics that have been observed in numerous studies to give a typical LLJ definition; some of these LLJ characteristics are also outlined in the review by Stensrud (1996):

- Fast moving air current near the surface (e.g. Wexler, 1961; Bonner, 1968).
- Large vertical wind shear above and below the jet core (e.g. Blackadar, 1957; Wexler, 1961; Bonner, 1968).
- Strong horizontal shear; extending high-speed flow for some appreciable horizontal distance (e.g. Wexler, 1961; Reiter, 1963).
- Maximum wind speed at least 12-20 m s^{-1} (peak of approximately 30 m s^{-1}), and 50-75% reduction of the maximum wind speed above the LLJ core (Bonner, 1968). Bonner (1968) proposed some speed criteria in order to establish a wind speed minimum and decrease in velocity above the core of LLJs. For example, the wind speed at the altitude of maximum wind must be equal to or exceed 12 m s^{-1} (16 m s^{-1}; 20 m s^{-1}) and must decrease by 6 m s^{-1} (8 m s^{-1}; 10 m s^{-1}) to the next highest minimum altitude or to the 3 km level, whichever is lower (Bonner, 1968).
- Strong diurnal oscillation in wind speed. The LLJs form in conjunction with a nocturnal inversion (Blackadar, 1957).

2.2.2 Climatology of LLJs

In the mid-latitudes, frequent LLJ occurrence is typically observed during the summer months in regions located either next a mountain range or where strong land–sea temperature gradients are present (Stensrud, 1996). For example, the Great Plains LLJ (most common as the southerly LLJ) is mainly observed in the spring and summer months (Holton, 1967). In the climatology study of Bonner (1968), it was found that this southerly jet is mainly characterised by strong diurnal oscillation with strongest wind speeds at night, and tends to have a wind maximum at average height 500-1000 m AGL. According to Bonner (1968), favourable synoptic conditions for the LLJ formation are those which create a strong west-to-east pressure gradient across the Great Plains and uninterrupted airflow from the Gulf of Mexico. Later on, a climatological analysis by Whiteman *et al.* (1997) has shown that more than 50 % of the Great Plains LLJ maxima actually occur below 500 m and that the winds at the nose of the LLJ are characterised by a diurnal clockwise rotation in wind direction and an oscillation in speed. Further details on the frequency of LLJs' development, the LLJs' characteristics, diurnal variation and climatology are available in several texts, such as Bonner (1968), Stensrud (1996) and Rife *et al.* (2010).

2.2.3 Overview of LLJs' studies

LLJs occurring worldwide are well-documented through theoretical studies (e.g. Blackadar, 1957; Wexler, 1961; Holton, 1967), observational studies (e.g. Blackadar, 1957; Crawford and Hudson, 1973; Parish *et al.*, 1988), climatological analyses (e.g. Bonner, 1968; Whiteman *et al.*, 1997), and numerical modelling (e.g. McNider and Pielke, 1981; Zhong *et al.*, 1996; Pan *et al.*, 2004; Parish and Oolman, 2010). This subsection presents a brief overview and Table 2.1 of the most known theories that have been proposed to explain the development, evolution and characteristics of LLJs observed over the world. Note that much of the early LLJs' documentation occurred as a result of the frequent Great Plains LLJ development.

In an earlier study, which focused on the Great Plains LLJ, Wagner (1939) considered the diurnal cycle of this LLJ to be a result of diurnal pressure and temperature oscillations. He stated that these diurnal oscillations arise by mountain–plain and land–sea circulations and he explained that the nocturnal maxima were a result of radiational cooling (e.g. Wexler, 1961; Bonner, 1968). An alternative approach was developed later by Blackadar (1957) who addressed the ageostrophic motions of the LLJ, which resulted from an inertial oscillation. Blackadar (1957) was one of the first researchers to consider the theory of the nocturnal jet and he was accredited the finding that the height of the wind speed maximum is related to the height and the magnitude of the temperature inversion. Soon after, Wexler (1961) explained the formation of the southerly LLJ as a result of northward deflection by the Rocky Mountains of westward moving air across the Gulf of Mexico. Later on, Holton (1967) suggested that the diurnal jet variation due to the daytime heating and nighttime cooling of a sloping terrain could be responsible for the intensity and persistence of the LLJ. This theory was also analysed by Bonner and Paegle (1970) when focusing on the geostrophic wind diurnal variations, which are mainly driven by the thermal wind response to the periodic temperature cycle over sloping terrain. At a later stage, Thorpe and Guymer (1977) modified the Blackadar's (1957) theory of the nighttime LLJ by considering a number of stress parameterisations. In particular, they introduced a three-layer (the free atmosphere and two sub-layers in the vertical) model of a diurnal wind variation to clarify the mechanism of nocturnal jet formation. An alternate hypothesis about the interaction of LLJs with upper-tropospheric jet streaks was introduced by Uccellini and Johnson (1979). Stensrud (1996) provided an extensive review of the Great Plains LLJ and an analytic description of the possible mechanisms for the LLJ formation.

Bonner (1968) described the climatology of low-level wind maxima that occurred over the Great Plains by using 2-year (January 1959–December 1960) of rawinsonde data. He defined low-level wind speed criteria and he also found that the LLJ of significant diur-

TABLE 2.1: An overview of the most known theories and studies that have been documented to explain the LLJs' development and characteristics worldwide.

Wagner (1939)	Pressure and temperature diurnal oscillations ;Land–sea and mountain–plain circulations
Blackadar (1957)	Inertial oscillation - frictional decoupling
Wexler (1961)	Blocking effects
Holton (1967)	Role of a sloping terrain; Thermal effects
Bonner (1968)	Climatology of LLJs; Wind speed criteria
Bonner and Paegle (1970)	Geostrophic wind diurnal variations due to sloping terrain effects
Crawford and Hudson (1973)	Observational study; Backing and veering of the wind vectors
Thorpe and Guymer (1977)	Modified the Blackadar theory; Introduced a three-layer model of the diurnal wind variation
Uccellini and Johnson (1979)	Upper and lower tropospheric jets are coupled
McNider and Pielke (1981)	Numerical study; The magnitude of the terrain slope is important to the strength of the LLJ
Parish *et al.* (1988)	Observational study; Combination of ABL processes; Isallobaric wind component
Stensrud (1996)	Provided a comprehensive review of the southerly LLJ
Whiteman *et al.* (1997)	Climatological analysis; Diurnal variation in wind speed and direction
Pan *et al.* (2004)	Numerical study; Role of topography
Ting and Wang (2006)	Numerical study; Topography is important; Thermal influences are insignificant
Jiang *et al.* (2007)	Numerical study; Combination of Blackadar and Holton theories
Parish and Oolman (2010)	Numerical study; Geographical frequency of the Great Plains LLJ; isallobaric wind component.

nal variation occurred with the greatest frequency during summer over Oklahoma and Kansas. Bonner's (1968) pioneering analysis is considered as the most complete climatological description of the southerly LLJ. Later on, Whiteman *et al.* (1997) presented a climatological analysis of the Great Plains LLJ characteristics by using rawinsonde data of high vertical and temporal resolution. Bonner's (1968) wind speed criteria were refined in Whiteman *et al.* (1997) to include slightly weaker LLJs. In their study, the strongest jets were frequently occurred between midnight and early-morning hours and in heights below 500 m AGL. Interestingly, a strong diurnal oscillation in both the wind speed and direction of the southerly jet was observed. The wind direction was characterised by clockwise turning with maximum speed at sunrise. Recently, Rife *et al.* (2010) provided a global climatology [21 year (1985-2005) global downscaled re-analysis was used] of diurnally varying LLJs.

Crawford and Hudson (1973) focused on the diurnal variation of wind speed and wind direction at a tower located in central Oklahoma. Their analyses showed a distinct diurnal variation in wind direction. Backing and veering of the wind vectors with height during a day was observed, with winds that turned clockwise during the night and counterclockwise during the day (Crawford and Hudson, 1973). Observations from southern England (pilot balloons were used) on the diurnal structure of the ABL in which a night-time LLJ was located, enabled Thorpe and Guymer (1977) to list conditions under which a LLJ develops. Parish *et al.* (1988) in their observational study (airborne radar altimetry was used) explained the development of the summertime Great Plains LLJ. A combination of physical mechanisms dependent on ABL processes (i.e. frictional decoupling and diurnal heating and cooling of a sloping terrain) was investigated by Parish *et al.* (1988) to explain the LLJ development. They also used the term of the isallobaric wind component.

The McNider and Pielke (1981) numerical study confirmed previous theories of the vital role of the horizontal pressure gradient oscillations due to the diurnal cycle in the temperature field over a sloping terrain. As reported in their study, the magnitude of the terrain slope is important to the intensity of LLJs. Later on, Zhong *et al.* (1996) used a three-dimensional mesoscale model to predict the position and diurnal oscillation in wind speed and direction of the Great Plains LLJ. Their study suggested that the sloping terrain effects are secondary to the inertial oscillation mechanism. Rodwell and Hoskins (2001) and Pan *et al.* (2004) numerically studied and focused on the effects of orography. Ting and Wang (2006) conducted sensitivity experiments with and without the North American topography. In their numerical study, the Great Plains LLJ disappeared when the topography was removed and the thermal forcing due to the North American topography was found secondary compared to the mechanical forcing in the Great Plains LLJs' development. The numerical study of Jiang *et al.* (2007) confirmed previous LLJs' theories, and suggested that Blackadar (1957) or Holton (1967) theory alone does not account for certain LLJ characteristics appearing in their model. Storm *et al.* (2009) evaluated the Weather Research and Forecasting model, which was able to capture the location and timing of observed Great Plains LLJ events. However, they overestimated the heights of the LLJs' core and underestimated the LLJs' wind speed. In a recent study, Parish and Oolman (2010) focused on the geographical frequency of the Great Plains LLJ. A simple analysis of the equation of motion and outputs from a 12 km NWP model were used to show the significance of the topography in driving the LLJ (Parish and Oolman, 2010).

Several theoretical, numerical and observational studies have indicated that LLJs occur across the globe in all seasons and in a range of large-scale environments, including the most studied Great Plains LLJ (e.g. Parish and Oolman, 2010), the LLJ along the California coast (e.g. Burk and Thompson, 1996) and the Greenland tip jet (e.g. Renfrew *et al.*, 2008). Most of these studies concluded that some of the strongest physical mechanisms underlying LLJs and their diurnal variation are the inertial oscillation of the ageostrophic wind and the diurnal cycle of the daytime heating and nighttime cooling of a sloping terrain (e.g. Blackadar, 1957; Holton, 1967; Zhong *et al.*, 1996; Parish and Oolman, 2010).

2.2.4 Mechanisms of LLJs' formation

Several physical mechanisms have been proposed in the literature to explain aspects of the development, intensity and location of LLJs. The most well-documented and well-studied physical mechanisms that explain the generation and development of low-level wind maxima are the following:

Inertial oscillation: The inertial theory accounts for the significantly supergeostrophic wind speeds observed at the lower-tropospheric levels and for the daily oscillation in LLJs' intensity. During the day the flow near the surface is considered to be in an equilibrium state with the horizontal pressure gradient, Coriolis and frictional forces balancing each other. As detailed in Blackadar's (1957) study, during strong daytime heating, the ABL tends to be coupled with the surface layer and because of friction the surface wind approaches the subgeostrophic. After the temperature inversion first begins to be established at about the time of sunset, rapid decay of the vertical mixing away above the nocturnal inversion is observed and the low-level winds become relatively smooth. Once surface heating ceases near nightfall, radiational cooling takes place at the surface, which results in stable ABLs. However, within the deepening temperature inversion some turbulence is maintained because of the large wind shear. Downward transfer of heat to the surface is observed where the heat is lost by radiation. This loss of heat, which is not compensated in the upper-tropospheric levels, results in the continuous upward growth of the nocturnal inversion.

In the same way, momentum is transferred downward to the surface where it is dissipated most effectively. It is worth noting that in the levels above the inversion layer no appreciable radiational cooling has yet taken place and thus no loss of momentum is observed (Blackadar, 1957). Therefore, once the turbulent mixing stops late in the day, the frictional constraints are released and the overriding air tends to be decoupled from the underlying air. According to Blackadar (1957), in the layer above the inversion, the imbalance between the pressure gradient force and the Coriolis force induces the wind vector to take part in an inertial oscillation, which leads to supergeostrophic values of the wind several hours later (Stensrud, 1996).

For simplicity, we assume that the horizontal pressure gradient is constant in time and that the motion is completely horizontal. Then, above the nocturnal inversion, the horizontal equations of motion can be written as:

$$\frac{\partial}{\partial t}(u - u_{geo}) = f(v - v_{geo}) \tag{2.9}$$

$$\frac{\partial}{\partial t}(v - v_{geo}) = -f(u - u_{geo}), \tag{2.10}$$

where u, v are the horizontal components of the actual wind, u_{geo}, v_{geo} are the horizontal components of the geostrophic wind and f is the Corioris parameter (Blackadar, 1957). If we differentiate equation 2.9 with respect to time and substitute from equation 2.10 we get:

$$\frac{\partial^2}{\partial t^2}(u - u_{geo}) = f\frac{\partial}{\partial t}(v - v_{geo}) = -f^2(u - u_{geo}). \tag{2.11}$$

Similarly, $\frac{\partial^2}{\partial t^2}(v - v_{geo}) = -f^2(v - v_{geo})$. The last two expressions have solution of the form: $(u - u_{geo}) = A\sin(ft + \alpha)$ and $(v - v_{geo}) = A\cos(ft + \alpha)$ and, thus, the period of an inertial oscillation is given as follows:

$$T = 2\pi/f, \tag{2.12}$$

where the Corioris parameter is $f = 2\Omega\sin\phi$. Therefore, the period of an inertial oscillation depends on the geometrical parameters ϕ and Ω, where ϕ is the latitude and Ω is the Earth's rotation rate (e.g. Bonner, 1968; Egger, 1999). For example, the period of an inertial oscillation near latitude 30 °N is 1 day (e.g. Bonner, 1968).

According to Blackadar (1957), the solution and geometric interpretation of equations 2.9 and 2.10 are facilitated by introducing the complex number $W = (u - u_{geo}) + i(v - v_{geo})$ which, when plotted in the complex plane, provides a vector representing the deviation from the geostrophic wind. Equations 2.9 and 2.10 then can be written as

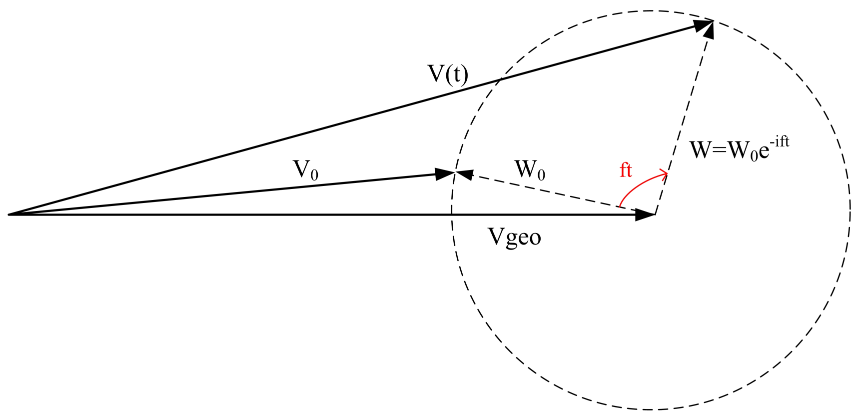

FIGURE 2.5: Relation of the complex number $W = W_0 \exp^{-ift}$ and the wind vector $V(t)$ to the initial values W_0, V_0, and the geostrophic wind vector V_{geo} at about sunset above the top of the nocturnal inversion during a frictionally initiated inertial oscillation. Note the clockwise rotation of the wind with time. Redrawn from Blackadar (1957).

$\frac{\partial W}{\partial t} = -ifW$ and give a solution of the form $W = W_0 \exp^{-ift}$, where W_0 is the deviation at the initial time (about sunset). Figure 2.5 shows the type of motion which the solution W represents above the top of the nocturnal inversion. It is worth noting that clockwise rotation of the wind with time is a characteristic of inertial motions (see Figure 2.5).

Baroclinicity over sloping terrain: Holton (1967) described the LLJ development as a response to the daytime heating and nighttime cooling of mountainous sloping terrain, which results in a diurnal variation in thermal wind and a consequent oscillation in the surface geostrophic wind.

The thermal wind relations are used in this section to determine the change in wind with height (vertically) and relate this change to the change in temperature (horizontally). The thermal wind relations are:

$$\frac{\partial u_{geo}}{\partial z} = -\frac{g}{f\overline{T}}\frac{\partial \overline{T}}{\partial y} \tag{2.13}$$

$$\frac{\partial v_{geo}}{\partial z} = \frac{g}{f\overline{T}}\frac{\partial \overline{T}}{\partial x} \tag{2.14}$$

where f is the Coriolis parameter, $\overline{T}$ is a layer-mean temperature, g is the gravity at the Earth's surface, u_{geo} and v_{geo} are the geostrophic wind components in the east-to-west and north-to-south direction, respectively (Andrews, 2000). To develop a simplified version of the LLJ, we consider only the north-to-south geostrophic wind component. From equation 2.14, if x increases and temperature decreases from west-to-east, then $\frac{\partial \overline{T}}{\partial x} < 0$ and the winds will decrease with height. Alternatively, if x and temperature increase from west-to-east, then $\frac{\partial \overline{T}}{\partial x} > 0$ and winds will increase vertically. Consequently, for a

LLJ to develop, a horizontal temperature gradient must exist with higher temperatures to the east (Piety, 2005).

In a mountainous sloping terrain, a slice of the atmosphere parallel to sea level is much closer to the ground at the higher terrain. During the day solar insolation warms the ground and, therefore, the lower atmosphere warms the most. When the mountain slopes are heated by the Sun, the air is warmer to the west over higher elevations than the air to the east well above the surface over the lower terrain. In this situation, a mixed layer is formed so that west-to-east temperature gradient is negative near the ground and aloft. By equation 2.14, we expect a gradually decrease of the southerly geostrophic wind with height. At night, this situation reverses. When radiational cooling occurs at the surface, the ground and the air near the surface cools more quickly that the air at higher altitudes. The air over the high terrain is also cooler than the air that is away from the mountain slopes and over the plain. As a result, the west-to-east temperature gradient is positive near the ground. The diurnal cycle in the horizontal temperature gradients results to a periodic variation in the geostrophic wind components through the thermal wind relationship. In the layers in which there is a strong temperature inversion, geostrophic winds increase with height. The decrease in wind speed near the ground because of friction and the lack of mixing during the night lead to a LLJ formation at the level of the temperature inversion. The stability of the air at night below the inversion helps the LLJ to persist (e.g Stensrud, 1996; Piety, 2005; Wallace and Hobbs, 2006).

Isallobaric forcing: In 1979, Uccellini and Johnson studied a case where the development and the magnitude of LLJs were influenced by upper-level jet streaks. In particular, coupling of upper- and lower-tropospheric jet streaks through mutual mass–momentum adjustments and vertical circulations within the exit region of an upper-level jet streak was observed. The formation of LLJs due to the transverse circulations that are associated with the upper-tropospheric jet streaks depends on the low static stability, the strong forcing, the orography and the surface heating, which allow the ageostrophic winds to become very strong. When an upper-tropospheric jet streak moves over a region of low static stability, such as the Great Plains of the United States, vertical motions and low-level convergence are usually produced because of an intense surface heating. In particular, Uccellini and Johnson (1979) found that the surface wind speed gains a component of acceleration perpendicular to and also to the right of the ageostrophic wind component. The LLJs are enhanced because of the increased isallobaric (ageostrophic) wind component in the low altitudes (e.g. Uccellini and Johnson, 1979; Stensrud, 1996).

Apparently, a number of different physical mechanisms can be used to explain the development, intensity, location and frequency of LLJs. Usually, none of these mechanisms alone can explain the LLJ formation, but a combination of the aforementioned mechanisms yields the best understanding of the observed LLJ worldwide. Given that the LLJ is a nighttime feature with a short temporal scale, measuring the LLJ has historically been difficult. This lack of observations made it difficult to examine the NWP models' performance to simulate the development and evolution of LLJs. Fine-scale continuous wind observations and a good understanding of the physical mechanisms underlying the LLJs offer a chance to a more accurate and complete numerical modelling of the LLJs (Stensrud, 1996). However, the accurate forecasting and numerical modelling of LLJs' with NWP models is still a challenging task because our understanding and modelling capability of stable boundary layers is limited (e.g. Cuxart *et al.*, 2006; Storm *et al.*, 2009). The modelling of stable boundary layers presents a particular challenge due to their low turbulence levels and the lack of a well-defined theory to describe their structure (Brooks *et al.*, 1999). However, a next-generation NWP model, the Weather Research and Forecasting (WRF) model, has the potential to forecast the development, intensity and location of LLJs because several studies have demonstrated the ability of this model to simulate such weather events (e.g. Storm *et al.*, 2009).

2.3 The surface energy balance

The surface energy balance drives the diurnal variation in the ABL. Sensible, latent and ground heat fluxes in addition to radiative fluxes are examined in this section. Further information on the radiative and turbulent fluxes may be found in many texts, such as Pitman (2003), Wallace and Hobbs (2006) and Marshall and Plumb (2008).

Solar (or shortwave) radiation emitted by the Sun is modulated by the Earth's rotation, resulting in a diurnal cycle of the shortwave radiation, which is zero at night and peaks at local noon (Wallace and Hobbs, 2006). A portion of the solar radiation (at wavelengths of the visible spectrum) is absorbed, reflected and transmitted by the atmosphere. The Earth's surface also absorbs an amount of the incoming shortwave radiation ($S\downarrow$), some of which is reflected back upward ($S\uparrow$) and is determined by the surface albedo a (the surface reflectivity of Sun's radiation). The surface albedo varies with geographic region, vegetation, time of the year, snowfall, clouds and precipitation. For example, albedos of typical surfaces vary from 0.95 for surfaces covered with fresh snow to approximately 0.02-0.1 for ocean, whereas the mean Earth albedo (planetary albedo) takes the value of approximately 0.3 (Marshall and Plumb, 2008).

Both the Earth's surface and the atmosphere emit longwave (or infrared) radiation. The amount of the longwave radiation that is emitted is a function of the temperature of the radiating body. Therefore, the longwave radiation depends on the Earth's skin temperature, surface emissivity, atmospheric temperature, cloud cover and water vapour profile (Pitman, 2003). The net heat transfer through longwave radiation is the sum of the emitted and absorbed infrared radiation. The longwave radiation is emitted upward with flux magnitude ($L\uparrow$) and received with flux magnitude ($L\downarrow$) by the Earth's surface. During the day, the incoming shortwave radiation usually offsets the longwave radiative cooling. At night, when shortwave radiation is zero, the net radiation is simplified to the difference between the incoming infrared radiation emitted by the atmosphere and the outgoing longwave radiation emitted by the surface (Wallace and Hobbs, 2006). In general, the sum of the inputs (incoming shortwave and downward longwave radiation) to the surface minus the outputs (reflected solar and emitted infrared radiation) yields the net radiation R_N absorbed at the Earth's surface:

$$R_N = S\downarrow - S\uparrow + L\downarrow - L\uparrow = S\downarrow(1-a) + L\downarrow - L\uparrow\,. \tag{2.15}$$

A sketch of contribution of the radiation fluxes at the Earth's surface toward the net radiation during a daily cycle is provided in Figure 2.6. As sketched in Figure 2.6 during a 24-hour period the solar and terrestrial radiation, and subsequently the net flux, vary on the Earth's surface. Before dawn there is no shortwave radiation, but the Earth radiates heat at a rate determined by the surface temperature; for example, the longwave radiation decreases as the skin temperature falls (via the Stefan-Boltzmann law). After dawn, the incoming solar radiation, which depends upon the daytime, latitude, altitude, terrain and season, increases as the Sun gets higher in the sky. As soon as the shortwave radiation exceeds the outgoing longwave radiation the surface temperature begins to rise. At the local noon, the solar irradiance reaches its peak and subsequently decreases and falls to zero once the Sun has set. However, because the surface temperature continues to rise until the longwave radiation becomes greater than the shortwave, the net radiation flux becomes negative during the night and increases during the day with positive values (that imply incoming radiation to the surface) and a peak near solar noon (Wallace and Hobbs, 2006).

Given 100 units of incoming energy (which represents the 342 W m^{-2} of incident solar radiation averaged over the Earth's surface), Figure 2.7 shows the partition of energy gain or loss at the Earth's surface and atmosphere. As seen in Figure 2.7, of the 100 units incident solar radiation on the top of the atmosphere, 19 are absorbed by water vapour, dust and ozone and 4 by the clouds in the troposphere. A total of 31 units (the Earth's albedo) are reflected back to the space: 6 from the surface, 17 from clouds and 8 are backscattered by air. The Earth absorbs energy by a combination of longwave radiation and turbulent fluxes (sensible and latent heat fluxes). The Earth's surface emits 115 units of longwave radiation and 31 units are exchanged as latent and sensible heat fluxes.

In addition to the radiative fluxes, the surface and the atmosphere exchange heat through the sensible and latent heat fluxes mentioned above. A temperature difference between the surface and the air above leads to a heat energy transfer known as sensible

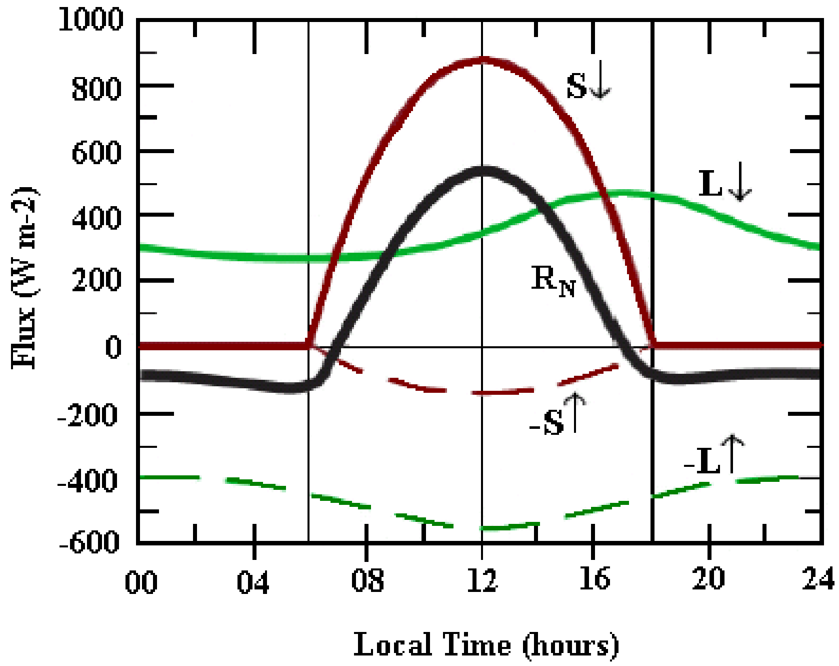

FIGURE 2.6: Sketch of contribution of radiative fluxes at the Earth's surface toward the net radiation, R_N, during a daily cycle under clear skies. Positive values show inputs toward the surface ($S\downarrow$ and $L\downarrow$ represent received shortwave and longwave radiation, respectively); negative are fluxes away from the surface ($-S\uparrow$ and $-L\uparrow$ represent emitted shortwave and longwave radiation, respectively). Redrawn from Wallace and Hobbs (2006).

heat flux (or thermal). Sensible heat flux (F_S) is the flux of heat from the Earth's surface to the atmosphere by conduction and convection. For example, with a warm surface and a cooler atmosphere, at the ABL heat will be conducted into the atmosphere and then convection will move the heat higher up into the atmosphere. Therefore, the sensible heat flux directly warms or cools the ABL air. In particular, positive sensible heat transfer is observed when the surface is warmer than the air above, which results in an air temperature increase and surface temperature decrease. Alternatively, negative sensible heat transfer is observed when the surface is cooler than the air above, which results in an air temperature decrease and surface temperature increase (Wallace and Hobbs, 2006). The sensible heat flux, which depends on the wind speed and the air–surface temperature difference, can be estimated using the bulk formula:

$$F_S = \rho c_p c_h (T_s - T_{air})U, \tag{2.16}$$

where ρ is the air density, c_p is the specific heat of air at constant pressure, c_h is a stability dependent transfer coefficient for heat (known as bulk transfer coefficient), T_s is the surface skin temperature, T_{air} and U are the air temperature and wind speed at standard surface measurements heights (2 and 10 m, respectively). A typical value of the

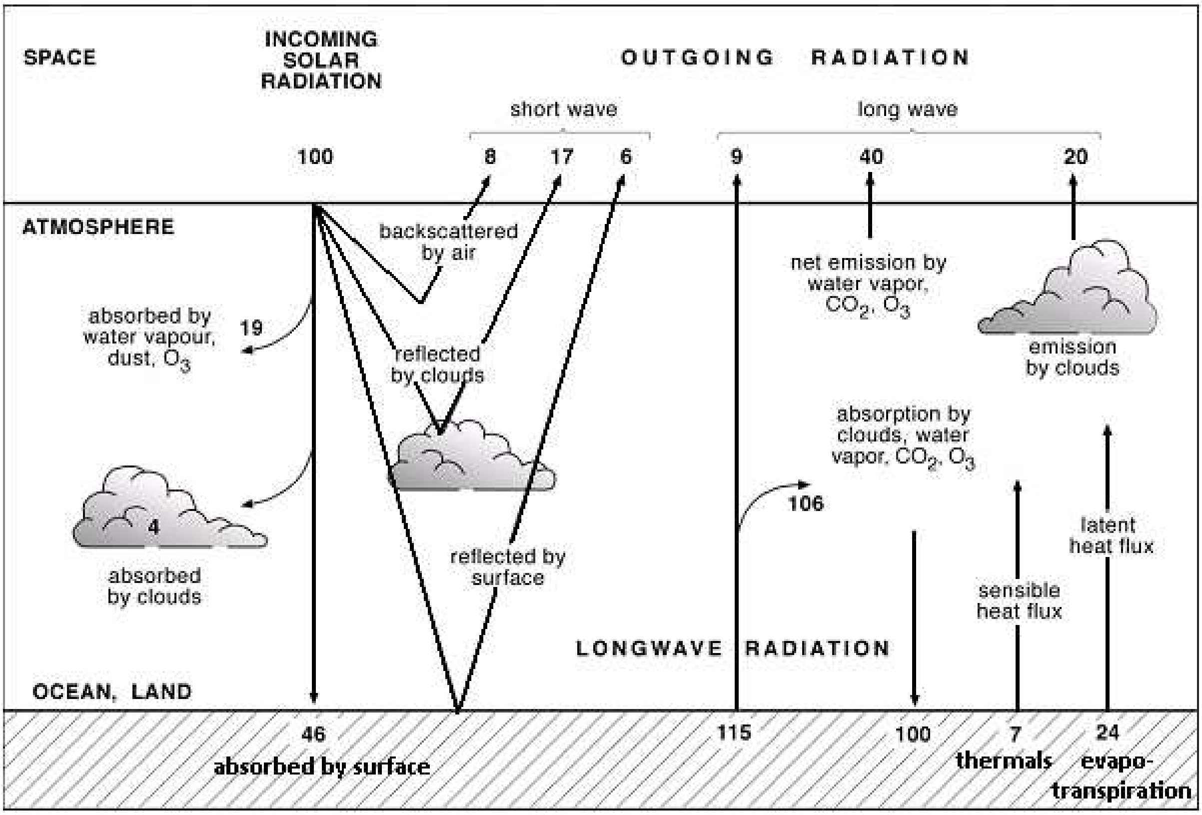

FIGURE 2.7: Schematic diagram of the annual mean global energy balance. The 100 units of incoming solar radiation represent the 342 W m^{-2} of incident solar radiation averaged over the Earth's surface. The shortwave fluxes are positioned on the left-hand side and the longwave fluxes are shown on the right-hand side. Redrawn from Pitman (2003).

bulk transfer coefficient, under statically neutral (unstable) conditions over the surface, ranges from 0.001 to 0.005 (0.003 to 0.015). However, the exact value of the bulk transfer coefficient is determined by the roughness length. Under statically stable conditions the reduced turbulence causes c_h to decrease toward zero (e.g Wallace and Hobbs, 2006; Marshall and Plumb, 2008).

Latent heat flux (F_L) is the process where heat energy is transferred from the Earth's surface to the atmosphere by evaporation and/or transpiration of water at the surface and subsequent condensation of water vapour higher up in the atmosphere. Positive latent heat transfer is observed when evaporation is taking place and the surface is losing energy to the air above, which results in a surface temperature decrease. The latent heat fluxes are released into the atmosphere mainly when the water vapour condenses in clouds (Wallace and Hobbs, 2006). The latent heat flux, which depends on the wind speed and relative humidity, can be estimated by the following equation:

$$F_L = \rho\lambda c_E(q_{sat}(T_s) - q_{air})U, \tag{2.17}$$

where λ is the latent heat of evaporation, c_E is the stability dependent bulk transfer coefficient for moisture (typical value: 0.001), $q_{sat}(T_s)$ is the specific humidity at saturation which depends on surface skin temperature and q_{air} is the specific humidity (e.g Wallace and Hobbs, 2006; Marshall and Plumb, 2008).

Heat energy also is transferred between the surface and the subsurface when a temperature gradient exists between the two. In particular, when the surface is warmer than the subsurface, heat is transferred downwards as a positive ground heat flux G. Alternatively, when the surface is cooler than the the subsurface, heat is transferred upwards as a negative ground heat flux. The ground heat flux can be estimated by the following equation:

$$G = -K\frac{dT_s}{dz}, \tag{2.18}$$

where K is the thermal conductivity and z is the soil depth (e.g Wallace and Hobbs, 2006; Marshall and Plumb, 2008).

The energy transfer to and from the surface varies over the course of the day. As previously mentioned, during the day positive net radiation values occur when incoming radiation exceeds outgoing radiation, which allows the surface to gain energy. This available energy is used to transfer heat upwards to warm the air above the surface, to evaporate water into the air in order to raise the air's humidity and to transfer heat downwards into the subsurface. At night this process is reversed (Wallace and Hobbs, 2006). The sensible heat flux F_S (positive upward into the air), the latent heat flux F_L (positive upward into the air) and the soil heat flux G (positive downward into the ground) balance the net radiation with the following equation:

$$R_N = F_S + F_L + G. \tag{2.19}$$

The exchange of sensible and latent heat with the atmosphere is partially influenced by the physical/climatic parameters (including temperature, wind speed and evaporation) and the land surface characteristics (including albedo, roughness length and leaf area index) of an area (Pitman, 2003). According to Pitman (2003), any land-use/land-cover modifications associated with changes in the key land surface parameters could be expected to affect the surface–atmospheric exchanges. For example, principal factors that influence the global distribution of vegetation are dependent on the incident solar radiation; temperature; rainfall and the occurrence of drought; cloudiness; potential evapotranspiration; wind; soil texture; land form, use and management (e.g OAS, 1991; Wallace and Hobbs, 2006). On the other hand, the terrestrial land also influences the climate through the hydrological cycle (e.g. the temperature can change by plants' evapotranspiration), the surface albedo (e.g. snow-covered forest is more reflective and, thus, cooler during the day than a snow-free forest) and the roughness length of the surface (e.g. 10 m wind speeds can be larger over the desert than over the forest).

2.4 Land-use/land-cover changes

Humans have continually altered the Earth's landscape and geographical distribution of grasslands, forests, wetlands and deserts for centuries. Semi-natural and man-made surfaces have been produced with the increase of urbanisation, tree removal, logging, forest fires, clearing wetland and expanding agriculture. Any modifications of the Earth's landscape (e.g. deforestation, desertification, afforestation) are associated with land-cover changes, such as shifts in surface albedo, leaf area index (LAI) and aerodynamic roughness length (Wichansky *et al.*, 2008). These changes modulate the energy, radiation and soil moisture budgets, which in turn affect the exchange of sensible and latent heat to the atmosphere (e.g. Pitman, 2003; Wichansky *et al.*, 2008). After Pitman (2003), conceptual diagrams of the effects of a decreased albedo and increased roughness length (as a result of increased vegetation coverage) on the surface energy budget and boundary layer are provided in Figure 2.8 and Figure 2.9, respectively. Note that the reduction or growth of vegetation is influenced by water availability, while the increase or decrease of vegetation also feeds back to affect the local and regional water balance (Yang *et al.*, 2009). A clear understanding of the vegetation–atmosphere–water interactions is essential for a wide range of fields, including meteorology, climatology, hydrology, water and land management and distribution (e.g. Gates and Liess, 2001; Angelini *et al.*, 2011).

The idea that land-use/land-cover modifications, in some way, influence and control the climate and hydrology has a long history (Angelini *et al.*, 2011). During the past four decades (since the mid 1970s), several observational and numerical studies have mainly focused on the way urbanisation, deforestation, reforestation, afforestation, and desertification affect the local, regional and global climate and hydrological cycle (e.g. Xue, 1993; Zheng and Ni, 1999; Chagnon *et al.*, 2004; Wichansky *et al.*, 2008; Bollasina and Nigam, 2011). Numerous sensitivity experiments of land surface–atmosphere interactions with mesoscale, general circulation and climate models have been conducted lately because of the advent of high performance computing (Angelini *et al.*, 2011). A brief review of deforestation, desertification, urbanisation and afforestation studies is provided in the following subsections.

2.4.1 Review of deforestation studies

Although it is widely recognised that large- and regional-scale land-cover changes can significantly alter the regional climate and the large-scale atmospheric processes, the effects of deforestation (forest or tree removal where the surface is thereafter converted to a non-forest area) on climate are not yet well understood (Kanae *et al.*, 2001).

Zheng and Eltahir (1997) studied the response of the West African monsoon to deforestation along the southern coastal areas of West Africa. It was found that deforestation lead to a complete collapse of the monsoon circulation and to a significant reduction in precipitation. A modelling study of Zhao and Pitman (2002) in Europe and India explored the impact of forest-to-crop changes which resulted in summer daytime evaporation enhancement and midday temperature decreases due to an increase in albedo and a decrease in minimum stomatal resistance. In contrast, Pitman *et al.* (2004) with their modelling study in Australia showed changes in the boundary layer structure, a temperature increase and a decline in precipitation and evaporation. Several sensitivity experiments have been conducted to address precipitation shifts as a result of large-scale deforestation in tropical regions [e.g. in the Amazon Basin and SE Asia by Henderson-Sellers *et al.* (1993); in the south-western United States by Zeng *et al.* (1996); in the Indochina Peninsula by Kanae *et al.* (2001); in the Amazon Basin by Chagnon *et al.* (2004) and D' Almeida *et al.* (2007); in global-scale by Bala *et al.* (2007)]. In general, tropical deforestation decreases evaporation and roughness length and increases surface radiation and temperatures (e.g. Zeng *et al.*, 1996; Bala *et al.*, 2007). Bala *et al.* (2007) conducted extreme global, tropical, temperate and boreal deforestation experiments. Their study suggested that complete tropical deforestation could result in global land mean warming by 0.9°C. In addition, Bala *et al.* (2007) showed that global, boreal and temperate deforestation could decrease the global temperatures. In one recent tropical deforestation study, Garcia-Carreras and Parker (2011) determined the impacts of vegetation–breezes interaction on precipitation that is locally generated in West Africa. Their results suggested a significant coupling between vegetation and locally-generated precipitation; rainfall increase over cropland was the main result of their study (Garcia-Carreras and Parker, 2011).

2.4.2 Review of desertification studies

A large number of numerical experiments have addressed the role of desertification (reduction or transformation of an arable or habitable land to a desert) on the climate. In 1975, Charney was one of the first researchers who showed that the high surface albedo of a desert could cause a decrease in precipitation (Charney, 1975). With their numerical study, Laval and Picon (1986) also observed lower rainfall and evaporation rates in addition to changes in circulation systems due to an increased albedo over Africa. Later, a sensitivity experiment was conducted by Xue and Shukla (1993) in order to show the reduction in rainfall and the changes in energy budget, circulation and hydrological cycle of the Sahel climate due to desertification. Xue (1996) investigated the impact of deser-

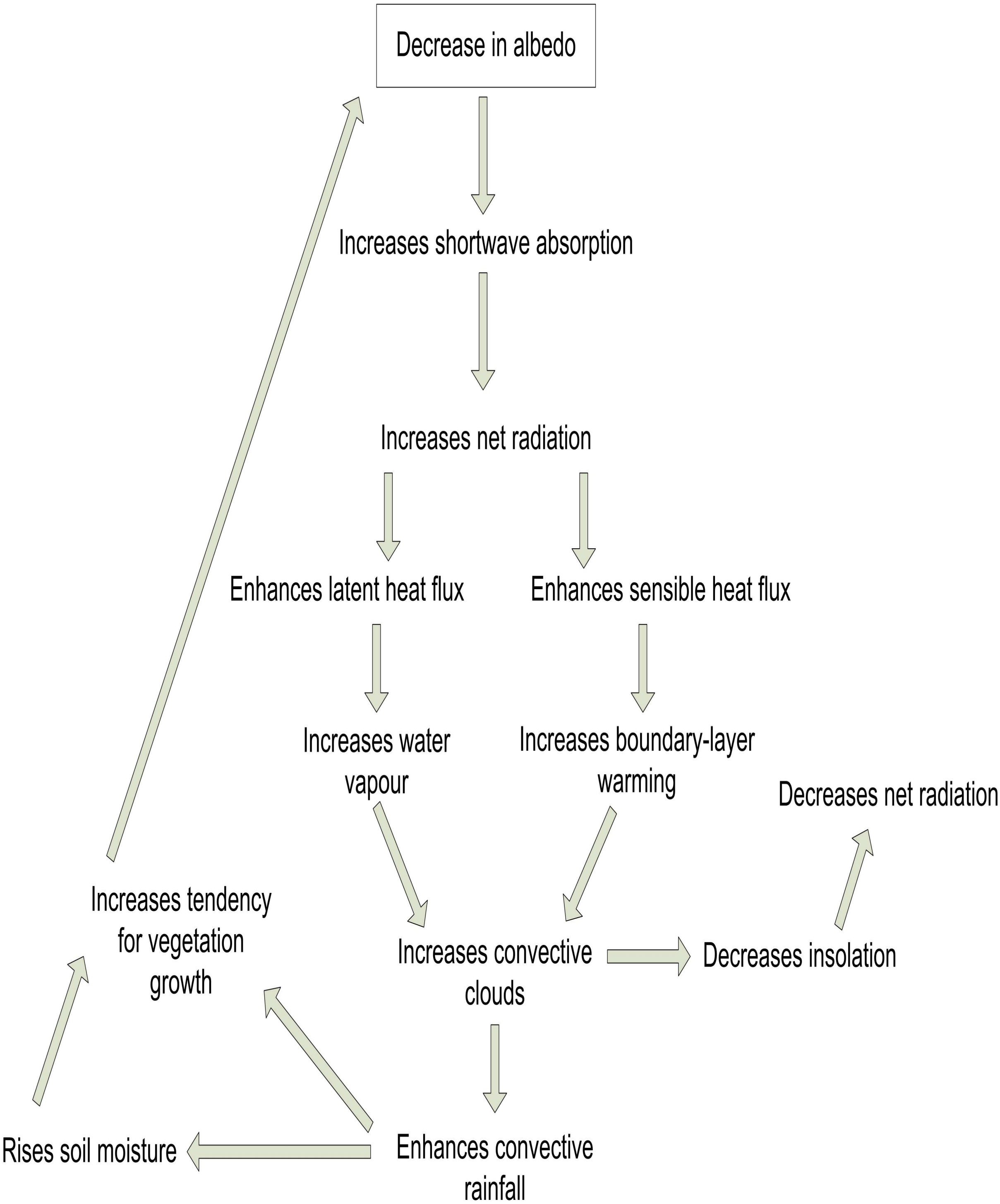

FIGURE 2.8: Conceptual diagram of the impact a decrease in albedo has on the surface energy budget and boundary layer. Redrawn after Pitman (2003).

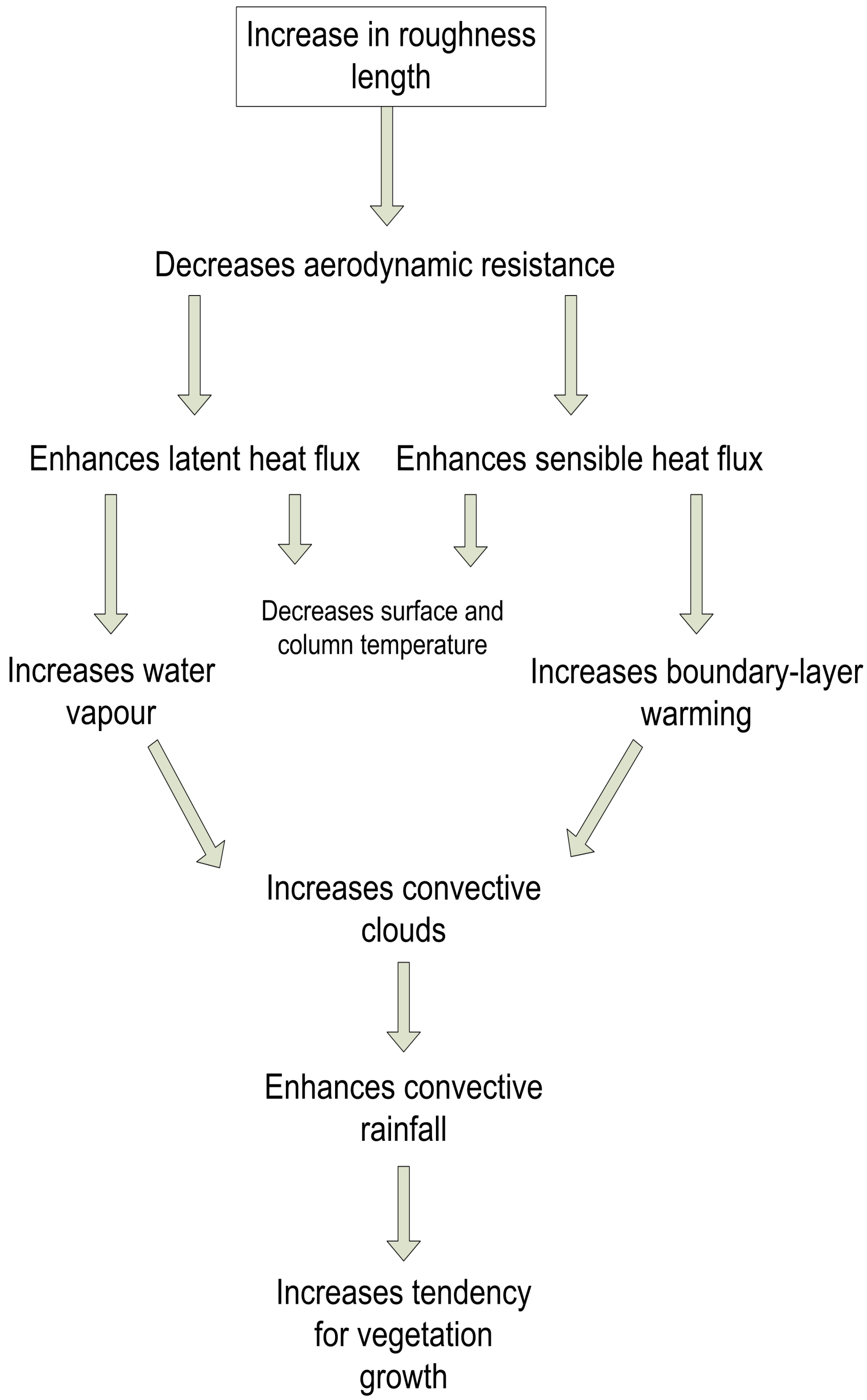

FIGURE 2.9: Conceptual diagram of the impact an increase in roughness length has on the surface energy budget and boundary layer. Redrawn after Pitman (2003).

tification in the Mongolian and Inner Mongolia areas and he observed evaporation and precipitation reduction and monsoon circulation weakening. These results were later confirmed by Purevjav and Luvsan (2004). Zheng and Eltahir (1997) studied the response of the West African monsoon circulation and regional (along the border with the Sahara) precipitation to the desert conditions. It is widely known that arid and semi-arid regions in China have experienced land-use modifications, such as desertification, which also reduced soil moisture and precipitation (e.g. Zheng and Ni, 1999; Wang and Takahashi, 1999). A general circulation model was used by Gates and Liess (2001) to determine the sensitivity of the local and regional climate to desertification (deforestation scenario that represented an extreme desert) in the Mediterranean basin. Decrease in evaporation, surface cooling and reduction in precipitation were their main results. Oyama and Nobre (2004) investigated the effects of a large-scale desertification in northeast Brazil. Locally, reduction in net radiation and hydrological cycle weakening (e.g. precipitation and evaporation decrease) were observed due to desertification. However, on a large-scale, desertification led to rainfall increase in the oceanic belt close to the study area. Finally, in one of the most recent studies of the desertification impacts on climate, Bollasina and Nigam (2011) used the WRF model to investigate the effects of an expanded desert on the South Asian summer monsoon circulation and to model the hydroclimate changes over the Indian subcontinent. In their study, the monsoon circulation and the atmospheric water cycle weakened because of desertification. Note that most of these studies have mainly focused on the impacts of desertification on precipitation, circulation and energy balance changes and not on potential evapotranspiration changes, which are crucial to understand the hydrological cycle.

2.4.3 Review of afforestation studies

For the past several years, numerical and observational afforestation (tree planting on surfaces where they have not recently existed) studies have been performed. Most studies showed that afforestation reduced the surface albedo and increased LAI, roughness length, solar radiation absorption by the ground and the net radiation. Therefore, sensible and latent heat transfer in the atmosphere were enhanced (e.g Bala *et al.*, 2007). The aforementioned changes also altered the surface temperature and wind speed, precipitation, evaporation, boundary layer, circulation patterns and large-scale weather systems (e.g Anderson *et al.*, 2011). In particular, Xue (1993) conducted a numerical experiment of the impacts of afforestation on the Sahel climate, which showed an increased precipitation in the tested area and decreased rainfall to the south of the afforested area. In 1996, Xue and Shukla also performed a numerical study in the sub-Saharan area in order to address the impacts of large-scale afforestation on the climate. According to their study, afforestation increased precipitation, latent and sensible heat fluxes and changed the mesoscale circulation (Xue and Shukla, 1996). Based on the Gates and Liess (2001) modelling study, afforestation in the Mediterranean basin led to an increase in precipitation and evaporation during the winter. Other afforestation modelling studies have shown a decrease in the diurnal temperature range and an increase in the dew-point temperature range (Wichansky, 2008). Jin *et al.* (2010) conducted sensitivity experiments with high and low LAI for the period 1983-2000 in order to explore the vegetation effects on the climate in northeast Tibetan Plateau. Their modelling results indicated that the deterioration of vegetation reduced the roughness length and resulted in more stable near-surface boundary layers.

2.4.4 Review of urbanisation studies

Urbanisation is considered the physical growth of urban areas. It is associated with population growth and the reduction or replacement of vegetated lands with urban areas. This removal of vegetative land tends to reduce soil moisture and creates less evaporative cooling which, in turn, allows surface temperatures to increase in cities, creating the *urban heat island* effect. The urbanisation effects on the local climate have been well studied and documented for several years (e.g. Adebayo, 1991; Changnon, 1992; Gallo *et al.*, 1996; Wichansky *et al.*, 2008), but are still not well understood (Wichansky *et al.*, 2008).

Although numerous modelling and observational studies have investigated the impact of afforestation, desertification, deforestation and urbanisation on atmospheric processes, the net influence of these land-cover changes on the local and regional climate in water-limited areas is still uncertain (Anderson *et al.*, 2011). In these water-limited environments, agriculture mostly depends on water availability, which results from the climate–hydrological interactions (Yang *et al.*, 2009). According to Dunn and Mackay (1995), land-cover changes have a direct impact on hydrology through its link with potential evapotranspiration (PET). Currently, there have been only a few observational and water balance studies that focus on the changes of PET, which is usually used to explore hydrologic impact and is important in studies relating to water supply and scarcity.

2.5 Potential evapotranspiration (PET)

PET is an important index in hydrology and in studies relating to water availability for agriculture. Accurate estimates of PET are needed to make sustainable regional terrestrial water distributions under changing conditions of climate and land-use (Shaw and Riha, 2011). Although PET has been extensively used and studied for more than half a century, a survey of the literature reveals that a number of different potential evaporation (PE) and PET definitions exist, varying from conditional descriptions to simple statements (Granger, 1989). PET is a calculated quantity and several calculation methods that are temperature and radiation based exist to estimate it.

2.5.1 PET definitions

Based on the work of Thornthwaite (1948), who introduced the PE term as a climatic index, PE represents the possible water transfer to the atmosphere under ideal vegetation and soil moisture conditions. Although PE was first introduced as a climatic index, it has been widely used in agriculture as a hydrological parameter (i.e. for the efficient use of water by different vegetation types) (Granger, 1989). PE is most commonly defined as the evaporation occurring over a free water surface (Mahrt and Ek, 1984); however, scientists do not always concur with this definition. According to Granger (1989), PE can be defined as the *evaporation rate which would occur if the surface was brought to saturation*; but this is not a practical definition. One of the widest used definitions is the Penman potential evaporation definition. Penman (1948) stated that PE is the *evaporation rate which would occur if the surface was brought to saturation and the atmospheric parameters and the energy supply to the surface were held constant* (Granger, 1989). To avoid any confusion between PE and PET definitions, according to Shuttleworth (1993), Wallace (1995) and Lhommel (1997), PET is defined by Penman (1956) as *the evapotranspiration rate from a short green cover completely shading the ground and adequately supplied with water in a given meteorological environment.*

2.5.2 PET calculation methods

A number of empirical methods have been developed by several scientists worldwide in order to estimate PET from different climatic variables. In 1948, Penman was accredited with the development of a radiation-based equation that uses standard meteorological variables and combines heat balance with mass transfer for estimating evapotranspiration from open-water surface or vegetation that is not water-limited. The Penman equation is the most widely used PET equation in hydrological and meteorological studies, although many studies are hard to compare because of the use of different versions of this equation (Mahrt and Ek, 1984).

For example, Monteith (1965) modified the Penman equation by using the aerodynamic and canopy resistance terms. This approach introduced the influence of vegetation on transpiration rates. Therefore, the Penman-Monteith equation is sensitive to vegetation specific parameters such as the stomatal resistance. The Penman-Monteith equation, which is often considered the most physically correct in hydrological and meteorological models, has a dependency on net radiation, air temperature, vapour pressure deficit, humidity and wind speed (Monteith, 1965). Because PET is computed from the aforementioned meteorological variables, any changes in these variables due to climate and land-cover changes are likely to change the value of PET (Chattopadhyay and Hulme, 1997). There is a consensus that the Penman-Monteith (Monteith, 1965) equation is capable of accurately reproducing these changes and can be applied to different land surfaces under varying climate conditions (e.g. Gao *et al.*, 2006; Shaw and Riha, 2011). However, one of the disadvantages of the Penman-Monteith approach is the parameterisation of the resistances. This is a problem that Priestley and Taylor (1972) tried to solve by introducing a simpler approach that uses a unitless constant related to soil moisture (Vinukollu *et al.*, 2011). The Priestley-Taylor equation was developed as a substitute to the Penman-Monteith equation to remove dependence on observations (Priestley and Taylor, 1972). For the Priestley-Taylor and Oudin (Oudin *et al.*, 2005) equations mainly observations for radiation are required. Mahrt and Ek (1984) also modified the Penman-Monteith relationship in order to include in the PET equation the effect of atmospheric stability on atmospheric transport of water vapour by using a stability-dependent aerodynamic resistance. According to Mahrt and Ek (1984), the aerodynamic resistance depends on an exchange coefficient for moisture which has a different form for stable and unstable cases. The dependence of the exchange coefficient for moisture on atmospheric stability is expressed in terms of a bulk Richardson (Ri) number (Mahrt and Ek, 1984).

Purely temperature-based methods, such as the Thornthwaite (Thornthwaite, 1948) and Hamon (Hamon, 1963) approaches are clearly more sensitive to temperature changes than the aforementioned radiation-based methods, and should be considered with caution (Shaw and Riha, 2011). A list of the aforesaid most widely used PET equations is provided:

Radiation-Based Equations

1. Penman (Penman, 1948)

$$PET = \frac{\Delta R_N + E_a \gamma}{\Delta + \gamma}, \tag{2.20}$$

   where PET is in mm d^{-1}; R_N is the net radiation (MJ m^{-2} d^{-1}); Δ is the slope of the saturation vapour pressure-temperature curve (kPa °C^{-1}); γ is the psychometric constant (kPa °C^{-1}); E_a is a parameter for the drying power of the air including wind speed and saturation deficit.

2. Penman-Monteith (Monteith, 1965)

$$PET = \frac{1}{\lambda}\left[\frac{\Delta(R_N - G) + k c_p \rho \frac{VPD}{r_a}}{\Delta + \gamma(1 + \frac{r_c}{r_a})}\right], \tag{2.21}$$

where PET is in mm d^{-1}; λ is the latent heat of vaporization (MJ kg^{-1}); G is the ground flux (MJ m^{-2} d^{-1}); k is a unit conversion (3.6×24 s d^{-1}); ρ is the density of water (kg m^{-3}); c_p is the specific heat of moist air (kJ kg^{-1} °C^{-1}); VPD is the vapour pressure deficit; r_c and r_a are the canopy and aerodynamic resistances (s m^{-1}), respectively.

3. Priestley-Taylor (Priestley and Taylor, 1972)

$$PET = \beta \frac{\Delta}{\Delta + \gamma}(R_N - G), \tag{2.22}$$

where PET is in mm d^{-1}; β is a unit-less constant (with a standard value of 1.26) reflecting equilibrium.

4. Oudin (Oudin *et al.*, 2005)

$$PET = \frac{R_S}{\lambda\rho}\left[\frac{T_{air} + 5}{100}\right], \tag{2.23}$$

where PET is in mm d^{-1}; R_S is the solar radiation as calculated from latitude and Julian day; T_{air} is the 2 m (or 10 m) air temperature (°C).

Temperature-Based Equations

1. Thornthwaite (Thornthwaite, 1948)

$$PET = \begin{cases} 0 & \text{if } T_{air} < 0°C \\ 1.6(\frac{10T_{air}}{I})^A & \text{if } 0 < T_{air} < 26.5°C \\ -27.7 + 2.15T_{air} - 0.029T_{air}^2 & \text{if } T_{air} > 26.5°C \end{cases} \tag{2.24}$$

where PET is in mm d^{-1}; $A = 6.75 \times 10^7 I^3 + 7.71 \times 10^{-5} I^2 + 1.79 \times 10^{-2} I + 0.4921$ is a 3^{rd}-order polynomial and I is the annual heat index computed from summing monthly heat indices $I = \sum_{i=1}^{12}(\frac{T_i}{5})^{1.514}$ where T_i is the mean air temperature for a given month i.

2. Hamon (Hamon, 1963)

$$PET = 29.8H_{day}\left[\frac{e_{sat}(T_{air})}{T_{air} + 273.2}\right], \tag{2.25}$$

where PET is in mm d^{-1}; H_{day} is the number of daylight hours; $e_{sat}(T_{air})$ is the saturation vapour pressure (kPa) at air surface temperature T_{air} (°C).

2.5.3 Review of PET studies

The aforesaid methods for estimating PET have been used, modified and compared by several researchers in order to study the impact of global warming and land-cover change on future water resources in many parts of the world. As described by Rind *et al.* (1990), a large future increase in drought over the United States by the 2050s is mostly driven by an increase in PET associated with the simulated climate warming. Based on six global climate change scenariors, Chattopadhyay and Hulme (1997) also found increased PET over most of the parts of India associated with the future warming. Contrary to these studies, Cohen *et al.* (2002) suggested that a climate warming will create a moister atmosphere, will enhance actual evaporation from the oceans and humid land surfaces and, in turn, will decrease PET. A modelling study was conducted by Herron *et al.* (2002) to investigate the impacts of afforestation and global warming on water resources, with regards to the context of precipitation and PET in a catchment in Australia. Their results indicated that water availability was mostly influenced by changes in the precipitation regime. A simple water balance model based on the Thornthwaite-Mather PET approach (Thornthwaite, 1948; Thornthwaite and Mather, 1955) was used by Trabucco *et al.* (2008) to show the impacts of global and local (Ecuador, Bolivia) afforestation/reforestation on the hydrological cycle.

The future water availability in Egypt, in the context of the Nile water resources, was studied by Conway and Hulme (1996) who used a water balance model to show the potential effects of global and local climate and land-use change. Comparison of the Nile water availability with demand projections for Egypt showed water deficits (surplus) by the 2025s, if the water demand for desert reclamation is (is not) considered. Later, Feddema (1999) used a water balance model based on the Thornthwaite-Mather PET approach in order to evaluate the effects of global warming and soil degradation (due to desertification) on future African water resources. Feddema (1999) indicated that the global warming is expected to dry the entire continent as a result of increased PET.

Wang and Jin (2006) analysed the water resources in north China and showed that the gardening and afforestation, with low precipitation and high PET, increased the water demands. Later, Sun *et al.* (2008) used the temperature-based Hamon approach (Hamon, 1963) to investigate the effects of vegetation coverage change on the water balance in southern China. A regional water balance modelling study also was conducted by Yang *et al.* (2009) in order to explore the impacts of different vegetation coverage on water budget in the non-humid regions of China. Their results have shown that the actual evapotranspiration changes were mainly controlled by rainfall and not by PET changes.

The temporal and spatial variation of PET is an aspect of particular interest. Numerous studies explored the impact of climate change on PET by using available climatic data of weather stations in Egypt (Ayyad, 1973), England (Dunn and Mackay, 1995), India (Chattopadhyay and Hulme, 1997), China (e.g. Thomas, 2000; Gao *et al.*, 2006; Liu *et al.*, 2008) and Turkey (Ozdogan and Salvucci, 2004). In one of the earlier studies, Ayyad (1973) used the Thornthwaite-Mather PET approach to provide an assessment of the water surplus for a study area in northern Egypt [averages of 15-year records (1950-1964) were used]. Dunn and Mackay (1995) focused on the spatial PET variation and the influence of land-cover change on catchment hydrology. In order to show how this PET variation impacts the hydrology of the Tyne Basin in NE England, the Penman-Monteith equation was used to predict PET. Chattopadhyay and Hulme (1997) explored the effects of recent and future climate change on PET. They analysed 50-years (1940-1990) of data in India to show decreasing PET during the recent years, although the increasing temperatures. These results are similar to those obtained later by Thomas (2000) and Gao *et al.* (2006) who found decreasing annual and monthly PET rates in some regions of China despite increasing temperatures. Both studies suggested that the temperature effects on PET changes are limited; sunshine, relative humidity and wind speed had greater impact on PET values than temperature (Thomas, 2000; Gao *et al.*, 2006).

The analysis of PET trends in different seasons over different land types (e.g. crop, mountainous, oasis, forest and urban regions) has also been a subject of several studies (e.g. Adebayo, 1991; Han *et al.*, 2009; Shaw and Riha, 2011). Adebayo (1991) in his observational study selected two urban sites and a typical rural site station in Nigeria to study the effects of urbanisation on temperature and PET. Adebayo (1991) found that PET was lower in the rural regions than in the city. Ozdogan and Salvucci (2004) used 23 years of meteorological observations to study the impacts of increasing crop irrigation in south-eastern Turkey on PET. The decreases in PET due to wind speed reduction and vapour pressure enhancement were their main results. Decreasing PET, because of reduction in the aerodynamic terms, in both mountainous and oasis regions in China was observed by Han *et al.* (2009). More recently, Shaw and Riha (2011) analysed meteorological and energy balance measurements from deciduous forests in the eastern United States in order to provide an assessment of different PET approaches. Based on their analysis, net radiation should be considered the primary climate factor that influences PET change. In one of the latest studies, Nizinski *et al.* (2011) focused on the water balance of two ecosystems (savannah and eucalyptus) in Congo, Africa. In their study, PET was calculated with the Penman formula (Penman, 1948) and their results showed that savannah had lower PET than eucalyptus for the period from 1996-1999.

It is worth noting that most of the research has been performed either on a global scale, or in regions with high human activity, such as China, India and the United States. However, none of these works have systematically simulated the PET changes in water-limited environments, such as the Nile Delta in Egypt, by using realistic meteorological models. Most of the aforesaid modelling studies have used simple surface-layer models and altered one parameter to study the model sensitivity of land-use change (Xue and Shukla, 1993). However, the real land-cover changes are complex processes and in order to properly simulate and study these changes someone needs to alter a large number of model parameters at one time to test the model sensitivity.

Chapter 3

Atmospheric Model and Input Data

A numerical weather prediction (NWP) and atmospheric simulation system, the Weather Research and Forecasting (WRF) model, Version 3, (Skamarock *et al.*, 2008) is presented in this chapter. The chapter proceeds with a section on the principal components of the WRF system, including the dynamics/numerics options, discretisation options, physics schemes that interact with the dynamics solvers and programs for initialisation. A description of the available global atmospheric re-analyses and topographic data that could be used as input datasets to a wide range of simulations with the WRF model is also provided. A presentation of the WRF properties and input data is required to identify and understand any limitations of the model and the datasets.

3.1 The Weather Research and Forecasting (WRF) Model

The WRF model has been developed via collaboration principally among the National Center for Atmospheric Research (NCAR), the National Centers for Environmental Prediction (NCEP), the National Oceanic and Atmospheric Administration (NOAA), and the Air Force Weather Agency (AFWA) for both research and operational applications (Skamarock *et al.*, 2008). Such applications include idealised simulations, real-time NWP, data assimilation and parameterisation research, regional climate simulations, forecast and hurricane research and coupled-model applications (Wang *et al.*, 2011). The WRF model consists of the following programs: the WRF Preprocessing System (WPS), the Advanced Research WRF (ARW) solver, the WRF-Var (variational data assimilation) and the post-processing and visualization tools. An initialisation program (real.exe) for real-time simulations, a numerical integration program (wrf.exe) and a program for one-way nesting (ndown.exe) are included in the WRF model code (Skamarock *et al.*, 2008). This chapter reviews in the following sections some of the principles of the WPS and the

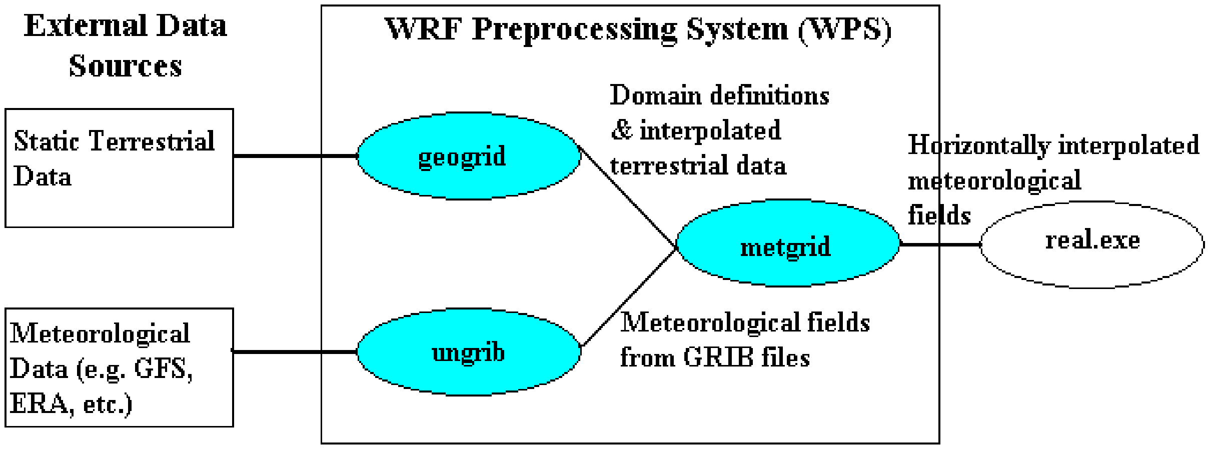

FIGURE 3.1: The data flow between the programs of the WPS (geogrid, ungrib and metgrid). The interpolated metgrid output are ingested by the program real of the WRF model. Redrawn after Wang *et al.* (2011).

ARW solver of the WRF model. Details and further information on the WRF model programs may be found in Skamarock *et al.* (2008) and Wang *et al.* (2011).

3.1.1 WRF Preprocessing System (WPS)

The aim of this section is to present and understand the purposes of the WPS and to describe how each component of the WPS works. The principle idea of the WPS is to prepare inputs to the ARW pre-processor program for real-data simulations by using meteorological and terrestrial data (Wang *et al.*, 2011). In particular, the WPS is a collection of Fortran and C programs and:

- defines the WRF model coarse and nested horizontal domains for simulation,
- horizontally interpolates time-invariant topographical data (e.g. land-use categories, soil type, terrain height) to simulation grids,
- computes map-scale factors for projections, latitude, longitude and Coriolis parameters at every grid point, and
- horizontally interpolates time-varying meteorological fields (e.g. wind, temperature, surface pressure) from another atmospheric models onto the defined simulation domains (Duda, 2011).

As indicated in Figure 3.1, the WPS is a set of three programs: the geogrid, ungrib and metgrid. The first program, geogrid, defines the model's simulation domain and horizontally interpolates various static terrestrial data (e.g. terrain height, land-use and soil categories, vegetation fraction and albedo) to the model grids. Map-scale factors and geographic location (latitude, longitude) are computed by the geogrid at every grid point (Wang *et al.*, 2011). The ungrib program reads GRIB (General Regularly-distributed Information in Binary) data [a World Meteorological Organization (WMO) standard file format for storing gridded fields], extracts the meteorological fields from these GRIB-formatted files and writes the requested fields to a simple format known as *intermediate format*. The metgrid program horizontally interpolates the meteorological data extracted by the ungrib program onto simulation domains generated by the geogrid program. This program also rotates wind components to the WRF model grid so that the westerly U and southerly V wind components are parallel to the x- and y-axis of the WRF modelling domain, respectively (Duda, 2011; Wang *et al.*, 2011).

The outputs from the WPS are passed to the real-data pre-processor in the ARW solver, known as the program real (real.exe), which generates the initial and lateral boundary conditions. The vertical interpolation of the meteorological fields is performed within the real program. The input to the ARW pre-processor is a complete three-dimensional snapshot of the atmosphere (Skamarock *et al.*, 2008). In particular, the WPS provides mandatory fields to the real program such as three-dimensional relative humidity, temperature and the horizontal components of momentum. Three-dimensional soil data (e.g. soil temperature and moisture), two-dimensional meteorological data [e.g. surface and sea-level pressure, surface u and v components, surface temperature and relative humidity, sea-surface temperature (optional but highly desirable field)], two-dimensional static data for the physical surface (e.g. terrain height) and two-dimensional data for the projection (e.g. Coriolis) are also provided (Skamarock *et al.*, 2008; Wang *et al.*, 2011).

The interpolation methods that can be used in both geogrid and metgrid programs are: four-point bilinear, sixteen-point overlapping parabolic, four-point and sixteen-point averaged (simple or weighted), nearest neighbour, breadth-first search and model grid-cell average interpolation. Different interpolation methods work best for different relative fields and different relative grid resolutions. It is worth noting that every interpolation method can handle masked points. Further information on the available interpolation methods may be found in Duda (2011) and Wang *et al.* (2011).

3.1.2 ARW Dynamics and Numerics

The ARW solver is also referred to as the Eulerian mass solver. The ARW dynamical solver supports a range of capabilities which include terrain representation, real-data and idealised simulations in global and regional scale, physics and filter options, digital filtering initialisation, several lateral boundary condition options, advection schemes, hydrostatic and non-hydrostatic options, nesting options, three-dimensional analysis and observation nudging (Skamarock *et al.*, 2008). In particular, the major features of the

ARW solver are listed below.

3.1.2.1 Equations, Vertical Coordinate, Map Projections

The ARW dynamics solver integrates the fully compressible, non-hydrostatic Euler equations with a run-time hydrostatic option available via a namelist option. The Euler equations are formulated using a terrain-following mass vertical coordinate, which is the typical η (or σ) coordinate used in many hydrostatic atmospheric models. The η coordinate ranges in value from one at the surface of the earth and decreases to a value of zero at the top of the atmosphere as defined by the WRF model. The surfaces in the η coordinate system follow the WRF model terrain and are steeply sloped in the regions where terrain itself is steeply sloped. The η coordinate system defines the vertical position of a point in the atmosphere as a ratio of the pressure difference between that point and the top of the domain to that of the pressure difference between a fundamental base below the point and the top of the domain. Therefore, the η coordinate is defined as

$$\eta = \frac{p - p_t}{p_s - p_t}, \tag{3.1}$$

where p is the pressure at a particular level in the atmosphere, p_s is the surface pressure below p, and p_t is the pressure at the top of the atmosphere above p. Note that the top of the WRF model is a constant pressure surface and the vertical grid spacing can vary with height (Skamarock *et al.*, 2008). The WRF model represents the Earth's atmosphere over a geographic region using a three-dimensional (x, y, z) grid. The horizontal dimensions (x, y) are in equally spaced Cartesian coordinates, while the third dimension z is over atmospheric vertical levels in the mass-based terrain-following coordinate (Michalakes and Vachharajani, 2008).

The ARW solver supports four map-scale factors for projections. For real-data simulation these are: polar stereographic (conformal), Lambert (conformal), Mercator (conformal) and latitude-longitude (allowing rotated pole). The ARW Version 3 release now supports isotropic projections (Lambert conformal, Mercator and polar stereographic) as well as anisotropic transformation (latitude-longitude grid). The isotropic transformation requires the $(\frac{\Delta x}{\Delta y})|_{earth}$ ratio to be constant everywhere on the model grid (Skamarock *et al.*, 2008). The polar stereographic projection is well-suited for high-latitude applications especially if the model domain contains a pole. The Lambert conformal projection is more suitable for mid-latitudes, whereas the Mercator projection is well-suited for low-latitudes. Finally, the latitude-longitude grid is suitable for global and large regional domain simulations (Duda, 2011; Wang *et al.*, 2011). Complete Coriolis and curvature terms are also included in the momentum equation, and their calculation methods differ between the isotropic and anisotropic projections (Skamarock *et al.*, 2008).

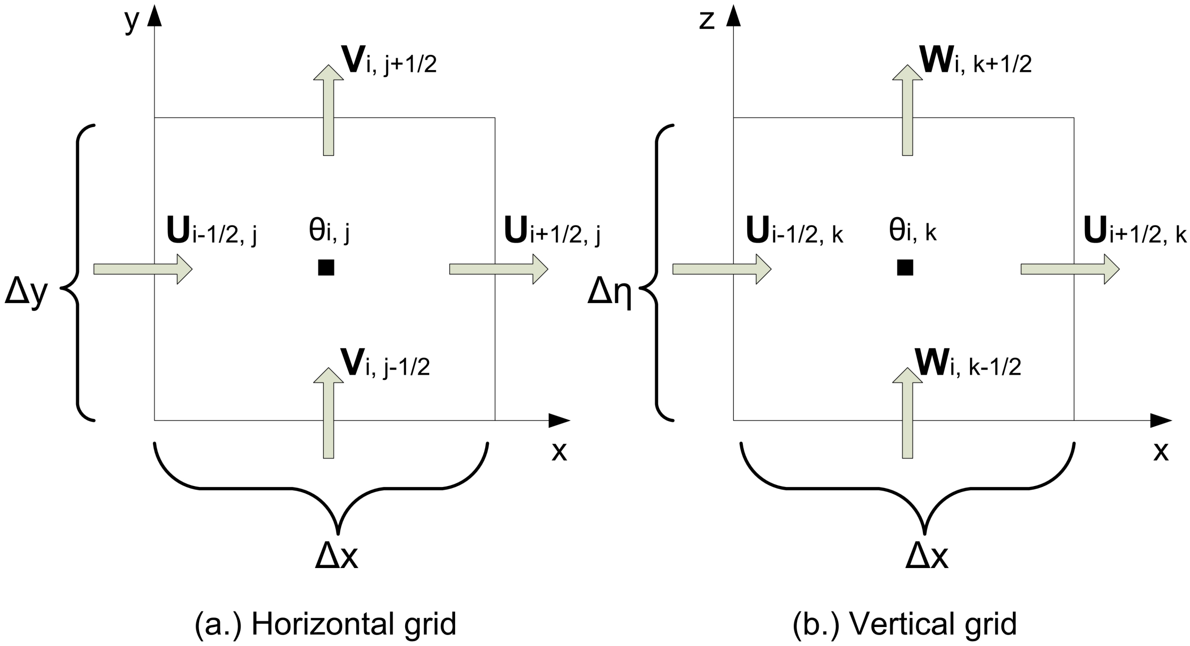

FIGURE 3.2: (a) Horizontal and (b) vertical grids of the ARW solver. The spatial discretisation in the ARW solver uses an Arakawa C-grid staggering. The variable indices, (i, j, k), show variable locations with $(x, y, \eta) = (i\Delta x, j\Delta y, k\Delta\eta)$. The wind components (U, V, W) are staggered one-half grid length from the thermodynamic variables (e.g. potential temperature, θ). Redrawn after Skamarock *et al.* (2008).

3.1.2.2 Model Discretisation and Advection

The ARW solver uses a third-order Runge-Kutta (RK3) time integration scheme which is third-order accurate for linear equations and second-order accurate for nonlinear. To sustain numerical stability, a time-split version of the RK3 scheme is used for the high-frequency acoustic and gravity wave modes. The time-splitting involves integrating terms associated with acoustic and gravity wave modes with smaller timesteps than the low-frequency modes (Skamarock and Klemp, 2008). In particular, the horizontally propagating acoustic modes and gravity waves are integrated using an explicit scheme (a forward-backward time integration scheme), while the vertically propagating acoustic modes and buoyancy oscillations are integrated implicitly (Skamarock *et al.*, 2008).

The WRF model uses an Arakawa C-grid staggering as spatial discretisation, which provides the most accurate representation of gravity waves (Skamarock and Klemp, 2008). On a staggered C-grid the westerly (U) wind component is evaluated at the centres of the left and right grid faces and the southerly (V) and vertically (W) wind components at the centres of the upper and lower grid faces (see Figure 3.2). The wind components (U, V, W) are staggered one-half grid length from the thermodynamic variables (e.g. potential temperature, θ). The diagnostic variables, such as the pressure (p) and inverse density $(a = 1/\rho)$, are computed at mass points (centre of the grids where θ is located in

Figure 3.2). In Figure 3.2(a), the minimum distance between adjacent grid points represents the horizontal model resolution. For a constant modelling domain, higher resolution means smaller grid cells which resolve more features and result to more computationally expensive models. Note that the horizontal grid lengths Δx and Δy are constant, while the vertical grid length $\Delta\eta$ is specified by the WRF user in the initialisation where η decreases monotonically with height (Skamarock *et al.*, 2008).

While the spatial discretization of the divergence and pressure gradient terms is second order and centered, second through sixth-order spatial discretisations of the advection (flux divergence) terms are available in the WRF model in both vertical and horizontal directions (Skamarock and Klemp, 2008). The fifth order horizontal and the third order vertical schemes are recommended by Wang *et al.* (2011). The odd-order advection schemes (dissipation) are upwind-biased, while the even-order schemes (no dissipation) are spatially centred. Positive-definite and monotonic advection schemes for moisture, scalar, turbulent kinetic energy (TKE) and chemical scalers are also available in the ARW solver. Wang *et al.* (2011) recommend the positive-definite advection option, which is beneficial for moisture variables in real-data simulations and improves the high precipitation bias in the WRF model by removing additional water mass. The monotonic option, which is better for chemistry applications, reduces diffusion, imposes consistency in mass advected over time and avoids spurious overshoots (e.g. Skamarock *et al.*, 2008; Wang *et al.*, 2011).

3.1.2.3 Turbulent Mixing and ARW Filters

Several formulations for turbulent mixing and filtering are available in the ARW solver. These include diffusion and damping options. The explicit spatial diffusion is categorized under three formulations which are: diffusion along coordinate surfaces (diffusion option), diffusion in physical (x, y, z) space (K option) and a sixth-order horizontal diffusion (Skamarock *et al.*, 2008). The diffusion option selects how the derivatives used in diffusion are calculated, and the K option determines how the K coefficients (the horizontal K_h and vertical K_v eddy viscosities) are calculated (Wang *et al.*, 2011). When a planetary boundary layer (PBL) option is selected the vertical diffusion is done by the PBL scheme and not by the diffusion scheme. In this ARW Version 3, vertical diffusion is also related to the surface fluxes (e.g. Skamarock *et al.*, 2008; Wang *et al.*, 2011). According to Skamarock *et al.* (2008), since vertical and horizontal mixing are treated independently the horizontal deformation or the constant horizontal K_h values are the most appropriate horizontal diffusion choices.

In order to prevent the WRF model from becoming unstable with locally strong vertical winds and to prevent unphysical reflections of gravity waves from model top, the upper damping option is available. This option offers either increased diffusion or Rayleigh relaxation or implicit gravity wave layer. To control horizontally (vertically) propagating sound waves, the divergence damping (time off-centering) has been found to be a very effective option. Finally, in order to control upper-surface waves, the external mode damping can be used (e.g. Skamarock *et al.*, 2008; Skamarock and Dudhia, 2011).

It is worth noting that a digital filtering initialisation (DFI) option is provided by this version of the ARW solver. By using DFI we are able to remove noise from the model initial state, which results from imbalances between wind and mass fields (Skamarock *et al.*, 2008).

3.1.2.4 Boundary Conditions

The lateral boundary conditions are specified from re-analysis data, global or regional models. Periodic, open (or gravity-wave radiative), symmetric (free-slip wall) and specified (coarse grid) lateral boundary conditions are available in the ARW solver. For real-data simulations the specified lateral boundary conditions are frequently used. In particular, the specified boundaries in the WRF model can be used with two ways: for the outer-parent (or coarse) domain or for the nested (see subsection 3.1.4) grid. The coarse grid specified lateral boundary includes both specified and relaxation zones. The specified zone is determined by temporal interpolation from an external file generated by WPS, and the relaxation zone is where the model is nudged towards the large-scale forecast. The width of the specified zone and the size of the relaxation zone are run-time options. For nesting options, the nest lateral boundary conditions are specified by the coarse domain at every parent-grid timestep and the relaxation zone is inactive (Skamarock *et al.*, 2008).

The WRF model bottom boundary condition is defined by the land surface model, while constant pressure is set at the top boundary condition. Gravity wave absorption by diffusion or Rayleigh damping can be also used at the top (Skamarock *et al.*, 2008).

3.1.3 WRF Physics

This subsection describes the physical parameterisation package of the WRF model. After all the explicit dynamical and numerical computations per time-step are performed, the physics schemes are called by the WRF model. These physics schemes are divided into several categories: radiation, land-surface model, planetary boundary layer, cumulus and microphysics, each containing several choices (see Figure 3.3). Turbulence and diffusion described in subsection 3.1.2 are also considered part of the physics. An analytic description of the physics parameterisation is provided by Skamarock *et al.* (2008), Dudhia (2011a) and Wang *et al.* (2011).

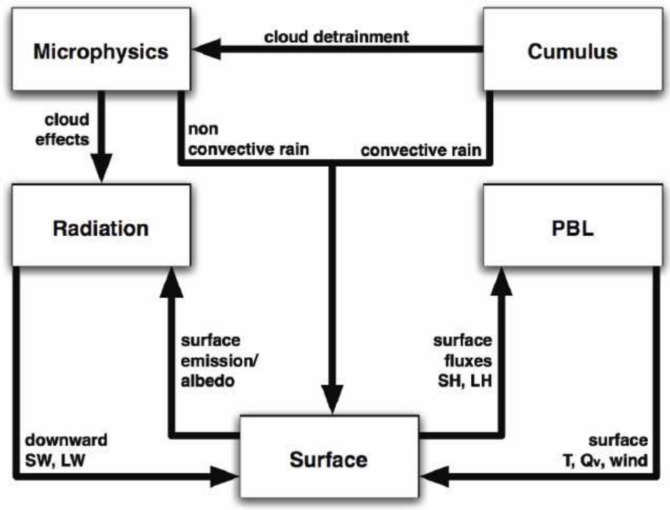

FIGURE 3.3: A schematic of the direct interaction of the WRF model's physical parameterisation package. Taken from Dudhia (2011a).

3.1.3.1 Radiation physics

The main forces that regulate the surface energy budget are the radiative fluxes (shortwave and longwave radiation). In meteorological models, such as the WRF model, the surface temperature and PBL height depend on the accurate representation and calculation of these radiative fluxes (Xiu *et al.*, 2011).

The radiation schemes in the WRF model provide atmospheric temperature tendencies in the simulated model domains and surface radiative (downward longwave and shortwave) fluxes for the surface heat budget (Skamarock *et al.*, 2008). In the WRF model, the radiation schemes are treated as a one-dimensional vertical column, where each column is treated independently. It is worth noting that the infrared spectrum is too big for computing absorptivity at each line, so radiation schemes divide infrared spectrum into bands (usually 8 to 19 bands) dominated by different absorption gases. The radiation schemes also take into account cloud–radiation interactions by using the values of cloud fraction and ice/liquid water content from the available WRF cloud schemes. In particular, the WRF model offers cloud fractions derived from relative humidity. The cloud fraction usually receives values between zero (not cloudy) and one (cloudy) in a model grid box (Dudhia, 2011a). For multiple layers of varying fraction overlap assumptions (random, maximum and maximum-random overlap) are also needed. Most of the WRF radiation schemes use maximum-random overlap (maximum for neighbouring cloudy layers and random for layers separated by clear air). Note that radiation schemes are one of the most expensive schemes in the WRF model, so only called every few timesteps (e.g. Skamarock *et al.*, 2008; Dudhia, 2011a; Wang *et al.*, 2011).

Shortwave radiation mostly includes visible wavelengths and uses astronomical equations to compute the Sun's position as a function of daytime and day of the year relative to a position on Earth (Dudhia, 2011a). Therefore, the shortwave radiation option in the WRF model includes diurnal and annual solar cycles, and it computes shortwave fluxes under clear-sky and cloudy conditions. The solar radiation is absorbed, reflected and scattered in the Earth's atmosphere and surface. Most solar flux schemes consider both downward and upward fluxes, where the upward shortwave radiation is reflection due to surface albedo (e.g. Skamarock *et al.*, 2008; Dudhia, 2011a). The available shortwave radiation options in the WRF model are:

- The Dudhia scheme (Dudhia, 1989): simple downward calculation (integration) of shortwave flux; allows for water vapour and cloud absorption, clear-sky scattering and cloud albedo; no ozone effect; for high-resolution regional simulations allows for terrain slope and shadowing effects on the surface shortwave radiation. This scheme is computationally efficient because it uses look-up tables for clouds (e.g. Skamarock *et al.*, 2008; Dudhia, 2011a; Wang *et al.*, 2011).

- The Goddard shortwave scheme: spectral method (11 spectral bands); cloud effects (scattering and absorption of cloud water droplet); can handle trace gases such as ozone from their own climatologies; carbon dioxide is fixed (e.g. Skamarock *et al.*, 2008; Wang *et al.*, 2011).

- The GFDL (Geophysical Fluid Dynamics Laboratory) shortwave scheme: an Eta operational scheme (12 spectral bands); ozone, carbon dioxide and atmospheric water vapour effects are considered (e.g. Skamarock *et al.*, 2008; Wang *et al.*, 2011).

- The CAM scheme [from the NCAR Community Atmosphere Model (CAM 3.0) used for climate predictions]: spectral method (19 bands); is well-suited for regional climate simulations; has the ability to handle aerosols and trace gases (Skamarock *et al.*, 2008; Xiu *et al.*, 2011).

- The RRTMG (Rapid Radiative Transfer Model for GCMs) shortwave scheme: spectral method (14 bands); allows the clouds to be randomly overlapped (Wang *et al.*, 2011); interacts with aerosols; trace gases are specified; is usually applied to climate simulations (Xiu *et al.*, 2011).

Longwave radiation includes infrared wavelengths emitted and absorbed by gases (e.g. carbon dioxide, ozone) and surfaces. The surface emissivity dependent on land type and the skin temperature determines the amount of the upward longwave radiation from the ground (Skamarock *et al.*, 2008). The infrared radiation at all wavelengths is strongly influenced by the clouds where it usually causes stronger warming at cloud base and cooling at cloud tops (Dudhia, 2011a). The available longwave radiation schemes in the WRF model are:

- The RRTM (Rapid Radiative Transfer Model) scheme (Mlawer *et al.*, 1997): spectral scheme (16 bands); K-distribution; the cheapest scheme for longwave radiation calculations; uses pre-set tables to efficiently represent longwave processes owing to carbon dioxide, ozone, water vapour, and trace gases; interacts with clouds (1/0 cloud fraction) (e.g. Skamarock *et al.*, 2008; Wang *et al.*, 2011).

- The GFDL radiation scheme: Eta operational spectral scheme (14 spectral bands); interacts with clouds (cloud fraction); the ozone profile is based on season and latitude; the carbon dioxide is fixed; clouds are randomly overlapped (e.g. Skamarock *et al.*, 2008; Wang *et al.*, 2011).

- The RRTMG longwave scheme: spectral scheme (16 bands); K-distribution; does not account for aerosol effects (Xiu *et al.*, 2011); the ozone, carbon dioxide and trace gases are specified (Dudhia, 2011a).

- The CAM scheme: spectral scheme (8 bands); interacts with clouds, trace gases and aerosols; the ozone profile is a function of month and latitude; has a year-dependent table of carbon dioxide values (Skamarock *et al.*, 2008; Dudhia, 2011a).

3.1.3.2 Planetary Boundary Layer physics

The PBL schemes are used to parameterise unresolved turbulent vertical fluxes of momentum, heat and moisture within the PBL (Hu *et al.*, 2010). Above the PBL top, these schemes are also responsible for vertical diffusion due to eddy transports (Dudhia, 2011a). Therefore, the PBL options are distributing the surface fluxes (sensible and latent heat fluxes) through turbulence in the entire atmospheric column, not just the boundary layer (see Figure 3.4). These surface fluxes are provided by the surface layer schemes and land-surface models (see Figure 3.5). The PBL schemes determine the flux profiles within the daytime well-mixed and nighttime stable boundary layers, and thus provide atmospheric tendencies of moisture, temperature, and momentum in the whole atmospheric column. The PBL options are one-dimensional schemes and consider dry mixing as well as saturation effects (Skamarock *et al.*, 2008).

Two main types of PBL schemes are available in the WRF model: the TKE prediction or local closure schemes (MYJ, MYNN, BouLac, TEMF, QNSE, CAM, UW PBL schemes) and the diagnostic non-local options (YSU, GFS, MRF, ACM2 PBL schemes). The local closure schemes assume that turbulent fluxes depend only on local values and gradients of atmospheric variables. They estimate these fluxes at each model grid point

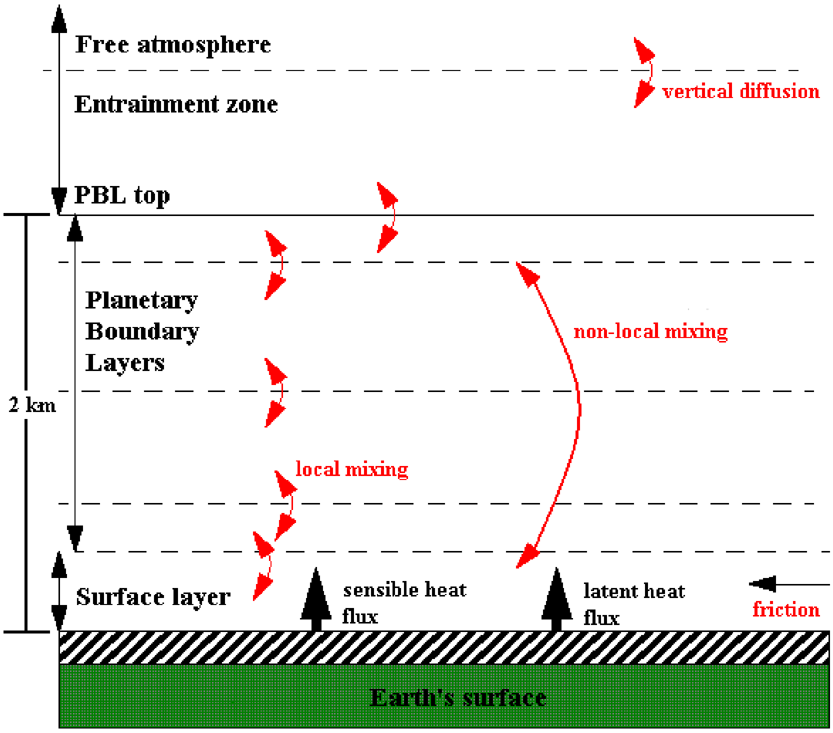

FIGURE 3.4: An illustration of the WRF model's PBL processes. The red arrows indicate mixing processes within and between the atmospheric layers (black arrows). Redrawn after Dudhia (2011a).

from the mean atmospheric variables and/or their gradients at that point (Hu *et al.*, 2010). The TKE schemes are responsible for buoyancy and shear production, vertical mixing and dissipation in each atmospheric column. TKE and length-scale are used to define the vertical eddy viscosities, K_v, for local vertical mixing. The local closure schemes can also use thinner surface layers (Dudhia, 2011a). The non-local schemes diagnose a PBL top from a critical bulk Richardson (Ri) number or stability profile. The non-local schemes specify a K-profile and some of these consider the non-local fluxes implicitly through a non-local term (YSU, MRF, GFS schemes) and other use a mass-flux term (ACM2, TEMF schemes) which is a flux between non-neighbouring layers (Hu *et al.*, 2010; Dudhia, 2011a).

The TKE schemes are:

- The Mellor-Yamada-Janjic (MYJ), which is based on the 1.5-order (level 2.5) turbulence closure model of the Mellor and Yamada (1982) to represent turbulence in the boundary layer and in the free atmosphere (Skamarock *et al.*, 2008; Hu *et al.*, 2010; Wang *et al.*, 2011). This scheme determines eddy diffusion coefficients from prognostically calculated TKE (Hu *et al.*, 2010). According to Pagowski (2004), the MYJ scheme may result in spurious oscillations of eddy diffusivity and viscosity.

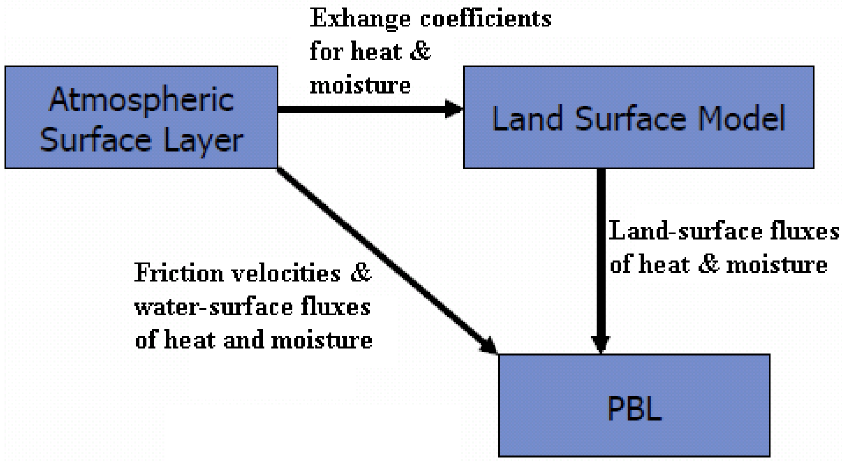

FIGURE 3.5: A schematic of the WRF model's surface physics components (surface layer, land surface model and PBL). The arrows indicate interactions between the surface physics components of the WRF model. Redrawn after Dudhia (2011a).

The scheme has near zero entrainment flux and provides very small values of diffusivity in the absence of shear, resulting in a slow PBL growth (Pagowski, 2004). According to Hu *et al.* (2010), this scheme is not recommended for stable flows.

- The Quasi-Normal Scale Elimination (QNSE), which is an alternative approach of deriving expressions for eddy viscosity and eddy diffusivity using the spectral theory and a quasi-normal scale elimination algorithm (Sukoriansky *et al.*, 2006). The QNSE scheme is a TKE prediction scheme (1.5 order closure) focusing on a new theory for stable stratification (Wang *et al.*, 2011), which is based on the quasi-Gaussian temperature and velocity mapping using the Langevin equations. First, this scheme uses primitive equations to resolve all scales. Then, perturbative solutions for the small scales are derived; the scheme implies partial averaging of these small scales eliminating them from the primitive equations. This scale elimination results in small corrections to viscosity and heat diffusivity. The aforementioned procedure is then repeated for the next band of small scales (up to a certain scale). Therefore, this PBL scheme is scale-dependent and takes into account the model's grid resolution, the spectral characteristics and degree of anisotropy. Some of the goals of the QNSE option is to treat waves and turbulence as one entity and to easily identify internal waves using the spectral method. Note that there is not a single value, but a range of Ri numbers at which turbulence is suppressed (Sukoriansky *et al.*, 2006). According to Sukoriansky *et al.* (2006), QNSE scheme improves the predictive skills of high-resolution NWP models (e.g. WRF model) for stably stratified atmospheric boundary layers.

- The Mellor-Yamada Nakanishi and Niino (MYNN) level 2.5 and 3 PBL schemes, which provide local TKE-based vertical mixing in the PBL and in the free atmosphere. The level 2.5 is a 1.5-order closure scheme that only predicts sub-grid TKE terms. The level 3 is a second-order scheme that predicts TKE and other second-moment terms (Wang *et al.*, 2011).

- The Bougeault-Lacarrère (BouLac) PBL option, which is a TKE prediction scheme designed to work with the BEP multi-layer urban model (Bougeault and Lacarrere, 1989).

- The University of Washington (UW) PBL parameterisation, which is a new PBL scheme developed to improve numerical stability and performance of climate models. This scheme includes explicit entrainment closure for convective mixed layers, TKE prediction of eddy diffusivities and a new formulation of TKE transport that is efficient when used with long climate model timesteps (Bretherton and Park, 2009). According to Bretherton and Park (2009), the UW scheme provides a practical and realistic treatment of marine stratocumulus–topped PBLs.

- The Total Energy - Mass Flux (TEMF) scheme, which is new in Version 3.3. The vertical mixing in this scheme is done by two methods: mass flux and eddy diffusivity. The eddy diffusivities are predicted from total turbulent energy (TE) and a length scale. The TE is the sum of turbulent potential energy and TKE. In statically neutral conditions, TE is equal to TKE, and under stable conditions the buoyancy destruction term of TE vanishes (Angevine *et al.*, 2010).

- Large Eddy Simulation (LES) option is a three-dimensional treatment of turbulence, where TKE and three-dimensional Smagorinsky options exist for the sub-grid turbulence. This scheme is more suitable for model grid sizes of up to about 100 m (Dudhia, 2011a).

The diagnostic non-local PBL schemes are:

- The Medium Range Forecast (MRF) scheme, which uses a counter-gradient term for moisture and heat in unstable conditions (Skamarock *et al.*, 2008). This scheme implicitly treats the entrainment layer as part of non-local K vertical mixing in the dry convective boundary layer (Wang *et al.*, 2011). The depth of the PBL is determined from a critical bulk Ri number (Skamarock *et al.*, 2008).

- The Yonsei University (YSU) scheme, which is the next generation MRF scheme. This scheme is a first-order non-local closure, with counter-gradient terms for u, v and θ. This scheme explicitly treats the entrainment layer at the top of PBL (Skamarock *et al.*, 2008). In order to enhance mixing in the stable boundary layer, a new stable BL diffusion algorithm is available in Version 3. Based on this new algorithm, the PBL top is defined by a bulk Ri number equal to 0.25 over land (Skamarock *et al.*, 2008; Hu *et al.*, 2010). The vertical mixing is strongest (weakest) when using the YSU scheme rather than the MYJ (MRF) scheme (Pagowski, 2004).

- The Asymmetrical Convective Model Version 2 (ACM2), which is a first-order closure. The ACM2 is a combination of a simple transilient model (a modification of the Blackadar convective model) and an eddy diffusion model. This scheme can simulate Blackadar-type thermal mixing upwards from the surface layer and local mixing downwards. The PBL height is determined by the Ri number (Skamarock *et al.*, 2008). The main goal of this scheme is to improve the shape of vertical profiles near the surface. Note that the ACM2 scheme uses local closure and not non-local transport for stable or neutral conditions (Hu *et al.*, 2010).

3.1.3.3 Surface physics

The surface layer schemes calculate friction velocities that are provided to the PBL schemes (described above) and exchange coefficients that allow the calculation of surface moisture and heat fluxes by the land surface models (see Figure 3.5). Note that over water surfaces, the sensible and latent heat fluxes are computed by the surface layer schemes (Skamarock *et al.*, 2008). The surface layer options use the similarity theory to determine diagnostic fields such as two-meter temperature and mixing ratio, and ten-meter wind speeds (Dudhia, 2011a). It is interesting to note that the surface layer schemes provide only stability-dependent surface layer information and no tendencies for the land surface and PBL schemes. Each of these surface layer options are tied to a particular PBL scheme (Skamarock *et al.*, 2008). The surface layer schemes also vary in stability functions and roughness length. For example, some schemes use larger roughness length for momentum than for heat. Over land the roughness length depends on the land-use type, while over water it is a function of surface wind speed (Dudhia, 2011a). The available surface layer schemes in the WRF model are:

- The MM5 surface layer scheme, which is based on the Monin-Obukhov similarity theory. It provides exchange coefficients to the land surface model and should be used with the MRF or YSU PBL schemes (Skamarock *et al.*, 2008).

- The Eta surface layer scheme (or MYJ surface scheme), which is also based on the Monin-Obukhov similarity theory with thermal roughness length over land that depends on vegetation height. This surface layer scheme must be run in conjunction with the MYJ PBL scheme (Skamarock *et al.*, 2008).

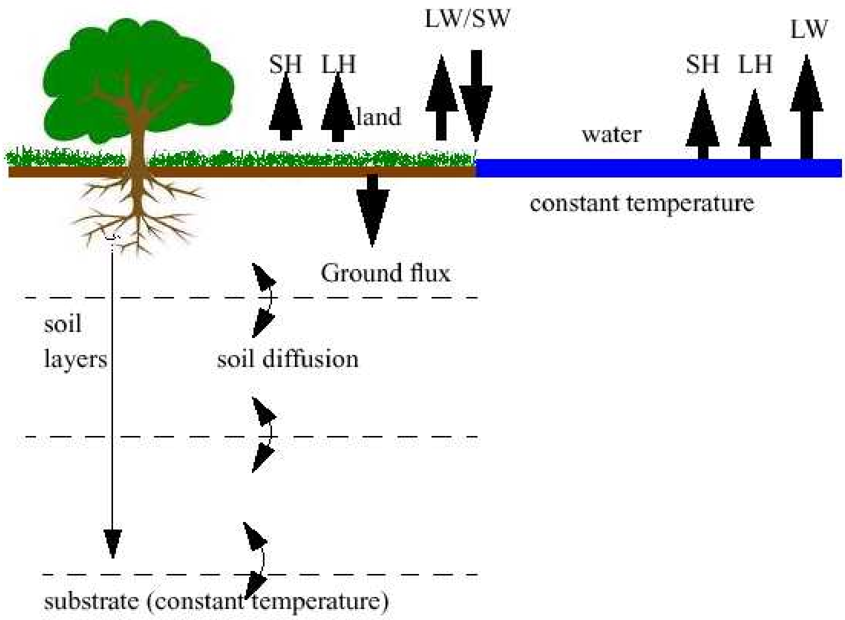

FIGURE 3.6: Illustration of the WRF model's surface processes. Longwave (LW) and shortwave (SW) radiation together with sensible (SH), latent heat (LH) and ground heat fluxes are shown. The dashed lines indicate the soil layers. Redrawn after Dudhia (2011a).

- The Pleim-Xiu (PX) surface layer, which is a new scheme (released in Version 3.1) for use together with the PX land surface model and the ACM2 PBL scheme.

- The QNSE surface layer scheme, which is run in conjunction with the QNSE PBL scheme. This scheme is very similar to the aforementioned MYJ surface scheme, but uses new stability functions (Sukoriansky *et al.*, 2006).

- The MYNN surface layer, which is a new scheme (released in Version 3.1) that must be run together with the MYNN PBL scheme (Wang *et al.*, 2011).

- The TEMF surface layer scheme, which is a new scheme available in Version 3.3 for use with the TEMF PBL option (Wang *et al.*, 2011).

The land surface models (LSMs) provide moisture and thermal fluxes [latent (LH) and sensible (SH) heat fluxes] over land and sea-ice points by using atmospheric information given from the aforesaid surface layer schemes, as shown in Figure 3.6. Radiative and precipitation forcing is provided by the radiation and microphysics/convective schemes, respectively. The heat and moisture fluxes calculated by the LSM are used as a lower boundary condition for the vertical transport calculated by the PBL or the vertical diffuse schemes. The LSMs predict soil temperature and moisture in multiple soil layers, and it can also perform root, vegetation, canopy moisture and surface snow-cover simulation (Skamarock *et al.*, 2008). The LSMs consider vegetation (e.g. desert, cropland, forest

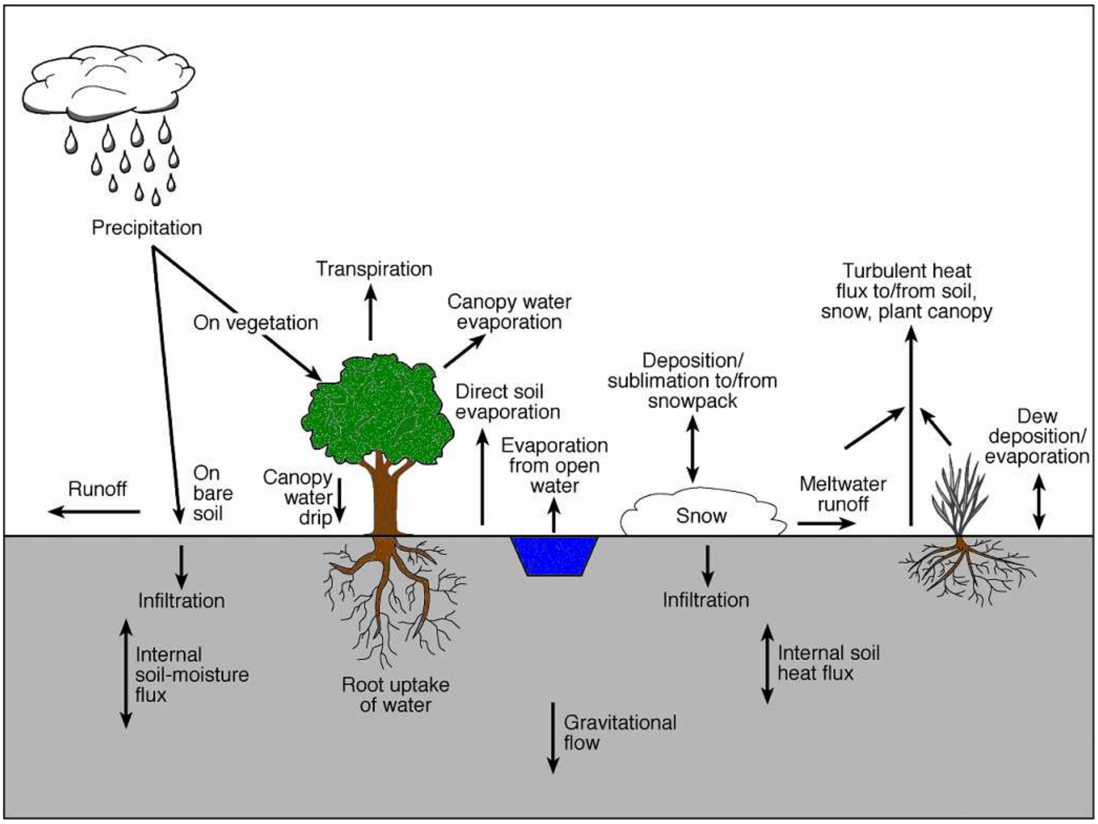

FIGURE 3.7: Illustration of the WRF land surface model processes. Redrawn after Dudhia (2011a).

types) and soil (e.g. clay, loam, sand) categories. As illustrated in Figure 3.7 the land surface processes include evapotranspiration, leaf and root zone effects (Dudhia, 2011a). Land's state variables such as skin and soil temperature, snow-cover, soil moisture and canopy properties are updated in the LSMs, but no tendencies are provided. The LSMs only perform computations in the vertical, hence there are no interactions between horizontal neighbouring grid points (Skamarock *et al.*, 2008). The available basic options for the LSMs in the ARW solver are:

- A 5-layer thermal diffusion scheme, which is a simple scheme that only predicts ground and soil temperature (no soil moisture or snow-cover prediction). The thermal properties as well as the moisture availability depend on land-use. This scheme uses 5 soil layers of 1, 2, 4, 8, and 16 cm thickness and provides sensible and latent heat fluxes to the PBL schemes. Note that there are no explicit vegetation effects (Skamarock *et al.*, 2008).

- The Noah LSM (Chen and Dudhia, 2001), which is a unified ARW code developed jointly by NCAR and NCEP for both research and operational purposes. This model predicts soil moisture and soil temperature in 4 layers (of 10, 30, 60 and 100 cm thickness). This scheme also diagnoses skin temperature and allows for snow-cover and canopy moisture prediction. The Noah LSM handles fractional snow-cover effects, predicts frozen soil and provides three urban canopy model options [Urban Canopy Model (UCM), Building Environment Parameterisation (BEP) and Building Energy Model (BEM)] for improved urban treatment. It additionally takes into account root zone, vegetation and soil categories, evapotranspiration, runoff and monthly vegetation fraction. This LSM provides heat and moisture fluxes for the PBL schemes (Skamarock *et al.*, 2008).

- The RUC (Rapid Update Cycle) LSM, which predicts soil temperature and moisture in 6-layers and includes canopy water and vegetation effects. This scheme also has a multi-layer snow model and a frozen soil physics. Sensible and latent heat fluxes are provided for the PBL schemes (Skamarock *et al.*, 2008).

- The Pleim-Xiu LSM, which is a 2-layer model that predicts soil temperature and soil moisture, includes the vegetation effects and has a simple snow-cover model. This scheme also provides turbulent fluxes for the PBL schemes (Skamarock *et al.*, 2008).

3.1.3.4 Cumulus parameterisation

The convection schemes are responsible for the sub-grid convective and/or shallow (non-precipitating) clouds effects. They operate only on individual atmospheric columns that completely contain convective clouds and are considered convectively unstable. These schemes re-distribute air in order to parameterise vertical convective motions at sub-grid scales owing to unresolved updrafts and downdrafts (Skamarock *et al.*, 2008). Updrafts take boundary layer flow upwards, and downdrafts take mid-tropospheric level air downwards (Dudhia, 2011a). Cumulus parameterisations provide atmospheric heat and moisture vertical profiles and some of these schemes also provide cloud and rainfall tendency profiles in the column. All the cumulus schemes provide the convective component of surface precipitation (Skamarock *et al.*, 2008). These schemes have to determine when to trigger a convective atmospheric column and how fast to make the convection act (Dudhia, 2011a). The precipitation provided by cumulus parameterisation is produced by moist air rising in convective clouds. Therefore, all the convection schemes should be used when the WRF model cannot resolve convective eddies itself (e.g. for coarse horizontal resolutions greater than 10 km). Usually, cumulus options should not be selected and used for horizontal resolutions less than 5 km because the WRF model can trigger convection itself (Skamarock *et al.*, 2008).

Convection schemes are divided into the adjustment type, which relaxes towards a mixed sounding, and the mass flux type, which determines updraft mass flux and sometimes momentum transport. For deep convection, mass flux cumulus schemes are responsible for the surface air transport to the top of the convective clouds. The subsidence around the convective clouds results in warming and drying of the troposphere and subsequently removes instability over time. The downward motions will result in a cooling of the PBL (Dudhia, 2011a). The available cumulus schemes in the WRF model are: the Kain-Fritsch (KF), Betts-Miller-Janjic (BMJ), Grell-Devenyi (GD), Simplified Arakawa-Schubert (SAS), Grell 3D (G3), Tiedtke, Zhang-McFarlane (ZM) and the New Simplified Arakawa-Schubert (NSAS). Several cumulus schemes include shallow convection (KF, SAS, G3, BMJ, Tiedtke schemes), where non-precipitating shallow mixing dries the PBL and moistens and cools the air above the PBL top. Some convection options also include momentum transport as a passive scalar (SAS, Tiedtke) or include a convective pressure gradient term (NSAS, ZM) (Skamarock *et al.*, 2008; Dudhia, 2011a; Wang *et al.*, 2011). Note that clouds activate in atmospheric columns under certain conditions: the presence of some convective available potential energy (CAPE) and when there is few convective inhibition (CIN) in sounding. Finally, closures in the cumulus schemes define the cloud mass-flux derived from several methods such as CAPE removal over time, moisture and mass convergence and quasi-equilibrium (Dudhia, 2011a).

3.1.3.5 Microphysics

Evaporation, condensation, sublimation, deposition, melting and freezing are responsible for the latent heat release within the microphysics schemes. Rain drops, cloud water, ice crystals, snow and graupel are some of the particle types that the microphysics schemes contain (Dudhia, 2011a). Therefore, explicitly resolved cloud, water vapour and rainfall processes are included in the microphysics parameterisations. In the ARW solver, the microphysics is an adjustment process that is carried out at the end of the calling sequence where no tendencies are provided. However, only approximations of atmospheric heat and moisture, conversion rates between microspecies and surface resolved-scale precipitation operating within clouds are provided by the microphysics schemes (Skamarock *et al.*, 2008).

There are two main types of microphysics schemes, and these are single and double moment parameterisations. The single moment schemes have one equation to predict mass mixing ratio per species. The particle size distribution is determined from fixed parameters. The double moment schemes predict mass mixing ratio and have an additional prediction equation for the number of concentration of species (Dudhia, 2011a). The microphysics options are further divided into subsets based on the number of moisture variables and whether ice or mixed-phase processes are included.

The available microphysics schemes in the WRF model are: Kessler (suitable for idealised cases; warm rain, no ice processes), Purdue Lin (ice, snow and graupel processes; well-suited for high horizontal resolutions), WRF Single-Moment (WSM) 3-class (simple and efficient; appropriate for mesoscale grid sizes; ice and snow processes), WSM 5-class (slightly modified version of the WSM 3-class; mixed-phase processes; super-cooled water; no graupel), WSM 6-class (well-suited for high-resolution simulations; ice, snow and graupel processes), Eta microphysics (simple and efficient; mixed-phase processes), Goddard (appropriate for high grid spacings; ice, snow and graupel processes), Thompson (suitable for high-resolutions; snow, ice and graupel processes), Milbrandt-Yau Double-Moment 7-class (double moment rain, cloud, snow, ice, graupel and hail processes), Morrison double-moment (double moment rain, ice, snow and graupel processes), WRF Double-Moment 5-class (like WSM 5-class but it also has double moment rain), WRF Double-Moment 6-class (like WSM 6-class but it also has double moment rain), and Stony Brook University (SBU) which is new in Version 3.3 (5-class cloud-scale single moment) (e.g. Skamarock *et al.*, 2008; Dudhia, 2011a; Wang *et al.*, 2011).

Skamarock *et al.* (2008) and references therein, and Wang *et al.* (2011) fully document all the aforementioned physics schemes.

3.1.4 WRF Nesting

In the ARW solver, the horizontal nesting allows resolution to be focused over a particular region by introducing a finer grid (or grids) into the simulation (Skamarock *et al.*, 2008). Therefore, the nested domain (or domains), which covers a portion of a coarse domain, allows a particular region to be better resolved. A nested run is, thus, defined as a finer-grid resolution model run in which multiple domains (of different horizontal resolutions) can be run either independently as separate model simulations or simultaneously. Note that the nested domain receives information from its parent domain and may also feed information back to the coarse domain (Duda, 2011). The nesting option enables running at finer horizontal resolution without facing the following problems: the selection of uniformly high-resolution over a large domain, which is computationally expensive, and the choice of high-resolution for a very small domain with mismatched time and spatial boundary conditions (Gill, 2011).

The ARW solver supports three different options for horizontal nesting. These are the one-way and two-way grid nesting techniques, where one-way and two-way refer to how a coarse and a fine domain interact, and the moving nests with specified or automated moves for each nest. In both the one-way and two-way nesting options, the initial and lateral boundary conditions for the nest domain are provided by the parent domain, together with input from higher resolution terrestrial fields and masked surface fields (Skamarock *et al.*, 2008; Wang *et al.*, 2011). In the one-way nesting option, information exchange between the coarse domain and the nest is strictly downscale, which means that the nest does not impact the parent domain's solution (Gill, 2011). The one-way nesting technique can be run in two different ways. The first method is to produce the nested run as separate simulations and the second option is to run the domains at the same time. In the first method, the WRF model is first run for the parent domain to create an output that is interpolated in time and space to provide boundary conditions for the nested domain, which is run after the outer domain has finished (Skamarock *et al.*, 2008). In the two-way nest integration, the exchange of information between the coarse domain and the nest goes both ways. The nest's solution also impacts the parent's solution. The same physics schemes (except the cumulus parameterisation) are usually selected on all domains (Gill, 2011).

It is worth noting that Soriano *et al.* (2002) in their modelling study explored the influence of one-way and two-way nesting techniques with the MM5 (Fifth-Generation Penn State/NCAR Mesoscale Model) model over a complex terrain in Europe. The differences in the results were significant when choosing one or another nesting option, yielding the two-way nesting simulation worst results when evaluating the MM5 model against station data (Soriano *et al.*, 2002).

3.1.5 WRF Nudging

The aim of the four-dimensional assimilation (FDDA), which is also known as nudging, is to keep the simulations close to the analyses or/and observations over a simulation period (Skamarock *et al.*, 2008). The available nudging options in the WRF model can be used for dynamical initialisation, to create four-dimensional meteorological datasets and to improve the boundary conditions. In particular, for dynamical initialisation the modelling domains are nudged towards analysis in a pre-forecast or pre-simulation period of 6 to 12 hours, resulting in a smooth initial forecast (or simulation) and more accurate boundary forcing at time zero. In addition, gaps between analysis times are filled in when analyses are produced with the nudging option during a long simulation period. Smoother boundary conditions for the inner domain can be also achieved with the addition and nudging of an outer and coarser nest (Skamarock *et al.*, 2008; Dudhia, 2011b).

The available nudging options are a three-dimensional and surface analysis nudging, an observation (or station) nudging and a spectral nudging. The analysis (or grid) nudging is suitable for coarse horizontal resolutions, while the observation nudging is appropriate for fine-scale or asynoptic observations. If analysis nudging is selected, each grid point is nudged towards a value which is time-interpolated from the analyses. Surface (two-dimensional) analysis nudging is only suitable for the surface and boundary layers. If observation nudging is selected, each grid point is nudged by a weighted average of differences from observations within a time window and radius of influence. The analysis and the observation nudging can also be combined. Finally, in the WRF model the spectral nudging is a new upper-air nudging option that can be selected to do a three-dimensional nudging only for large scale flows (Skamarock *et al.*, 2008; Dudhia, 2011b).

The grid and observation nudging options only nudge horizontal winds, temperature and water vapour, while the spectral option also nudges geopotential height. The nudging terms are fake sources of mass and momentum, therefore it is better to avoid nudging in the energy budget and in dynamics studies (Skamarock *et al.*, 2008; Dudhia, 2011b).

3.2 Input Data

The WRF model uses a series of terrestrial data (such as land-use, terrain and soil types) and meteorological data (such as forecast, re-analysis and climate model data) of different origin and different horizontal resolution and projections.

3.2.1 Terrestrial datasets

The available terrestrial data used as input to the WPS geogrid program include land-use/vegetation types, terrain height, soil categories, monthly vegetation fraction, annual mean deep soil temperature, monthly albedo, maximum snow albedo, slope category and static data for the gravity wave drag scheme. Most global datasets of these fields are available at five horizontal resolutions which are 1 degree (111.0 km), 10 (18.5 km), 5 (9.25 km) and 2 (3.70 km) minutes, and 30 (0.925 km) seconds (Wang *et al.*, 2011).

By default, the geogrid program will interpolate land-use datasets to the WRF grids from the USGS (United States Geological Survey) global cover classification (e.g. Anderson *et al.*, 1976; Loveland *et al.*, 1991) with the appropriate spatial resolutions (10, 5, 2 minutes and 30 seconds) (Wang *et al.*, 2011). The USGS dataset was derived from the AVHRR (Advanced Very High Resolution Radiometer) data which acquired between April 1992 and March 1993 to map global land-cover (Friedl *et al.*, 2002). In general, the AVHRR data have 1, 4 and 16 km spatial resolutions, but the 1 km resolution is considered as the most appropriate for global land-cover mapping (Loveland *et al.*, 2000). However, the information content of the AVHRR data is limited for land-cover mapping applications; several uncertainties are present in these maps (Loveland *et al.*, 1999; Friedl *et al.*, 2002). Note that the WRF user needs to be careful in selecting the appropriate USGS data resolution to be close to that resolution selected for the WRF domain (Wang *et al.*, 2011).

The USGS has 24 land-use categories and is considered to represent dominant vegetation types in the WRF model (Wang *et al.*, 2011). Some vegetation characteristics

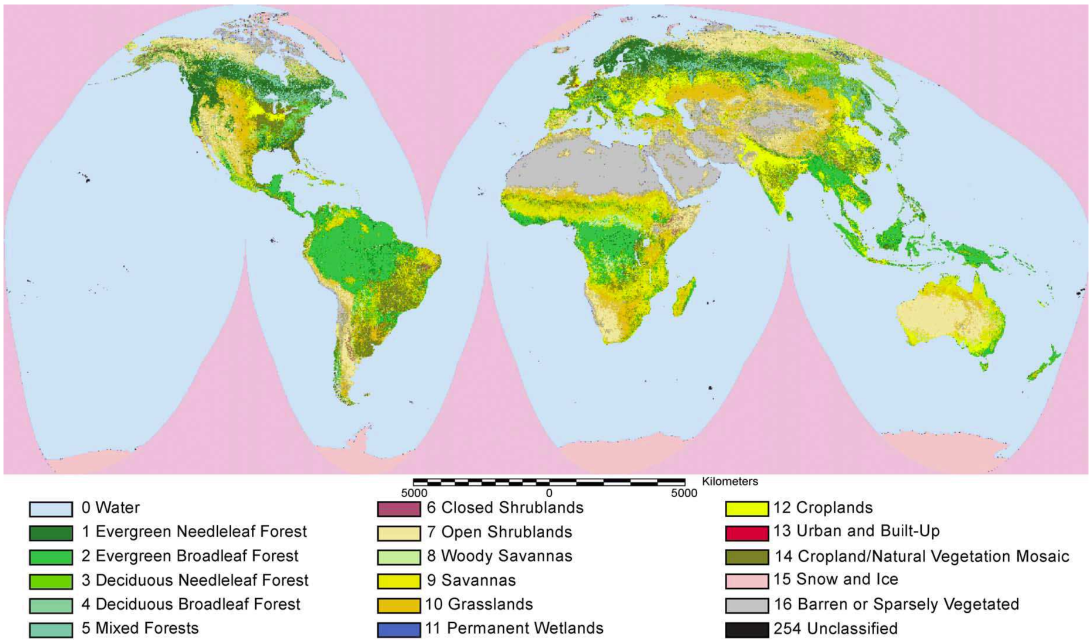

FIGURE 3.8: MODIS data showing the global map of land-cover based on the seventeen IGBP classes. Taken from Friedl *et al.* (2002).

may vary monthly. For example, global monthly green fraction and surface albedo are available at each of the WRF model grid points (Chen and Dudhia, 2001; Wang *et al.*, 2011). The land-water mask data are also derived from the USGS vegetation datasets. At each latitude-longitude grid points, there is one number indicating either land or water at that point. The default 16-category soil type is provided as part of the WPS static data, which contains classifications that are matched with the USGS land-use categories. The annual mean deep soil temperature is provided at 1 degree resolution, which is rather low (Wang *et al.*, 2011).

In the WRF model, an alternative dataset of land-cover categories is provided by the 20-category MODIS (MODerate resolution Imaging Spectroradiometer) land-use classification (not a subset of the 24-category USGS), which is modified for use only with the Noah LSM (Wang *et al.*, 2011). The MODIS data reflect recent land-use changes, since acquired between October 2000 and October 2001 (Giri *et al.*, 2005). The MODIS on-board Terra and Aqua platforms include 36 spectral bands (2 at 250 m, 5 at 500 m and 29 at 1 km) which are explicitly designed for land-cover mapping applications (Friedl *et al.*, 2002; Ozdogan and Gutman, 2008). Spectral information is also provided by the enhanced vegetation index product, which is a measure of the vegetation amount and fractional cover (Friedl *et al.*, 2002). The MODIS land-cover project includes two main parameters. The first parameter offers global land-cover maps at 1 km spatial resolution updated every 96 days. For global modelling applications, the MODIS project also provides land-cover maps at coarser (28 km) spatial resolution. The second parameter offers global land-cover maps at 1 km spatial resolution updated at annual intervals (Friedl *et al.*, 2002). Both Terra and Aqua MODIS land-cover data also provide sub-daily global coverage at 250 and 500 m spatial resolutions, thereby providing improved mapping and monitoring of vegetation activity (Ozdogan and Gutman, 2008).

The MODIS land-cover principally used the International Geosphere Biosphere Programme (IGBP) classification system along with other numerous classification systems (Friedl *et al.*, 2002; Giri *et al.*, 2005). A set of seventeen land-cover classes (related to vegetation) was developed by the IGBP (Friedl *et al.*, 2002). The seventeen IGBP classes can be aggregated into eight major land-cover classes: savanna/shrubland, forest, grassland, cropland, barren/sparsely vegetated, cropland/natural vegetation mosaic, urban/built-up, and wetland (Friedl *et al.*, 2002; Giri *et al.*, 2005). Figure 3.8 presents a global land-cover map based on the seventeen IGBP classes [taken from Friedl *et al.* (2002)]. Note that the MODIS project offers the user a way to determine alternatives to the primary seventeen IGBP classes (i.e. IGBP-modified MODIS 20-category land-use categories defined in the WRF model). Lately, MODIS land-cover data have been an integral part of production of a range of land-use maps, including irrigation (Friedl *et al.*, 2002; Ozdogan and Gutman, 2008).

Different data sources, methodologies, classification schemes and spatial resolutions were used to prepare the aforementioned global land-use datasets. According to Friedl *et al.* (2002), the MODIS data have improved spatial, spectral, geometric, and radiometric attributes relative to the AVHRR data. The MODIS data have been designed for operational land-cover mapping, thereby providing a useful tool for meteorological applications that need land-cover information at both continental and regional scales (Friedl *et al.*, 2002). According to Giri *et al.* (2005), one of the advantages of the MODIS data is that the project adopts a reliable methodology across the globe and is repeatable. However, both USGS and MODIS land-cover data provide the same major land-cover classes (Wang *et al.*, 2011).

3.2.2 Meteorological data

Time-varying meteorological fields, typically from another global or regional models such as the ECMWF (European Centre for Medium-Range Weather Forecasts) or the GFS (Global Forecast System) models, can be used to initialise the WRF model. Meteorological data that can be provided to the WRF model are the GFS, the National Centers for Environmental Prediction/National Center for Atmospheric Research (NCEP/NCAR) re-analysis archived at NCAR, the ECMWF re-analyses (e.g. ERA-40, Era-Interim) and other datasets (Wang *et al.*, 2011). Major parameters that are included in most of the aforementioned datasets are surface and sea-level pressure, air and sea-surface temperature, geopotential height, soil information, relative humidity, ice cover, horizontal winds, vorticity, vertical motion and ozone. For the purposes of this thesis a particular focus will be placed on the ECMWF ERA-40 and ERA-Interim re-analysis projects.

3.2.2.1 ERA-40 re-analysis

By using data assimilation methods, the first generation re-analysis [e.g. FGGE (First GARP Global Experiment), ERA-15, NCEP/NCAR] projects were successful and widely used for atmospheric and oceanic processes. However, these products exhibit a number of limitations and problems, such as severe drying of the western Amazonian land surface and too cold surface temperatures in winter. The ECMWF in collaboration with many other institutions produced the ERA-40 archive, which is a re-analysis of meteorological observations that covers the period from September 1957 to August 2002. This also includes the period of the earlier ECMWF re-analysis, ERA-15, which covered the period 1979-1993. The main objective with ERA-40 was to produce a better set of analyses with higher spatial resolution and more vertical levels in the PBL and stratosphere than provided by the earlier re-analysis projects (Uppala *et al.*, 2005).

The ECMWF used a spectral model to generate the ERA-40 re-analysis. Note that spherical harmonics are used in the spectral models to calculate their parameters since it is more computationally efficient. The 3-dimensional variational (3D-Var) technique was applied using the Integrated Forecasting System (IFS) with a T159 spectral model resolution (T106 used for the ERA-15) and 60 vertical model levels (with the top level at about 64 km) to produce the ERA-40 re-analysis every 6 hours (Uppala *et al.*, 2005). The entire 6-hourly and monthly means ERA-40 dataset are available through the British Atmospheric Data Centre (BADC) and other services (e.g. ECMWF Data Services). The upper data are stored in T159 spectral form, while the surface data are provided on a N80 Reduced Gaussian grid (almost equivalent to a 125 km spatial resolution). The ERA-40 data can also be converted to a regular latitude-longitude grid (e.g. $1° \times 1°$ grid), which is the simplest type of grid for surface or single level fields (ECMWF, 2006).

Both conventional (e.g. radiosondes, aircraft) and satellite observations are used to make the ERA-40 analysis. The main difference between ERA-40 and ERA-15 re-analysis is in the use of satellite data. ERA-40 used the TOVS (Tiros Operational Vertical Sounder) radiances directly, while in the ERA-15 datasets temperature and humidity retrievals were used (ECMWF, 2006). A better global analyses of the state of the atmosphere, land and surface conditions were provided over the period 1957-2002 primary due to changes in the schemes of the stable PBL and land surface. The atmospheric model included improvements in the radiation, deep convection, cloud and orography parameterisations, and was coupled with a 1.5° spatial resolution ocean wave model. The 3-D

Var analysis and the revised and more accurate surface orography description employed in ERA-40 also improved the quality of this dataset. However, problems and limitations were diagnosed in ERA-40 products (e.g. excessive tropical oceanic precipitation and a cold bias in the lower troposphere). These deficiencies can be attributed for example to the fact that the ERA-40 data assimilation system was not designed to impose any hydrological balance. The system was only designed to generate analyses of atmospheric temperature, humidity, horizontal winds and ozone, and a number of surface variables (Uppala *et al.*, 2005).

3.2.2.2 ERA-Interim re-analysis

The latest global atmospheric re-analysis produced from the ECMWF is the ERA-Interim project, which covers the period from 1979 to present (near-real time), replacing the earlier ERA-40 re-analysis (Dee *et al.*, 2011). The ERA-Interim data are available online through BADC on spectral and reduced Gaussian grids (ECMWF, 2009). In particular, gridded data products include 3-hourly surface parameters (e.g. 2 m temperature and humidity) and 6-hourly upper-air atmospheric parameters (e.g. wind, temperature, ozone, humidity) covering the troposphere and stratosphere (Dee *et al.*, 2011).

As addressed above, there are a number of data assimilation difficulties encountered in the production of ERA-40. The ERA-Interim project was conducted by ECMWF in order to provide a new and improved atmospheric re-analysis to deal with the problems that are mainly related to the hydrological cycle representation, the quality of the stratospheric circulation and the time-consistency of re-analysed geophysical fields. The ERA-Interim data assimilation system uses a 2006-release of the IFS with improvements both in the forecasting model and analysis methodology relative to the ERA-40 project (Dee *et al.*, 2011). In particular, according to Dee *et al.* (2011) some of the main advances in the ERA-Interim data assimilation compared to ERA-40 are the followings:

- The ERA-Interim archive is produced with the 4-dimensional variational (4D-Var) data assimilation technique, advancing forward in time using 12-hourly analysis cycles (6-hourly 3D-Var for ERA-40). 4D-Var compared to 3D-Var results in more effective use of observations.

- The atmospheric model used for the ERA-Interim re-analysis has a spectral T255 horizontal resolution (T159 for ERA-40), which is equivalent to approximately 79 km horizontal resolution on a N80 reduced Gaussian grid (125 km for ERA-40). The vertical resolution is 60 model levels for both ERA projects.

- New humidity and ozone analysis schemes were developed.

- The ERA-Interim project is characterised by improved model physics. For example, better representation of the hydrological cycle, cloud and convection schemes were implemented. For more stratocumulus production in previously under-predicted areas, a moist boundary layer scheme was introduced. The representation of surface drag effects on the atmospheric flow was also revised.
- Improvements in bias handling.
- The ERA-Interim uses rain-affected satellite radiances instead of using derived rain rates.

The ERA-Interim uses the same sea surface temperature and sea ice concentration input data as was used for ERA-40. Observations assimilated in the ERA-Interim project until 2002 consist the sets of observations originally acquired for ERA-40 (Dee *et al.*, 2011). These observations and their sources are described in detail in Uppala *et al.* (2005). However, according to Dee *et al.* (2011) there are a few noteworthy exceptions:

- Variational bias correction of satellite clear-sky radiance data.
- Automated bias correction scheme for surface pressure observations.
- Ozone data expansion.
- Altimeter wave-heights.
- Additional scatterometer ocean surface wind data.

Various other changes in physics schemes, data usage and data assimilation relative to ERA-40 are described in detail in Dee *et al.* (2011). According to Dee *et al.* (2011), there are areas where further work is needed in order to improve the ERA-Interim re-analysis performance. For example, progress is possible in areas such as global mean precipitation, heat and moisture fluxes in the atmospheric boundary layer, clouds representation and observational data on wind and humidity (Dee *et al.*, 2011).

Chapter 4

Comparison of Planetary Boundary Layer Schemes in the WRF model

Accurate depiction of meteorological conditions, within the planetary boundary layer (PBL), is essential for understanding low-level jets' (LLJs) development, and the PBL parameterisations play a critical role in simulating the boundary layer. This chapter examines the sensitivity of the performance of the Weather Research and Forecasting (WRF) model to the use of different PBL parameterisations. Three days in 1982 were simulated using four different PBL schemes in a domain covering the Arabian Peninsula. The four PBL schemes include two turbulent kinetic energy (TKE) closure schemes-the Quasi-Normal Scale Elimination (QNSE) and the Bougeault-Lacarrere (BouLac) PBL, and two first-order closure schemes-the Yonsei University (YSU) PBL and the Asymmetric Convective Model version 2 (ACM2). Regarding PBL structures, the local TKE closure schemes show better performance in stable conditions, where LLJs observed, than the non-local schemes which are favourable in unstable conditions.

4.1 Introduction

The PBL schemes in the numerical weather prediction (NWP) models deal with the problem of parameterising the turbulent layer that develops over the Earth's surface due to wind shear, surface heating and frictional effects. As discussed in chapter 2, vertical transport of moisture, momentum, heat and other physical properties of the lower tropospheric levels are driven by PBL processes (Shin and Hong, 2011; Garcia-Diez *et al.*, 2012). Different PBL schemes in the NWP models adopt different assumptions regarding the vertical transport of moisture, mass and energy, which usually lead to differences in the boundary layer (Hu *et al.*, 2010). A correct parameterisation of the turbulent layer is essential to achieve realistic simulations, especially regarding surface variables (Shin and Hong, 2011; Garcia-Diez *et al.*, 2012).

PBL schemes have been evaluated and compared in the framework of the Weather Research and Forecasting (WRF) model (Borge *et al.*, 2008; Shin and Hong, 2011; Garcia-Diez *et al.*, 2012). For example, Garcia-Diez *et al.* (2012) explored the seasonal dependence of the WRF model surface temperature biases and sensitivity to PBL schemes over Europe. They found that the YSU PBL scheme performs better during summer. However, it is widely known that the performance of the PBL schemes in the WRF model depends on the area of interest, the meteorological variables examined, season and time of day considered, and one cannot identify a best model configuration in a general sense (Zhang and Zheng, 2004; Garcia-Diez *et al.*, 2012). The most common approach to deal with this problem is to carry out statistical studies over a sensible set of model configurations and finally use the PBL scheme that reproduces better the observations in an average sense. It is worth noting that there are no numerical studies that analyse typical characteristics of one PBL scheme compared to others in stable PBL regimes such as those observed in the Arabian Peninsula.

In the PBL schemes, subgrid-scale turbulent fluxes are parameterised using prognostic mean variables through vertical diffusion equation (Skamarock *et al.*, 2008). As discussed in chapter 3, the WRF model has several PBL parameterisations which can be classified depending on how they approach the turbulence closure problem. Local closure schemes (e.g. MYJ, QNSE, BouLac) use variables and parameters that are defined at each model level or its neighbours (e.g. local gradients), while non-local closure schemes (e.g. YSU, MRF, ACM2) use parameters that can depend on the whole vertical profile, or on relationships between separated model levels (e.g. diffusion coefficients dependent on the PBL thickness).

In this chapter, we explore the differences between the local and non-local approach to PBL modelling, focused on wind speed, by selecting two recently added local and two frequently used non-local PBL schemes. The four PBL parameterisations in the WRF model-the YSU (Yonsei University, Hong *et al.* (2006)), ACM2 (Asymmetric Convective Model version 2, Pleim (2007)), QNSE (Quasi-Normal Scale Elimination, Sukoriansky *et al.* (2005)), and BouLac (Bougeault-Lacarrére, Bougeault and Lacarrere (1989)) PBL- are compared for three days with observations obtained from seven weather stations in the Arabian Peninsula and with radiosonde data. The YSU and the ACM2 PBL schemes are first-order closure schemes and they do not require any additional prognostic equation to express the impact of turbulence on mean variables. However, the QNSE and the BouLac schemes are classified as TKE closure (1.5-order closure) and they require one additional prognostic equation of the TKE. These four parameterisations are explained in detail in Hong *et al.* (2006), Pleim (2007), Sukoriansky *et al.* (2005) and Bougeault and Lacarrere

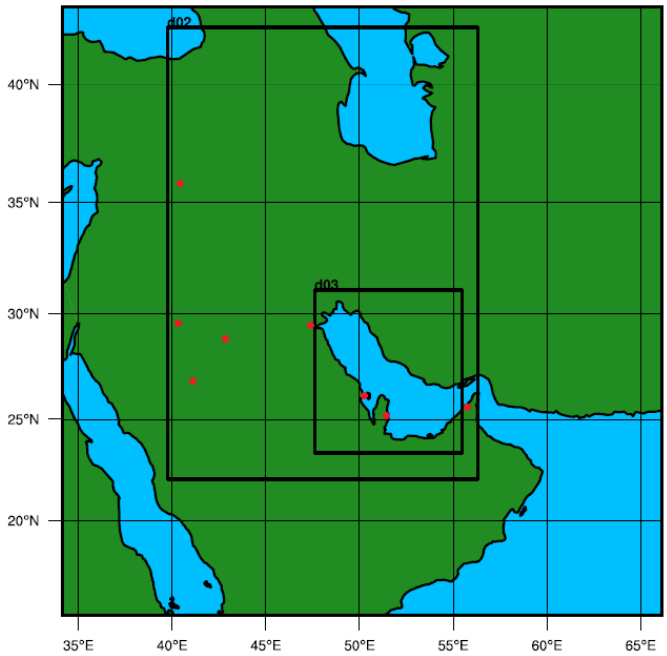

FIGURE 4.1: Map of the WRF modelling domains [27 km (d01), 9 km (d02) and 3 km (d03)] and locations of weather stations (red circles) and radiosonde observation sites (brown circle).

(1989).

4.2 Model Configuration

The Advanced Research WRF (ARW) numerical model version 3.2 was adopted. This is based on the fully compressible, non-hydrostatic Euler equations and for the purposes of this research we chose Mercator grids. A 3rd order Runge-Kutta (RK3) integration scheme and Arakawa C-grid staggering were used for temporal and spatial discretization, respectively.

A set of 27, 9 and 3 km one-way nested domains with 50 vertical levels (no specified eta levels were provided, but the model calculated a nice set of vertical levels with thinner layers at the model bottom and thicker layers at the model top) were selected. In particular, the model configuration consists of a parent domain (d01) with 115×117 horizontal grids (centred at 30.0 °N and 50.0 °E), an intermediate nested domain (d02) of 9 km spatial resolution (178×259 horizontal grids), and an innermost domain (d03) with 3 km spacing and 247×271 horizontal grids (Figure 4.1).

The physics subset contained the WRF Single Moment (WSM) 3-class scheme, which is a simple ice microphysics scheme suitable for mesoscale grid sizes (Hong *et al.*, 2004). The WSM3 scheme predicts three categories of hydrometers: cloud/ice, rain/snow and water vapour. This is a computationally efficient scheme because the cloud water and cloud ice are counted as the same category. In addition, cumulus physics for deep and shallow convection was modelled with the Kain-Fritsch scheme (Kain, 2004), which was turned off in the fine grid spacing (3 km) selected for these simulations. Theoretically, it is only valid for parent grid sizes greater than 10 km (Skamarock *et al.*, 2008). For radiation, the RRTM (Rapid Radiative Transfer Model) longwave scheme developed by Mlawer *et al.* (1997) and the Dudhia shortwave scheme developed by Dudhia (1989) were selected because they are widely used by the WRF community and due to their computational efficiency. Land-surface interactions were simulated with the Noah land surface model (Chen and Dudhia, 2001) which is a four-layer soil model predicting soil moisture and temperature. Vegetation and land-use classifications are provided by the USGS (United States Geological Survey) dataset containing 24 different land-use categories.

Four simulations with four different PBL schemes and their relevant surface-layer schemes are conducted: the YSU (Hong *et al.*, 2006) and ACM2 (Pleim, 2007) PBLs of the first-order closure schemes, and the QNSE (Sukoriansky *et al.*, 2005), and BouLac (Bougeault and Lacarrere, 1989) PBLs of the TKE closure schemes. As discussed in chapter 3, the role of surface-layer parameterisations in the WRF model is to calculate the surface exchange coefficients (c_d and c_h) in order to compute the turbulent fluxes (sensible and latent heat fluxes), and momentum flux. Each PBL scheme in the WRF model is tied to particular surface-layer schemes, except for the BouLac PBL scheme which is flexible in selecting the surface-layer scheme. The surface-layer schemes tied to each PBL scheme were: the MM5 similarity for the YSU PBL parameterization, the Pleim-Xu surface-layer for the ACM2 PBL scheme, the QNSE surface-layer for the QNSE PBL scheme and the MM5 similarity for the BouLac PBL parameterization. The experiments with these PBL schemes are designated as the WRF-YSU, WRF-ACM2, WRF-QNSE, and WRF-BouLac experiments, respectively.

The experiments began at 00:00 UTC (03:00 h local time) on 10 June 1982 and ended at 00:00 UTC on 13 June 1982. The initial and lateral boundary conditions were provided by ERA-40 re-analysis data produced by the European Centre for Medium-Range Weather Forecasts (ECMWF). The ERA-40 re-analysis project was chosen for initialisation since it covers the period from 1957 to 2002. The ERA-40 dataset has T159 spectral resolution which is equivalent to 125 km horizontal resolution on a reduced Gaussian grid (Uppala *et al.*, 2005). The re-analysis has temporal resolution of 6 hours and is available from the British Atmospheric Data Centre (BADC). Note that the coarse domain provided lateral boundary conditions for the fine nested domains at every time step. Because the purpose of this study was to test the performance of the WRF model with different PBL schemes rather than to keep the simulations close to the aforementioned re-analysis, the four-dimensional data assimilation (FDDA) was not used (Skamarock *et al.*, 2008).

4.3 Data

Data for model validation include surface and boundary layer observations. Hourly and daily measurements of mean (T) and maximum (T_{max}) temperature (°C), mean (U) and maximum (U_{max}) wind speed (m s^{-1}) obtained from the NOAA Satellite and Information Service (available at http://www.ncdc.noaa.gov/cgi-bin/res40.pl?page=gsod.html) for seven weather stations in the Persian Gulf and its surrounding countries, during the period 10 June 1982, 00:00 UTC to 13 June 1982, 00:00 UTC, are used for testing the performance of the WRF model with different PBL schemes. The characteristics of the weather stations are shown in Table 4.1 and the locations of the stations are shown in Figure 4.1.

Historical data are generally available from 1929 to the present, with data from 1973 to the present being the most complete. For some periods, one or more countries' data may not be available due to data restrictions or communications problems. In deriving the summary of the daily data, a minimum of four observations for the day must be present. The average of the daily values presented in Table 4.1 are based on the hours of operation for each weather station. The data are reported and summarized based on Greenwich Mean Time (GMT, 00:00Z - 23:59Z) since the original synoptic/hourly data are reported and based on GMT. It is worth noting that we expect that a very small percent of random errors will remain in the summary of the daily data. Therefore, the results of the validation of the WRF model runs against this dataset should be interpreted with caution.

Atmospheric soundings obtained from the University of Wyoming have been used to check the model behaviour on vertical levels other than the surface. The quality of the data, the availability of the vertical levels and the frequency depend on the station that we considered. Most stations only provide two daily soundings at 00:00 UTC and 12:00 UTC. The variables used in this study are air temperature (°C), potential temperature (K), wind speed (m s^{-1}) and wind direction (degree). In general, radiosonde data suffer from several deficiencies; many missing and incorrect data are present. Therefore, only stations with 80 % or more sounding data have been considered. Evaluation in this chapter will focus on the domains with 3 and 9 km horizontal resolution (Figure 4.1).

It is worth noting that during the period 10 June 1982, 00:00 UTC to 13 June 1982, 00:00 UTC, strong LLJs with northwesterly direction over the Persian Gulf were observed. According to Membery (1983), the northwesterly winds occurred as a result of the interaction of two circulating pressure centres: a low-pressure cell over Iran and a semi-permanent high over northwestern Saudi Arabia. The northwesterly flow was enhanced by the strong west-to-east pressure gradients. This was most pronounced when a low-pressure centre developed near the Gulf of Oman. The LLJs over the Persian Gulf and southern Iraq resulted from the combination of the complex terrain of the Zagros

TABLE 4.1: Characteristics of seven weather stations in the Arabian Peninsula and averages of mean (T) and maximum (T_{max}) air temperature (°C), mean (U) and maximum (U_{max}) wind speed (m s^{-1}) during the period 10-13 June 1982, 00:00 UTC.

Weather Stations	**Lat (°N)**	**Long (°E)**	**Height (m)**	T **(°C)**	T_{max} **(°C)**	U **(m s^{-1})**	U_{max} **(m s^{-1})**
Dhahran (404160)	26.26	50.16	17	36.46	41.04	8.83	12.45
Doha Int. Airport (404280)	25.26	51.55	11	34.87	41.24	8.66	11.95
Sharjah (404490)	25.35	55.38	2	32.48	40.33	2.67	6.29
Hassakah (400160)	36.5	40.75	308	29.67	36.93	2.73	4.25
Al-Jouf (403610)	29.78	40.1	689	29.22	37.63	5.08	7.53
Rafha (403620)	29.61	43.48	444	31.26	40.57	3.05	6.16
Hail (403940)	27.43	41.68	1002	32.61	37.30	3.17	6.16
Average				**32.37**	**39.29**	**4.88**	**7.86**

Mountains to the east of the Persian Gulf, the Gulf waters, the presence of the aforementioned semi-permanent pressure systems, the topographical features of central Saudi Arabia and a trough to the lee of the Zagros Mountains. The radiosonde soundings showed that the PBL maximum nighttime wind speeds ranged from about 20 m s^{-1} to 26 m s^{-1} at 300-500 m AGL.

4.4 Results

4.4.1 Comparison with weather station data

To obtain a detailed view of the behaviour of the four PBL schemes, hourly weather station data are compared in Figure 4.2 with the 9 km WRF simulations (YSU, ACM2, QNSE and BouLac). As an example, Figure 4.2 shows the daily cycle for wind speed

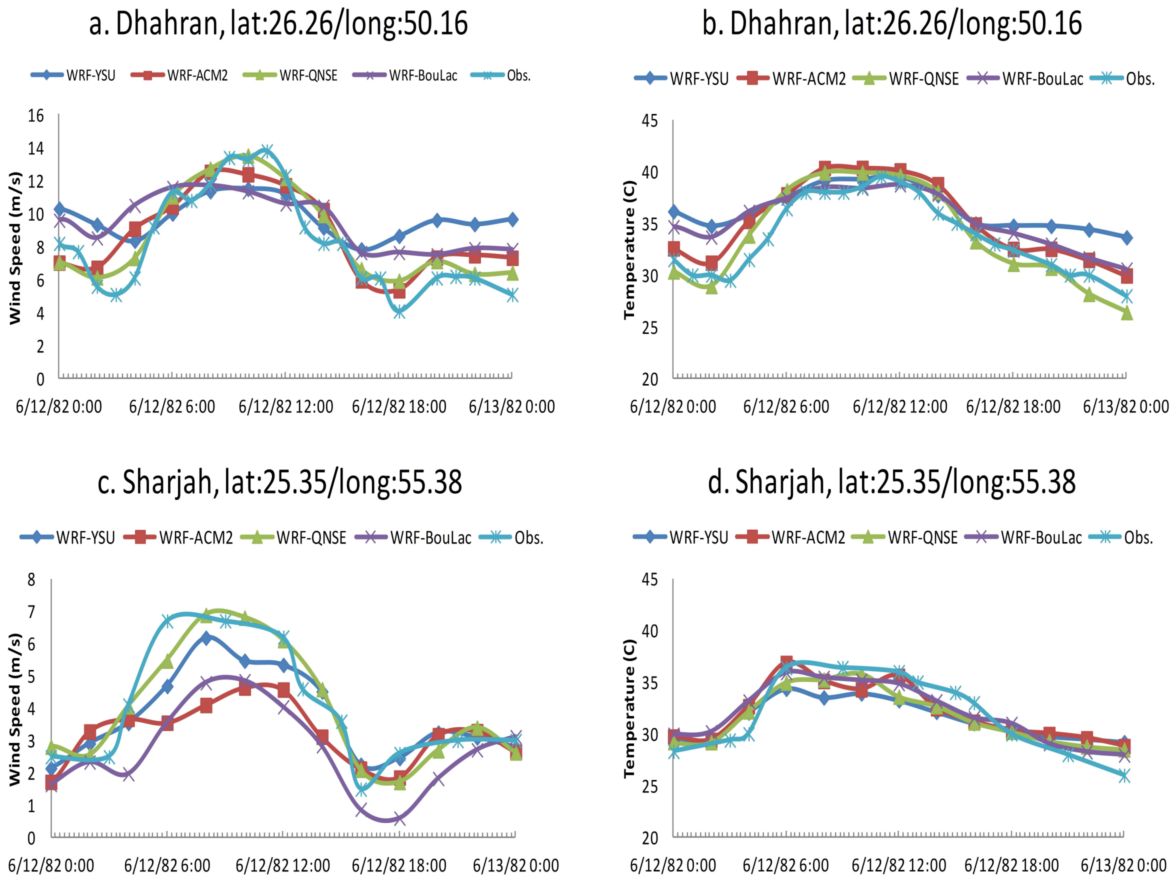

FIGURE 4.2: Hourly time series of simulated 2-m temperature (°C) and 10-m wind speed (m s^{-1}) with corresponding observational data (light blue with asterisks) obtained from the Dhahran (lat:26.26 °N, long:50.16 °E) and Sharjah (lat:25.35 °N, long:55.38 °E) weather stations for the 12 June 1982. The simulated results are from the YSU (blue), ACM2 (red), QNSE (green), and BouLac (purple) experiments.

and temperature at the levels of two representative weather stations (the Dhahran and Sharjah weather stations) in the Arabian Peninsula on 12 June 1982.

As can be seen in Figure 4.2(a, c), the wind speeds in both weather stations are well reproduced by the QNSE PBL scheme. In particular, the 10 metre wind speeds from the QNSE experiment are close to the upper value of the observation range. The other PBL experiments tend to underestimate the wind speeds by around 2 m s^{-1} during the daytime; while, the nighttime wind speeds in Dhahran were overestimated by the two first-order closure schemes and the BouLac parameterisation. As evident from the Figure 4.2(b), the model run with the QNSE PBL scheme predict lower temperatures in Dhahran during the night, thus showing better agreement with the observational data. In particular, during the nighttime cooling period, the evolutions of the near-surface temperatures from the QNSE experiment nearly follow those of the station, while the ACM2 and the BouLac PBL schemes produce warmer temperatures near the surface by approximately 2 °C. The temperature from the YSU experiment still keeps increasing at 18:00 UTC, when the temperatures from observations and other PBL experiments decrease. During the daytime heating period up to 16:00 UTC in Sharjah, the temperatures are slightly underestimated by all PBL experiments (Figure 4.2(d)). Even though the simulated 2 metre temperatures from all the experiments converge at the nighttime, they show positive biases.

According to Hu *et al.* (2010), one possible cause of the nighttime lower temperatures produced with the QNSE scheme would be a difference in the turbulent (sensible and latent) heat fluxes delivered by the surface layer scheme (used with the QNSE) when compared with those delivered by the surface layer schemes used with the two non-local PBL schemes and the BouLac parameterisation. To check this possibility, the sensible and latent heat fluxes for Dhahran are shown in Figure 4.3 for all the WRF PBL experiments. It is evident that the daytime sensible heat fluxes show that the QNSE (YSU) simulation produces the largest (smallest) sensible heat flux (Figure 4.3). This is in agreement with the temperature gradient in the daytime (see Figure 4.2(a)). It is also evident that the QNSE scheme predicts lower nighttime 2 metre temperatures but higher sensible heat fluxes than the YSU, ACM2 and BouLac simulations. Another aspect of the surface-layer parameterisations' performance is the Bowen ratio, the ratio of surface sensible heat flux to latent heat flux ($B = F_S/F_L$). Thus in addition to the sensible heat flux, the diurnal variations of the latent heat flux and Bowen ratio at Dhahran are shown in Figure 4.3. During nighttime, the QNSE simulation has lower Bowen ratio than the YSU run. The lower Bowen ratio is shown to be partially responsible for the colder and drier PBL predicted by the QNSE simulation. It also seems likely that the cooler conditions associated with the QNSE parameterisation, by enhancing the land-air temperature difference, causes the surface layer scheme to respond with larger sensible heat flux.

It must be stressed that the goal of this work is to find the PBL scheme that gives results closer to the observations. For that reason, in order to estimate the variability of the WRF results, the mean and the standard deviation of the near-surface temperature and wind speed differences between the observations and the WRF simulations for the seven weather stations in Arabian Peninsula are computed and provided in Table 4.2. The mean and the standard deviation of the maximum near-surface temperatures and wind speed differences between the station data and the WRF simulations are also provided in Table 4.3. Initially, the hourly temperature and wind speed differences between the station data and the WRF simulations were calculated for all weather stations of Table 4.1. Then the mean difference and the standard deviation of the difference were computed.

It is apparent from Tables 4.2 and 4.3 that the standard deviation (STD) of the QNSE experiment is smaller for all variables than the STD of the three other PBL experiments. These reduced STDs indicate that the near-surface variables became less variable in the

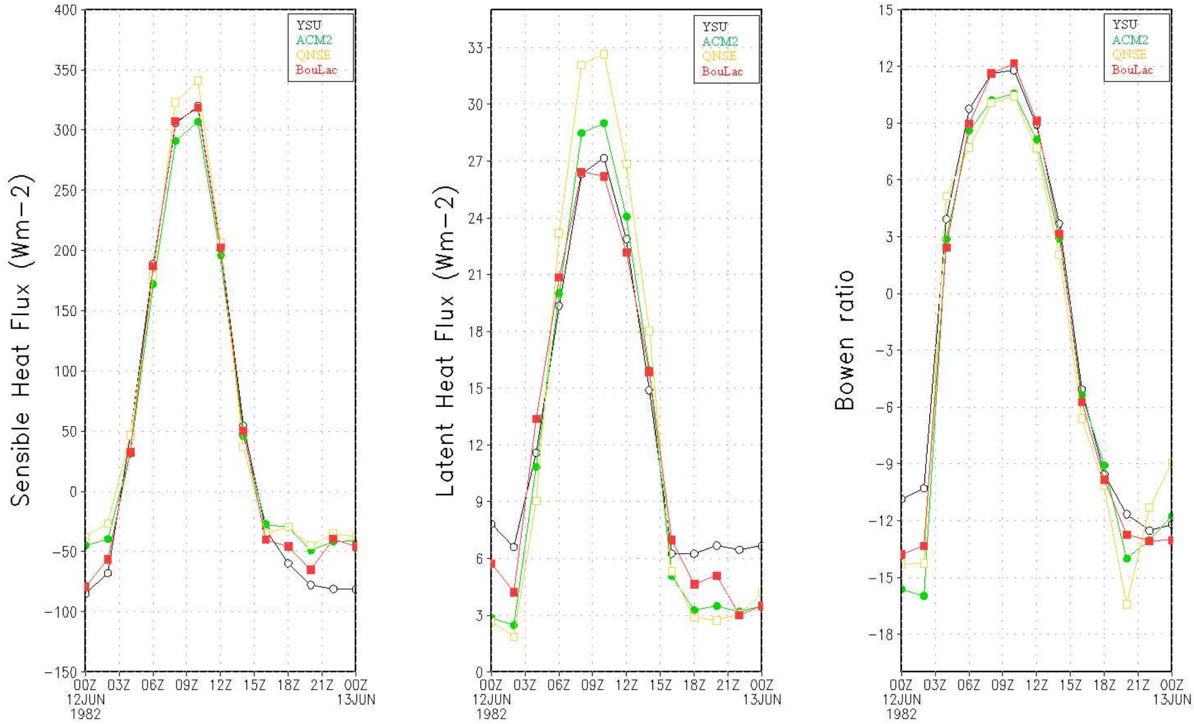

FIGURE 4.3: Time series of surface sensible and latent heat fluxes and Bowen ratio at Dhahran (lat: 26.26 °N, long: 50.15 °E) for all the PBL experiments: YSU (black), ACM2 (green), QNSE (yellow) and BouLac (red).

seven weather stations when the QNSE scheme is used. In agreement with other studies (Shin and Hong, 2011), this result suggests that the QNSE local-closure scheme shows better performance in stable conditions than the other PBL parameterisations. It is worth noting that the QNSE simulated wind speeds are in exceptionally good agreement with the observed ones; the QNSE experiment overestimates in average the wind speeds by only 0.18 m s^{-1} and has STD equal to 0.79. It is also apparent from the Table 4.3 that all PBL experiments underestimate both the maximum temperatures and wind speeds with larger STDs than the one computed for the mean near-surface temperatures and wind speeds. That result can be attributed to the coarse (9 km) horizontal resolution that was selected to validate the WRF simulations. Finally, it seems that for these seven weather stations the local closure schemes (QNSE and BouLac) underestimate the near-surface temperatures, while the non-local closure schemes (YSU and ACM2) overestimate them. According to Hu *et al.* (2010) and to Shin and Hong (2011), the surface-layer schemes tied to these local (non-local) PBL parameterisations calculate large (small) surface exchange coefficient, c_h, in the WRF model. Based on Equation 2.16, the large (small) surface exchange coefficient will give large (small) sensible heat flux, F_S, which in turn will create cooler (warmer) surfaces.

Based on Tables 4.2 and 4.3, there is strong evidence that on average the QNSE PBL scheme does lead to improvements. In order to compare the measurements more

TABLE 4.2: Mean and standard deviation of the 2 metre temperature (T) and 10 metre wind speed (U) differences between the station data and the WRF simulations (YSU, ACM2, QNSE and BouLac) for the whole simulation period.

Experiments	**Mean**		**STD**	
	T(°C)	U(m s^{-1})	T(°C)	U(m s^{-1})
YSU	-0.14	-0.08	1.30	0.81
ACM2	-0.27	0.46	1.19	0.86
QNSE	0.37	-0.08	1.00	0.77
BouLac	0.002	0.74	1.17	0.97

TABLE 4.3: Mean and standard deviation of the 2 metre maximum temperature (T_{max}) and 10 metre maximum wind speed (U_{max}) differences between the station data and the WRF simulations (YSU, ACM2, QNSE and BouLac) for the whole simulation period.

Experiments	**Mean**		**STD**	
	T_{max}(°C)	U_{max}(m s^{-1})	T_{max}(°C)	U_{max}(m s^{-1})
YSU	1.97	0.87	1.91	1.23
ACM2	0.93	0.77	1.76	1.23
QNSE	0.90	0.12	1.72	1.11
BouLac	1.07	1.47	1.78	1.59

objectively the correlation between the QNSE simulation results and the station observations has been calculated for the seven weather stations. The QNSE experiment was selected because showed better performance than the other PBL simulations. Figure 4.4 shows scatter plots of the simulated versus observed mean and maximum temperatures (°C), mean and maximum wind speeds (m s^{-1}). Each point corresponds to one of the seven weather stations in the Arabian Peninsula (see Figure 4.1 and Table 4.1). The correlation coefficients are shown in the upper middle of each plot. The mean and maximum simulated temperature rates over all the data points are 32.00 °C and 38.39 °C, respectively, versus 32.37 °C and 39.29 °C observed (Table 4.1). The WRF model slightly under-predicts the mean and maximum temperature, and hence yields to correlation coefficients 0.93 and 0.81, respectively (Figure 4.4). The mean and maximum simulated wind speed rates over all the data points are 4.96 m s^{-1} and 7.74 m s^{-1}, respectively, versus 4.88 m s^{-1} and 7.86 m s^{-1} observed (Table 4.1). Therefore, the QNSE experiment slightly overestimates the mean wind speed and underestimates the maximum winds; the correlation coefficient for both the mean and maximum wind speed is 0.88 (Figure 4.4). This

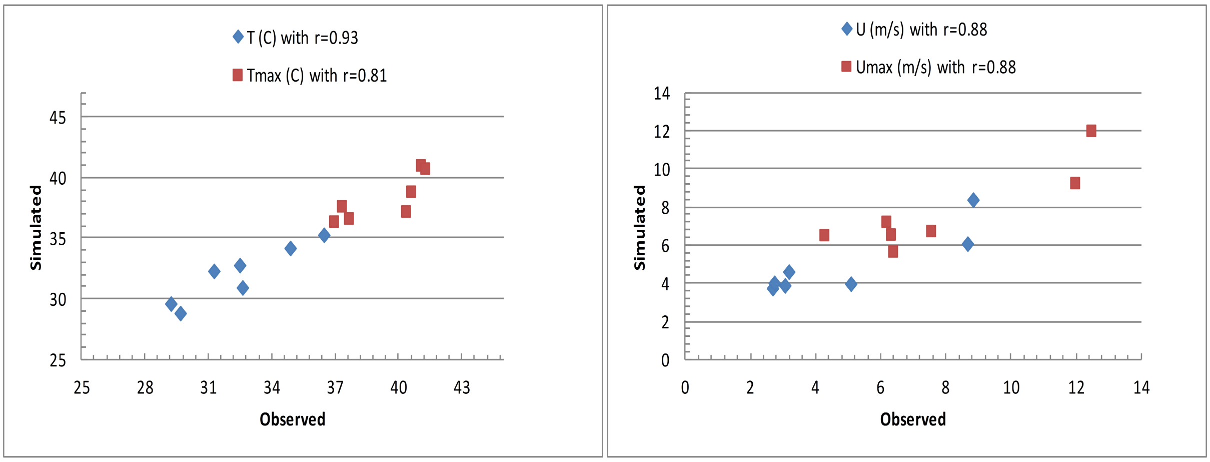

FIGURE 4.4: Scatter plots of the QNSE simulated versus observed mean and maximum temperatures (°C), mean and maximum wind speeds (m s^{-1}). Each point corresponds to one of the seven weather stations in the Arabian Peninsula.

demonstrates the advantage of using the QNSE PBL scheme in simulating the largest wind speeds.

4.4.2 Comparison with atmospheric soundings

The most direct way to investigate the PBL vertical structure is by inspecting of the temperature and wind vertical profiles. The simulated mean and potential temperature and wind profiles corresponding to sounding measurements at 00:00 UTC 13 June 1982 in the geographic location with latitude 29.22 °N and longitude 47.98 °E are presented in Figure 4.5.

It seems that both non-local PBL schemes (YSU and ACM2) and the BouLac parameterisation simulate a warmer PBL than that observed (Figure 4.5(a, b)). For example, the YSU and BouLac runs predict higher temperature than the other runs below 300 m and predict lower temperature above. This implies that the YSU and BouLac schemes transport less heat away from the surface than the QNSE and ACM2 parameterisations. The QNSE and the ACM2 runs forecast the stable profile well, while the YSU and the BouLac experiments produce a more neutral profile (Figure 4.5(b)). According to Shin and Hong (2011), the differences between the potential temperature profiles of the PBL runs is attributed to differences in non-local mixing and entrainment formulations. The QNSE scheme is appropriate for all stable and slightly unstable flows, the ACM2 parameterisation for stable conditions shuts off non-local transport and uses local closure, and the YSU and BouLac schemes tend to enhance mixing in the stable boundary layer. The similar temperatures at night suggest that the QNSE and ACM2 have similar magnitude of local mixing and both seem to lead to vertical temperature profiles in better agreement with the observed ones. The low temperatures observed near the surface with the QNSE

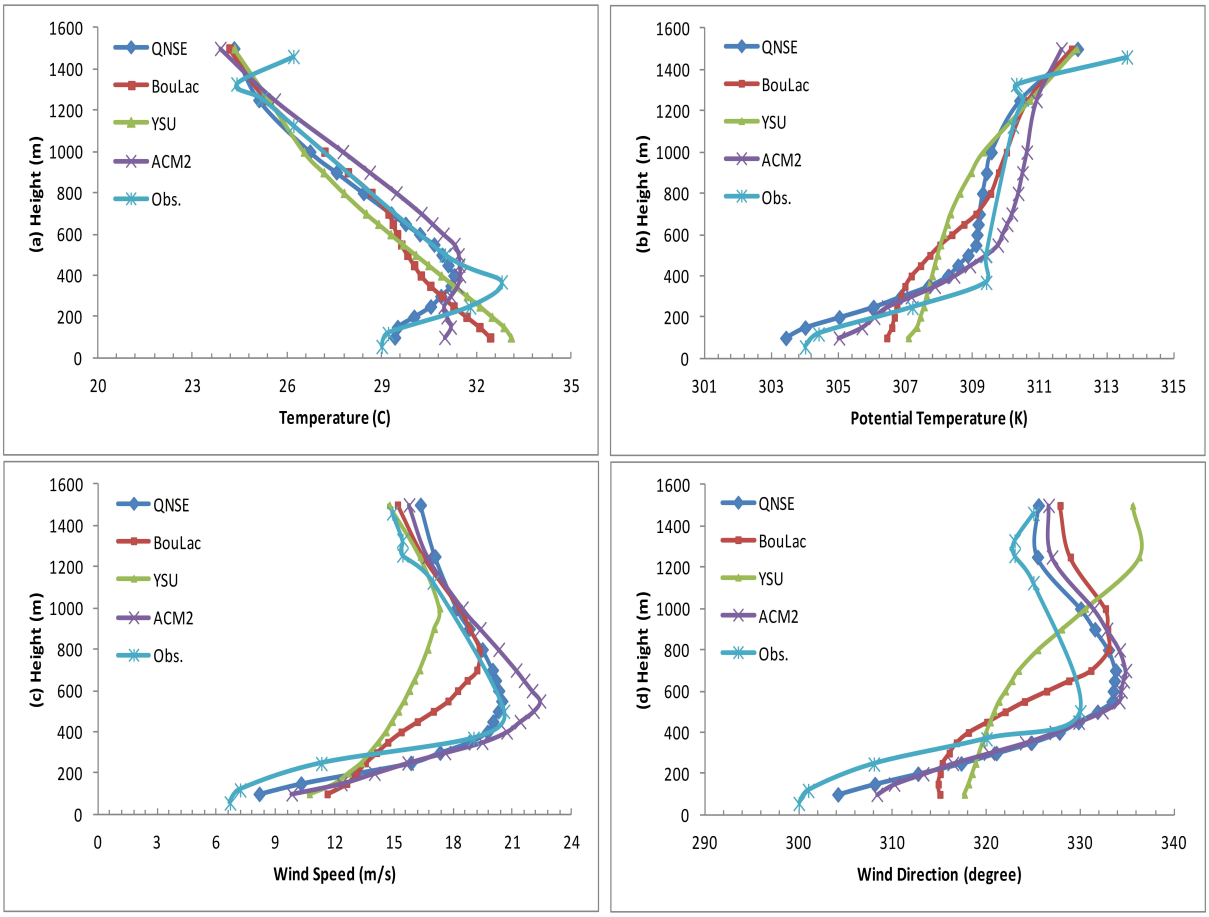

FIGURE 4.5: Vertical profiles up to 1500 m AGL of the (a) simulated mean temperature (°C), (b) potential temperature (K), (c) wind speed m s^{-1}, and (d) wind direction (degree) at 00:00 UTC 13 June 1982 with corresponding radiosonde soundings (light blue line with asterisks). The simulated results are from the QNSE (blue line), BouLac (red line), YSU (green line), and ACM2 (purple line) experiments. Location: lat: 29.22 °N and long: 47.98 °E.

simulation imply the strong radiative cooling that occurred. It is thus shown that all experiments, expect the QNSE run, overestimate the temperatures below 300 m and underestimate the stability of the inversion layer. This surface and near-surface temperature overestimation is possibly caused because of an underestimated surface cooling.

In addition to differences in thermodynamic scalars, important differences between the PBL runs are present in the vertical structure of wind speed and wind direction (Figure 4.5(c, d)). It seems that the QNSE and ACM2 runs produce less bias in wind speed profile in the PBL, with higher wind speeds at 500 m than the YSU and BouLac simulations. The wind speeds increase with height rapidly in the lowest 500 m and a low-level jet develops with the QNSE and ACM2 parameterisations. The wind speed predicted with the ACM2 scheme increases more rapidly in the lowest 500 m than that predicted by the QNSE scheme, resulting in a stronger LLJ than that observed. The ACM2 run predicts maximum wind speed of the order of 22 m s^{-1}, while the QNSE simulation in agreement with the observations predicts maximum wind speed of about 20 m s^{-1} at 500 m level. This implies that the nighttime vertical mixing of momentum near the surface predicted with the ACM2 run is weaker than that predicted with the QNSE simulation. Hu *et al.* (2010) also reported that during nighttime the ACM2 scheme can lead to stronger LLJs. On the other hand, the YSU and BouLac runs underestimated the wind speeds possibly because of an underestimated shear-driven turbulence. The intermittent turbulence during nighttime allows the upper portion of the PBL to decouple from surface friction, and in turn to accelerate the flow above the surface layer (Stull, 1988; Shin and Hong, 2011). Therefore, to accurately predict the magnitude of the LLJ at night, the WRF model should reasonably reproduce the intermittent turbulence. It seems that the QNSE scheme is capable of simulating the decoupling.

For wind direction, the QNSE and the ACM2 are capable of predicting some wind turning in the stable boundary layer close to the one observed (Figure 4.5(d)). The observed wind direction was about 300° near the surface while the simulated wind direction with the QNSE and ACM2 schemes was about 304° and 308°, respectively. A wind turning of about 30° was predicted by both schemes at 500 m AGL in agreement with the observations. The BouLac and YSU runs overestimated the wind direction by about 20° below 250 m and predicted a wind turning at higher levels (about 800 m and 1200 m AGL, respectively) than the observed.

4.5 Conclusions

In this chapter, a series of simulations spanning three days during summer 1982 was conducted with the WRF version 3.2 with two local closure PBL schemes (QNSE and BouLac) and two non-local closure PBL schemes (YSU and ACM2) and compared with surface and boundary layer observations in the Arabian Peninsula. The primary cause of differences in PBL structures was diagnosed as differences in vertical mixing strength and entrainment flux predicted by these four PBL schemes. Use of the local closure QNSE scheme produced the smallest bias. During nighttime the WRF model with the QNSE PBL scheme produced temperatures and wind speeds near the surface and within the PBL closer to the observations than with the other three PBL schemes. The YSU and BouLac schemes both led to predictions of higher temperatures near the surface and lower temperatures above 300 m, and thus larger biases, than the QNSE and ACM2 schemes because of their stronger vertical mixing. The wind speed and wind direction vertical profiles were well simulated when the QNSE scheme was selected. A LLJ with maximum wind speed of the order of 20 m s^{-1} was captured in agreement with the observations. The ACM2 run predicted a more rapidly wind speed increase within the PBL than that predicted by the QNSE scheme because of its weaker mixing during nighttime. It can be concluded that the PBL schemes are responsible for both the shape and the variability of the vertical profiles. Under stable conditions, the QNSE PBL scheme satisfactorily simulated the stable boundary layer.

Chapter 5

The Persian Gulf Summertime Low-Level Jet over Sloping Terrain

The motivation to study the summertime low-level jet (LLJ) over the Persian Gulf, known as the summer Shamal, comes from their significant impact on the meteorological conditions over the Arabian Peninsula (e.g. Ali, 1994). The winter and summer Shamal wind events are well-documented theoretically (e.g. Walters and Sjoberg, 1990; Ali, 1994). However, there are few observational and numerical Shamal studies (e.g. Membery, 1983; Rao *et al.*, 2003; Atkinson and Zhu, 2005). The summertime LLJ is not just a challenge of modelling and forecasting its development, duration and intensity using numerical weather prediction (NWP) models but is also limited by scientific understanding. Deeper understanding of the fundamental physical mechanisms that are responsible for the Shamal development is needed. This chapter reviews the general climatic and weather conditions of the Persian Gulf and briefly describes the wind meteorology of this region. Emphasis is placed on the Shamal (northerly/northwesterly) winds that blow with particular persistence during the summer and their effects are felt over the entire Persian Gulf and southern Iraq.

Understanding the physical mechanisms underlying these summertime LLJs is the ultimate goal of this study. This work provides a thorough investigation of the previously proposed physical mechanisms for the generation and development of LLJs observed worldwide and extends the previous work on the summer Shamal winds by focusing on their diurnal variation. In contrast to other Shamal studies, which largely explain the LLJ formation as a result of the frictional decoupling (Blackadar's theory), this work investigates the relationship between mountainous sloping terrain and Shamal characteristics. In this thesis, we focus on the importance of the Persian Gulf topography on the Shamal intensity, direction, diurnal variation and duration by modelling a strong summer Shamal wind event already identified by Membery (1983). Sensitivity experiments

Figure 5.1: Map of the Middle East which consists of Turkey, Cyprus, Syria, Lebanon, Jordan, Israel, Egypt, the Arabian Peninsular, Iraq and Iran. The original figure is posted in UniMaps.com (http://unimaps.com/mideast/).

with and without the Persian Gulf topography were carried out using the Weather Research and Forecasting (WRF) model. To determine and understand the mountainous height and sloping terrain effects on the Shamal development, mountain height and novel mountain slope sensitivity experiments, in addition to a land–sea sensitivity run, were conducted.

Part of the work presented in this chapter has been published in Giannakopoulou and Toumi (2011).

5.1 The Persian Gulf climate and meteorology

A comprehensive discussion of the general climate and meteorology of the Persian Gulf, also known in some local countries as the Arabian Gulf, is provided by Walters and Sjoberg (1990) and Ali (1994). In this study, the Persian Gulf is defined as the region located between latitudes 24 °N - 30 °N and longitudes 48 °E - 58 °E (Kampf and Sadrinasab, 2006). It is entirely surrounded by desert landmass and it is bounded to the south by Oman and United Arab Emirates (UAE), to the west by Qatar, Bahrain and Saudi Arabia, to the north by Kuwait and Iraq and to the east by Iran (see Figure 5.1). The terrain on the northeastern and eastern shore of the Persian Gulf is in sharp contrast to the rest of the region. High and steep mountains (Zagros Mountains in Iran) are oriented parallel to the shore of the Persian Gulf (Walters and Sjoberg, 1990).

According to Ali's (1994) climatological analysis, the Persian Gulf region is mainly characterized by an arid, sub-tropical climate with relatively cool winters and very hot and dry summers. Mean daily air temperatures below 20 °C and in excess of 30 °C have been recorded during winter and summer, respectively. The annual mean temperature is about 24 °C. However, the temperature distribution in the Gulf region varies due to topographic features and local circulations. For example, in the northern parts of the Persian Gulf (e.g. Kuwait) the air temperature is higher (lower) than it is in the southern parts of the Gulf during summer (winter). It has been recorded that in the northern areas of the Persian Gulf summer temperatures can frequently exceed 49 °C, while winter temperatures can be less than 0 °C (Ali, 1994).

During winter and spring seasons, the Persian Gulf climate is associated with low mean precipitation and high humidity rates. This sparse rainfall mainly occurs between November and April (Ali, 1994). However, from late December to early March thunderstorms can occur along cold fronts over the northern Persian Gulf (Walters and Sjoberg, 1990). According to Walters and Sjoberg (1990), the rain distribution of the Persian Gulf region is closely related to the complex topography of the surrounding countries. For example, annual mean precipitation on the west side of the Persian Gulf is about 50 to 75 mm, while over the middle and southern Persian Gulf, along the Iranian coast and to the south of the Zagros Mountains in Iran it is about 100 to 125 mm (Walters and Sjoberg, 1990). The upper-tropospheric air troughs, the subtropical and polar front jets as well as the migration of cyclones (which are mostly centred on areas of low atmospheric pressure) from the eastern Mediterranean Sea into the Persian Gulf produce frontal systems which bring precipitation in the northern parts of the Persian Gulf and lower the winter temperatures (Ali, 1994).

The climatological studies of Walters and Sjoberg (1990), Ali (1994) and Zhu and Atkinson (2004) revealed four climatological regimes over the Persian Gulf in a year. Based on their analyses, the following four periods with different tropospheric circulations are commonly observed in the Persian Gulf region:

(i) From December to March, the dominant system over the Persian Gulf is a northeast monsoon which is associated with northeasterly low-level winds across the Gulf. A deep Australian thermal low and an Asiatic high-pressure centre over Siberian Russia control the northeasterly low-level flow over the Persian Gulf. The upper-tropospheric flow is sustained westerly (Walters and Sjoberg, 1990; Zhu and Atkinson, 2004).

(ii) From April to May, the whole area is dominated by a spring transition which is characterised by atmospheric boundary layer instability (Ali, 1994). The Persian Gulf climate and weather are mostly influenced by the migration of low-pressure systems from the western Arabian Peninsula. These troughs or depressions are the result of the Inter-Tropical-Convergence-Zone (ITCZ), which is more active during this period in the region near Sudan (Ali, 1994). A Pakistani heat low and its associated secondary lows in Saudi Arabia replace the northeasterly circulation observed from December through March (Walters and Sjoberg, 1990).

(iii) From June to September, a southwest thermal monsoon trough is established across the Persian Gulf. During the dry season this thermal monsoon low increases surface wind speeds and relative humidity (Ali, 1994). The low-level flow over the southern edge of the Persian Gulf is mostly characterised by southwesterly direction. The upper-tropospheric flow is sustained easterly (Walters and Sjoberg, 1990).

(iv) From October to November, the whole area is dominated by a fall transition. The Pakistani low-pressure centre breaks down and the Asiatic high-pressure centre is re-established. Low-level winds that are coming form northwest again dominate the Persian Gulf (Walters and Sjoberg, 1990).

Along with the aforementioned tropospheric circulations the numerous coastlines and mountain ranges, such as the Zagros Mountains of Iran in the east, Higaz and Assir Mountains of Saudi Arabia in the west to southwest, and the Hajar mountains of Oman to the south also modify the local climate and weather (Ali, 1994). According to Warner and Sheu (2000), there is a significant mesoscale local forcing resulting from the existence of the Persian Gulf Sea and the orographic gradients associated with the Tigris-Euphrates Valley in Iraq, the Zagros Mountains in western Iran, and the mountains near the Gulf of Oman. In addition, there are modest variations in the vegetation of the desert landmass that can influence PBL processes in the Persian Gulf through effects on the energy, radiation and soil moisture budgets (Warner and Sheu, 2000). It is worth noting that the numerical study of the Persian Gulf climate and weather is a challenge for researchers due to this complex relationship between topography and climate (Evans *et al.*, 2004).

5.2 Wind meteorology of the Persian Gulf

The literature and scientific knowledge of the climate and wind meteorology of the Persian Gulf is limited and incomplete (Boer, 1997). For instance, the meteorological characteristics of the regional winds that prevail in the Persian Gulf and the mechanisms for predicting the development, duration and magnitude of these winds have not been investigated in detail (Ali, 1994). According to Ali's (1994) study, three main types of winds prevail over the Persian Gulf during the year. These are the winter and summer Shamal winds, the Kous winds and the winds that exist in the coastal areas of Persian Gulf due to sea breezes. The most prominent feature of the Persian Gulf weather system is the Shamal which produces hazardous weather in the region and its surrounding countries (Perrone, 1979; Membery, 1983; Ali, 1994; Rao *et al.*, 2003; Mostafaeipour, 2010; Vishkaee *et al.*, 2012). The Shamal wind events are responsible for adverse weather conditions such as sand and dust storms, dust mobilisation, shear of the low-level winds, low visibility, thunderstorms, and rough seas (e.g. Rao *et al.*, 2003).

Shamal is an Arabic word that means north and is the name given by the local inhabitants to describe the northerly/northwesterly direction of the winds that blow in the Persian Gulf during winter and summer (Perrone, 1979; Ali, 1994). The Shamal is a mesoscale wind phenomenon and the seasonal variations are associated with the relative strengths of the Arabian and Indian thermal lows (e.g. El-Sabh and Murty, 1989; Kampf and Sadrinasab, 2006). Note that the Shamal characteristics of the two seasons are different and someone has to consider their differences in any discussion of these weather phenomena (Perrone, 1979). Although the Shamal winds have been studied for centuries, a survey of the literature reveals that there is no universally accepted Shamal definition. In the present study, Shamal is defined as a northerly/northwesterly wind which blows with particular persistence in summer over southern Iraq and the Persian Gulf and it is often strong at the surface during the day and decreases at night; however, it reaches a wind speed maximum at night above the surface (Membery, 1983). In this thesis, we mainly focus on the summer Shamal wind events and we briefly describe the winter Shamal. A detailed description of the other wind events observed in the Persian Gulf may be found in Perrone (1979), Walters and Sjoberg (1990) and Ali (1994).

5.2.1 Winter Shamal

In winter, the Shamal is of intermittent nature and usually occurs from November to March in association with mid-latitude upper-air low-pressure systems moving from west to east (e.g. Perrone, 1979; El-Sabh and Murty, 1989; Ali, 1994; Thoppil and Hogan, 2010). In particular, the onset of a typical winter Shamal occurs after the passage of a cold upper-air trough from eastern Mediterranean Sea into the northern parts of the Persian Gulf (Ali, 1994). The passage of this cold front pushes heat away and drops temperatures in some places over the Persian Gulf more than 10 °C. Strong northwesterly winds are produced over the Persian Gulf because of the presence of a large pressure gradient that develops behind the cold front passage (e.g. Perrone, 1979; Ali, 1994). A Saudi Arabian surface high (that develops because of upper-level subsidence) and the lower pressure ahead of this frontal system near the Gulf of Oman enhance the surface Shamal winds (e.g. Perrone, 1979; Ali, 1994; Thoppil and Hogan, 2010). The onset and duration of the winter Shamal are difficult to predict, mainly because of the difficulty in forecasting the associated upper-air systems (El-Sabh and Murty, 1989). According to Perrone (1979) and Ali (1994), in order to properly predict the winter Shamal onset, intensity and duration, it is important to consider the relationship between the upper-level jet streams and distribution of lower-tropospheric pressure zones.

Based on the duration, there are two types of winter Shamal: the winter Shamal that can last 12-36 hours and the Shamal that can persist for a period of 3 to 5 days (Perrone, 1979; Thoppil and Hogan, 2010). The main difference between the aforementioned types is that during the shorter-duration Shamal, the upper-air trough moves away quickly to the east (Vishkaee *et al.*, 2012). Note that the winter Shamal is relatively rare; it occurs two or three times per month (Rao *et al.*, 2001). A typical winter Shamal begins in the northwest corner of the Persian Gulf and the strong northwesterly flow is spread southeast behind the cold frontal trough (Perrone, 1979). During winter, Shamal winds can reach wind speeds of 15-20 m s^{-1} near the surface during the daytime (Perrone, 1979; Thoppil and Hogan, 2010). Diurnal variation in wind speed is another winter Shamal characteristic discussed by Perrone (1979). Diurnal variability in the surface wind fields was also observed by Shi *et al.* (2004) and Zhu and Atkinson (2004). Two areas of stronger than average Shamal winds are near the Qatar Peninsula and near the Lavan Island (Perrone, 1979). Perrone (1979) also mentioned the influence of the mountainous terrain on the northwesterly flow; the Shamal is intensified by a lee low effect west of the Zagros Mountains in Iran.

It is worth noting that before the Shamal onset, the vertical structure of the boundary layer in the northern Persian Gulf typically is conditionally unstable (Perrone, 1979). Warner and Sheu (2000) focused on the physical mechanisms that are responsible for the daytime PBL depth in the Arabian Desert during winter. Based on their numerical study, the PBL structure and depth are influenced by coastal-breeze and mountain-valley circulations. Warner and Sheu (2000) suggested that thermally driven mountain-valley circulations on the southwest side of the Zagros Mountains in Iran generate vertical motions that affect the PBL stability.

5.2.2 Summer Shamal

Although the winter Shamal wind events are relatively rare and of short duration, they have been widely studied compared to the summer Shamal winds (Rao *et al.*, 2001; Vishkaee *et al.*, 2012). Rao *et al.* (2001), in a study at Doha, found that 51 % of the Shamal occured in the summer months (May to July) compared with 26 % during the winter months (November to March). The summer Shamal brings some of the strongest winds of the season in the Persian Gulf and dust storms associated with this wind phenomenon are generally very intense in both horizontal and vertical scale (Ali, 1994). The dust sources in the Middle East are significantly active in the summer and the summertime Shamal is responsible for dust mobilisation over the countries surrounding the Persian Gulf (Vishkaee *et al.*, 2012).

The summer Shamal winds usually occur throughout the southwest monsoon season but are strongest during June and July (Walters and Sjoberg, 1990; Rao *et al.*, 2003). According to Rao *et al.* (2003), the two peak periods (June and July) in Shamal activity are related to two Indian monsoon distinct phases. The first period coincides with the onset of the Indian monsoon and the second is related to the most active monsoon phase. Possibly, during these two periods, the northwest Indian and Pakistani thermal lows are intensified and in turn enhance the west-to-east pressure gradients which make the Shamal winds northerly/northwesterly over the Persian Gulf (Rao *et al.*, 2003). The summertime Shamal is of continuous nature and persists for a period of more than 30 days, known as '40-day Shamal' (e.g. Membery, 1983; Walters and Sjoberg, 1990; Ali, 1994; Rao *et al.*, 2003). The '40-day Shamal' term indicates the duration of the whole event including a number of shorter and weaker wind events. The summer Shamal affects regions such as Oman, Abu Dhabi, Qatar, Bahrain, central areas of Saudi Arabia, Kuwait and southern Iraq (Ali, 1994).

According to Walters and Sjoberg (1990), the summertime Shamal results from the combination of synoptic systems and terrain effects. A typical summer Shamal is usually linked with the thermal lows observed over southern Saudi Arabia, Pakistan, northwest India and Iran (e.g. Walters and Sjoberg, 1990; Ali, 1994; Rao *et al.*, 2003). For the Arabian Peninsula, the dominant surface systems in the summer months are: a semi-permanent high-pressure centre, which persists over the eastern Mediterranean Sea and extends eastward over northwestern Saudi Arabia, and a semi-permanent low-pressure zone over Iran, which results because of the expansion of the Indian monsoon low (e.g. Ali, 1994; Rao *et al.*, 2003). The west-to-east pressure gradients developed by the aforementioned synoptic systems make the general flow at the surface northerly/northwesterly over the Persian Gulf (Rao *et al.*, 2003). The complex interaction between the heat low over Pakistan and Afghanistan (enhanced by monsoon circulation) and the terrain features (Zagros and Omani Mountains) results in a secondary low-pressure centre to the south of the mountain range near the Gulf of Oman (Membery, 1983; Walters and Sjoberg, 1990). This secondary low tightens the west-to-east pressure gradients which strengthen the summer Shamal (Walters and Sjoberg, 1990). During the summer, the intense heat gives rise to local low-pressure systems over southern Iraq, resulting in strong north-to-south pressure gradients which also enhance the Shamal winds at the surface (Rao *et al.*, 2003). The mountainous terrain to the east of the Persian Gulf shore (Zagros Mountains) and the gradual up-sloping terrain of the central Saudi Arabia also tend to intensify these northwesterly winds near the Earth's surface (Membery, 1983; Rao *et al.*, 2003).

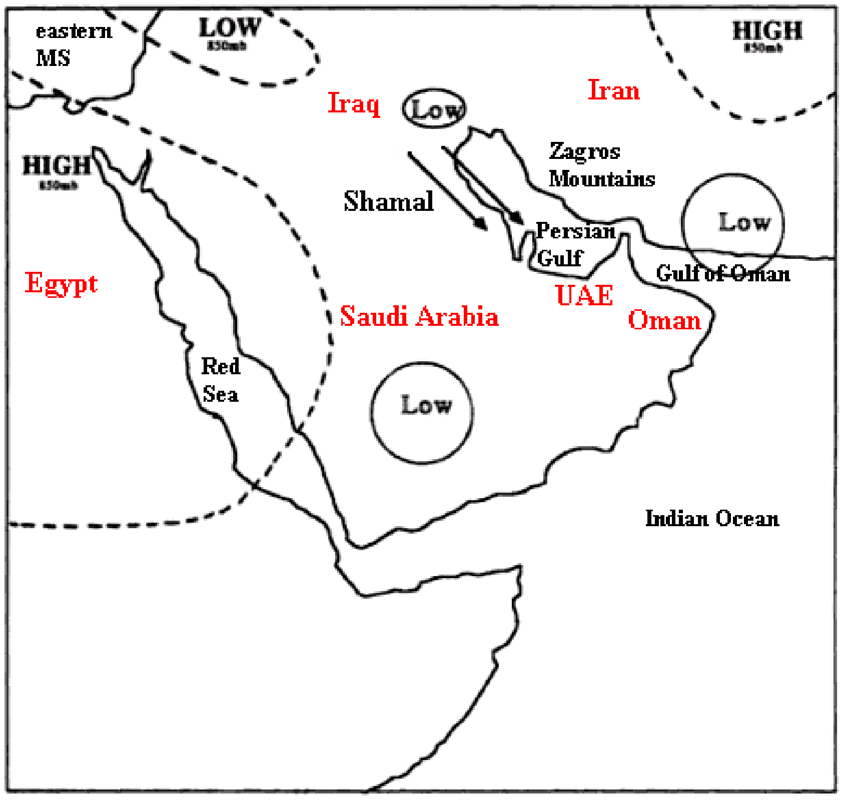

Figure 5.2: Typical summer Shamal synoptic conditions. Location of upper-air high- and low-pressure systems at an elevation of 1500 m above the surface (850hPa geopotential height: HIGH_{850hPa} and LOW_{850hPa}) over the region with respect to the surface low-pressures would result to an average Shamal with northwesterly direction and wind speed that varies from 12.5 m s^{-1} to 17.5 m s^{-1}. Redrawn from Ali (1994).

Synoptic systems that also influence the summer Shamal are: a low-pressure centre over the southern Saudi Arabia and a closed low that develops over Lavan Island near the Gulf of Oman (see Figure 5.2). Figure 5.2 shows a typical synoptic situation favourable for summer Shamal activity. Note that the Shamal winds are restricted to the western Persian Gulf Sea by a compaction of the west-east pressure gradient along the Zagros Mountains (Rao *et al.*, 2003).

The average Shamal wind speed is about 13 m s^{-1}, but in extreme cases Shamal reaches a wind speed greater than 30 m s^{-1} above ground level (AGL), whilst the wind at the surface has geostrophic values (Ali, 1994). The winds are often strong during the daytime and generally drop during the night at the surface level; however, they do not decrease at higher altitudes. As described by Membery (1983), the Shamal winds are nighttime low-level wind maxima within the lowest 1 km level and a possible physical mechanism for their formation is the well-documented inertial oscillation which was first studied by Blackadar (1957).

According to Membery's (1983) study, in the Persian Gulf region during intense daytime heating, the conditions near the surface are unstable causing turbulent flow that transports momentum to the ground. The ABL tends to be coupled with the surface layer and the surface wind approaches the subgeostrophic due to frictional effects (Stensrud, 1996). During the night, since the sky is clear enough, radiational cooling takes place at the surface and for this reason the lower atmospheric levels become stable. According to Membery (1983), sand and gravel of the Persian Gulf lead to a maximum radiational loss (the surface conditions affect the magnitude of the cooling). Subsequently, very little mixing occurs; the low-level flow becomes relatively smooth and strong temperature inversion occurs to affect the winds. Once the turbulent mixing stops late in the day, the frictional constraints are released and the overriding air tends to be decoupled from the underlying air. According to Blackadar (1957), in the layer above the temperature inversion, the imbalance between the pressure gradient force and the Coriolis force induces the wind vector to take part in an inertial oscillation leading to supergeostrophic values of the wind several hours later (Stensrud, 1996). The result is the development of a nocturnal low-level jet profile with a low-level wind maximum usually between 300 to 700 m AGL (Membery, 1983). The summer Shamal wind profile is characterised by uniformity in wind direction and a marked temperature inversion (e.g. Membery, 1983; Ali, 1994). These factors combine to make the Shamal a significant challenge to climate and meteorological models.

5.3 Review of Shamal studies

The first extensive meteorological analysis that provides a description of the atmospheric conditions of the Persian Gulf and subsequently of the Shamal wind events was performed during and after the 1991 Gulf War. Prior to this, Perrone (1979) gave a comprehensive description of the winter Shamal. Membery (1983) in his observational study explained the nocturnal features of summertime Shamal wind events by using the inertial oscillation theory. Later, Walters and Sjoberg (1990) in their comprehensive climatological study focused on the four climatological regimes that are dominant over the Persian Gulf during the year and briefly discussed the winter and summer Shamal characteristics. Ali (1994) analysed the general wind meteorology of the Persian Gulf and examined the dust storms associated with the summer Shamal. Rao *et al.* (2001) examined aspects of winter Shamal wind events and updated Perrone's (1979) work. Rao *et al.* (2003) analysed surface and upper-air data from a 7-year period (1990-1997) during the summer Shamal months. They gave particular emphasis on the synoptic systems that influenced the Shamal intensity and direction.

Several researches focused on the near-surface wind fields (at 10 m AGL) over the Persian Gulf. For example, Shi *et al.* (2004) analysed the fields from a 2-month reanalysis (January-March 1991) in order to provide a picture of the winter synoptic and near-surface conditions of the Persian Gulf. Their main results were: light and variable nocturnal surface winds, diurnal variation due to the land–sea circulation, barrier effects of the Zagros Mountains to the westerly flow. Zhu and Atkinson (2004) found that the near-surface winds over the Persian Gulf were dominated by a land–sea breeze circulation that varied diurnally and seasonally throughout the year. Other researchers have focused on the heat-budget (e.g. Thoppil and Hogan, 2010), the strong surface radar-duct and boundary layer characteristics on a typical winter Shamal day (e.g. Brooks *et al.*, 1999; Brooks and Rogers, 2000; Atkinson and Zhu, 2005) and the dust transport associated with winter Shamal (e.g. Vishkaee *et al.*, 2012) over the Persian Gulf. Some of these studies acknowledged the Shamal wind characteristics, the synoptic conditions on particular Shamal wind events, the effects of the Zagros Mountains in the low-level flow, the importance of the land–sea distributions and the strong diurnal variability in the wind speed (e.g. Brooks and Rogers, 2000; Shi *et al.*, 2004; Zhu and Atkinson, 2004; Atkinson and Zhu, 2005), but none of these works have systematically studied the summertime Shamal wind events and the effects of the Zagros Mountains on the diurnal variation of the Shamal wind using realistic high-resolution meteorological models.

5.4 Background to the problem

The effects of summertime LLJs on events such as dust and sand storms in the Persian Gulf (Ali, 1994) have demonstrated the need for a clear understanding of the physical mechanisms underlying such LLJs. As discussed in detail in section 2.2, several physical mechanisms have been proposed to describe and explain the occurrence, development and characteristics of LLJs including those occurring over the Great Plains of the United States (e.g. Parish and Oolman, 2010), along the California coast (e.g. Burk and Thompson, 1996) and Greenland (e.g. Renfrew *et al.*, 2008). In particular, two well-documented theories based on ABL processes have been studied during the past five decades. The first theory was developed by Blackadar (1957), who addressed the ageostrophic motions of LLJs which result from an inertial oscillation, and their importance for the development of nighttime inversions. A second theory was proposed by Holton (1967), who noted that the development of diurnal wind variations due to the daytime heating and nighttime cooling of sloping terrain could affect the LLJs' intensity (see section 2.2).

As mentioned in section 5.1, the Persian Gulf is near-complex terrain with high and steep mountains, including the Zagros Mountains in Iran to the east (Figure 5.3(a)), the mountains of Saudi Arabia in the west, and the Hajar mountains of Oman to the south (Ali, 1994). From late May to early July, a frequent weather phenomenon in the Persian Gulf is the long and persistent summer Shamal, whose significance lies in the strong flow at levels within the ABL (Membery, 1983). The northerly/northwesterly Shamal is a

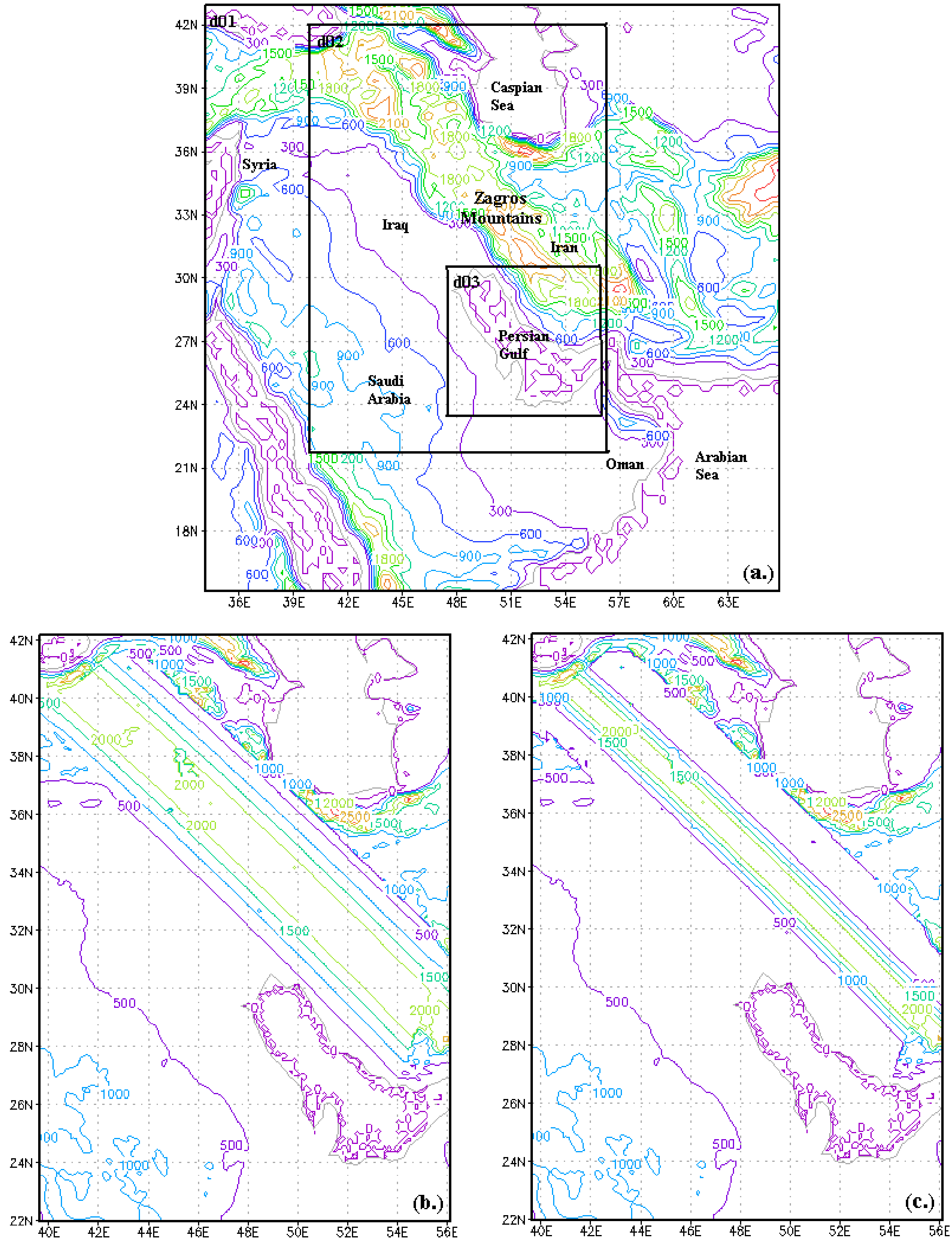

FIGURE 5.3: (a)WRF modelling domain: 27 km (d01), 9 km (d02) and 3 km (d03) grid spacing for the control run. Terrain contours are drawn every 300m, with elevations above 900 m lightly contoured. (b) and (c) show the WRF 9 km (d02) modelling domain with topography for (b) the shallow and (c) the steep mountain slope experiments; terrain contours are drawn every 500 m, with elevations above 1500 m lightly contoured. Taken from Giannakopoulou and Toumi (2011).

prominent LLJ of the Persian Gulf and southern Iraq (Membery, 1983); however, there has been no detailed analysis to explain the intensity, development, frequency, direction and diurnal variation of this summertime wind maximum. This LLJ is primarily a thermal phenomenon and reaches heights where the vertical temperature profile forms an inversion (e.g. Membery, 1983; Rao *et al.*, 2003). At the surface, the Shamal is strong during the daytime and generally decreases at night; however, this is not the case above the surface. In fact the wind speed reaches its maximum at night at low levels (300-700 m) of the atmosphere. These nighttime features of the Shamal have been considered to be a form of nocturnal jet (Membery, 1983).

Membery (1983) was one of the first researchers to study and explain the nighttime features of the summer Shamal wind events by using Blackadar's (1957) theory. So far the only proposed physical mechanism to describe the formation and development of this nocturnal maximum is the inertial oscillation, but uncertainties still exist regarding the understanding of what forces the Shamal as a whole. Membery (1983), in his observational study, did not focus on the significance of the land–sea distribution and mountain ranges in the Persian Gulf region. According to Walters and Sjoberg (1990), the climatology and the topographical features of the region play a dominant role in the Shamal formation. Previous work has investigated the near-surface atmospheric conditions of the Persian Gulf, indicating the influence of the surface characteristics, terrain, and the land–water distribution on the near-surface (10 m AGL) wind fields (Shi *et al.*, 2004; Zhu and Atkinson, 2004). Although their work was not a summertime Shamal study, their results provided some interesting information about the near-surface conditions of the Persian Gulf that might be useful to consider in our Shamal study. Their study is an indication that the complex terrain features of the region could have a profound influence on the summertime Shamal wind events. Unlike the Great Plains LLJ (e.g. Parish and Oolman, 2010), it seems that the land–sea topographical features also play a significant role in the Shamal intensity. Thus, Membery's (1983) conclusion that the Shamal winds were a simple result of the inertial oscillation requires further examination.

The current understanding and modelling capability of the summer Shamal wind events is limited. Most of the modelling studies in the Persian Gulf have been focused on the PBL characteristics, near-surface wind fields and land/sea breeze circulations over the region (e.g. Zhu and Atkinson, 2004; Atkinson and Zhu, 2005). There is a need to improve fundamental understanding that will help to establish the physical causes of this summertime LLJ. To improve this situation, we need to use NWP models that are accurate and sensitive enough to capture the Shamal development, intensity, duration and direction. According to Storm *et al.* (2009), the Weather Research and Forecasting (WRF) model has the potential to capture LLJs' characteristics.

Although many studies have been focused on the interaction of the fronts and barrier jets with the orographic height, little attention has been given to the interaction of the along-mountain LLJ with the mountain slope. In this chapter, the WRF model is used to conduct a control run and terrain height sensitivity experiments and to determine how the Zagros Mountains' slope affects the Shamal flow. In order to achieve this, we extend the analysis of Pierrehumbert (1984) by considering a Gaussian-shaped range with relatively gentle slopes. The effects of the slope are assessed with two sensitivity experiments in which the Zagros Mountains in Iran are replaced by the Gaussian range of different slopes (shallow and steep slope) for a particular summer Shamal event (Figure 5.3(b, c)). To the best of the author's knowledge, the present application is the first detailed model study of summertime Shamal wind events. Applying mountain slope sensitivity experiments to any LLJ where the local terrain, synoptic scale and surface forcing are treated realistically is also novel. Finally, we also conduct a land–sea sensitivity experiment (the Persian Gulf Sea is replaced by barren vegetated land) in order to determine and understand the physical mechanisms through which the land–sea distribution affects the intensity and diurnal oscillation of the Shamal winds.

The main objectives that we aim to examine in this chapter are:

(i) the ability of a high-resolution model to accurately simulate the vertical structure, intensity and wind direction of the Shamal winds;

(ii) the factors that determine the Shamal wind strength, duration and direction;

(iii) the physical mechanisms that explain the diurnal oscillation of the Shamal wind speed and wind direction; and

(iv) the orographic effects on the Shamal wind development.

5.5 Methodology

5.5.1 Model description

To address the aforementioned issues, we have used the WRF model, Version 3.2 (Skamarock *et al.*, 2008). This is based on the fully compressible, non-hydrostatic Euler equations and for the purposes of this research we chose Mercator grids. A 3rd order Runge-Kutta (RK3) integration scheme and Arakawa C-grid staggering were used for temporal and spatial discretization, respectively.

In order to simulate the Shamal winds efficiently, a set of 27, 9 & 3 km one-way nested domains with 50 vertical levels (no specified eta levels were provided, but the model calculated a nice set of vertical levels with thinner layers at the model bottom and thicker layers at the model top) were selected. This series of nested grids was chosen to model

Table 5.1: WRF physics and dynamics options used for the study of the summertime LLJ over the Persian Gulf.

Dynamics	Non-hydrostatic
Map projection	Mercator
Grid type	Arakawa C-grid
Spatial integration	Positive-definite advection option for both moisture and scalars
Time integration	3rd-order Runge-Kutta
Domain configuration	3 domains (27, 9 & 3 km); grids (115×117, 178×259, 247×271); 50 vertical levels
Time step	135 s, 45 s and 15 s for each domain
Integration time	168 h (CTRL run), 216 h (sensitivity experiments)
Physics schemes	PBL–QNSE; Land surface–Noah; Longwave radiation–RRTM; Shortwave radiation–Dudhia; Microphysics-–WSM 3-class; Cumulus—Kain-Fritsch
Land-use classification	USGS 24-category
Initial and lateral boundary conditions	ERA-40 re-analysis

a large geographic area and to include dynamically important terrain features, since the Shamal is a mesoscale wind phenomenon and the terrain can influence its development (see section 5.2). The WRF model was built over a parent domain (d01) with 115×117 horizontal grids (centred at 30.0 °N and 50.0 °E), an intermediate nested domain (d02) of 9 km spatial resolution (178×259 horizontal grids), and an innermost domain (d03) with 3 km spacing and 247×271 horizontal grids (Figure 5.3(a)).

Within the WRF model, the vertical mixing and diffusion were performed by the planetary boundary layer (PBL) scheme alone. For this study, the Quasi-Normal Scale Elimination (QNSE) boundary layer scheme, which provides a new approach for stably stratified cases, was added (Sukoriansky *et al.*, 2006). In this new PBL scheme, turbulence and waves are treated as one entity and there is not a critical Richardson number to determine the PBL depth (Sukoriansky *et al.*, 2006). This scheme was selected because of its computational efficiency and its capability to realistically represent the boundary layer structure in stably stratified conditions (see chapter 4). The QNSE Monin-Obukhov similarity theory (Sukoriansky *et al.*, 2006) for the surface-layer option was tied to this particular PBL scheme. The physics subset for this study contains the WRF Single Moment (WSM) 3-class scheme, which is a simple ice microphysics scheme suitable for mesoscale grid sizes (Hong *et al.*, 2004). The WSM3 scheme predicts three categories of hydrometers: cloud water/ice, rain/snow and water vapour. This is a computationally efficient scheme because the cloud water and cloud ice are counted as the same category. In addition, cumulus physics for deep and shallow convection was modelled with the Kain-Fritsch scheme (Kain, 2004), which was turned off in the fine grid spacing (3 km) selected for these simulations. Theoretically, it is only valid for parent grid sizes greater than 10 km (Skamarock *et al.*, 2008). For radiation, the RRTM (Rapid Radiative Transfer Model) longwave scheme developed by Mlawer *et al.* (1997) and the Dudhia shortwave scheme developed by Dudhia (1989) were selected because they are widely used and tested by the WRF community and due to their computational efficiency.

Land-surface interactions were simulated with the Noah land surface model (Chen and Dudhia, 2001) which is a four-layer soil model predicting soil moisture and temperature. Vegetation and land-use classifications are provided by the USGS (United States Geological Survey) dataset containing 24 different land-use categories. Note that the terrestrial datasets' resolution has a direct effect on the representation of orography on the WRF model. If the terrestrial dataset is coarse, it cannot provide details about the orography to high-resolution WRF modelling domains. It was, therefore, needed to chose the appropriate spatial resolution of these datasets for each WRF modelling domain. In this study, the USGS dataset was used with the appropriate spatial resolution for each modelling domain (5 minutes, 2 minutes, and 30 seconds resolution for d01, d02 and d03, respectively). The soil effects were included by using a 16-category soil dataset which took into account the root zone, soil drainage and runoff. An overview of the WRF dynamics and physics used for this case study is provided in Table 5.1.

It is widely known that atmospheric NWP models face a challenge in precisely modelling and forecasting boundary layer regimes. For accurate numerical modelling of the Shamal winds, several tests were conducted prior to the final simulation to investigate the impacts of different physical parameterisations, horizontal and vertical resolutions on the Shamal development, intensity and direction. Note that the setup described above was found to produce more accurate estimations of wind and temperature fields within the PBL than any other configuration.

5.5.2 Experiments

Six sensitivity studies for comparison with the control run were conducted. In the first numerical experiment, the terrain height over the simulated domains was set equal to zero. The second study was a case where the Zagros Mountains height was reduced by 50 percent and in the third case the mountainous terrain height above 500 m was replaced with a 500 m plateau. In the fourth run, the Zagros Mountains in Iran were replaced by a Gaussian mountain range with shallow slopes, while the fifth sensitivity simulation was a case with steep slopes (Figure 5.3(b, c)). In the mountain slope sensitivity experiments the mountain shape was specified by the two-dimensional elliptical Gaussian function:

$$f(x, y) = Ae^{-\left(\frac{(x-x_0)^2}{2\sigma_x^2} + \frac{(y-y_0)^2}{2\sigma_y^2}\right)}. \tag{5.1}$$

The coefficient A was the height of the mountain's peak, (x_0, y_0) was the centre of the Gaussian Mountain for each model domain and (σ_x, σ_y) were the (x, y) spreads of the mountain chain, respectively. For simplicity $A = 2500$ m and the values that control the mountain slopes were chosen on the basis of changes in the standard deviation. A low standard deviation indicated that the points tend to be very close to the centre of the mountain (steep slope - narrow mountain); whereas high standard deviation indicated that the points are spread out over a large range of values (shallow slope - broad mountain). For example, in the shallow mountain slope sensitivity experiment for the first nested domain (d02) the mountain top was $A = 2500$ m, the centre point was $(x_0, y_0) = (92, 156)$ and the mountain width defined by the $\sigma_x = 10^{-9}$ and $\sigma_y = 0.07$.

Finally, the sixth sensitivity experiment involved changing the water bodies over the Persian Gulf into sparsely vegetated land. Correspondingly, surface albedo, roughness length, vegetation cover and several other parameters (e.g. leaf area index, emissivity) in the Noah land surface model were modified too. Tests showed that a spin-up time of at least 48 hours is advantageous for all the sensitivity experiments, so that the model is able to adjust to the topographic changes. The surface energy budget equations, the land surface parameters, the initial temperature and wind profiles were left unmodified for the terrain height and the Gaussian mountain range sensitivity experiments. That created some instabilities in the beginning of the simulation to which the model adjusted during the aforementioned 48 hours.

5.5.3 Case study: 11 June 1982 Shamal wind event

A strong summer Shamal wind event already identified by Membery (1983) was selected as our study period for this work. The 11 June 1982 Shamal event was one of the first observationally studied LLJs over the Persian Gulf and was a typical summer Shamal with northwesterly direction. According to Membery (1983), the northwesterly winds occurred as a result of the interaction of two circulating pressure centres: a low-pressure cell over Iran and a semi-permanent high over northwestern Saudi Arabia. The northwesterly flow was enhanced by the strong west-to-east pressure gradients. This was most pronounced when a low-pressure centre developed near the Gulf of Oman. The Shamal over the Persian Gulf and southern Iraq resulted from the combination of the complex terrain of the Zagros Mountains to the east of the Persian Gulf, the Gulf waters (which acted as a source of sensible heat), the presence of the aforementioned semi-permanent pressure systems, the topographical features of central Saudi Arabia and a trough to the lee of the Zagros Mountains.

The control experiment began at 0000 UTC (0300 h local time) on 07 June 1982 and ended at 0000 UTC on 14 June 1982. The initial and lateral boundary conditions were provided by ERA-40 re-analysis data produced by the European Centre for Medium-Range Weather Forecasts (ECMWF). The ERA-40 re-analysis project was chosen for initialisation since it covers the period from 1957 to 2002. The ERA-40 dataset has T159 spectral resolution which is equivalent to 125 km horizontal resolution on a N80-reduced Gaussian grid (Uppala *et al.*, 2005). The re-analysis has temporal resolution of 6 hours and is available from the British Atmospheric Data Centre (BADC). Note that the coarse domain provided lateral boundary conditions for the fine nested domains at every time step of the parent domain. Because the purpose of this study was to perform the sensitivity experiments rather than to keep the simulations close to the aforementioned re-analysis, the four-dimensional data assimilation (FDDA) was not used (Skamarock *et al.*, 2008).

5.6 Simulation Results

5.6.1 Control experiment

Simulation results from the 3 and 9 km horizontal resolutions for the 11 June 1982 Shamal event are used here to show the potential of the WRF model to capture the basic vertical structure and characteristics of the LLJ. In chapter 4, we showed that the WRF model is able to simulate the LLJs' horizontal and vertical structure, direction, intensity and nocturnal features in good agreement with surface and boundary layer observations obtained from the NOAA Satellite and Information Service and from the University of Wyoming, respectively. In this section the simulation results are also compared with Membery's (1983) observations [information from wide-bodied aircrafts equipped with Inertial Navigation Systems (INS)].

Low-level wind speeds in excess of 25 m s^{-1} at 300 m AGL are simulated from the finest (3 km) horizontal resolution in exceptionally good agreement with Membery's (1983) observations. As an example, Figure 5.4(a) shows the LLJ vertical profile at selected time (2200 UTC on 11 June 1982) over mid-Gulf (lat: 28.0 °N, long: 50.0 °E). We focused on

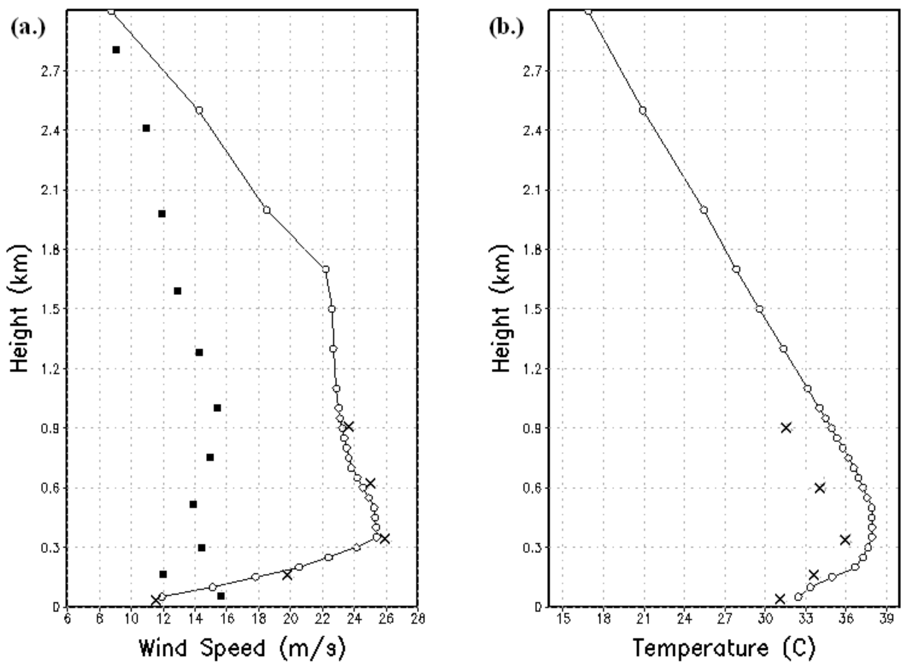

FIGURE 5.4: (a) Total and geostrophic wind speed (m s^{-1}) and (b) temperature (°C) profiles up to 3 km AGL over mid-Gulf (28.0 °N, 50.0 °E) at 2200 UTC on 11 June 1982 (control run; 3 km resolution). The black curve with the empty circles indicate the simulated values, the black squares the geostrophic wind and the crosses are Membery's (1983) observations at 2145 UTC on 11 June 1982. Taken from Giannakopoulou and Toumi (2011).

this particular site because of the high frequency of strong Shamal wind events and also because some limited observations are available for comparison with our model results. According to Stensrud (1996), a LLJ is commonly defined by examining the vertical profile of the horizontal winds to determine if a wind speed maximum occurs at the low levels of the troposphere (see section 2.2). As evident from the Figure 5.4(a), a LLJ profile develops because of the low-level wind maximum at 300 m AGL, the small values of the wind speed (11 m s^{-1}) near the surface due to friction (the frictional drag disrupts the geostrophic balance and slows the actual wind) and the geostrophic wind (9 m s^{-1}) above the boundary layer. The simulation results also indicate that the height of the wind maximum is related to the height and the magnitude of the temperature inversion (Figure 5.4(b)). This result is consistent with the Blackadar's (1957) study, which was credited with finding that the height of the velocity maximum is in agreement with the height of the top of the nocturnal inversion. It is worth noting that because of the model configuration described in subsection 5.5.1 and the fine horizontal (3 km) and vertical (50 vertical levels) resolution, the fine structure of the observed LLJ was captured, unlike similar studies in which the wind speed was underestimated and the height of the LLJ core was overestimated (e.g. Atkinson and Zhu, 2005; Storm *et al.*, 2009).

It should, however, be noted that these observations over mid-Gulf cannot provide ev-

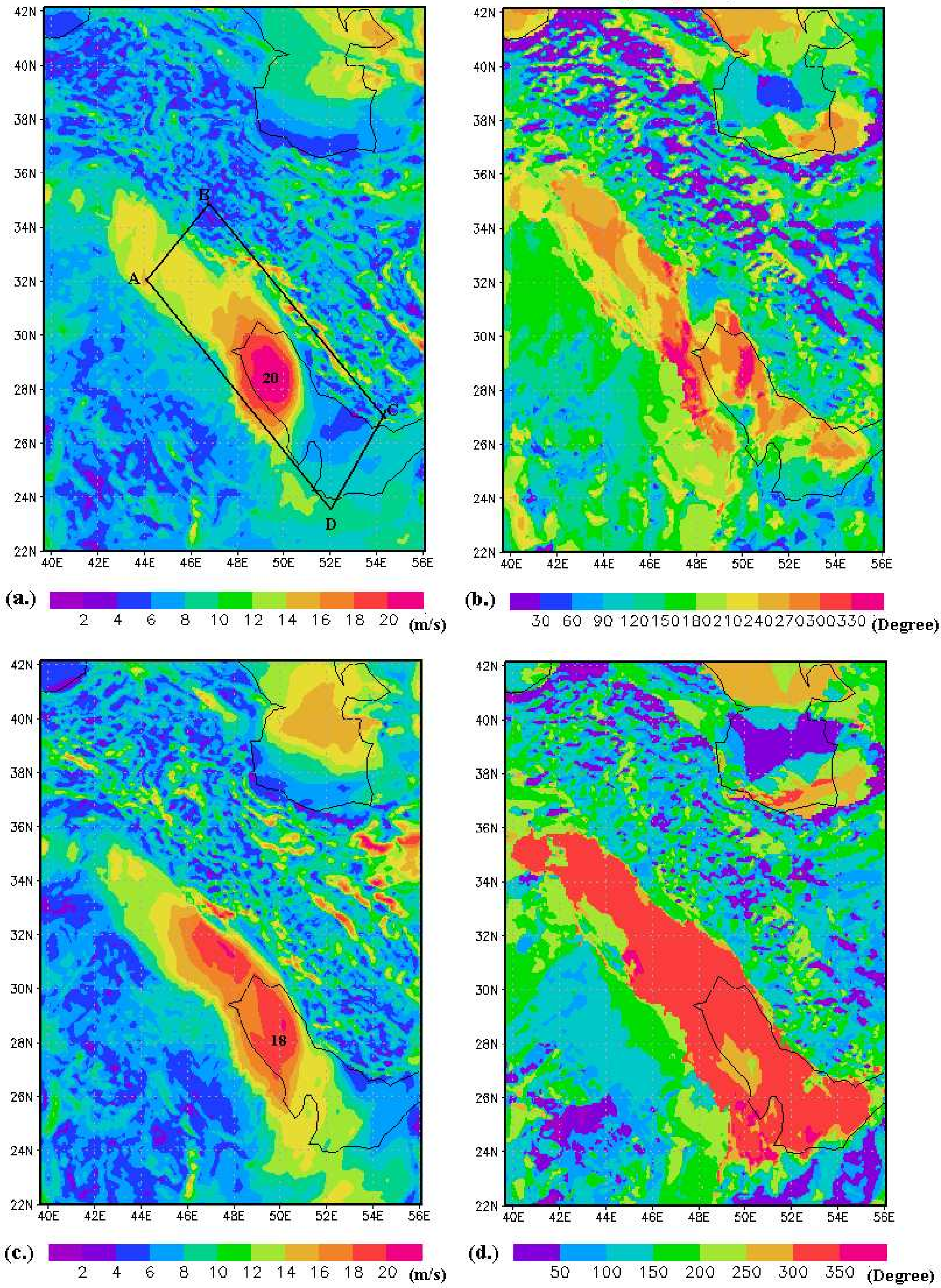

FIGURE 5.5: (a) Nighttime (2200 UTC) wind speed (m s^{-1}) and (b) wind direction (degrees) at 300 m AGL from the control run (9 km resolution) were averaged over the first four simulation days (less extensive period). (c, d) are as (a, b), but the nighttime (2200 UTC) wind speed and direction were averaged over the last three simulation days (extensive period). In (a), the box ABCD denotes the region for the spatial averaging of wind speed and direction. Taken from Giannakopoulou and Toumi (2011).

idence of the potential of the WRF model to simulate two Shamal periods characterised by different wind speeds and wind directions. The whole study period can be divided into a period during which the Shamal is less spatially extended (the less extensive period is characterised by strong flow only over the Persian Gulf) and a period during which it is spatially extended (the extensive period is characterised by strong flow covering the Persian Gulf and southern Iraq), as illustrated by Figures 5.5(a) and (c), respectively. Figure 5.5 shows the 300 m AGL time-average Shamal wind speed and direction at the time of the maximum occurrence over the first nested domain (9 km horizontal resolution) for both observed periods. For the less extensive period, all the peak nighttime (2200 UTC) Shamal were averaged over the first four simulation days and for the extensive period, all the peak nighttime (2200 UTC) Shamal were averaged over the last three simulation days. It is worth noting that in both periods offshore wind maxima are observed over the Persian Gulf Sea (an area of reduced friction). The less extensive period (0000 UTC on 7 June 1982 to 0000 UTC on 11 June 1982) is characterised by a narrow time-average velocity maximum of 20 m s^{-1} and westerly/northwesterly wind direction (250° to 300° in persistence) over the Persian Gulf (Figure 5.5(a, b)). It is also evident from Figure 5.5(b) the prevailing westerly/southwesterly flow in the northern parts of Iraq.

The extensive period (0000 UTC on 11 June 1982 to 0000 UTC on 14 June 1982) is characterised by strong winds (more than 19 m s^{-1} at 300 m level) which prevail in the central provinces of Iraq and northern Persian Gulf (Figure 5.5(c)). In both periods, wind speeds in excess of 15 m s^{-1} also extend northeast, suggesting the significance of the heating differences resulting from the Zagros Mountains' slopes. But, this is most pronounced in the extensive period (see Figure 5.5(c)). The northwesterly direction (300° to 330° in persistence) along the 9 km modelling domain can be seen in Figure 5.5(d). As mentioned in subsection 5.5.3, the northwesterly direction is mainly a result of the west-to-east pressure gradients caused by the semi-permanent synoptic systems over the Arabian Peninsula. A small increase in the magnitude of the west-to-east pressure gradients, because of a surface low-pressure area to the lee of the Zagros Mountains, possibly enhances the northwesterly flow during the extensive period. It seems that the larger flow patterns determine if the Shamal wind is extensive.

The strong northwesterly winds blew with particular persistence from 1200 UTC on 11 June 1982 to 1200 UTC on 14 June 1982, affecting areas such as southern Iraq, Kuwait, Saudi Arabia, Strait of Hurmoz, Qatar, Abu Dhabi and Bahrain. Figure 5.6 is a 3-D visualisation of the Shamal flow at 1800 UTC on 12 June 1982 over the d01 (27 km resolution) modelling domain at 530 m AGL. In order to give an indication of how strongly the wind is blowing, the wind vectors are coloured according to the wind speed (weak winds have red colour and strong winds have green colour). As evident from the Figure 5.6, strong northwesterly winds with their origin in eastern Mediterranean Sea

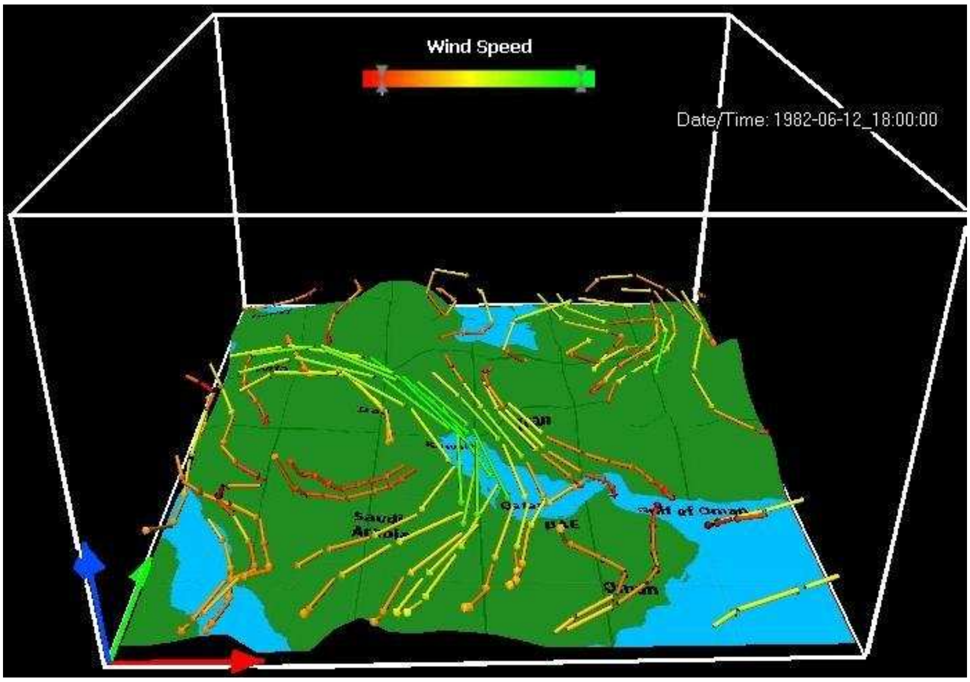

FIGURE 5.6: 3-D wind vectors showing the Shamal flow at 1800 UTC on 12 June 1982 over the d01 (27 km resolution) modelling domain at 530 m AGL. The vertical height of the box is 10 km and the arrows are used as a simple indicator of the wind direction. The wind vectors are coloured according to the wind speed (weak winds have red colour and strong winds have green colour).

affect the central provinces of Iraq and the Persian Gulf Sea. It is also apparent from Figure 5.6 that over the west coast of the Persian Gulf, near Qatar, the northwesterly winds veer to a northeasterly sea breeze. Two possible reasons for this phenomenon are proposed. Firstly, it seems that the northeasterly winds are driven by the large-scale flow patterns; the semi-permanent high-pressure cell to the northwest of Saudi Arabia contributes to this onshore flow. Secondly, the land surface at the southern Saudi Arabia is hotter (32 °C) than the Persian Gulf waters (27 °C) resulting in a near-surface superadiabatic temperature lapse rate, which in turn produces thermals that could initiate a sea breeze.

It appears that the Zagros Mountains in western Iran are responsible for the low-level channelling of the mountain-parallel Shamal winds (Figure 5.5), so that for both less extensive and extensive periods the LLJ is restricted to the west of the mountain range (Figure 5.5(a, c) and Figure 5.7(a)). The fact that the LLJ only persists to the west of the Zagros Mountains, again suggests that the heating of the elevated terrain is important and that the Blackadar (1957) mechanism is secondary to the heating in forcing the Shamal. In Figure 5.7(a) we show the vertical cross-section of the time-average wind speed (in m s^{-1}) and temperature (in °C) taken for all the simulation days at 2200 UTC (0100 h). The west-to-east cross-section near 28 °N extends from 47 °E to 55 °E; the

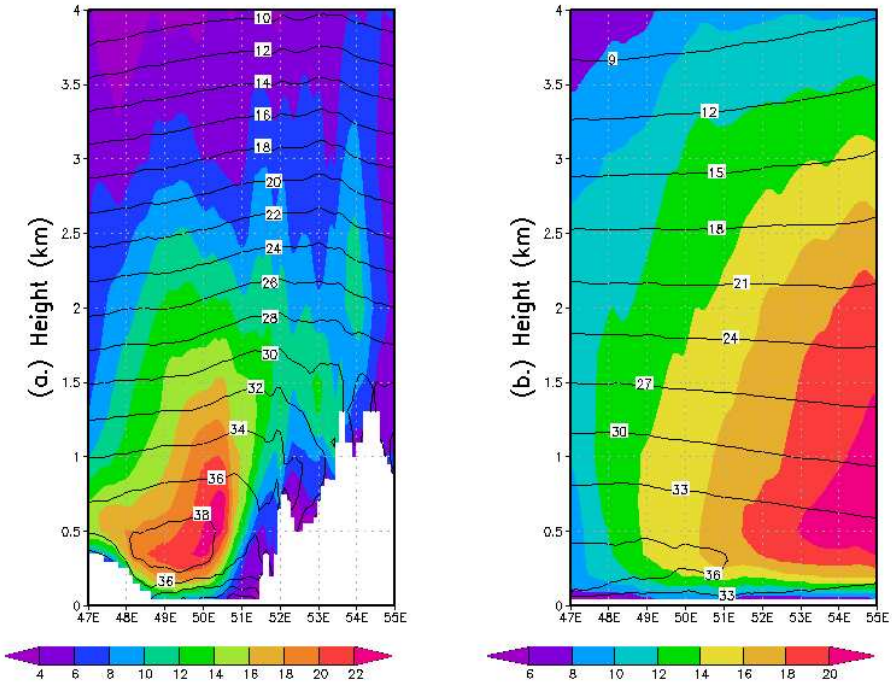

FIGURE 5.7: Cross-sections at latitude 28 °N extending from longitudes 47 °E to 55 °E showing wind speed (shading, m s^{-1}) and temperature (solid contours, °C) for (a) the control and (b) the Zzero experiments (9 km resolution), both time averaged over the whole study period at 2200 UTC. The vertical height is 4 km. In (a), the blank region on the right denotes the Zagros Mountains.

mountainous terrain appears blank for the control run. Prominent on the cross-section in Figure 5.7(a) is the strong LLJ (22 m s^{-1}) between 300 m and 700 m located over the mid-Gulf (lat: 28 °N, long: 50 °E) close to the coastal terrain. It seems that the topographical features of the Persian Gulf, with the gradual up-sloping terrain to the west in Saudi Arabia and the sharply rising mountain range to the east of the Persian Gulf Sea, contribute to the enhancement of the LLJ and tend to direct the low-level flow in a general northerly/northwesterly orientation. This is in good agreement with the results obtained in the previous summer Shamal studies of Membery (1983) and Rao *et al.* (2003). The largest nighttime wind speeds are located close to the coastal terrain just below the halfway level (1.5 km) of the Zagros Mountains. Note that the jet core lies within the temperature inversion, in line with other LLJ observational and modelling studies (e.g. Membery, 1983; Burk and Thompson, 1996).

The scale of the terrain is 300-400 km (the plain is about 300 km wide and the Zagros Mountains are nearly 400 km wide). In order to calculate the Rossby radius of deformation (RRD), several east-west cross-sections are taken perpendicular to the Zagros Mountains all along the 9 km resolution modelling domain (d02). For the nocturnal simulated value of Brunt-Vaisala frequency N = 0.0028 s^{-1} over mid-Gulf, and taking an average scale height $H = 8500$ m and Coriolis parameter $f = 7 \times 10^{-5}$ s^{-1}, the Rossby deformation radius [based on the equation $RRD = NH/f$ for mesoscale flows, e.g. Hunt *et al.* (2004)] is nearly 340 km. Given the above numbers, it is concluded that the RRD and the scale of the terrain are almost of the same order; an indicator that the terrain can persistently change the large scale pressure gradient.

A calculation of the Rossby number (Ro) is also provided in order to justify the neglect of the Coriolis force. The Rossby number is defined as $Ro = U/fL$ (the ratio of inertial to Coriolis force), where f is the Coriolis parameter, U and L are, respectively, the characteristic velocity and length scales of the flow (Marshall and Plumb, 2008). For typical mesoscale flows in the Persian Gulf region, $f = 7 \times 10^{-5}$ s^{-1}, $U = 10$ m s^{-1} and $L \approx 10^5$. Therefore, given our typical numbers, $Ro \approx 1.42$, indicating a system in which inertial and centrifugal forces dominate. It seems that the Coriolis force is relative unimportant, the pressure gradient force dominates, and acceleration and ageostrophic motions are large.

Inspection of the spatial average wind speed and wind direction [over the box ABCD in Figure 5.5(a)] at the 300 m level (see Figure 5.8) for the whole study period shows that the WRF model is able to capture the daily mechanisms that control the atmospheric layers near the surface. It is apparent that strong diurnal variation of the wind speed (Figure 5.8(a)), with an intense period from 0000 UTC on 11 June 1982 to 0000 UTC on 13 June 1982, is observed. As presented in chapter 4, the diurnal cycle of the near-surface winds is realistically simulated for representative weather stations over the Arabian Peninsula (see Figure 4.2). As also reported by Membery (1983) and confirmed by the simulation results, from midnight to midday a decrease of about 45% in the maximum wind speeds is observed for the last study day (see Figure 5.8(a)). The maximum wind speeds (and hence, maximum kinetic energy) are simulated between midnight and dawn (Figure 5.8(a)); these results appear to be in line with the Membery's (1983) observations and are also in agreement with the recent findings (for the nighttime occurrence of the Great Plains LLJ) of Parish and Oolman (2010). Based on Membery's (1983) research, the nocturnal wind speed maxima are formed as a result of the inertial oscillation. However, the observed periodic variation of the wind throughout the simulation days, and the fact that the average wind directions are mainly characterised by counterclockwise rotation after the nocturnal wind maximum (Figure 5.8(b)) are indicators that the LLJ is not a simple Blackadar (1957) theory operation. As discussed in chapter 2 and shown in Figure 2.5, the clockwise rotation is a characteristic of inertial motions (Blackadar, 1957; Anderson *et al.*, 2001; Parish and Oolman, 2010).

The strong diurnal cycle of the summertime Shamal wind direction (Figure 5.8(b)) has not previously been considered in the literature. This diurnal variation of the wind direction strongly indicates a topographically-induced wind regime. A possible physical

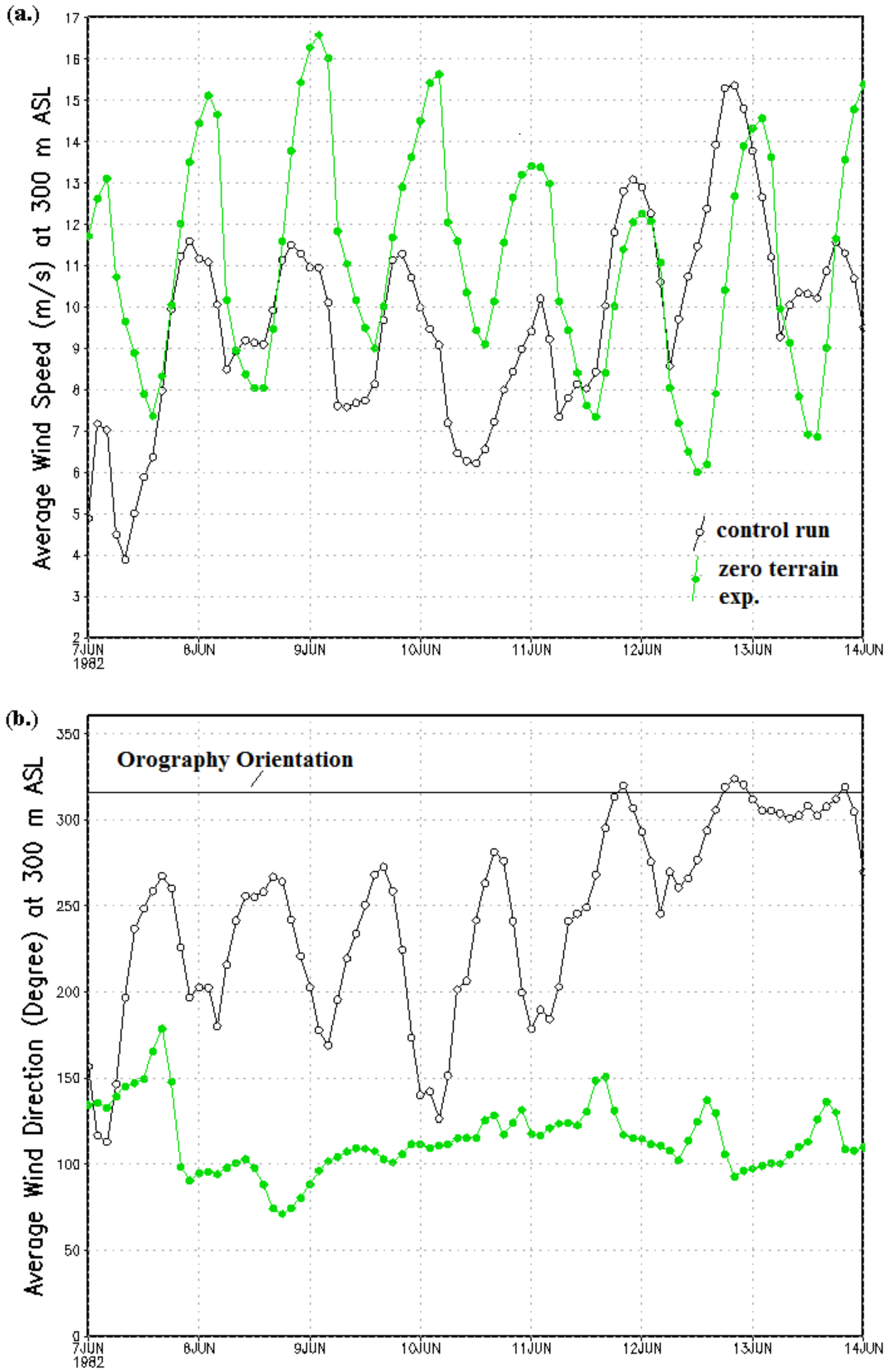

FIGURE 5.8: Time series of (a) average wind speed (m s^{-1}) and (b) wind direction (degrees) over the Persian Gulf and southern Iraq at 300 m ASL; the black curve with the empty circles denotes the control run and the one with the shaded circles the Zzero experiment, 9 km resolution. The x-axis shows UTC time. In (b), the horizontal black line represents the Zagros Mountains orientation. Taken from Giannakopoulou and Toumi (2011).

mechanism responsible for this Shamal wind oscillation is the mountain–plain circulation. Over the complex terrain of the Persian Gulf, diurnal mountain winds are generated by horizontal temperature differences that develop daily over the heated and cooled sloping terrain of the Zagros Mountains. These diurnal mountain winds are characterised by wind direction reversal twice per day (see Figure 5.8(b)). The horizontal temperature gradients caused by solar daytime heating and longwave nighttime cooling result in horizontal pressure gradients. The resulting horizontal pressure differences cause the winds near the surface to blow from areas of low temperatures and high pressures toward areas of high temperatures and low pressures. The aforementioned mechanism is illustrated in Figure 5.9. During the day, surface heating causes the air nearer the Zagros Mountains' slope to be warmed more rapidly than the air well above the surface over the plain. This daytime heating reduces the pressures in the mountain atmosphere relative to plain. Subsequently, a pressure gradient forms normal to the sloping terrain. This pressure gradient force induces the winds to blow from the plain toward the Zagros Mountains slopes. At night, this situation reverses. The daily heating cycle over sloping terrain has been studied by several authors (as discussed in section 2.2) in order to explain the Great Plains LLJ formation (e.g. Wagner, 1939; Holton, 1967; Bonner and Paegle, 1970; McNider and Pielke, 1981; Parish *et al.*, 1988; Jiang *et al.*, 2007; Parish and Oolman, 2010).

The simulation results indicate that south/southeasterly to west/southwesterly (150-250°) winds blow from the plain (areas with low temperatures and high pressures) toward the Zagros Mountains (areas with high temperatures and low pressures) during the day (Figure 5.8(b) and Figure 5.9). During the nighttime, the air next to the Zagros Mountains' slope cools faster than that at the same level away from the mountain range over the plain (Figure 5.9). Therefore, we observe the opposite circulation, with northwesterly to northerly (250-330°) winds flowing from the mountain range toward the plain (Figure 5.8(b)). During the extensive period the spatial average wind direction is characterised by uniformity, with 315° in persistence. In Figure 5.8(b), comparing the black curve with the empty circles (the control run) with the black straight line (Zagros Mountains' orientation) for the aforementioned period shows that the northwesterly Shamal winds are positioned parallel to the Zagros Mountains. This along-mountain direction due to orographic control on either side of the Persian Gulf implies a link between the mountainous topography and the strong Shamal wind events that has been noted previously (e.g. Thoppil and Hogan, 2010).

According to Bonner and Paegle (1970), the diurnal oscillation in the geostrophic wind components is driven by changes in thermal wind which results from the daytime heating and nocturnal cooling of a sloping terrain. Therefore, diurnal changes in the meridional geostrophic wind component near the mountain range (Figure 5.10(b)) should

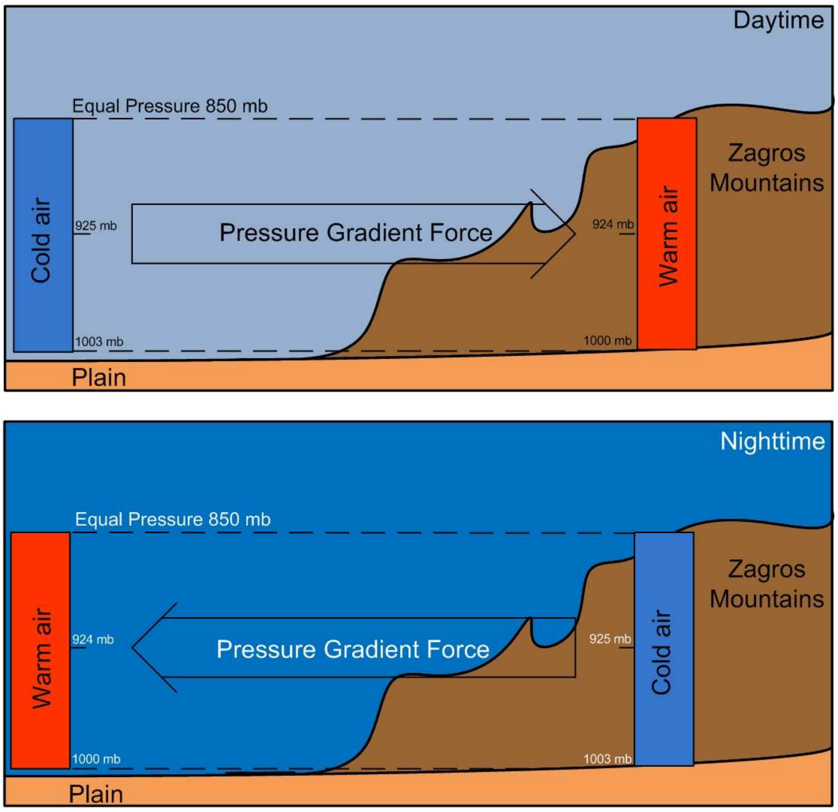

FIGURE 5.9: Schematic of the mountain—plain wind system. Two columns of air: one in the mountain slopes and one over the plain. The top of both columns is defined by the height of the mountain range top and the bottom by the sea level. Horizontal temperature gradients caused by solar daytime heating and longwave nighttime cooling result in horizontal pressure gradients which, in turn, cause diurnal variation of the Shamal wind direction.

be observed due to the daily heating cycle over the Zagros Mountains' sloping terrain. Figure 5.10 represents the 300 m ASL time-average wind components in the zonal and meridional directions at grid points over the land next to the mountains (Figure 5.10(a, b)) and over the mid-Gulf (Figure 5.10(c, d)); the total wind (u, v), geostrophic wind (u_{geo}, v_{geo}), and ageostrophic wind (u_{ageo}, v_{ageo}) are shown. Note that the simulation results in Figure 5.10 are for both the less extensive and extensive periods, since minor differences are observed between the individual periods. Over land near the mountain range the meridional ageostrophic wind, v_{ageo}, is as expected from the inertial oscillation (Blackadar, 1957) with a period of oscillation roughly that of the inertial period T discussed in subsection 2.2.4. Based on the study of Bonner and Paegle (1970), in the case of northerly/northwesterly flow west of the Zagros Mountains, we expect the geostrophic wind oscillation to be in phase with the temperature cycle. Therefore, we expect to observe the maximum geostrophic speed at the time of the maximum temperature. Indeed, the phase of the diurnal variation in the v_{geo} (Figure 5.10(b)) is in good agreement with the sloping terrain effects (e.g. Holton, 1967; Bonner and Paegle, 1970). Over the sea

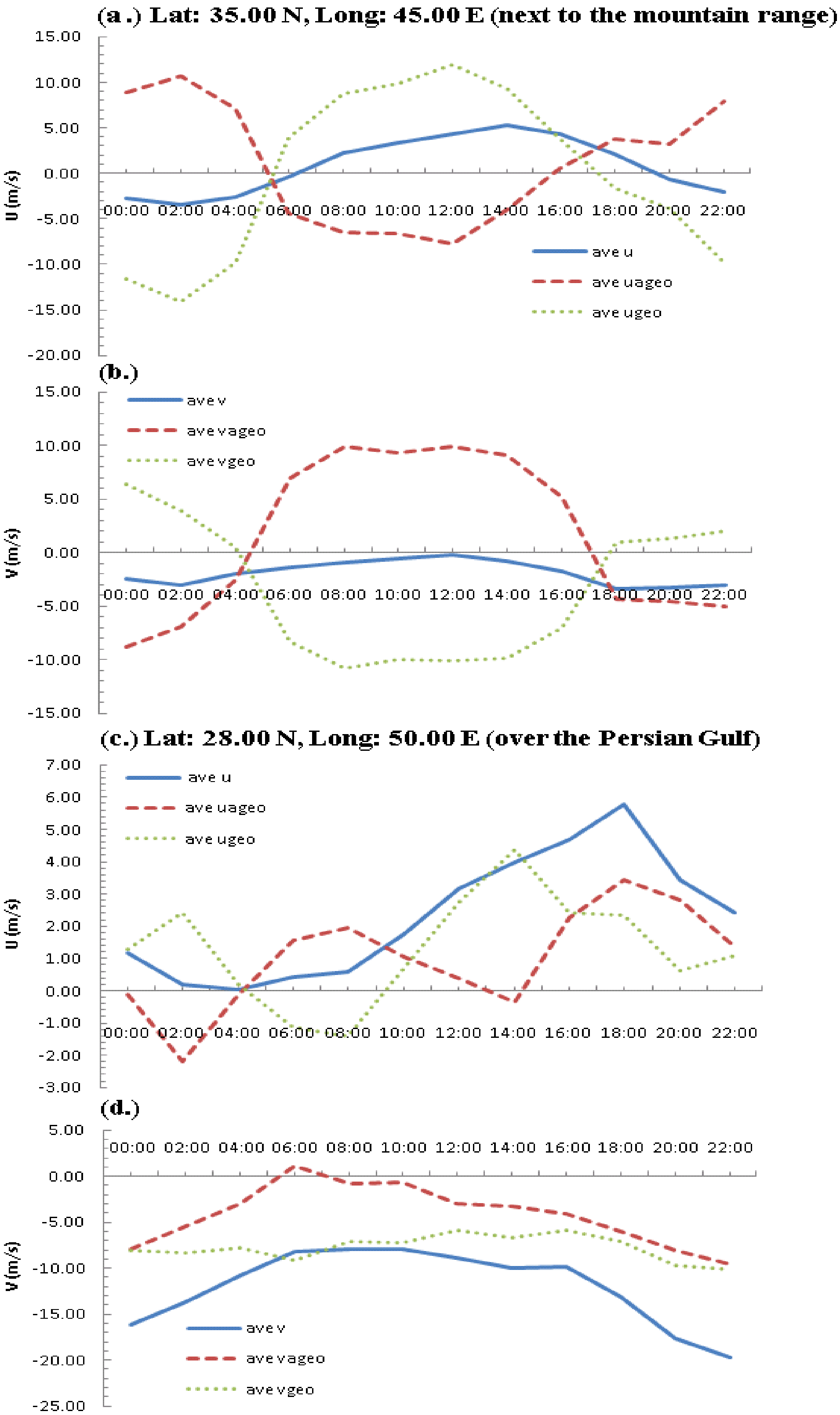

FIGURE 5.10: Averaged (a) zonal component and (b) meridional component versus time (UTC) at (35.0 °N, 45.0 °E) next to the mountain range at 300 m AGL from the 9 km resolution control run. (c, d) are as (a, b), but at a point over the mid-Gulf (28.0 °N, 50.0 °E). The solid, dashed and dotted curves denote the total, the ageostrophic and the geostrophic components. Taken from Giannakopoulou and Toumi (2011).

the meridional ageostrophic wind is again the same as over the land (Figure 5.10(b, d)), but the zonal geostrophic and ageostrophic winds (u_{geo} and u_{ageo}) are out of phase (Figure 5.10(a, c)). This is in line with a land/sea breeze circulation, as will be shown later in subsection 5.6.5.

It is concluded that the Blackadar (1957) process is not a key factor for the development of the summertime Shamal wind events; the diurnal cycle of the Shamal wind direction is considered to be a result of the pressure and temperature gradients created by the summertime daily heating and cooling of the Zagros Mountains' sloping terrain. In addition, the land and sea breezes contribute to the diurnal change in the zonal geostrophic wind component.

5.6.2 Zero terrain height sensitivity experiment

For a better understanding of the effects of the Persian Gulf topography on the Shamal winds' generation, intensity and direction, the terrain height along the modelling domain is set equal to zero. Our initial interest is to observe the effects of removing the terrain on the intensity, direction and structure of the summertime LLJ.

Prominent on the cross-section in Figure 5.7(b) is a LLJ with the maximum wind speed being 20 m s^{-1} above the flat terrain which previously was mountainous (near longitude 54 °E) as compared to 22 m s^{-1} for the control run. In the zero terrain height (Zzero) experiment, the LLJ is broad and diffuse compared to the narrow and concentrated LLJ observed in the control run (Figure 5.7). As evident from Figure 5.7(b), the LLJ extends horizontally and vertically with the largest wind speeds between 300 m and 1.4 km. Note that the jet core extends to the east and is not observed within the temperature inversion. We can assume that the thermal-wind mechanism contributes to the strength of the jet at the low levels of the atmosphere in the control run.

The strong land–sea temperature contrasts in the Persian Gulf cause horizontal pressure gradients that drive shallow, diurnally varying circulations: daytime sea breezes and nighttime land breezes (Wallace and Hobbs, 2006). As can be seen in the plane of vertical cross sections normal to the coastline (as in Figure 5.12) the wind oscillates back and forth between land and sea, reversing directions during the morning and evening hours. When the orography excluded the Zagros Mountains, the Shamal flow over the Persian Gulf and southern Iraq was still characterised by strong periodic variation in wind speed (Figure 5.8(a)), indicating the importance of the land–sea interface for the low-level flow development. As indicated in Figure 5.8(a), the spatial average wind speed in the Zzero experiment is surprisingly high compared to the one simulated in the control run. When we excluded the Zagros Mountains, the intense solar heating during the day and radiational cooling during the night contribute to the stronger nighttime wind speeds in the

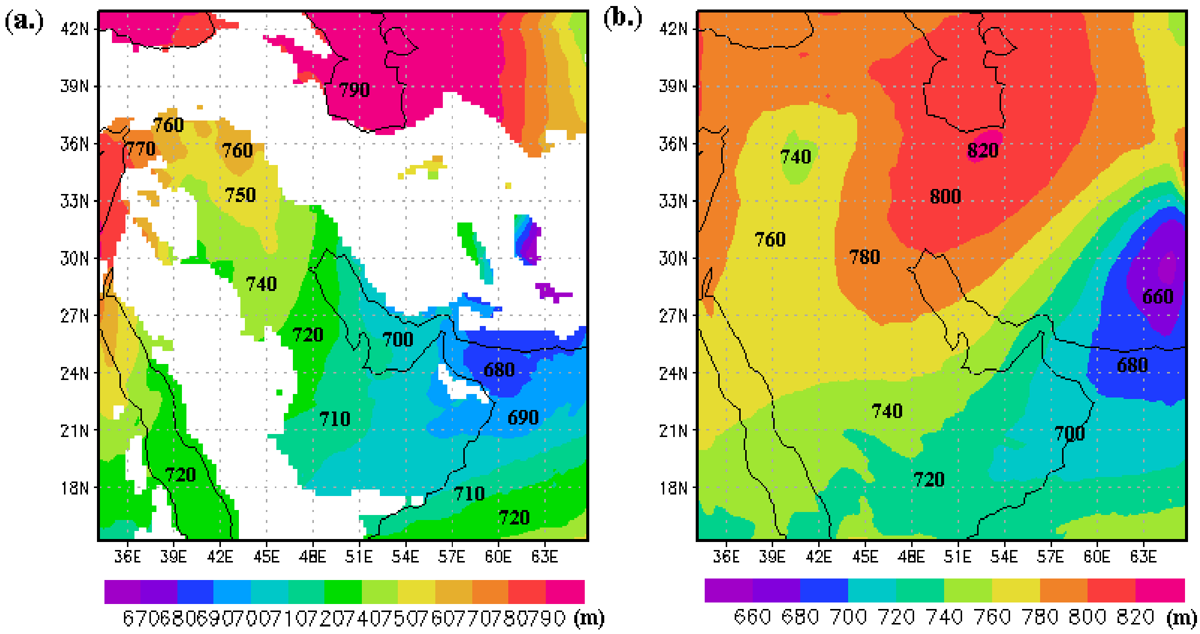

Figure 5.11: The 925 hPa geopotential height (m) from the 27 km resolution WRF modelling domain (d01) at 2100 UTC on 9 June 1982 for (a) the control run and (b) the Zzero experiment. Blank areas appear where the model terrain exceeds 925 hPa. Taken from Giannakopoulou and Toumi (2011).

Zzero experiment. The large diurnal oscillation of the wind speed also implies a diurnal pressure gradient force that is associated with the land surface heating. In other LLJ numerical studies (e.g. Burk and Thompson, 1996; Doyle, 1997; Ting and Wang, 2006) the mountainous terrain removal was associated with a reduction in the LLJ strength because of the absence of the low-level blocking. However, in our study region we have easterly flow from the monsoon circulation that would replace the northwesterly Shamal wind in the absence of the Zagros Mountains. The absence of the mountains leads to an average wind speed maximum of 16.8 m s^{-1} (Figure 5.8(a)) and to an expected uniform spatial average wind direction, with 100° (easterly/southeasterly direction) and no diurnal variation (Figure 5.8(b)). Although the strongest temperature gradients that develop in the Zzero run and the subsequent diurnal varying circulations (sea and land breezes), the strong monsoon flow dominates with the easterly direction so we cannot clearly observe the changes in wind direction. We therefore show that the Zagros Mountains act as a barrier for the strong monsoon easterly flow and this observation is at least as important as the more obvious mountain effects on the northerly/northwesterly Shamal winds.

According to Ali (1994), the possible blocking and deflection of the airflow to the northwest of the Zagros Mountains into Syria and the strong synoptic scale pressure gradient are likely to be features which also affect the location and direction of the Shamal wind events. Figure 5.11 presents the 925 hPa geopotential height for the parent modelling

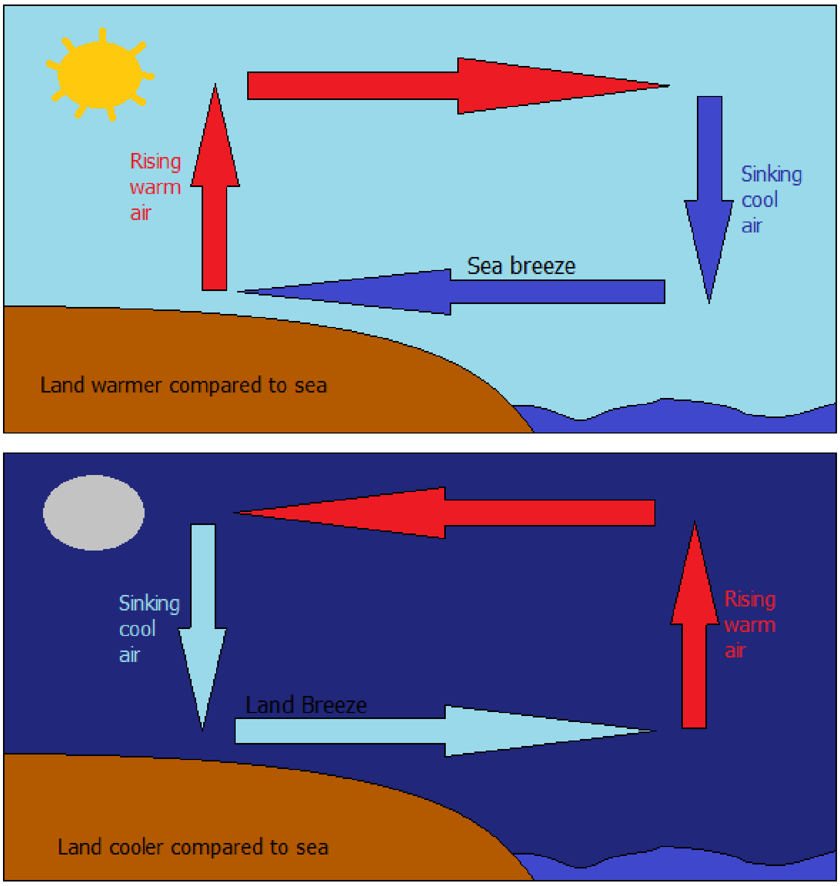

FIGURE 5.12: Schematic of a sea and land breeze circulation. In the plane of vertical cross sections normal to the coastline the wind oscillates back and forth between land and sea, reversing directions during the morning and evening hours. The vertical extent of sea/land breeze circulation cell is about 1 km and a typical horizontal extent is about 20 to 100 km (Wallace and Hobbs, 2006). Redrawn from Wallace and Hobbs (2006).

domain (d01; 27 km horizontal resolution) at 2100 UTC on 9 June 1982 for both the control and Zzero experiments. Prominent in Figure 5.11(a) are the ridge of high pressure over northern Iraq and the cyclonic circulation over the Gulf of Oman. According to Parish and Oolman (2010), if a stably stratified low-level flow approaches a mountain, it slows down due to the blocking effects as the air is forced to ascend the sloping terrain. In the present study, this flow retardation should result in low-level convergence on the western slopes of the Zagros Mountains and must increase the pressure. Indeed, higher pressures are situated in the northwestern mountainous slopes near Syria (approximately at lat:36 °N and long: 44 °E in Figure 5.11(a)). However, it appears that no blocking is taking place for the northwesterly Shamal flow, as there is no evidence of higher pressures along the Zagros Mountains than found to the southwest of the mountain range. When the Shamal winds blow towards the Persian Gulf, lower pressures are observed along the elevated sloping terrain of the Zagros Mountains compared to those seen away from the mountain range. This is an indication that the LLJ is thermally forced owing to the mountainous terrain. The resultant large-scale pressure field forms the westerly/northwesterly mountain-parallel flow. The strong land–sea influence, as implied by the north-to-south gradient of the height contours, is also observed in the Zzero sensitivity study (Figure 5.11(b)). The Zzero experiment more clearly shows an anticyclone over the Caspian Sea and a cyclone over Pakistan. It seems that the interaction of these synoptic systems enhances the easterly/southeasterly flow.

By removing the mountains, it is concluded that the Shamal is not generated over the Persian Gulf since the northwesterly winds change to easterly/southeasterly. The Blackadar (1957) process has a secondary role to the LLJ forcing, since with an inertial oscillation we expect to observe changes in wind direction as the ageostrophic wind oscillates. Therefore, the above simulation results confirm that the Shamal development is closely associated with the mountainous and coastal topography over the Persian Gulf and Iraq.

5.6.3 Mountain height sensitivity experiments

The effects of the Zagros Mountains orographic height on the Shamal intensity, direction and spatial distribution are further assessed by two mountain height sensitivity experiments. In the first experiment, we have replaced the Zagros Mountains real orography in areas that have heights greater than 500 m with altitudes of 500 m (500 m plateau). In the second sensitivity study, an alternative procedure where the real mountain height is reduced by 50 percent is tested.

The results from the sensitivity experiments show differences both in spatial structure and in Shamal intensity and wind direction. Figure 5.13 shows the horizontal wind speed, wind vectors and potential temperature at 2200 UTC on 12 June 1982. The west-to-east cross-section at latitude 27.5 °N extends from 49.5 °E to 54 °E; the mountainous terrain appears blank. Figure 5.13(a) reveals a strong and broad jet core (around 22 m s^{-1}) between 300 m and 700 m AGL over the Persian Gulf Sea for the control experiment. A slightly weaker and narrow LLJ is observed with the 50 % reduction of the realistic terrain height; the largest wind speed of 20 m s^{-1} is simulated between 400 m and 600 m AGL (Figure 5.13(b)). A further decrease in the Shamal intensity (nearly 37 % lower than its equivalent in the CTRL run) is captured in the 500 m plateau experiment with the core of the jet closer to the surface (Figure 5.13(c)). Although the strenght of the Shamal is considerably weaker in the mountain height sensitivity experiments, the LLJ core is positioned over the Persian Gulf Sea for all the experiments. In the first instance, this wind speed difference could be a result of the weaker horizontal pressure gradients created by the lower heights in the sensitivity runs. According to Burk and Thompson (1996), enhanced baroclinicity because of the high terrain of a mountain range should result, through the thermal wind, in large wind speeds at levels just below the mountain range top. Indeed, at the longitude of the LLJ core (50 °E), the control run gives a wind speed of approximately 20 m s^{-1} at 1 km, whereas the half mountain height and the 500 m plateau experiments have a value of 16 m s^{-1} and 13 m s^{-1}, respectively.

Similarities exist in the meteorological and physiographic features of the Persian Gulf and the California coast; northwesterly LLJs form with an inversion in the ABL and mountains of about 2.5 km elevation are positioned to the east of a water body (e.g. Membery, 1983; Burk and Thompson, 1996). Burk and Thompson (1996) in their work for the LLJ that occurs along the California coast mainly focused on the synoptic-scale divergence and the thermal-wind mechanism. Compared to the Burk and Thompson (1996) study, the thermal wind effect resulting from horizontal temperature gradients due to the presence of the Zagros Mountains exists but it is also important to consider the effects of the inertial oscillation and the land/sea breeze circulations. According to Burk and Thompson (1996), the maximum baroclinicity near the surface occurs in the early afternoon and the thermal wind applies to a balanced state between the momentum and mass field. However, in the present study the summertime Shamal wind maximum occurs late at night and, as presented in subsection 5.6.1, the Shamal shows strong diurnal variability in both wind speed and wind direction. Therefore, there is a time lag between the maximum baroclinicity and the maximum Shamal wind speed. Sea/land breeze and mountain-plain circulations contribute to the aforementioned diurnal variations and complicate the coastal meteorology of the Persian Gulf. As can be seen in Figure 5.13, the axis of the maximum Shamal wind speed tilts more to the west in the sensitivity experiments than in the CTRL run. This is mainly attributed to the lower terrain which allows for northeasterly winds to penetrate into the Persian Gulf and push the LLJ core farther away from the mountain range. In this respect, the present results only partly agree with those of Burk and Thompson (1996). We can conclude that the Shamal is not simply a balanced wind state in which the jet intensity is directly determined by the strong coastal baroclinicity and associated thermal wind.

Comparison of the results for mountains of different heights, but with the same initial synoptic conditions, verifies that the orographic height determines the character of the Shamal–orography interaction. These results suggest that the Shamal wind events are very sensitive to the Iranian orography and the coastline geometry, and are comparable to similar studies (e.g. Atkinson and Zhu, 2005). As revealed by the mountain height experiments, when the orography is increased, the LLJ (e.g. in the CTRL run) is stronger and oriented parallel to the Zagros Mountains [northwesterly direction is observed in Figure 5.13(a)]. Model results are consistent with the barrier jet theory in that maximum low-level wind speeds generally occur at heights just below the halfway level of the mountain range (Olson and Colle, 2009). As evident from the Figure 5.13(b, c),

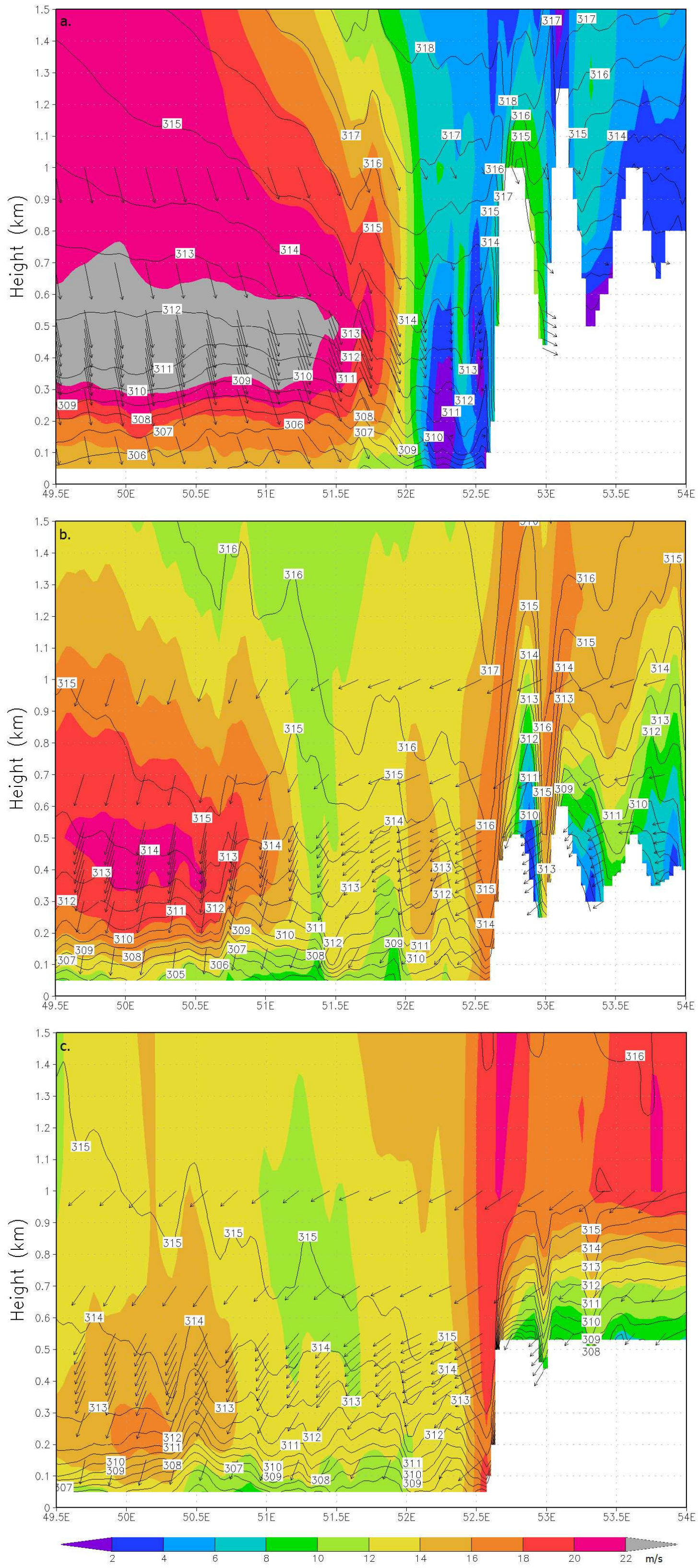

FIGURE 5.13: Vertical cross-section up to 1.5 km level at latitude 27.5 °N extending from longitude 49.5 °E to 54 °E showing wind speed (shading, m s^{-1}), wind vectors (green wind barbs) and potential temperature (solid contours, K) for (a) the control, (b) the 50 % mountain height reduction and (c) the 500 m plateau experiments (3 km resolution), at 2200 UTC on 12 June 1982. The blank region on the right denotes the Zagros Mountains.

reduction in the mountain elevation lowers the Shamal wind maximum, creates a more northerly/northeasterly direction and moves the LLJ core farther away from the east coast (although its maximum remains over the Persian Gulf waters).

5.6.4 Mountain slope sensitivity experiments

Smith (1979), Pierrehumbert (1984), Zehnder and Bannon (1988) were some of the researchers in the twentieth century who have studied the frontal retardation and acceleration affected by mountainous terrain and the low-level orographic blocking defined by no dimensional parameters, such as the Froude (Fr), Rossby (Ro) and Burger (Bu) numbers. Pierrehumbert (1984) detailed the barrier effects through a Fr and Ro number analysis and, based on his studies for symmetric mesoscale mountains (e.g. British Columbia, the mountain ranges in California coast, Zagros Mountains in Iran) the character of the flow is dependent on the slope for broad mountains (small Ro) and on the height for narrow mountains (large Ro). Pierrehumbert and Wyman (1985) presented the significant role of the Rossby deformation radius for a flow in a rotating case in which the airflow is blocked by ridge-like obstacle. The importance of the effect of steep coastal mountains on a barrier jet has also been intensively demonstrated in later idealized studies worldwide (e.g. in western United States & Canada by Braun *et al.* (1999), in Alaska by Olson and Colle (2009)). Further insight into the interaction of LLJs with mountainous terrain has been gained through sensitivity experiments in which the real orographic height was set equal to a fixed number (e.g. a plateau, Atkinson and Zhu (2005); or zero, Burk and Thompson (1996)). Although this approach improves the understanding of the mountain height impacts on the LLJ formation, it is limited to simplified terrain geometries.

The mountain slope sensitivity experiments in this study explore the role of the Zagros Mountains' slope and width. In order to achieve that, we extend the analysis of Pierrehumbert (1984) by considering a Gaussian shaped mountain range. Two scenarios are presented in this chapter; we choose to include the Zagros Mountains as a very broad mountain range (Zshallow experiment) and as a sloping wall (Zsteep experiment) parallel to the coastline (see Figures 5.3(b, c)). The broad mountain is placed just next to the Persian Gulf coast, whereas the narrow mountain is positioned 200 km to the right of the coast in order to create the shallow and steep slopes, respectively.

It is evident from Figure 5.14(a) that the nighttime amplification and diurnal variation of the spatial average wind speeds [over the box ABCD in Figure 5.5(a)] in both mountain slope experiments are fairly similar to those observed in the control run (Figure 5.8(a)), although the average 300 m level Shamal winds are slightly enhanced during the less extensive period in the Zsteep simulation compared with the Zshallow. As discussed in section 2.2, McNider and Pielke (1981) noted that the magnitude of the sloping terrain is

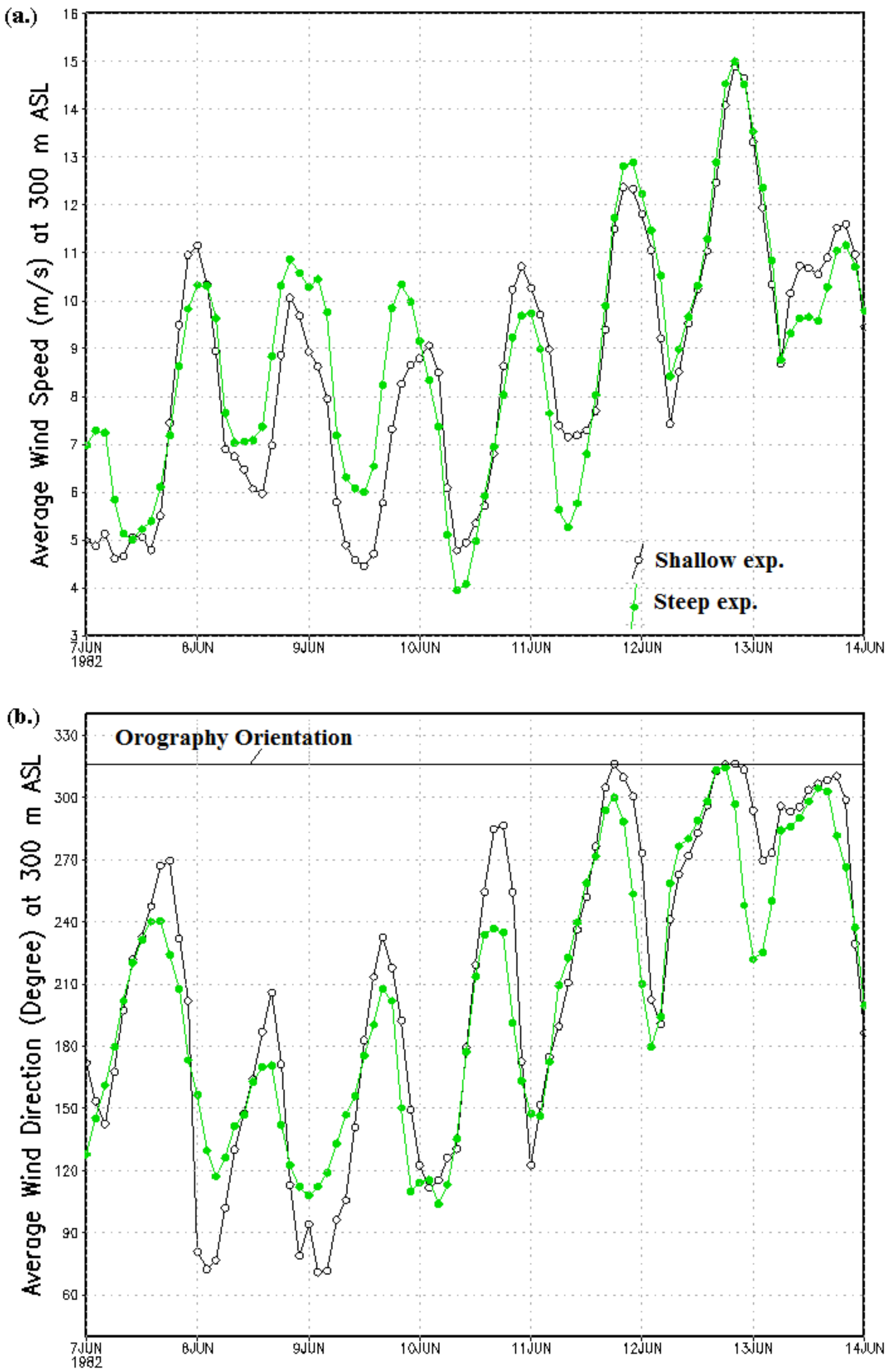

FIGURE 5.14: Time series of (a) average wind speed (m s^{-1}) and (b) wind direction (degrees) over the Persian Gulf and southern Iraq at 300 m ASL. The black curve with the empty circles denotes the Zshallow experiment and the one with the shaded circles the Zsteep experiment (9 km resolution). The x-axis shows UTC time. In (b), the horizontal black line represents the Zagros Mountains orientation. Taken from Giannakopoulou and Toumi (2011).

essential to the LLJ intensity. In their idealized study in which they doubled the terrain slope and subsequently created stronger pressure gradients, they produced a stronger LLJ, which is consistent with our simulation results. Therefore, it is concluded that the stronger horizontal temperature gradients are significant for the nighttime LLJ maximum formation, since the steeper terrain slope increases the low-level wind speeds during the less extensive period. However, during the extensive period (11 June 1982 - 14 June 1982), the Shamal winds are fully developed in both cases with a nocturnal low-level wind speed maximum of 15 m s^{-1} and wind direction of about 315°, which is surprisingly similar to the control simulation (Figure 5.8).

The results in Figure 5.14(b) indicate the strong variation with time of the averaged wind direction over the Persian Gulf and southern Iraq. The daytime heating and nocturnal cooling of the sloping terrain is still the major mechanism for the diurnal oscillation of the wind direction for both Zshallow and Zsteep experiments. However, during the less extensive period, the broad sloping terrain allows more heating to take place during the day and subsequently more cooling during the night, resulting in stronger daily horizontal temperature differences in the Zshallow case than in the Zsteep experiment. Subsequently, the Zshallow experiment causes stronger daily horizontal pressure gradients and thus a greater reversal of the wind direction. For example, from midnight [2100 UTC (0000 h) on 9 June 1982] to midday [0900 UTC (1200 h) on 9 June 1982], a difference of the order of 200° in the wind direction is observed for the shallow mountain range run, while for the steep experiment a difference of only about 120° is simulated. It is also apparent from Figure 5.14(b) that, as expected, the Shamal wind alignment is most sensitive to shallow sloping terrains, since the broad Gaussian mountain is similar in shape and width to the real Zagros Mountains' topography.

The LLJ, simulated in the mountain slope sensitivity experiments, is positioned slightly higher in the atmosphere, at 500 m AGL compared to 300 m in the control run. We attribute this to the effective mountain height of our Gaussian range which is larger than that observed in the control study; according to Olson and Colle (2009), the maximum barrier jet speeds generally occur at heights just below the halfway level of a mountain. During the less extensive period (7 June 1982 - 11 June 1982), the nocturnal wind speed maxima at low atmospheric levels (500 m AGL) are larger for the steep than for the shallow mountain slope experiment. This is especially observed for small speeds (see Figure 5.15), and a possible reason is the strong temperature gradient. In order to compare the heating patterns of different mountain slopes, in Figure 5.15 we show a vertical cross-section of the wind speed and virtual potential temperature at 0800 UTC on 9 June 1982 for both mountain slope experiments from the 3 km horizontal resolution, extending from grid point $(x_1, y_1) = (26.4, 104.5)$ to $(x_2, y_2) = (97.0, 180.2)$. The model's ABL structure is well defined in the cross-section by the virtual potential temperature

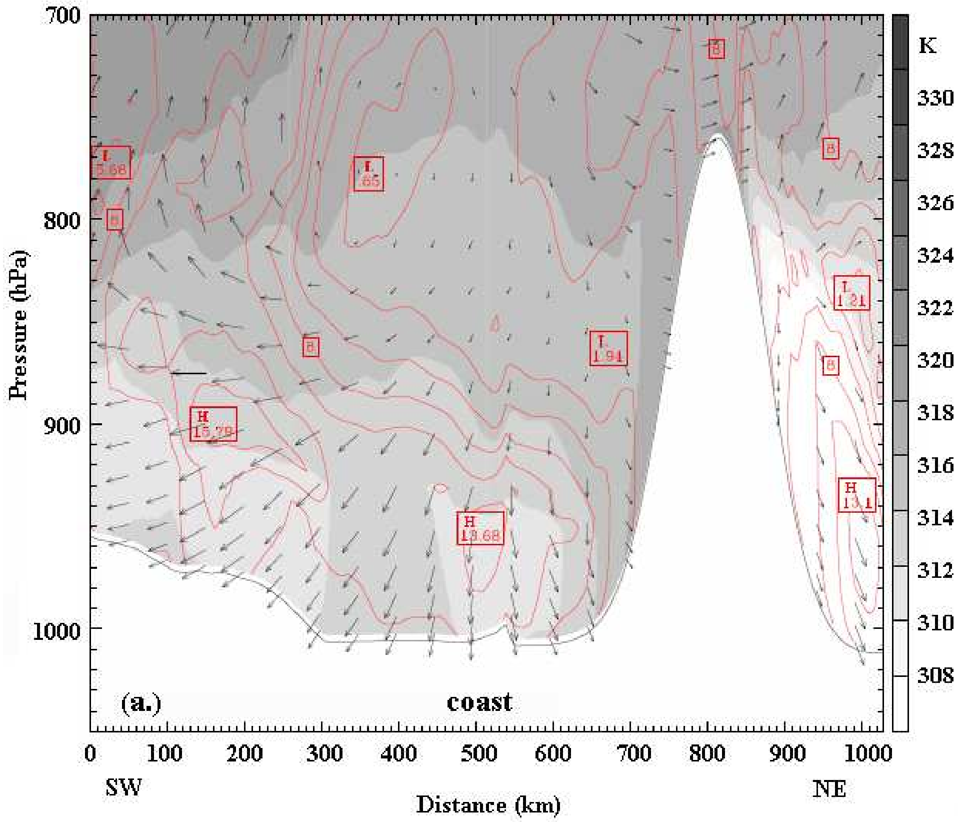

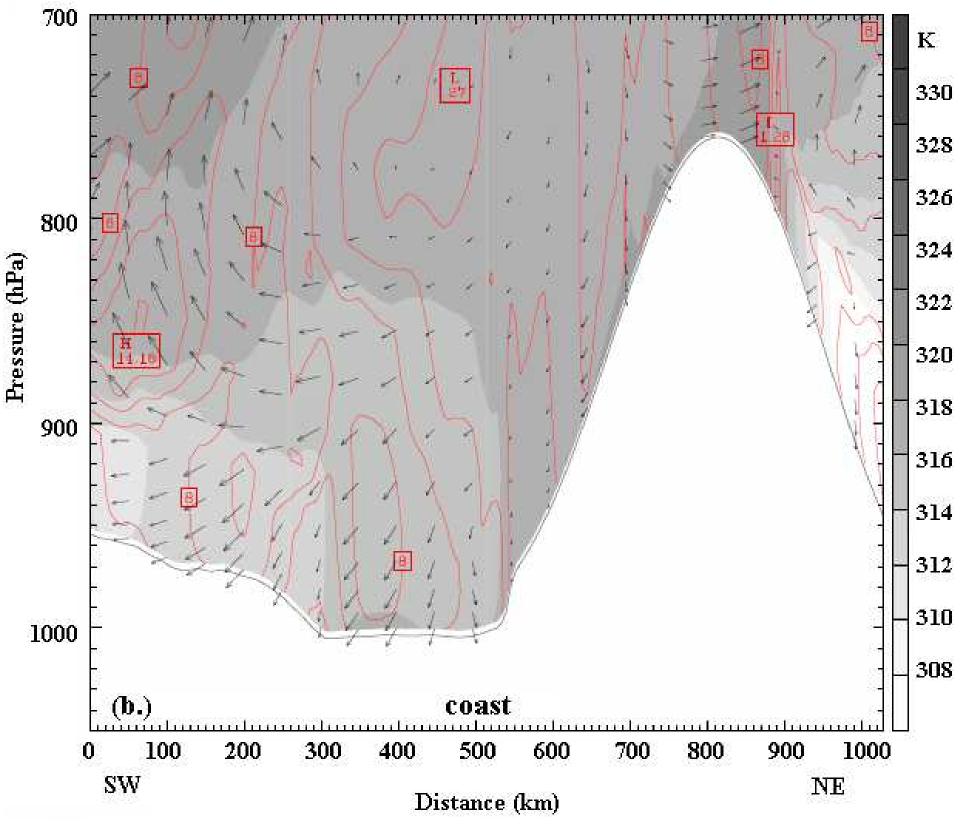

FIGURE 5.15: Cross-section from $(x_1, y_1) = (26.4, 104.5)$ to $(x_2, y_2) = (97.0, 180.2)$ at 0800 UTC on 9 June 1982 for (a) the Zsteep and (b) the Zshallow experiments (3 km resolution). The shading denotes the virtual potential temperature (K), the contours the wind speed (m s^{-1}) and the wind barbs are the horizontal wind vectors. Taken from Giannakopoulou and Toumi (2011).

(see Figure 5.15). Close to the coast, the low-level winds are partially driven by coastal baroclinicity and take the form of a LLJ at the top of the ABL, which is capped by temperature inversion. Northwesterly winds parallel to the mountain range are observed; these are reported in Figure 5.15(a) in which the LLJ core lies just within the mixed layer of 310 K, parallel to the coastline. Apparently, the LLJ is much stronger in the Zsteep experiment (up to 14 m s^{-1}) than in the Zshallow case (up to 8 m s^{-1}). The LLJ in the Zshallow study is broad, slightly lower in the atmosphere and moves closer to the west of the coast (nearly 100 km) than does the jet core in the steep case.

Summarizing the main simulation results obtained from the mountain slope sensitivity experiments, it is concluded that the different mountain slopes have a negligible effect on the Shamal phase, but they can affect the magnitude of the wind speed and the amplitude of the wind direction diurnal cycle.

5.6.5 Land–Sea sensitivity experiment

Shi *et al.* (2004), in their meteorological re-analysis for the Persian Gulf, acknowledged the importance of the surface characteristics, the terrain and the land–sea distribution on the near-surface flow. In this chapter we attempt to understand how the land and sea breeze forcing may account for the diurnal variation of the Shamal wind components and the acceleration and intensity of the LLJs generated over the Persian Gulf. In the final sensitivity experiment, referred to as LS experiment, the Persian Gulf Sea is replaced by flat sparsely vegetated land. The surface forcing of the WRF model and the initial wind and temperature profiles are left unaltered, however the surface albedo and roughness length are increased and the emissivity is decreased.

In the LS study, the spatial average wind speed [over the box ABCD in Figure 5.5(a)] is 30% to 40% weaker during the daytime in the less extensive period than in the control run (Figure 5.16(a)). In the control study, the strong north-to-south temperature gradients created by the land–sea distribution accelerate the winds and contribute to the LLJ intensity over the mid-Gulf. In particular, strong northwesterly winds are observed over the north coast in southern Iraq which accelerate the flow in the control run (Figure 5.17(a)). Figure 5.17 is an illustration of rotation of wind vectors through time (0000, 0600, 1200 and 1800 UTC) on 8 June 1982 at 300 m ASL for both the control run and the LS sensitivity experiment.

A physical mechanism responsible for the observed diurnal variation in wind speed and the nighttime wind speed maxima seems to be the diurnal oscillation of heating and cooling in both the control and LS experiments (see Figure 5.16(a)). The spatial average maximum (15.5 m s^{-1}) in the LS study appears to be similar to the one observed in the control run. Therefore, the strength and diurnal mechanism that controls the

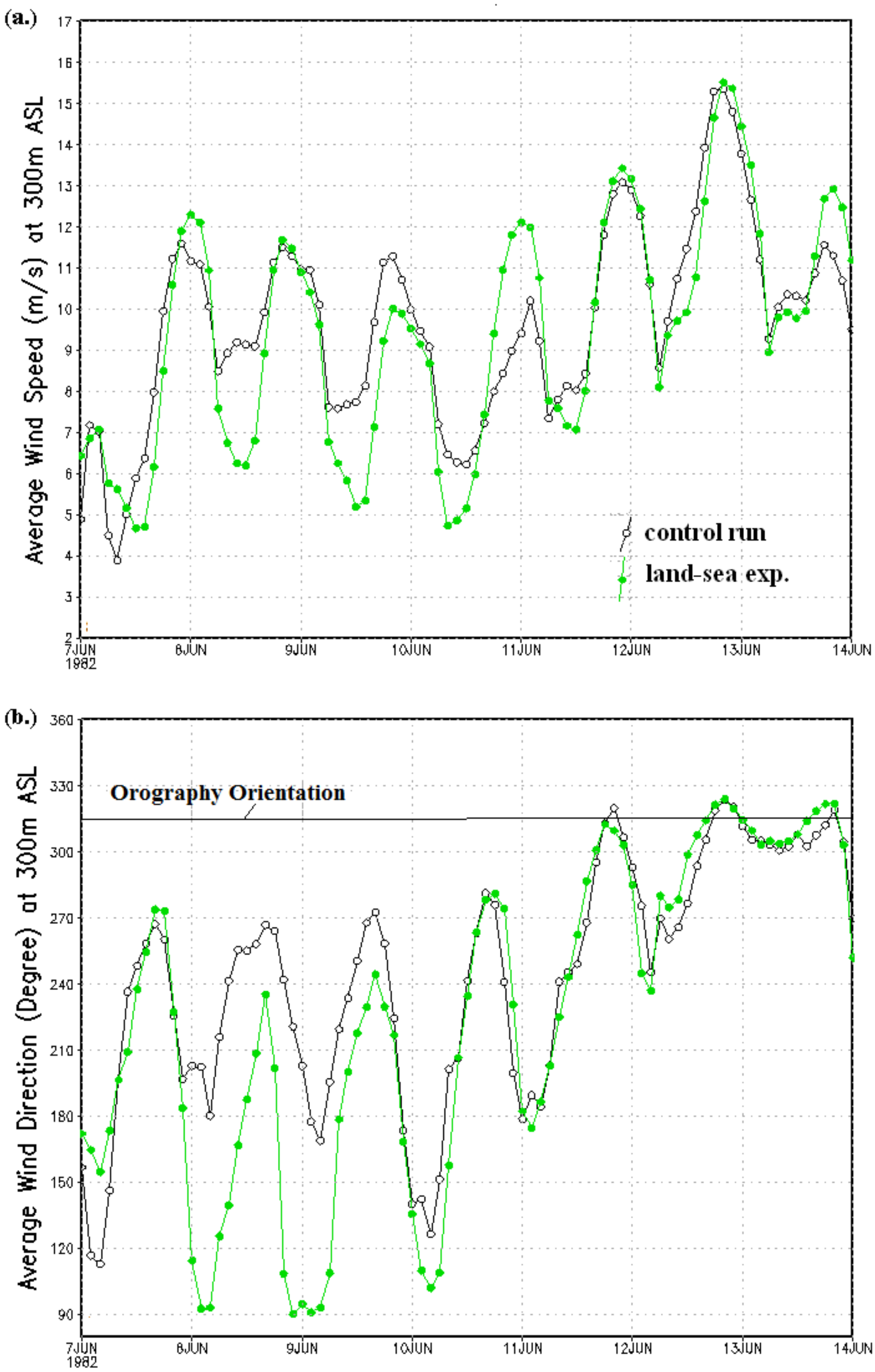

FIGURE 5.16: Time series of (a) average wind speed (m s^{-1}) and (b) wind direction (degrees) over the Persian Gulf and southern Iraq at 300 m ASL. The black curve with the empty circles denotes the control run and the one with the shaded circles the LS experiment (9 km resolution). The x-axis shows UTC time. In (b), the horizontal black line represents the Zagros Mountains orientation. Taken from Giannakopoulou and Toumi (2011).

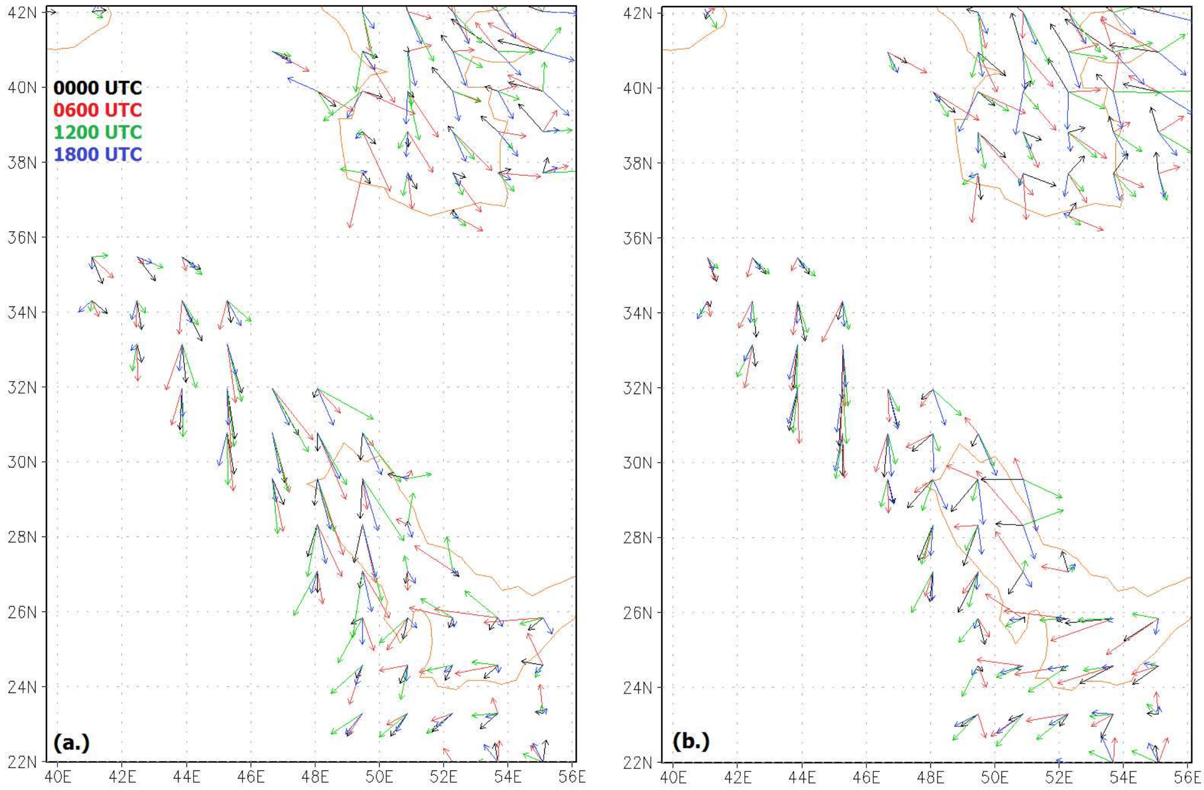

FIGURE 5.17: Wind vectors at 0000 (black), 0600 (red), 1200 (green) and 1800 (blue) UTC 8 June 1982 at 300 m ASL for (a) the control run and (b) the LS experiment (9 km resolution). Blank regions indicate terrain heights above 300 m level.

strongest Shamal wind events during the extensive period are unaffected by the land and sea breezes. However, during the less extensive period in the control study, the land breeze accelerates the nocturnal LLJ over the Persian Gulf Sea (see Figure 5.18(a)). Figure 5.18 shows the time-average wind speed at the time of the maximum occurrence (2200 UTC) for both control and LS experiments during the less extensive period. The shaded contours in Figure 5.18(a) indicate that the land breezes in the control run are associated with greater time-average wind speeds (20 m s^{-1}) than in the LS experiment (4 m s^{-1} decrease in the average maximum wind speed).

As evident from the Figure 5.16(b) and 5.17, the less extensive Shamal period reveals a considerable change in wind direction especially during the early morning hours. In the less extensive period, there are more daytime easterly winds caused by the new land friction. As indicated in Figure 5.16(b) and 5.17, in the control experiment the thermal effects which lead to the sea breeze circulation during the day tend to increase the southerly flow. The average wind direction for the LS simulation is characterised by greater differences of the order of 180° in the diurnal oscillation between day and night (Figure 5.16(b)), which is a characteristic of the stronger heating and cooling of the areas to the west of the sloping terrain. However, during the extensive Shamal period, the

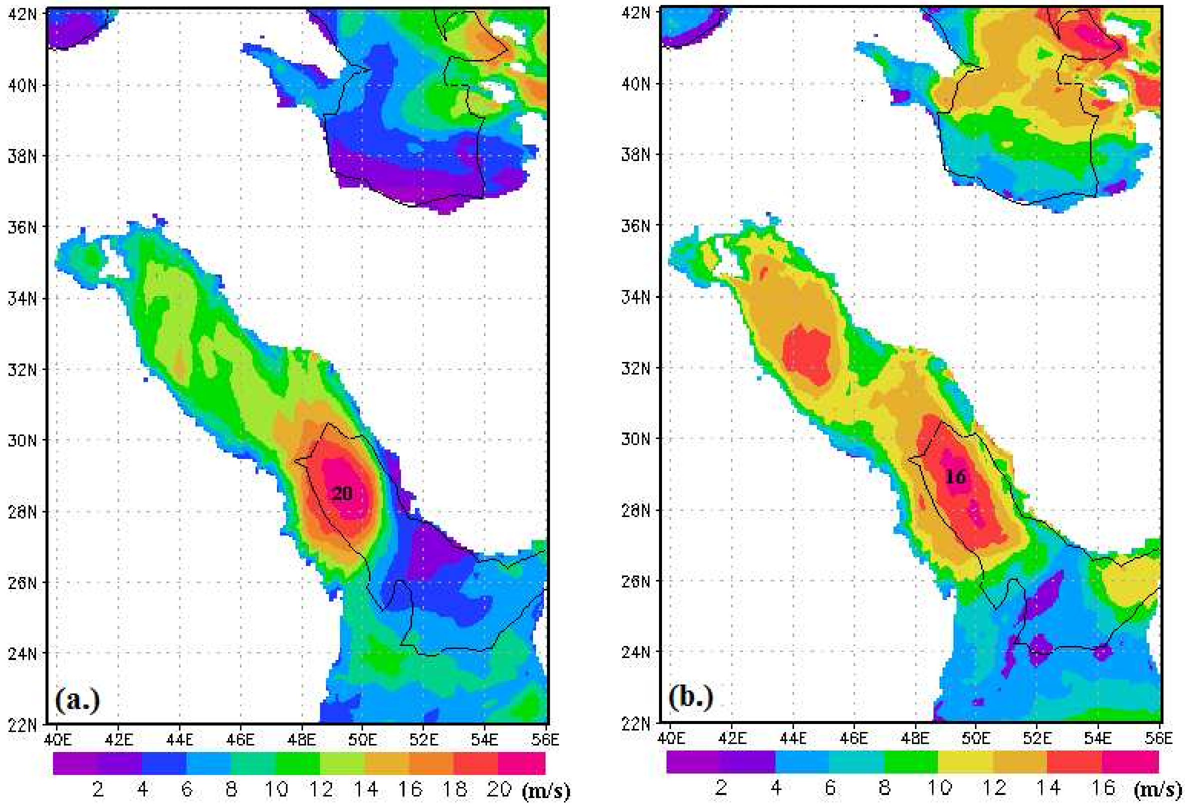

FIGURE 5.18: Time-average wind speed (m s^{-1}) at 2200 UTC at 300 m ASL for the less extensive period from (a) the control run and (b) the LS experiment (9 km resolution). Blank regions indicate terrain heights above 300 m level. Taken from Giannakopoulou and Toumi (2011).

average wind direction in both simulations is oriented parallel to the mountain range.

Analysis of the time-average (over the whole study period) Shamal wind components over mid-Gulf (Figure 5.19) shows the similarities with the Parish and Oolman (2010) study of the Great Plains LLJ; in the LS experiment the topography now has more the appearance of the Great Plains region (no land–sea interface). Comparing our control results (Figure 5.10) and those observed by Parish and Oolman (2010) for the Great Plains LLJ, it is evident that the diurnal changes in the zonal geostrophic wind component are essentially different. According to their theory, an almost constant u_{geo} component should be expected, since the Zagros Mountains' sloping terrain upwards to the east. However, the absence of the land–sea distribution in the LS experiment explains the nearly constant u_{geo} component (Figure 5.19(a)). In addition, the maximum of the u component occurs 2 hours earlier than that observed in the control simulation (Figure 5.19(a) versus Figure 5.10(c)), possibly owing to the greater thermal convection which over the new terrain (which now has land characteristics) is most pronounced during early afternoon. The time of the maximum v component (2200 UTC) is in line with the results of Parish and Oolman (2010). This analysis indicates the significance of the sea–LLJ interactions

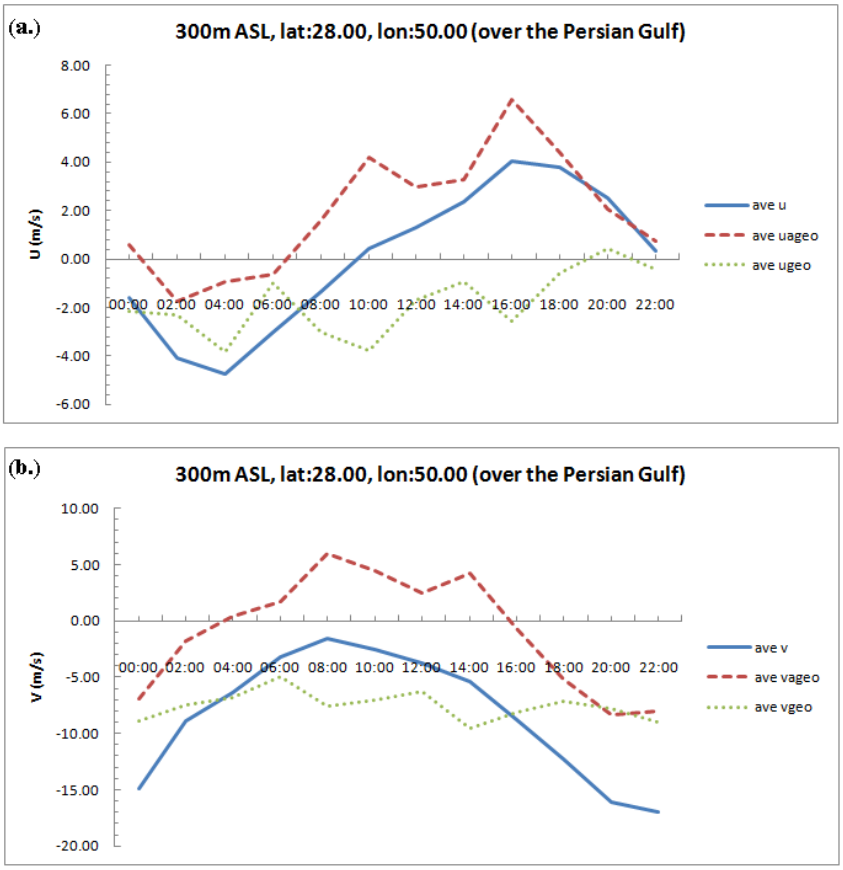

FIGURE 5.19: Averaged (a) zonal component and (b) meridional component versus time (UTC) at 300 m ASL over the mid-Gulf (28.0 °N, 50.0 °E) from the LS experiment (9 km resolution). The solid, dashed and dotted curves denote the total, the ageostrophic and the geostrophic components. Taken from Giannakopoulou and Toumi (2011).

for the Persian Gulf and southern Iraq.

The results shown in Figure 5.10 and Figure 5.19 are taken from selected grid points; however, analysis of the spatial average [over the box ABCD in Figure 5.5(a)] geostrophic winds (see Figure 5.20) is also needed in order to confirm and conclude that the Shamal wind events are largely determined by the terrain-induced pressure gradient force and friction. It is apparent from Figure 5.20(a) that the average geostrophic wind speed, for both the control and LS experiments, is mostly influenced by the diurnal heating and cooling of the Zagros Mountains' terrain slopes; strong diurnal oscillation of the geostrophic wind is observed. Maximum average geostrophic wind speeds are simulated near 1200 UTC for both the control run and the LS experiment; an indicator that the daytime heating intensifies the geostrophic winds. For the LS study, especially during the less extensive period, smaller geostrophic wind speeds are captured than the ones observed for the control run [Figure 5.20(a): control versus LS experiments]. It is thus evident that the land–sea distribution (strong north-to-south pressure gradient) enhances the geostrophic

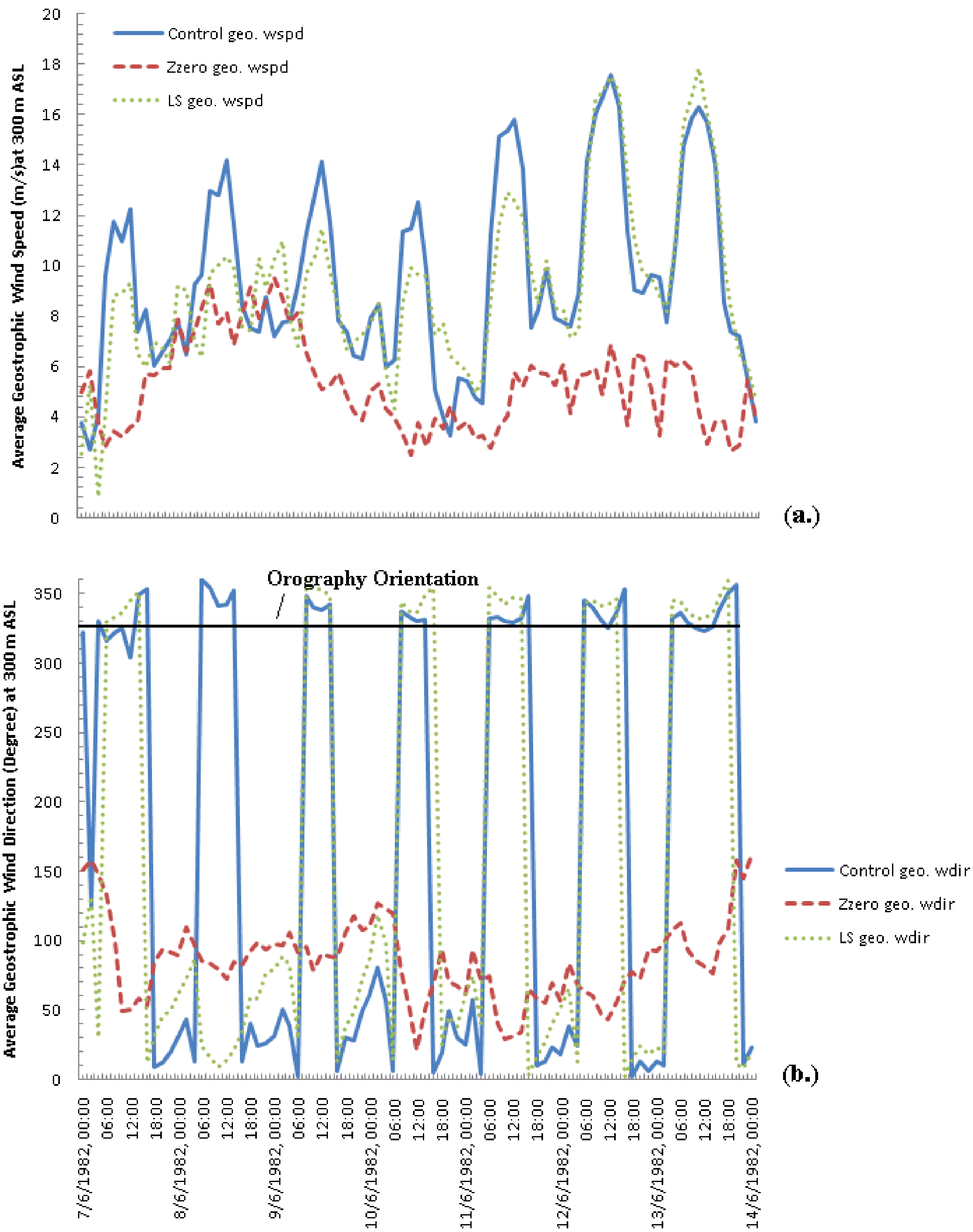

FIGURE 5.20: Time series of (a) average geostrophic wind speed (m s^{-1}) and (b) wind direction (degrees) over the Persian Gulf and southern Iraq at 300 m ASL. The solid curve denotes the control run, the dashed curve the Zzero experiment and the dotted curve the LS study. The x-axis shows UTC time. Taken from Giannakopoulou and Toumi (2011).

wind speeds; a key factor that is absent in the Parish and Oolman (2010) studies. Comparing the black straight line (Zagros Mountains' orientation) in Figure 5.20(b) with the solid curve (control run) and the dotted curve (LS experiment) shows that the maximum north/northwesterly geostrophic winds (for the whole study period) are positioned parallel to the mountainous topography. Finally, the stronger diurnal variations that are seen in the geostrophic wind direction for both the control and LS studies compared with that in the Zzero experiment also imply the significance of the elevated sloping terrain (Figure 5.20(b)); if inertial oscillation was a key factor for the LLJ formation, an almost constant geostrophic wind direction would accompany the wind cycle.

5.7 Summary of findings

The case study in this chapter provided a detailed investigation of the previously documented theories for low-level jet (LLJ) development, focusing on the diurnal features of the summertime LLJ generated over the Persian Gulf and southern Iraq, known as the Shamal. In this study, the Weather Research and Forecasting (WRF) model captured the horizontal and vertical structure of a typical summertime Shamal wind event in line with Membery's (1983) observations. Interestingly, the control simulation provided evidence of the strong diurnal variation in both Shamal wind speed and wind direction. A spatially extensive period, covering the Persian Gulf and southern Iraq, as well as a less extensive period, covering only the Persian Gulf, were identified. In general, the Shamal was oriented parallel to the mountainous topography (Zagros Mountains in Iran) mainly due to the daily heating cycle over the sloping terrain and was composed of a well-defined nighttime maximum over the mid-Gulf at 300 m level. The west-to-east pressure gradient caused by two semi-permanent pressure centres, a semi-permanent high-pressure cell over northwestern Saudi Arabia and a low-pressure centre over Iran, also resulted in the northerly/northwesterly flow over the Persian Gulf.

The results from the sensitivity experiments lead to the conclusion that several factors contributed to the summertime LLJ development, strength, direction and diurnal variation. Based on the zero terrain height experiment, the Blackadar's (1957) mechanism appeared to be secondary to the heating in forcing the LLJ, contrary to Membery's (1983) study. The results of the diurnal oscillation of the wind speed and wind direction revealed the importance of the daytime heating and nighttime cooling of the Zagros Mountains' sloping terrain. Based on the mountain height sensitivity experiments, the decreased mountain height resulted in a narrow and weak jet which moved farther away from the east coast of the Persian Gulf. The northeasterly land breeze contributed to the changes in the position of the nocturnal jet over the Persian Gulf Sea. The land and sea breeze circulations also modulated the Shamal behaviour in terms of the diurnal changes in the zonal geostrophic wind component. This was significantly different from the widely-studied Great Plains LLJ (e.g. Parish and Oolman, 2010). We can, therefore, conclude that the factors influenced the summertime LLJ were the semi-permanent synoptic systems, the Persian Gulf topography and orography, the land/sea breezes and the aforementioned ABL processes (e.g. daily heating cycle over a sloping terrain and inertial oscillation). Specific conclusions from the sensitivity experiments presented in this chapter can now be drawn:

(i) The Shamal wind direction is to a great extent modulated by the mountainous topography. The Zagros Mountains in Iran channel the northwesterly winds and provide a barrier for the easterly monsoon airflow.

(ii) During the less extensive period, the land breeze and the lower friction over the sea increase the intensity of the nocturnal jet over the Persian Gulf.

(iii) Only the less extensive period showed sensitivity to the mountain slope scenarios. For steep slopes a stronger LLJ is observed. However, a larger diurnal variation of the Shamal wind direction is found in the shallow mountain slope experiment.

(iv) The extensive Shamal period was weakly affected by the sloping terrain and the presence of the sea.

Chapter 6

Impacts of the Nile Delta land-use on the local climate

Humans have continually altered the Earth's landscape, weather and climate for centuries (Wichansky *et al.*, 2008). The Nile Delta in Egypt provides evidence of the effect humans have had on land-use/land-cover modifications. The landscape of the Nile Delta has been extensively transformed to the present-day land-cover by increasing agriculture and urbanisation. Egyptians have been intensively farming in the Nile Delta for 5000 years (Stanley and Warne, 1993). In the absence of human activity much of the Nile Delta would have remained desert-like (Holmes, 1993; Hassan, 1997). The Nile Delta is bordered by the eastern Mediterranean Sea (MS) to the north and its weather and climate are mostly influenced by eastern Mediterranean weather systems. For the purposes of this thesis, the climatic and weather conditions of the eastern Mediterranean region and northern Egypt are briefly described in this chapter, with a specific focus on the Nile Delta region.

The work in the present chapter relies on desertification sensitivity experiments, which employ the pre-historic Nile Delta land-cover. The Weather Research and Forecasting (WRF) model was integrated for the 2007/2008 winter months (December, January, February) and 2008 summer months (June, July, August) with climatological surface conditions (control runs) and desert conditions (desertification experiments). The broad aim of this study is to explore the effects of the present-day Nile Delta man-induced greening on the local climate. Particular emphasis is placed on understanding the factors influencing potential evapotranspiration (PET) and energy, radiation and moisture budgets in the agricultural Nile Delta and a storm event over the eastern MS.

Part of the work presented in this chapter has been published in Giannakopoulou and Toumi (2012).

6.1 The climate of the eastern Mediterranean basin

A brief overview of the climate of the eastern Mediterranean basin is provided in this section, as there are a few pertinent aspects of this basin that influence the Nile Delta climate and weather. Further information on the climate variability and trends of the Mediterranean region, including the western and eastern basins, may be found in Bolle (2003).

In this study, the eastern Mediterranean basin is defined as the area between latitudes 28 °N and 42 °N and longitudes 20 °E and 38 °E (see Figure 6.1). It is bounded to the north by Greece and Asia Minor (the western two thirds of the Asian part of Turkey); to the east by Cyprus, Syria, Lebanon, Israel, and Jordan; and to the south by Egypt and Libya (Dayan, 1986). The eastern Mediterranean basin has complex orography with high and steep mountains (Taurus Mountains) in western Turkey and land–eastern MS coastal features (Mehta and Yang, 2008).

The eastern Mediterranean is characterised by a wide length and broad density of available meteorological records, including the most important indices for circulation types, temperature and rainfall. These three major indices will be briefly discussed to quantify the climate of the eastern Mediterranean region.

For circulation, based on the study of Dayan (1986), mid-latitude and sub-tropical climate systems (e.g. eastern Atlantic and Balkan patterns, Asian and African monsoons) influence the eastern Mediterranean climate and in particular its regional wind patterns, temperatures, evaporation, precipitation, moisture transport and atmospheric water budget (e.g. Dayan, 1986; Mehta and Yang, 2008). The pressure systems developed over the Atlantic, Eurasia and Africa determine the following synoptic conditions that affect the eastern Mediterranean basin. Throughout the whole year its climate is controlled by northwest (NW) maritime air masses which cross the eastern MS from NW Europe (cold depression over the eastern MS). During winter and spring the humid climate of the eastern Mediterranean is affected by the continental tropical south/southwest flow from the North African coastal areas. During the fall season, the synoptic pattern is mostly characterised by southeasterly winds from the Arabian Peninsula (well-developed Red Sea trough) and during the summer months the northeastern dry continental air masses control the eastern Mediterranean's weather (Dayan, 1986).

The continental surrounding areas of the eastern MS, between latitudes 32 °N and 45 °N, encompass the Mediterranean climate, which is a moist mesothermal climate with cold and rainy winters and warm to hot/dry summers. Strong temperature difference between the cold winters and the hot summers is one of the main characteristics of this climate (Bolle, 2003). In addition, seasonal temperature and precipitation variability is observed between the different continental eastern Mediterranean regions. Countries

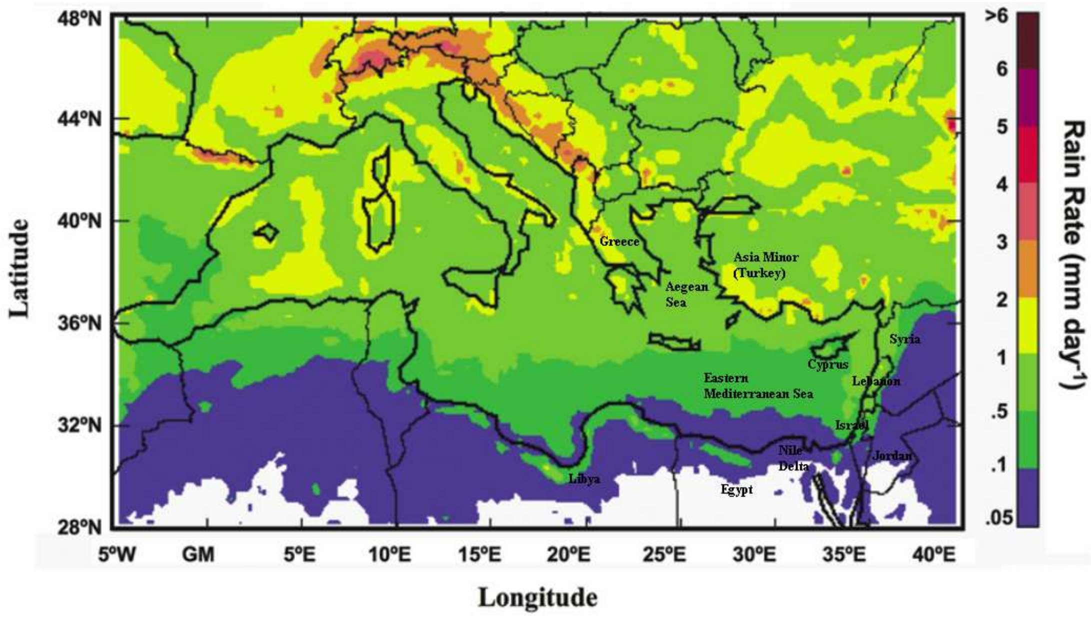

FIGURE 6.1: As indicated by Mehta and Yang (2008), mean rain rates (mm d^{-1}) over the Mediterranean basin from January 1998 to July 2007 using the Tropical Rainfall Measuring Mission (TRMM) measurements. In this study, the eastern Mediterranean basin is defined as the area between latitudes 28 °N and 42 °N and longitudes 20 °E and 38 °E. Its surrounding continental countries are: Greece, Asia Minor, Cyprus, Syria, Lebanon, Israel, Jordan, Egypt and Libya.

below 33 °N, such as Israel, Egypt and Libya are characterised by arid climatic conditions. As noted by Bolle (2003), the average temperatures of the coldest month in the North African (Egypt and Libya) regions can be less than 12.5 °C and can be more than 32.5 °C during the hottest month. However, the average temperatures for the regions extending between latitudes 37 °N and 42 °N can be less than 7.5 °C during the winter and more than 22.5 °C during the summer. Over the eastern MS temperatures vary from 10 °C to 20 °C during the winter and spring seasons. In summer, the temperature can be more than 22.5 °C and ranges from 15 °C to 25 °C in autumn (Bolle, 2003).

The amount of rainfall over the whole year is higher between latitudes 36 °N and 42 °N than in latitudes below 36 °N. Based on the recent climatological precipitation study of the Mediterranean basin by Mehta and Yang (2008), the rain distribution in the eastern Mediterranean region is closely related to the complex topography of the surrounding continental areas. In particular, the maximum rain (about 3-5 mm d^{-1}) is found near the Taurus Mountains in western Turkey and rainfall minima (about 0.5 mm d^{-1}) are observed over the North African regions. The average precipitation over the eastern MS is about 1 mm d^{-1} (Figure 6.1) and occurs from October to March with a peak during November and December (Mehta and Yang, 2008). In the cold period, regional and seasonal variations of the eastern Mediterranean precipitation are mostly associated with synoptic and mesoscale cyclonic systems. In particular, west-to-east and north-to-south mesoscale rain systems, with origin in mid-latitudes, usually enter the eastern Mediterranean region (Mehta and Yang, 2008). However, the majority of precipitation over the eastern MS is associated with cyclogenesis inside the Mediterranean basin (Lionello *et al.*, 2006). The genesis, development and passage of these cyclones usually result from a combination of factors, such as complex topographical features, strong land–sea temperature gradients and large-scale circulations (e.g. Lionello *et al.*, 2006; Mehta and Yang, 2008). During the winter season, the southern part of the eastern Mediterranean region is considered as an area where significant and frequent cyclonic activity develops. The cyclonic intense rain in the southern part of the eastern MS is mostly associated with cyclonic systems that start their development in the south-western regions of the MS, and then migrate to the east near Cyprus (Lionello *et al.*, 2006).

The summer dryness is a characteristic of the eastern Mediterranean climate, because the sub-tropical high-pressure systems are displaced to the north and cause drought (Rohling and Hilgen, 1991). The Atlantic high-pressure system (Azores high) and the easterly monsoon airflow above the Indian Ocean and Persian Gulf are two semi-stationary weather systems that define the climatic conditions during this dry season in the Mediterranean basin. Strong pressure gradients are formed between the western and eastern Mediterranean coasts as a result of this anticyclone and monsoon activity that enhances the regional winds (e.g. Kallos *et al.*, 1998; El-Askary *et al.*, 2009). Also, during the summer period (from about June to September), the combination of a high-pressure system over the Balkan Peninsula and a deep Asiatic continental depression (which is centred over southwest Asia and sometimes is extended to the west near Cyprus) creates steady strong and dry north/northwesterly winds, known as the Etesians, over the whole eastern Mediterranean. Usually a secondary depression develops over Cyprus and the Etesian winds become more humid and blow from a direction which may be between southwest and west (e.g. Rohling and Hilgen, 1991; Kallos *et al.*, 1998; Lionello *et al.*, 2006). A decrease of precipitation also is noted in the summer over the eastern Mediterranean, with some south-to-north cyclonic rain systems suggesting their origin from a sub-tropical region (Mehta and Yang, 2008). Usually, a strong southward flow from the eastern MS brings moisture into the dry Egyptian and Arabian Peninsula regions (Mariotti *et al.*, 2002).

6.1.1 Cyclones in the eastern Mediterranean region

The impact of cyclones on weather and climate has demonstrated the need for a clear understanding of the cyclone generation, development, duration, intensity, and frequency. In the literature two different ways of cyclone definition are proposed. Because cyclonic circulation and low surface air pressure usually coexist, first and most common way to define the cyclone (with counter-clockwise direction in the Northern Hemisphere) is as a weather system of relatively low atmospheric pressure compared with the surrounding air (e.g. Glickman, 2000; Lionello *et al.*, 2006). Another way is to define cyclones as vorticity (relative or geostrophic) maxima (e.g. Lionello *et al.*, 2006). It is important to note that mesoscale and climate models have limited capability to simulate and forecast cyclones because of the critical effects of horizontal resolution (low resolution will fail to reproduce small-scale cyclones; high resolution will miss large-scale cyclones). Thus, the number, spatial scale and location of cyclonic circulations can differ regarding the choice of cyclone definition and meteorological model (Lionello *et al.*, 2006). However, there is a general agreement on the spatial position of cyclogenesis over the Mediterranean region, despite the different data, models, methods and criteria that have been used in most of the cyclone studies (e.g. Petterssen, 1956; Trigo *et al.*, 1999; Maheras *et al.*, 2001).

Several well-documented studies show that the Mediterranean region experiences one of the highest concentration of cyclogenesis (the birth and development of a cyclone) in the world (e.g. Petterssen, 1956; Radinovic, 1987; Lionello *et al.*, 2006). Cyclones have been a subject of numerous studies because of their significant influence on the weather and climate over the Mediterranean region, but also farther east in northeastern Africa, the Arabian Peninsula, Iran and even northern India (e.g. Petterssen, 1956; Radinovic, 1987; Trigo *et al.*, 1999; Maheras *et al.*, 2001; Lionello *et al.*, 2006).

Cyclogenesis usually occurs in the eastern Mediterranean basin because of the frequent formation of low-level shallow depressions by the complex orography of the region. The topographical features and the great amount of latent heat that is released in the eastern Mediterranean region seem to have an important role in the cyclogenesis. Large-scale southward synoptic systems from Europe also seem to control the intensity, duration and location of cyclones in the eastern Mediterranean basin. In winter, cyclones form as a combination of strong upper-troughs, topography and strong baroclinic instability. In spring and summer, the latitudinal temperature differences along with the aforementioned mechanisms favour the cyclone development. Considering the physical mechanisms that are responsible for the generation and development of cyclones, the topographical characteristics and geographical location of the eastern Mediterranean region, lee cyclones, thermal, Mediterranean and Middle East lows usually form over the eastern Mediterranean basin and its surrounding continental areas (Lionello *et al.*, 2006).

According to Trigo *et al.* (1999), the typical seasons of the cyclone birth and development over the eastern Mediterranean are the winter, spring and summer. Trigo *et al.* (1999) proposed four main regions where cyclogenesis occurs and affects the eastern Mediterranean weather and climate. These four regions are: the Aegean Sea (during the winter and spring), the eastern Black Sea (during the whole year), Cyprus and the Middle East (during the spring and summer) (Trigo *et al.*, 1999). In the Aegean Sea, Cyprus and the Black Sea, lee cyclones can be observed to the south of the mountain ridges. During autumn and winter seasons, thermal and Mediterranean lows are generated over the eastern MS because of the land—sea temperature differences and air–sea temperature contrasts, respectively. The Middle East lows, with origin in Cyprus (Cyprus and Syrian lows) and Red Sea (Red Sea troughs), have different generation, intensity and seasonality. The Cyprus and Syrian lows are mostly produced due to the topographic effects of Cyprus (Lionello *et al.*, 2006). During the spring (April) and fall (October and November), the complex terrain in the Red Sea region generates the Red Sea trough, which brings intense precipitation (e.g. Tsvieli and Zangvil, 2005; Lionello *et al.*, 2006).

6.2 The climate of North Egypt

Egypt lies between latitudes 22 °N and 31 °N and longitudes 24 °E and 36 °E and is bordered by Israel to the northeast, the Red Sea to the east, Sudan to the south, Libya to the west and the eastern MS to the north. Egypt has an arid climate because it lies within the North African desert belt (the desert landscape of Egypt includes parts of the Sahara Desert and of the Libyan Desert), with hot, dry, rainless summers and mild winter temperatures. Its climate is mainly characterised by high evaporation and low annual precipitation with small amounts of rainfall to fall in the winter months along the northern Egyptian coastal areas, the agricultural Nile Delta, and the area south of Cairo (e.g. Yates and Strzepek, 1998; Rana and Katerji, 2000).

After Bolle (2003), the general precipitation and temperature distributions in the northern Egyptian coasts and the eastern MS are presented in Table 6.1. The seasonal evolution of precipitation over northern Egypt is fairly similar to that previously described for the eastern MS but with a much smaller amount of rainfall that varies from one year to the next (e.g. Ayyad, 1973; Mehta and Yang, 2008). In particular, the maximum frequency and amount of rainfall (about 2.25 mm d^{-1}) usually are observed between October and February, whereas the rain minima (about 0.5 mm d^{-1}) are found in the dry period from June to August (e.g. Ayyad, 1973; Bolle, 2003; Mehta and Yang, 2008). The MS is a significant source of atmospheric moisture that flows from the western to the eastern MS and brings rain into the Nile Delta and the Arabian Peninsula (Mariotti *et al.*, 2002). The precipitation in northern Egypt usually is associated with cyclones which are mostly generated or intensified by the aforementioned moisture transport in the eastern MS. The differential heating between eastern Mediterranean water bodies and Egyptian land along with the complex terrain of north Egypt favour the genesis and development of these thermal circulations (Kallos *et al.*, 1998).

One of the northern Egyptian climatic characteristics is the strong seasonal and diurnal temperature variability. The annual mean temperatures of northern Egypt range from

TABLE 6.1: Mean surface air temperature (°C) and rainfall (mm d^{-1}) for the North African coastal areas (e.g. north coastal areas of the Nile Delta in Egypt) and the eastern MS according to the European Climate Support Network (1995) for the period 1960-1990 [after Bolle (2003)].

Season	Temperatures (°C) Coastal areas & Eastern MS	Rainfall (mm d^{-1}) Coastal areas & Eastern MS
Winter	12.5 ± 2.5 & 15.0 ± 5.0	0.25 ± 2.0 & 2.0 ± 10.0
Spring	17.5 ± 5.0 & 15.0 ± 5.0	0 ± 2.0 & 0 ± 2.0
Summer	32.5 ± 10 & 22.5 ± 5.0	0 ± 0.5 & 0 ± 1.0
Autumn	20.0 ± 5.0 & 20.0 ± 5.0	0 ± 2.0 & 0.5 ± 5.0

approximately 15 °C to 27 °C with the maximum annual temperatures to be captured inland (27 °N) in July. During the winter, the air becomes very moist along the shoreline and the temperatures can drop to 10 °C (see Table 6.1). Farther landward, the winter surface temperatures average between 12.5 °C and 15 °C. The summer temperatures are approximately 26 °C in Egypt's northern coasts and 32.5 °C inland (Bolle, 2003). The latitudinal temperature gradient between the eastern MS and the land regions of northern Egypt enhances steady winds to flow from north/northwest and, subsequently, lowers the temperatures near the coast. This is most pronounced during the dry season whenever the strong pressure gradients between the Azores high and the easterly monsoon flow over the Arabian Peninsula intensify this wind system (El-Askary *et al.*, 2009). These temperature/pressure differences are greater during the daytime in the summer period and cause the strong northerly winds to penetrate over the Nile Delta (Kallos *et al.*, 1998). During the spring, northern Egypt is affected by westerly flow (from Sahara desert), which brings sand and dust and raises the temperatures. Usually south-to-north tropical air in the spring creates cyclones in the desert (El-Askary *et al.*, 2009).

6.2.1 The climate of the Nile Delta in Egypt

One of the world's largest river deltas is the Nile Delta in northern Egypt, extending from Alexandria (lat: 31.13 °N, long: 29.58 °E) in the west to Port Said (lat: 31.28 °N, long: 32.23 °E) in the east and Cairo (lat: 30.2 °N, long: 31.21 °E) to the south (see Figure 6.2).

The Nile Delta has Mediterranean climate (where climate is considered the average of instantaneous weather) characterised by mild to cold/wet winters, and warm to hot/dry summers. The notable trends in the mean temperature and precipitation for the Nile Delta region are consistent with the previously described seasonal mean temperature and

FIGURE 6.2: Map of the Delta area of Nile River. The original figure was posted in Google Maps: Egypt, Nile Delta by Elliott Back on April 8th, 2005.

rainfall trends for the North African coastal areas (see Table 6.1). Based on the Strzepek *et al.* (1995) research, the average annual precipitation in the central Nile Delta (Cairo) is 48 mm (25.5 mm), the mean annual PET is 139 mm (178 mm) and the mean annual temperature is 19.8 °C (20.8 °C). In addition, according to Frenken (2005), the climate of the Nile Delta is characterised by its aridity, with average October–May annual rainfall that varies from 190 mm in the Nile Delta coastal areas to 20-50 mm in the south. In the Nile Delta the mean monthly temperature ranges from 13 °C in January to 27 °C in August. The monthly precipitation (PET) varies from 0 mm (216 mm) in June to 24 mm (71 mm) in January (Esteban *et al.*, 2003).

Because of the arid climate of Egypt and the absence of precipitation, almost all of the vegetated land in the Nile Delta is irrigated and the water supply comes mostly from the Nile River (Strzepek *et al.*, 1995). In 1973, Ayyad provided a water budget assessment from 1950 to 1964 of an Egyptian coastal area 48 km west of Alexandria (Ayyad, 1973). After Ayyad (1973), Figure 6.3 compares the 15-year average precipitation with both potential and actual evapotranspiration [calculated using the Thornthwaite and Mather PET approach (Thornthwaite and Mather, 1955)]. Based on his water balance computations for this region, precipitation exceeded the water demand (expressed as PET) during December–February and the additional available water was used for agricultural purposes. From February to November rainfall was less than the water demand and actual evapotranspiration (AET) was less than PET, which created a lack of moisture (Ayyad, 1973). Later on, Conway and Hulme (1996) explored the effects of climate variability and future

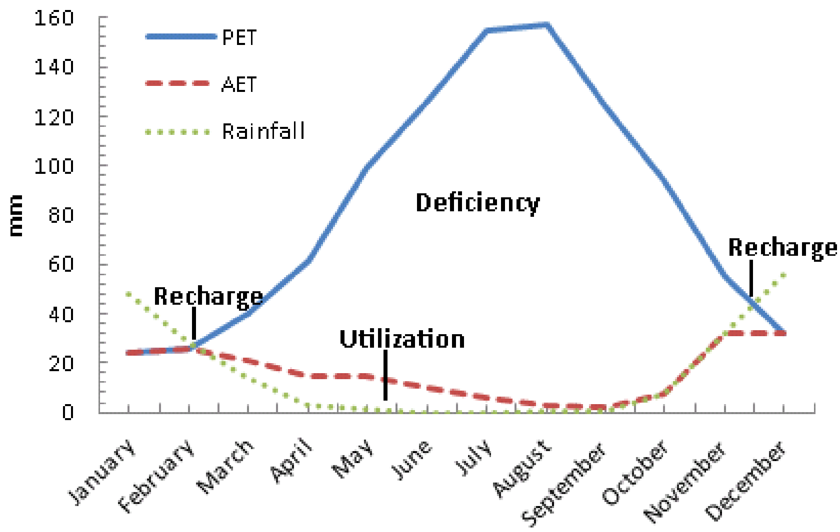

FIGURE 6.3: Seasonal variation in precipitation, potential (PET) and actual (AET) evapotranspiration for the Burg El-Arab area (48 km west of Alexandria) in Egypt (redrawn after Ayyad (1973)). All values are the averages of 15-year records (1950-1964) obtained from the Egyptian Meteorological Department and are in mm.

climate change on water resources in Egypt. Based on their study, Egypt's water use during the period 1981-1990 exceeded the availability. Conway and Hulme (1996) also suggested that future temperature and PET changes would have a major impact on the water resources in Egypt. Therefore, understanding the PET changes in the Nile Delta land is crucial because the water availability is in general below the water demand and because more irrigated lands are required due to the increase in population.

Each circulation pattern observed over the Nile Delta can be subjectively classified according to the weather systems that cross the eastern MS. On local scales, the Nile Delta climate depends on multiple subtle features such as latitude, geography (it is surrounded by desert), orography (it is very flat), vegetation, land–eastern MS contrasts and the typical paths of air masses over the eastern MS and northern Egypt (e.g. Kallos *et al.*, 1998; El-Askary *et al.*, 2009; El-Banna and Frihy, 2009). The Nile Delta is principally influenced by a trade wind system which results by differential heating between the eastern MS and the bare and dry landscape of North Africa and the partially vegetated Southern Europe. The resulting circulation patterns over the Nile Delta are northerly winds that intensify the sea breezes along the coastline (Kallos *et al.*, 1998; El-Askary *et al.*, 2009). During the winter, cold northerly winds blow over the Nile Delta from central Europe and a low-pressure system near Cyprus brings rain to the region usually from December to February. A westerly/northwesterly flow is also dominant 60-65 % of the year because maritime air masses cross eastern MS from NW Europe. For 10-15 % of the year, particularly in the summer season, the winds have a northeast (NE) direction over the Nile Delta due to the NE continental air masses with origins in Eastern Europe (e.g.

Dayan, 1986; El-Banna and Frihy, 2008; El-Askary *et al.*, 2009). The average winds over the Nile Delta are characterised by stronger intensity of aproximately 5-7 m/s during the cold period; whereas, in the summer and spring lower speeds are observed of the order of 3-5 m/s (El-Banna and Frihy, 2008).

6.3 Components of the Nile Delta as depicted by various datasets

For a brief climatological analysis of the Nile Delta region, basic meteorological variables from the ECMWF and NCEP/NCAR re-analysis projects are analysed in this section. The ERA-Interim re-analysis covers the period from 1979 to 2011 and the 79 km spacing data have a temporal resolution of 6 hours and 60 vertical model layers. The ERA-40 re-analysis project is run at a grid size of 125 km and a temporal resolution of 6 hours and covers the period from 1957 to 2002. The NCEP/NCAR R1 re-analysis covers the years 1948-2011 with an approximate grid size of 1.92×0.96 degrees, a temporal resolution of 4 hours and 28 sigma levels. All the data and produced plots for this section are available from KNMI Climate Explore.

A period of 23 years (1979-2002) was chosen for this study in order to analyse by the aforementioned re-analysis projects the climatological winter (December-January-February; DJF) and summer (June-July-August; JJA) precipitation, sea-level pressure, surface temperature and wind speed in the eastern Mediterranean region, including the Nile Delta in Egypt. The examined area extends between latitudes 26 °N and 39 °N, and longitudes 21 °E and 38 °E (see Figure 6.4). The specific focus on this area is motivated by the influence of the climatic and weather conditions of the eastern Mediterranean Sea (MS) on the Nile Delta climate.

A comparison of the seasonal DJF and JJA rainfall in the eastern Mediterranean region is presented in Figure 6.4. Based on all re-analyses the eastern Mediterranean precipitation centre persists during the cold period near Cyprus (see Figure 6.4). According to Mehta and Yang (2008), the majority of rainfall sources in eastern MS are cyclones and Cyprus is considered to be an area where significant and frequent cyclonic activity develops (see section 6.1). Based on the Lionello *et al.* (2006) study, cyclonic intense rain is mainly associated with the Cyprus low-pressure systems. As evident from the Figure 6.5, all re-analyses predict a surface low-pressure to the west/southwest of Cyprus which possibly indicates the spatial scale of these cyclones. All datasets also indicate that the northern Egypt is drier in both seasons (with winter rainfall about 0.5 mm d^{-1}) than the other surrounding countries of the eastern Mediterranean. These results are in line with the Bolle's (2003) observations of the North African coastal area's winter mean

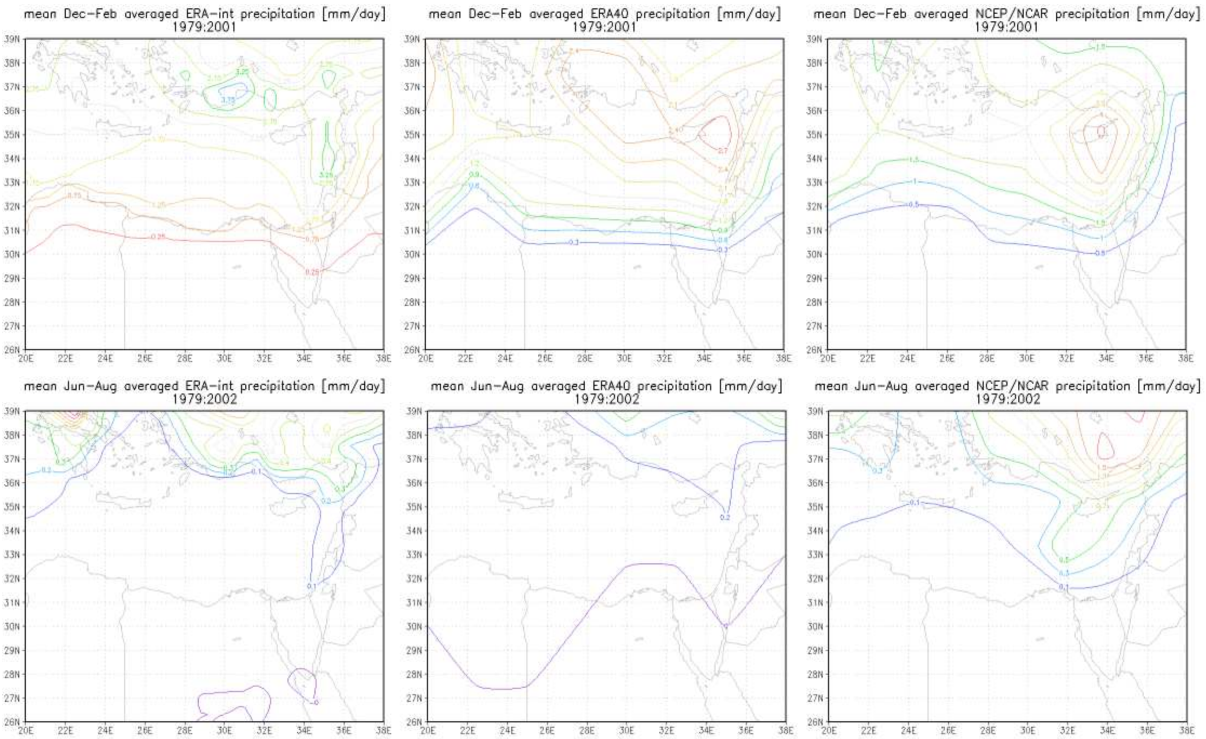

FIGURE 6.4: Climatological winter (DJF; 1st row) and summer (JJA; 2nd row) mean precipitation in the eastern Mediterranean region. (1st column) Means derived from the ERA-Interim re-analysis; (2nd column) means from ERA-40; (3rd column) means from NCEP. (Period 1979-2002, units mm d^{-1}).

precipitation in section 6.2. Focusing on the maximum precipitation, it is apparent in Figure 6.4 that the datasets are not consistent; ERA-Interim gives north of 33 °N the highest winter precipitation and ERA-40 the lowest. In particular, the ERA-Interim rain maximum during winter is about 3.75 mm d^{-1} in the lee of the Taurus Mountains in Turkey (37 °N), whereas the ERA-40 and NCEP re-analysis projects give 2.7 mm d^{-1} and 4.5 mm d^{-1} maximum precipitation in Cyprus (35 °N), respectively. During the summer, all the datasets agree that the whole eastern Mediterranean region south of 36 °N is dry, receiving less than 0.5 mm d^{-1}.

In both seasons, the meridional temperature gradient between the eastern MS and the Nile Delta region (see Figure 6.6) favours the development of the rainy systems in the eastern MS (as discussed in subsection 6.1.1). Despite the limited resolution available, all the re-analyses are able to define this land–sea temperature difference. As seen in Figure 6.6, the temperature difference is most clearly observed during the winter because of the highest temperatures of eastern MS and the cool areas along the northern Egyptian coast. During the winter season, the sea surface temperatures vary from 10 °C to 15 °C, with maximum values near the coastal areas of Egypt, and during the warm season from 24 °C to 28 °C (Figure 6.6). These results are in line with the mean eastern MS surface temperatures provided by Bolle (2003) for the 1960-1990 period (see section 6.2). On

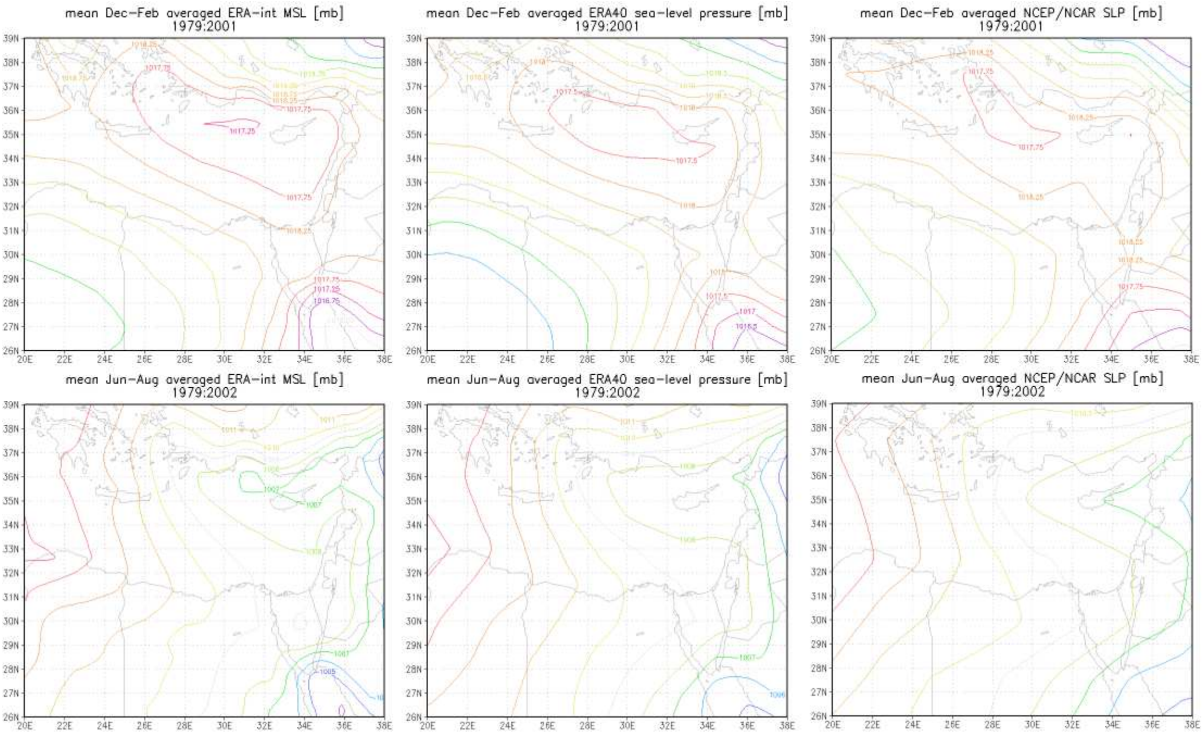

FIGURE 6.5: Climatological winter (DJF; 1st row) and summer (JJA; 2nd row) mean sea-level pressure in the eastern Mediterranean region. (1st column) Means derived from the ERA-Interim re-analysis; (2nd column) means from ERA-40; (3rd column) means from NCEP. (Period 1979-2002, units mbar).

land the winter surface temperatures vary between -3 °C and 15 °C, whereas the summer temperatures range from 20 °C to 32 °C. The coldest region is the eastern part of Turkey and the warmest is Egypt. In particular, the winter temperatures in the Nile Delta vary from 12 °C to 15 °C and the summer temperatures range from 24 °C to 28 °C, which is in reasonable agreement with the Bolle's (2003) analysis discussed in section 6.2. It is important to note that the ERA-40 and NCEP data also predict a zonal temperature gradient in the Nile Delta area between longitudes 24 °E and 35 °E. It is possible that the land-cover differences between the vegetated Nile Delta and the surrounding deserts create this west-to-east temperature gradient that is most evident during winter.

During the winter, in both ERA-Interim and ERA-40 projects the eastern Mediterranean surface wind speed is the largest over the Aegean Sea (see Figure 6.7). The NCEP data shifts the centre of the maximum winds to the south of the island of Crete and gives considerably lower wind speeds than the ERA re-analyses. However, all datasets in both cold and warm periods tend to have weak winds over the surrounding continental areas of eastern MS. These weak winds are especially evident over the flat Nile Delta and the orographic regions of Greece and Turkey. During the summer, ERA-40 re-analysis is consistent with NCEP because both datasets have the centre of the strongest winds (about 6 m s^{-1}) to the southeast of the Crete Island between latitudes 33 °N and 35

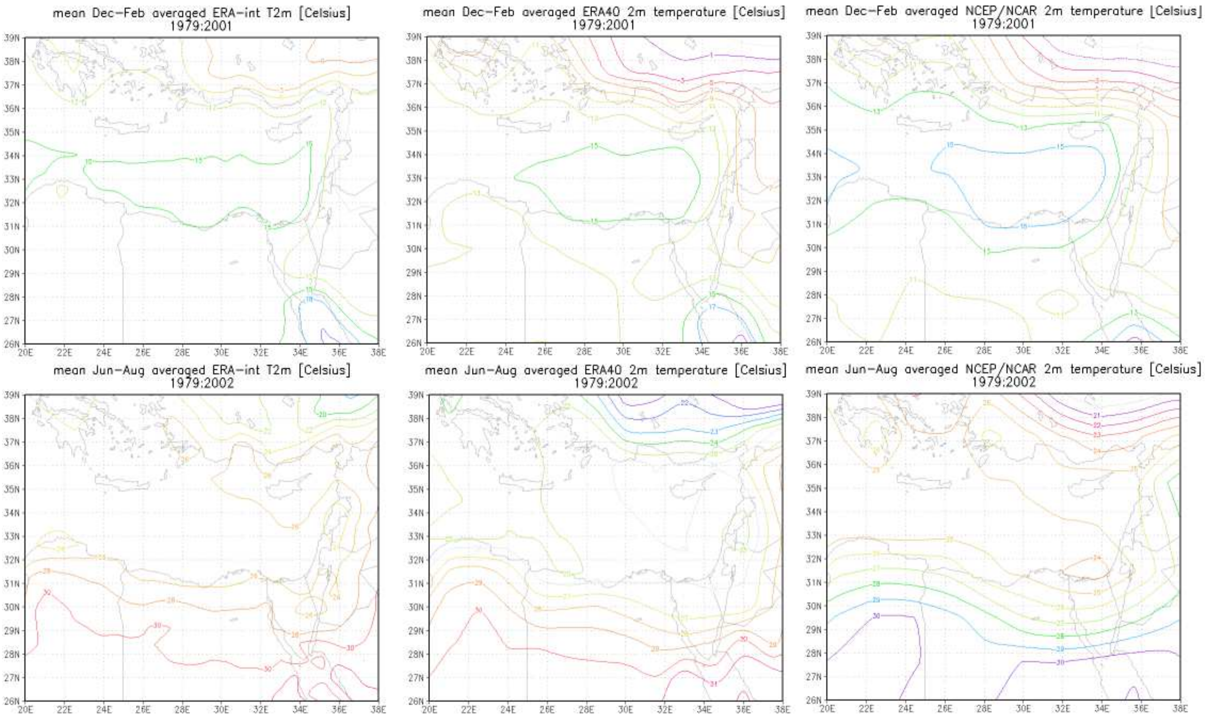

FIGURE 6.6: Climatological winter (DJF; 1st row) and summer (JJA; 2nd row) mean 2 m temperature in the eastern Mediterranean region. (1st column) Means derived from the ERA-Interim re-analysis; (2nd column) means from ERA-40; (3rd column) means from NCEP. (Period 1979-2002, units °C).

°N, whereas ERA-Interim re-analysis tends to have the maximum flow (about 7 m s^{-1}) between latitudes 35 °N and 37 °N.

6.4 Background to the problem

The Nile Delta provides evidence for the land-use/land-cover alterations by developing human activity (El-Banna and Frihy, 2008). As discussed in section 2.4, understanding the impact of anthropogenic land-use/land-cover changes (e.g. vegetation changes) on local, regional and global climate is important for a wide range of fields, including meteorology, climatology and hydrology (e.g. Gates and Liess, 2001; Angelini *et al.*, 2011). Lately, because of the advent of high performance computing, several numerical studies have shown the effects of land-cover changes on rainfall, atmospheric circulations, energy, radiation and moisture budgets (e.g. Xue and Shukla, 1996; Gates and Liess, 2001; Wichansky *et al.*, 2008). Land-use changes have also been shown to influence potential evapotranspiration (PET) (e.g. Zhang *et al.*, 2001; Han *et al.*, 2009), as presented in section 2.5.

PET is a significant index in hydrology and in studies relating to water availability for agriculture. As discussed in section 2.5, accurate estimates of PET, under a changing

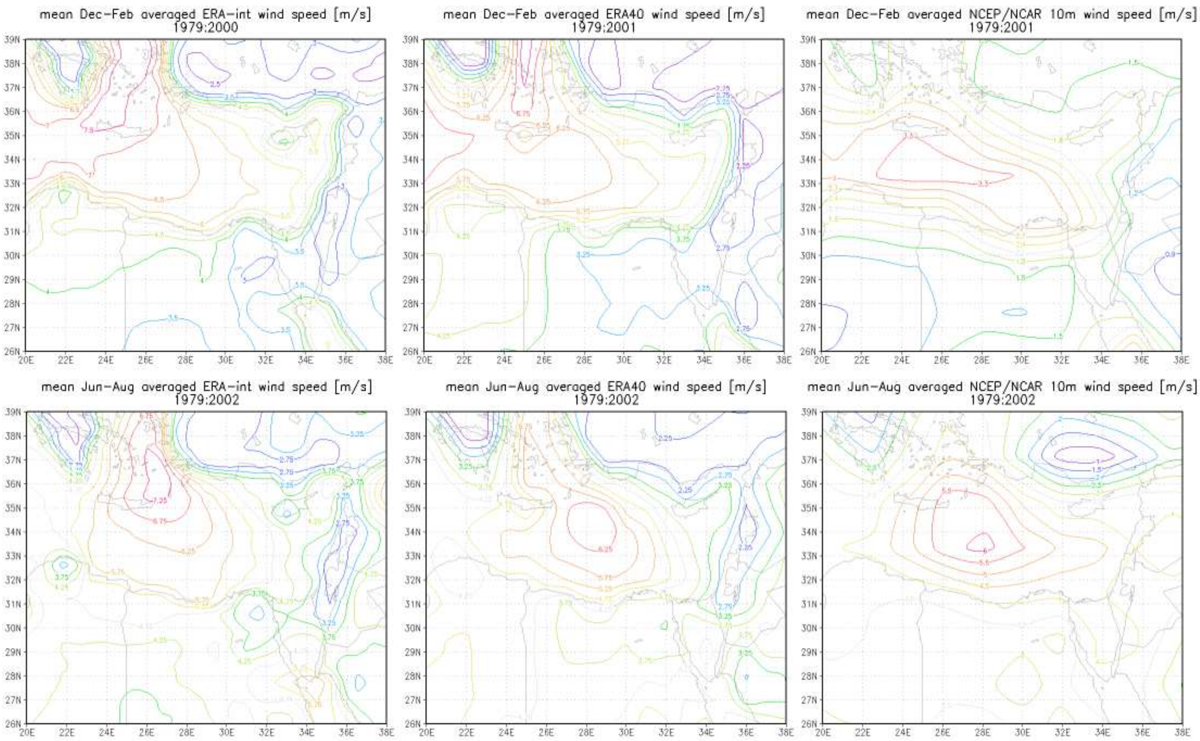

FIGURE 6.7: Climatological winter (DJF; 1st row) and summer (JJA; 2nd row) mean surface wind speed in the eastern Mediterranean region. (1st column) Means derived from the ERA-Interim re-analysis; (2nd column) means from ERA-40; (3rd column) means from NCEP. (Period 1979-2002, units m s^{-1}).

climate and land-cover, are important for water supply and scarcity (Shaw and Riha, 2011). As also presented in section 2.5, several researchers have addressed the temporal and spatial variations of PET based on available weather station data (e.g. Chattopadhyay and Hulme, 1997; Gao *et al.*, 2006). The analysis of PET trends in different seasons over different land types (e.g. crops, mountainous, oasis, forest and urban regions) has also been a subject of numerous studies (e.g. Han *et al.*, 2009; Shaw and Riha, 2011). Most of these studies have been performed either on a global scale, or in regions with high levels of human activity, such as China and India (see section 2.5). However, in water-limited environments such as the Nile Delta in Egypt, where agriculture mostly depends on water availability, the net influence of greening/farming on climate is still uncertain.

According to Hassan (1997), the Nile Delta pre-historic land-cover included beach sand, which blanketed the seaward part of the Nile Delta; brackish water deposits, which accumulated in lagoons behind the beach, and alluvial silt and sand along the Nile channels and farther landward into the central Nile Delta. Therefore, the sediments would have been mostly sand in the pre-historic times when the Nile Delta was characterised by a period of aridity and low Nile floods (Hassan, 1997). The Nile Delta assumed this land-cover configuration until its modification by farming and irrigation in the late Holocene period (Hassan, 1997; Stanley and Bernhardt, 2010). According to Holmes (1993), the

Nile Delta in the late pre-historic times was an inhospitable landscape and no early agricultural settlement was expected. However, one of the first fundamental steps in the development of the Egyptian civilisation was the establishment of agriculture (Holmes, 1993). The initial agricultural settlements on the Nile Delta began around 5000 BC (e.g. Holz, 1969; Holmes, 1993; Stanley and Warne, 1993; Hassan, 1997). Stanley and Warne (1993) linked this agricultural development to a deceleration in sea-level rise (e.g. Holmes, 1993; Hassan, 1997). Slowing of sea-level rise after 3000 BC, subsidence and reduction of flood discharge led to remarkable changes in the principal branches and distributaries of the Nile Delta, highlighting the instability of the Nile Delta land-cover. During the development of the Egyptian farming, silt deposits from the Nile River made the surrounding land fertile because the annual flood rejuvenated the soil (Hassan, 1997). Since then, the Nile Delta has been intensively cultivated, leading today to substantial greening relative to the ambient desert conditions, which are characterised by large evaporation and minimal rainfall (El-Banna and Frihy, 2008). Therefore, in the absence of human activity much of the Nile Delta would have remained desert-like (e.g. Holmes, 1993; Hassan, 1997).

Today the Nile Delta is a very rich agricultural region. From west-to-east and north-to-south, the Nile Delta covers 240 km of the eastern Mediterranean coastline and 160 km of cultivated land (see Figure 6.9), respectively (e.g. El-Banna and Frihy, 2008). The Nile Delta is considered to be the most important agricultural area of Egypt because it accounts for 60 percent of the vegetated land with field crops and vegetables (Yates and Strzepek, 1998). Therefore, the Nile Delta has a great economic dependence on agriculture. It is very heavily populated [more than 60 percent of the population in Egypt (Yates and Strzepek, 1998)] and has a significant role in daily life and development aspects of the region (El-Banna and Frihy, 2008). Based on the El-Banna and Frihy (2008) study, the cultivated Nile Delta area with its rich mud, clay and silt has approximately doubled (around 864 km^2 agriculture), and the urban/built-up areas have been increased by 474 % over a 47-period (1955-2002). Therefore, the Nile Delta landscape was dramatically different in the pre-historic times than it is in the 21^{st} century.

The Nile Delta has also received considerable attention from researchers because the effects of global warming and the potential increase in sea level make it a vulnerable coastal zone (e.g. Broadus *et al.*, 1986; Sestini, 1989; Frihy *et al.*, 1991; Yates and Strzepek, 1998; El-Banna and Frihy, 2008; El-Nahry and Doluschitz, 2010). The entire Nile Delta is a very flat agricultural region only few meters above sea level and scientists believe that its northern part is threatened by sea-level rise (SLR) and land subsidence due to global climate change (e.g. Broadus *et al.*, 1986; El-Raey *et al.*, 1995; El-Banna and Frihy, 2008; El-Nahry and Doluschitz, 2010). For example, in one of the earlier studies, Broadus *et al.* (1986) indicated a land loss of 12-15 % of Egypt's agricultural land due to a one-meter SLR (e.g. Broadus *et al.*, 1986; Strzepek *et al.*, 1995). El-Raey *et al.* (1995) suggested that agricultural losses would occur because of soil salinization. Strzepek *et al.* (1995) provided a description of the expected impacts of the global warming in the Nile basin and the influence of these climatic changes on water resources and vegetation. Based on the recent El-Banna and Frihy (2008) 47-year period (1955-2002) estimations for the landscape changes in the northeastern Nile Delta, approximately 77 % of the sandy beaches have been reduced and about 95 % of the agricultural land has been gained because of reclamation of coastal dunes and lagoons. According to the El-Nahry and Doluschitz (2010) climate study, the agricultural production was estimated to decline more than 50 % based on the worst two-meter SLR scenario.

Currently, there is no numerical study of this region with regard to the effects of greening on its local climate. Therefore, the physical understanding of the impacts of the Nile Delta land-use/land-cover modifications on the local climate is limited. It can be assumed that the climate and land-use/land-cover changes had and will have an effect on the Nile Delta with regard to water resources and agricultural production. Any major changes in the terrestrial water budget will have a major impact on hydrologic processes and, consequently, on the economy and welfare of the Egyptians (El-Nahry and Doluschitz, 2010). There are several studies that have assessed the impact of climate change on the Egyptian water resources and economy (e.g. Conway and Hulme, 1996; Yates and Strzepek, 1998). However, the lack of information about PET changes in the Nile Delta, which are fundamental to understand the water balance and demand, motivates this study. Therefore, in this context PET studies are essential.

In the present study, we investigate the impact of the Nile Delta man-made greening on local climate, circulation patterns and a storm event. To accomplish this, we compare control (CTRL) simulations, which employ the present-day Nile Delta vegetation coverage as a result of anthropogenic activity, with desertification (DES) experiments in which the Nile Delta is replaced by desert. The control (CTRL) runs are carried out for the mean wintertime [December 2007–February 2008 (DJF)] and summertime [June 2008–August 2008 (JJA)] months. We make a simplified assumption that the Nile Delta in pre-historic times was desert-like without irrigation. To the best of the authors' knowledge, there are no modelling studies that have examined the potential effects of land-cover change within a highly cultivated and populated region that was once primarily desert-like in the pre-historic times. This study focuses on how the Nile Delta local climate has changed from a past period when human-induced activity did not exist; this is not a future climate scenario. The Nile Delta is our case study here and the present application is the first modelling study of the Nile Delta greening effects on PET and on other meteorological parameters. Applying sensitivity experiments to this region where the local terrain, synoptic scale and surface forcing are treated realistically is also novel.

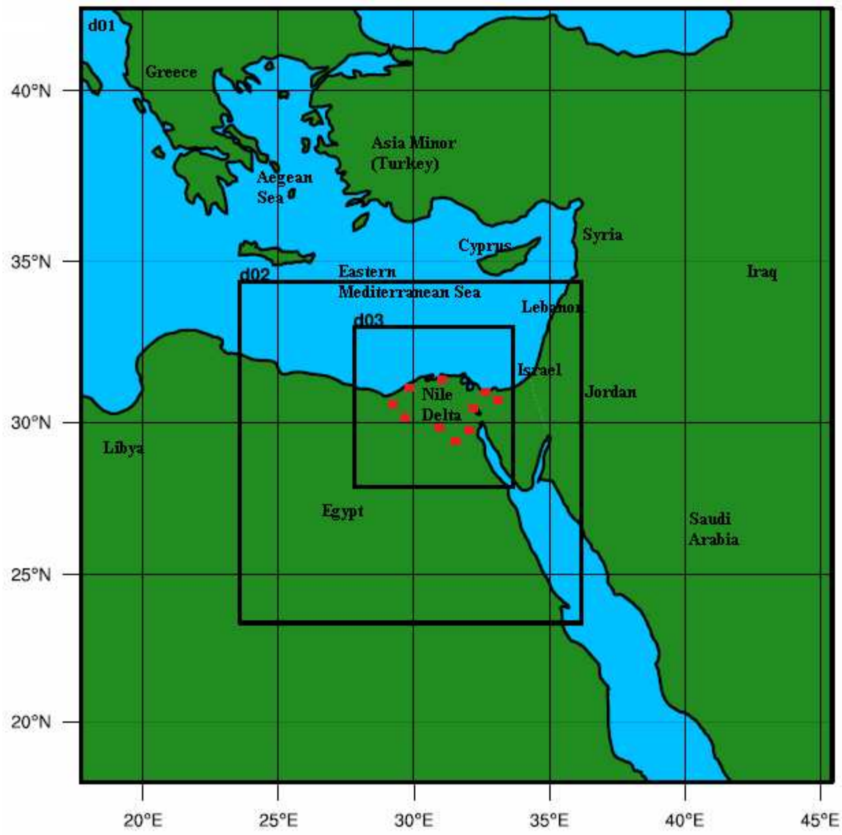

FIGURE 6.8: WRF modelling domain: 81 km (d01), 27 km (d02) and 9 km (d03) grid spacing for the control (CTRL) and sensitivity (DES) experiments. Locations of weather stations are indicated in the d03 domain (red squares).

6.5 Methodology

6.5.1 Model description

In this study, we have used the Weather Research and Forecasting (WRF) model, Version 3.2.1 (Skamarock *et al.*, 2008). This is based on the fully compressible, non-hydrostatic Euler equations and for the purposes of this research the Mercator grids were chosen. A third order Runge-Kutta (RK3) integration scheme and Arakawa C-grid staggering were used for temporal and spatial discretization, respectively.

The WRF model was run in a series of one-way nested grids (centred in the Nile Delta at 30.5 °N and 31.15 °E) with 50 vertical levels. In particular, the WRF model was built over a parent domain (d01) with 35×37 horizontal grid points at 81 km, an intermediate nested domain (d02) of 27 km spatial resolution (46×46 grid points), and an innermost domain (d03) with 9 km spacing (61×61 grids) (Figure 6.8). This set of nested domains was selected to model a large geographic area that would enable us to study the Nile Delta greening effects on large-scale weather systems. Note that this one-way nested grid configuration allows us to downscale large-scale systems into appropriate lateral boundary

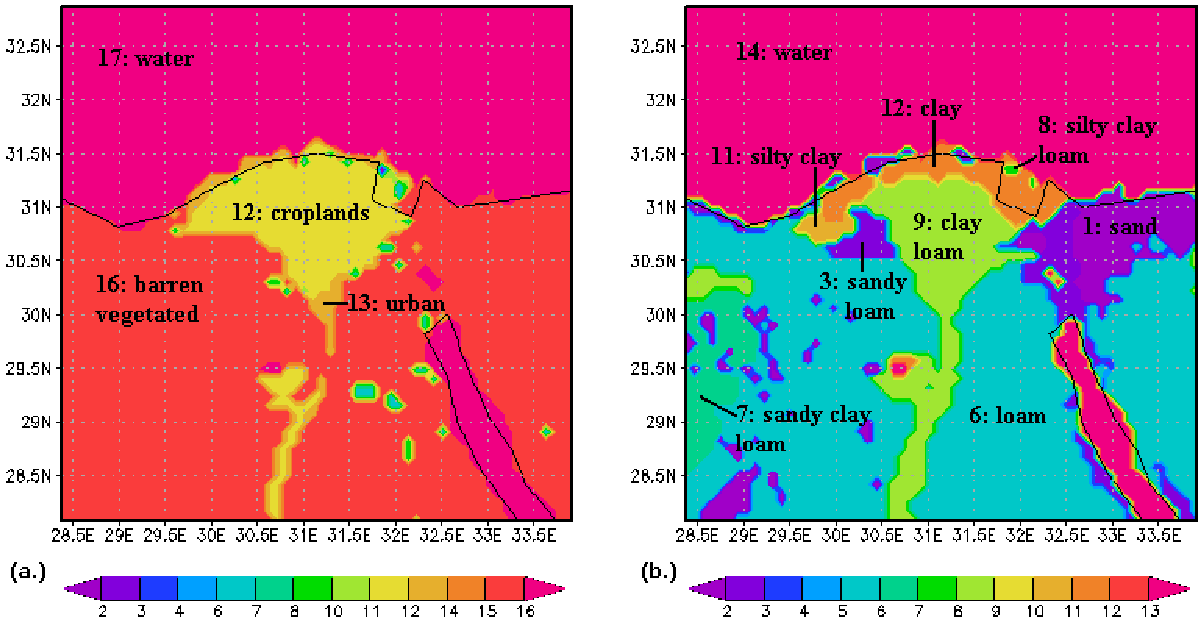

FIGURE 6.9: Distribution of the dominant present-day (a) IGBP-modified MODIS vegetation and (b) soil types for the Nile Delta and its surrounding states, provided by the WRF model for the CTRL run (9 km spacing). Taken from Giannakopoulou and Toumi (2012).

conditions for the fine-grid domains, on which we can more reasonably capture the details of the small-scale atmospheric dynamics (e.g. sea/land breezes) that respond most closely to the surface forcing. Ideally, one would like, for maximum effect, to conduct these experiments with the higher horizontal resolution of 3 or 1 km; fine resolution allows for detailed treatment of the physics, topography and vegetation. However, these fine simulations are computationally expensive and may hide information that develops only over the long periods of time and the large domains that were selected for this study.

Within the WRF model, the vertical mixing and diffusion were performed only by the planetary boundary layer (PBL) scheme. For these experiments, the Quasi-Normal Scale Elimination (QNSE) boundary layer scheme was added (Sukoriansky *et al.*, 2006). This scheme was selected because of its computational efficiency and its capability to realistically represent the boundary layer structure in stable atmospheric conditions. The QNSE Monin-Obukhov similarity theory (Sukoriansky *et al.*, 2006) for the surface-layer option was tied to this particular PBL scheme in order to calculate friction velocities and exchange coefficients. In addition, cumulus physics for deep and shallow (non-precipitating) convection was modelled with the Kain-Fritsch scheme (Kain, 2004). However, the cumulus parameterisation was turned off in the fine grid spacing selected for these simulations. Theoretically, it is only valid for spatial resolutions greater than 10 km (Skamarock *et al.*, 2008). We assume that at 9 km updrafts may be sufficiently resolved to provide the convective vertical transports. It is worth noting that although different quantitative

Table 6.2: Modified IGBP land-cover classes observed in the Nile Delta and its surrounding states, and their class description after Giri *et al.* (2005).

Modified IGBP classes	**Description**
Cropland (class 12)	Lands covered with temporary crops followed by a bare soil and harvest period mosaic lands.
Urban/built-up (class 13)	Land covered by buildings and other man-made structures.
Barren/Sparsely Vegetated (class 16)	Lands with exposed soil, sand, rocks, or snow. Never has more than 10% vegetated cover during any time of the year.
Water (class 17)	Rivers, reservoirs, lakes, seas and oceans. Fresh or salt water bodies.

results would likely be obtained with the convection scheme on, the overall results are not impacted. For radiation, we selected the RRTM (Rapid Radiative Transfer Model) longwave scheme developed by Mlawer *et al.* (1997) and the Dudhia shortwave scheme (Dudhia, 1989) because of their computational efficiency. Microphysics was modelled using the WRF Single Moment (WSM) 3-class scheme, which is a simple and efficient microphysics scheme suitable for mesoscale grid sizes (Hong *et al.*, 2004).

The Noah land surface model (LSM) was chosen to simulate soil moisture and temperature and canopy moisture (Chen and Dudhia, 2001). It is a four-layer soil temperature and moisture model that provides the surface fluxes (reflected shortwave radiation, emitted longwave radiation, momentum, latent and sensible heat fluxes) required by the PBL scheme. For vegetation and land-use classifications, the Noah LSM was configured to use the new IGBP (International Geosphere-Biosphere Programme) MODIS (MODerate resolution Imaging Spectroradiometer) 20-category land-use dataset with monthly updated vegetation fraction, surface albedo and emissivity (Giri *et al.*, 2005). The MODIS land-use classification was used to interpolate the topography, land-cover and land-water masked fields with the appropriate spatial resolution for each modelling domain (10 minutes, 2 minutes, and 30 seconds resolution for d01, d02 and d03, respectively). The major IGBP land-cover classes observed over the 9 km modelling domain are: cropland, urban, barren vegetated and water (see Table 6.2). The soil effects were provided by a 16-category soil dataset which took into account the root zone, soil drainage and runoff. The dominant present-day vegetation and soil types over the 9 km spacing are represented in Figure 6.9. It is worth noting that accurate identification of the vegetation and soil types is essential for estimating PET. In the Noah LSM, the PET was calculated by a diurnally varying Penman-based energy balance approach of Mahrt and Ek (1984) that reduces the influence of stability by using the aerodynamic resistance (Mahrt and Ek, 1984; Chen and Dudhia, 2001).

The model configuration described above represents one of the most common land surface, radiation, cumulus and microphysics configurations used by the WRF community (e.g. Storm *et al.*, 2009; Bollasina and Nigam, 2011). Several tests were conducted prior to the final simulations to investigate the sensitivity of the model's performance to the choice of surface-layer and PBL parameterization schemes. The setup described above was found to produce more realistic representation of the present-day Nile Delta climate than any other model configuration.

6.5.2 Experiments

In order to simulate the effects of the pre-historic and present-day Nile Delta land-cover on the local climate, desertification (DES) experiments were conducted for comparison with control (CTRL) runs. For the winter months, the CTRL experiment was run continuously from 1 December 2007 through 29 February 2008 (DJF). For the summer months, the CTRL experiment was run from 1 June 2008 through 31 August 2008 (JJA). The desert conditions were prescribed by changing the present-day Nile Delta landscape [approximately 80 % of the vegetation type is cropland (class 12)] to barren/sparsely vegetated land (class 16) with sandy soils (see Figure 6.9). Correspondingly, the surface albedo was increased, roughness length and vegetation cover were reduced and several other parameters [e.g. leaf area index (LAI), emissivity, vegetation fraction, root depth, stomatal resistance] in the Noah LSM were modified too (see Table 6.3). As shown in Table 6.3, barren vegetated land (class 16) was characterised by an increased albedo (equal to 0.38), considerably reduced LAI (that ranges from 0.1 to 0.75) and slightly decreased emissivity (equal to 0.9) and roughness length (equal to 0.01). Since the aforementioned land surface parameters were altered to reflect the pre-historic desert conditions, we initialised the land surface state of the DES experiments, and their soil moisture, using a short spin-up period of 48 hours. A simplification was included in the DES experiments, as the modified surface albedo was assumed not to vary monthly. The surface energy budget equations, the initial temperature and wind profiles were left unmodified for the DES experiments. That created some instability in the beginning of the simulations to which the model adjusted during the aforementioned 48 hours.

The initial and lateral boundary conditions were provided by ERA-Interim re-analysis data produced by the European Centre for Medium-Range Weather Forecasts (ECMWF). The re-analysis project covers the period from 1979 to present, has a spectral T255

Table 6.3: Land surface parameters and their values for the dominant vegetation types observed in the Nile Delta and its surrounding states (WRF model, Version 3.2.1).

Land surface parameters	**Cropland (class 12)**	**Urban (class 13)**	**Barren (class 16)**	**Water (class 17)**
Surface albedo	0.17 - 0.23	0.15	0.38	0.08
Leaf area index	1.56 - 5.68	1.0	0.10 - 0.75	0.01
Emissivity	0.92 - 0.985	0.88	0.90	0.98
Roughness length	0.05 - 0.15	0.5	0.01	0.0001

horizontal resolution (around 79 km spacing on a N80 reduced Gaussian grid) and 60 vertical model levels (Dee *et al.*, 2011). The data with temporal resolution of 6 hours are available from the British Atmospheric Data Centre (BADC) on a reduced Gaussian grid. Finally, because the purpose of this study was to perform the sensitivity experiments rather than to keep the simulations close to the aforementioned re-analyses, the four-dimensional data assimilation (FDDA) was not used.

6.6 Validation of the WRF model

To evaluate the WRF model results, basic surface meteorological variables from the CTRL runs are compared with ground based measurement data obtained from the NOAA (National Oceanic and Atmospheric Administration) Satellite and Information Service (available at http://www.ncdc.noaa.gov/cgi-bin/res40.pl?page=gsod.html). Daily averages of several surface locations that represent urban, coastal and rural (with dominant vegetation types: cropland and barren) low elevation areas across the 9 km WRF modelling domain are compared for both 2007/2008 DJF and 2008 JJA months. In particular, daily measurements of mean and maximum temperature (at 2 m), mean and maximum wind speed (at 10 m), mean sea level pressure, and mean 2 m dewpoint temperature obtained from the NOAA Satellite and Information Service for ten weather stations in the Nile Delta area, during the 2007/2008 winter and 2008 summer months, are used for testing the performance of the WRF model. The characteristics of the weather stations are shown in Table 6.4 and the locations of the stations are shown in Figure 6.8.

As an example, the time evolution of daily averaged surface temperatures (°C) and wind speeds (m s^{-1}) as simulated with the WRF model and obtained from NOAA is shown in Figure 6.10 for two representative weather stations. The simulation results from the CTRL experiments for the 2007/2008 winter months (DJF) and 2008 summer months

Table 6.4: Characteristics of ten weather stations in the Nile Delta area and averages of mean (T) temperature (°C) and mean (U) wind speed (m s^{-1}) for the 2007/2008 DJF winter months (in black) and 2008 JJA summer months (in red).

Weather Stations	**Lat(°N)**	**Long(°E)**	**Elev.(m)**	T**(°C)**	U**(m s^{-1})**
Dabaa (623090)	31.01	28.43	18	14.67/ 26.71	3.57/2.95
Alexandria (623180)	31.16	29.93	7	14.34/27.29	3.63/4.20
Baltim (623250)	31.55	31.1	2	14.53/27.13	2.18/3.00
Port-Said/ El Gamil (623320)	31.28	32.23	6	15.11/27.31	4.69/4.71
El Arish (623370)	31.08	33.81	32	12.49/26.89	2.29/1.95
Borg El Arab Int. (623601)	30.91	29.68	54	13.07/26.32	4.56/5.08
Cairo airport (623660)	30.1	31.4	74	14.33/29.63	3.23/3.42
Ismailia (624400)	30.6	32.25	13	13.27/28.72	3.45/4.05
Nekhel (624520)	29.91	33.73	403	8.35/26.80	3.25/3.45
Ras Sedr (624550)	29.58	32.71	16	14.64/30.32	2.69/3.83
Average				**13.48/27.71**	**3.36/3.66**

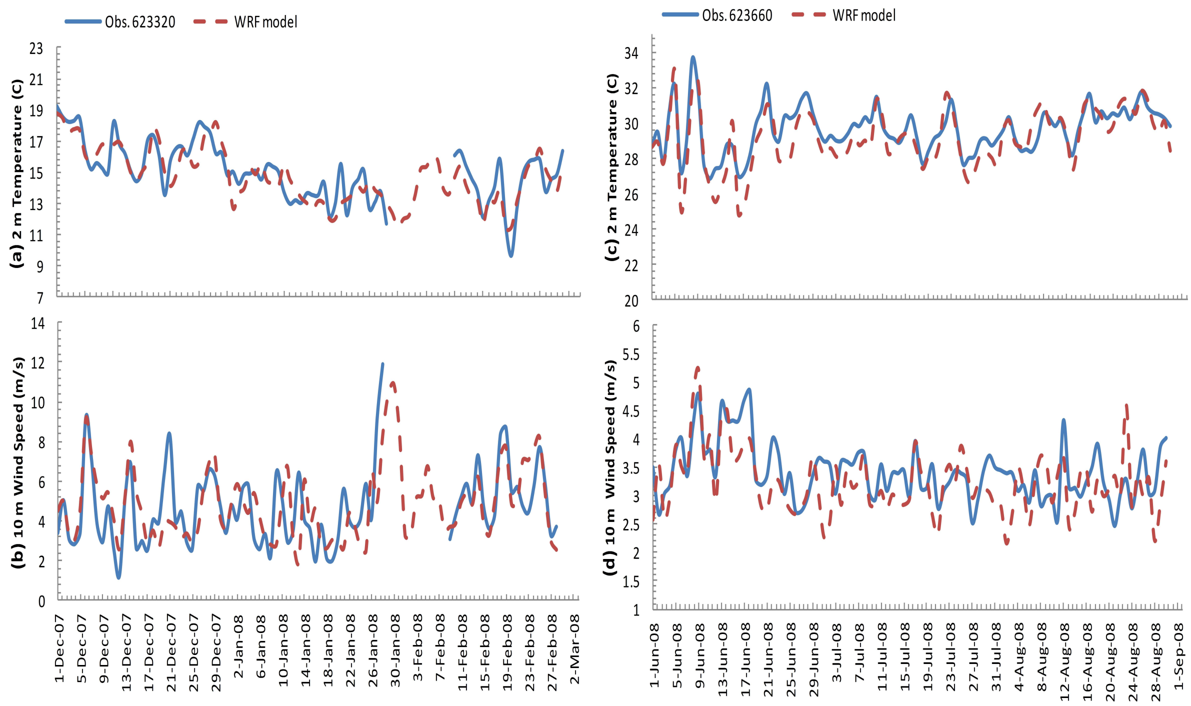

FIGURE 6.10: CTRL (9 km spacing) simulation results (dashed curve) versus station data (solid curve). Daily average (a) 2 m temperature (°C) and (b) 10 m wind speed (m s^{-1}) for the 2007/2008 DJF months at lat: 31.28 °N & long: 32.23 °E (station number: 623320, Port Said/ El Gamil). (c), (d) same as (a), (b) except for 2008 JJA months at lat: 30.1 °N & long: 31.4 °E (station number: 623660, Cairo airport).

(JJA) are compared with the Port Said/ El Gamil station data (latitude: 31.28 °N and longitude: 32.23 °E) and the Cairo airport station data (latitude: 30.1 °N and longitude: 31.4 °E), respectively. The simulation results are in exceptionally good agreement with the observations, especially during the winter months over Port Said. The WRF model tends to slightly underestimate the surface temperatures in the dry season, probably because of the variable degree of data uncertainty across stations. The coarse (9 km) horizontal resolution that is chosen for this study and the lack of higher grid resolution (e.g. of the order of 3 km) can also create additional inaccuracies when modelling near-surface temperatures. Maximum temperature is about 34 °C in the dry season over Cairo and 19 °C in the wet season over Port Said. During the JJA months, the day by day variation of surface temperature is higher than the seasonal variation. Minor surface wind speed differences between the simulation results and the station data also are observed for both wet and dry months. The surface winds are strong during winter over Port Said (maximum velocity of about 12 m s^{-1}) and the day by day variation of wind speed is higher than the seasonal variation. During the summer, in Cairo the maximum wind speed is about 4.5 m s^{-1} (much lower than the one that is observed over Port Said during the winter) possibly because of the increased roughness length of the urban area. In

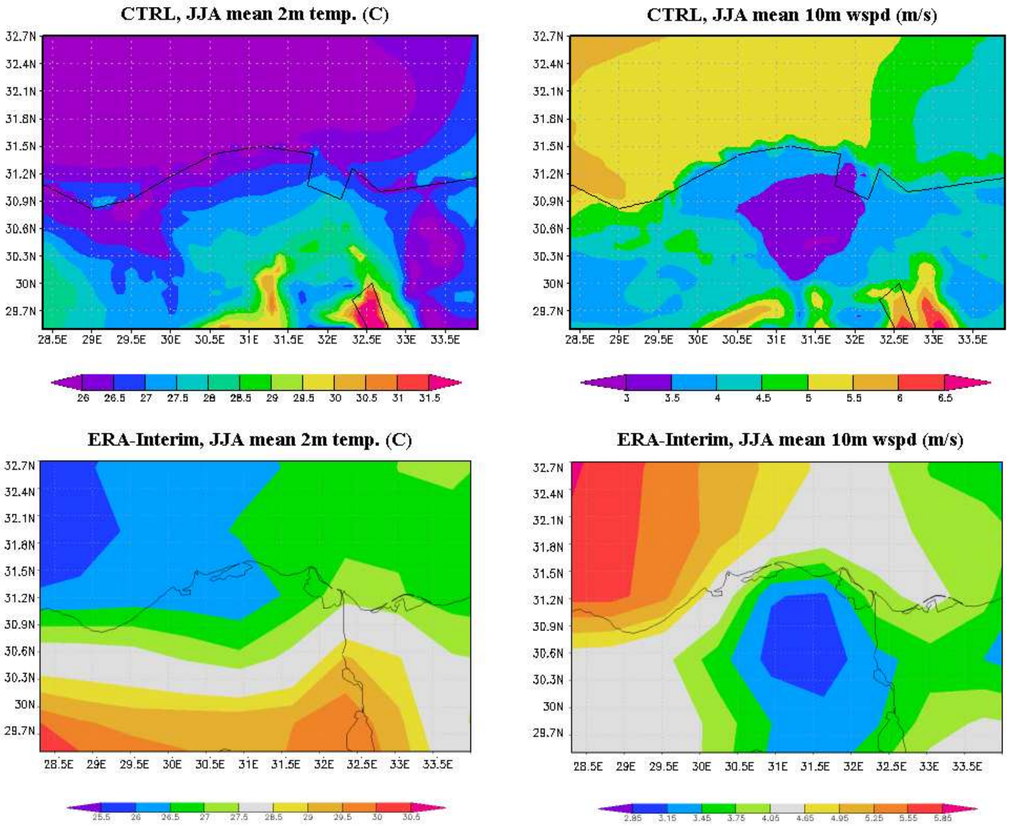

FIGURE 6.11: The 2008 mean seasonal JJA surface temperature (°C) and wind speed (m s^{-1}): (1st row) WRF model CTRL run (9 km spacing), (2nd row) ERA-Interim re-analysis data.

average, for the winter DJF months, the model shows decreased temperatures by 0.22 °C and weaker winds by 0.03 m s^{-1}. For the summer JJA months, the model underestimates the daily averaged temperatures by 0.47 °C and the wind speeds by 0.2 m s^{-1}.

As evident from Table 6.4, the average (of the ten weather stations) winter temperature is 13.48 °C and the average summer temperature is 27.71 °C, in agreement with the climatological analysis of section 6.3 as depicted by various datasets (ERA-40, ERA-Interim and NCEP/NCAR) and in line with the Bolle's (2003) observations as presented in section 6.2. The performance of the WRF model in simulating the mean wintertime (DJF) and summertime (JJA) climate in the Nile Delta is also evaluated against the ERA-Interim re-analysis data. As an example, Figure 6.11 compares the simulated 2008 seasonal JJA mean surface temperature and wind speed with the aforesaid re-analysis data. The examined area extends between latitudes 29.5 °N and 32.7 °N, and longitudes 28.3 °E and 34 °E. The CTRL run realistically simulates the main features of the aforementioned variables, which are in reasonable agreement with the re-analysis over most of the domain. In both CTRL run and re-analysis data, the sea surface temperatures (SST) vary from 25.5 °C to 27 °C, the warmer temperatures in the Nile Delta range from 26 °C

TABLE 6.5: Mean, standard deviation and correlation coefficient of the 2 metre mean (T) and maximum (T_{max}) temperature (°C), 10 metre mean (U) and maximum (U_{max}) wind speed (m s^{-1}), 2 metre (DEW) dewpoint temperature (°C) and mean (SLP) sea level pressure (mbar) differences between the station data and the DJF winter WRF simulation.

	T(°C)	T_{max}(°C)	U(m s^{-1})	U_{max}(m s^{-1})	DEW(°C)	SLP(mbar)
Mean	1.89	2.14	-0.75	-0.24	1.18	-1.53
Standard Deviation	1.31	1.47	1.14	1.71	2.64	1.27
Correlation Coefficient	0.77	0.83	0.79	0.72	0.67	0.96

along the coast to 30.5 °C inland, and the minimum wind speed is about 3 m s^{-1} between latitudes 30 °N and 31.2 °N. Therefore, the model captures the land–sea temperature contrasts and the decrease in wind speeds (due to friction) over the greater area of the Nile Delta. In general, the seasonal cycles of surface temperature and wind speed are well reproduced by the WRF model, giving confidence to the comparison of the land-use sensitivity experiments.

In order to estimate the variability of the WRF simulations, some basic statistics are provided in Tables 6.5 and 6.6 for the 2007/2008 DJF winter and 2008 JJA summer months, respectively. In particular, mean differences of basic meteorological parameters (e.g. mean and maximum near surface temperature and wind speed, mean sea level pressure and 2 m dewpoint temperature), standard deviation of the differences and correlation coefficients between the station data and the WRF runs are included in Tables 6.5 and 6.6. Initially, the daily differences between the station data and the WRF simulations were calculated for all weather stations of Table 6.4. Then the mean difference and the standard deviation of the difference were computed. Finally, the average of the means and standard deviations of the ten weather stations was calculated. It is worth noting that we expect that a very small percent of random errors will remain in the summary of the daily data. Therefore, the results of the validation of the WRF model runs against this dataset should be interpreted with caution. In order to compare the measurements more objectively the correlation between the WRF results and the station observations has been calculated for these ten weather stations.

In order to obtain general insight in the model performance it is common practice to look at the verification of the mean sea level pressure, since this parameter is slowly varying and rather independent on local conditions. In contrast typical boundary layer parameters like 10 m wind and 2 m temperature are influenced by local conditions. For

TABLE 6.6: Mean, standard deviation and correlation coefficient of the 2 metre mean (T) and maximum (T_{max}) temperature (°C), 10 metre mean (U) and maximum (U_{max}) wind speed (m s^{-1}), 2 metre (DEW) dewpoint temperature (°C) and mean (SLP) sea level pressure (mbar) differences between the station data and the JJA summer WRF simulation.

	T(°C)	T_{max}(°C)	U(m s^{-1})	U_{max}(m s^{-1})	DEW(°C)	SLP(mbar)
Mean	1.32	1.37	-0.73	-1.35	0.62	-0.44
Standard Deviation	0.79	1.19	0.81	1.43	1.73	0.74
Correlation Coefficient	0.83	0.78	0.53	0.29	0.70	0.95

both winter and summer months, it seems that the WRF model underestimates the mean and maximum near surface temperatures and dewpoint temperatures and slightly overestimates the mean and maximum wind speeds and mean sea level pressures (see Tables 6.5 and 6.6). It is also apparent that the standard deviation (STD) is smaller for all meteorological parameters during JJA than during DJF. These reduced standard deviations indicate that the near-surface parameters became less variable in these ten weather stations in the Nile Delta area during the hot and dry summer months.

6.7 Simulation Results

In Figure 6.12, results from the CTRL run (9 km horizontal grid spacing) are used to show the potential of the model to capture the atmospheric circulation brought by the European and North African trade winds during the winter months. As detailed in Figure 6.12(a), the flow over the eastern MS has a north/northwesterly direction, which results from the maritime air masses that cross eastern MS from Northwest Europe. Over land, the west/southwesterly direction is connected to the southwesterly flow along the North African coast, which is frequent during winter (Dayan, 1986). This flow regime is weakened in regions within the vegetated Nile Delta and in urban areas, such as Alexandria (latitude: 31.13 °N, longitude: 29.58 °E) and Cairo (latitude: 30.2 °N, longitude: 31.21 °E), possibly due to friction. A strong land–sea differential heating is marked during the wet season, with surface temperatures from 9 °C to 12 °C over the Nile Delta and 17 °C over the eastern MS (see Figure 6.12(b)). Interestingly, the CTRL run also predicts a zonal temperature gradient between longitudes 29 °E and 33 °E because of the different vegetation coverage; the vegetated Nile Delta is surrounded by desert landmass.

During the summer JJA months, the dominant synoptic pattern is mostly charac-

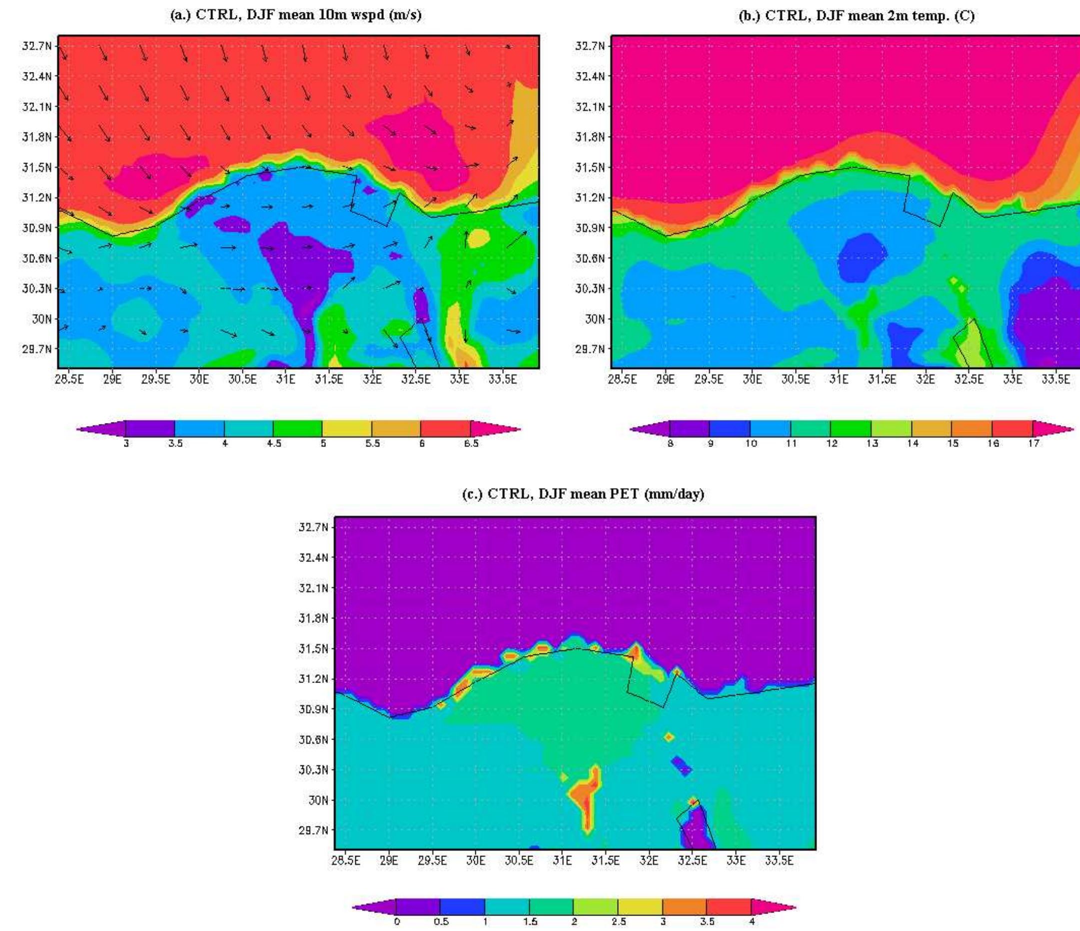

FIGURE 6.12: Mean seasonal DJF (a) surface wind speed (m s^{-1}), (b) surface temperature (°C), and (c) PET (mm d^{-1}) for the CTRL run (9 km spacing). Taken from Giannakopoulou and Toumi (2012).

terised by northwesterly winds from Northwest Europe (Figure 6.13(a)). According to El-Askary *et al.* (2009), the strong north-to-south temperature gradient between the eastern Mediterranean water bodies and the Nile Delta enhances these steady winds to flow from northwest (see section 6.2). This is more pronounced during the daytime and causes the winds to penetrate over the Nile Delta. It is evident from Figure 6.13(a) that friction reduces the wind speed in the vegetated Nile Delta, with minimum wind speed of the order of 3 m s^{-1} near latitude 30.5 °N and longitude 31.5 °E. As seen in Figure 6.13(b), the aforesaid wind system lowers the temperatures along the shoreline. The average JJA temperatures range from 25 °C in the eastern MS to approximately 30.5 °C over Cairo (Figure 6.13(b)). The high temperatures in Cairo are possibly a result of the urbanisation effects. Urbanisation over Cairo is expected to have significant impacts on surface temperature, wind speed and PET through changes in albedo, surface roughness and soil moisture. The urban class in the CTRL experiments is defined using a surface albedo value of 0.15 and roughness length value of 0.5 (see Table 6.3). A decrease in albedo because of urbanisation leads to more solar radiation absorption by the ground and, thus,

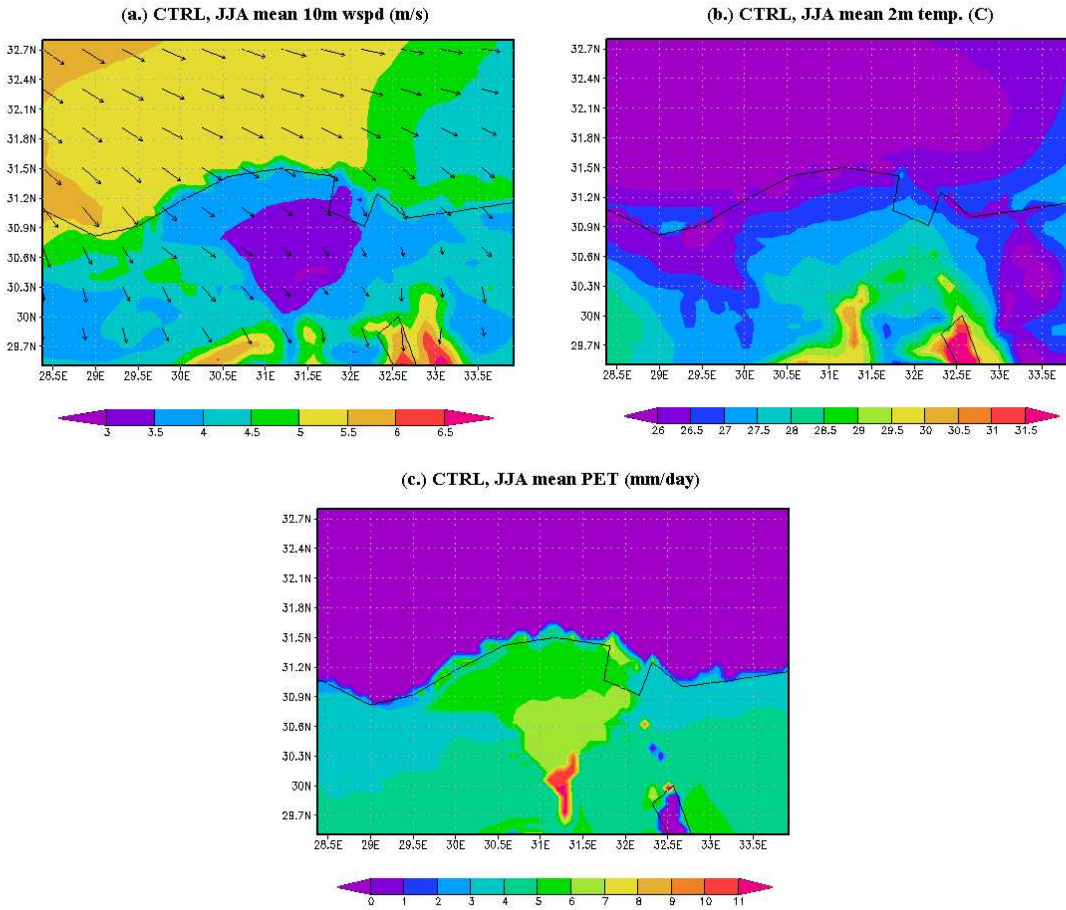

FIGURE 6.13: Mean seasonal JJA (a) surface wind speed (m s^{-1}), (b) surface temperature (°C), and (c) PET (mm d^{-1}) for the CTRL run (9 km spacing).

to surface warming. Therefore, urbanisation is accompanied by a lower surface albedo and an increased surface roughness and net shortwave radiation, which contribute to the well-defined urban warming and wind speed reduction.

Overall, the differential heating between the eastern MS and the Nile Delta is marked in both the winter and summer seasons. Strong seasonal variability (cold winter versus hot summer) is also one of the main characteristics observed for the climate in the Nile Delta and is consistent with the study of Bolle (2003) for northern Egypt (introduced in section 6.2).

6.7.1 Factors influencing PET

As discussed in section 2.5, different definitions and calculation methods exist to study PET. In the present study, PET is defined as the amount of water that can potentially transpire and evaporate from a vegetated surface without constraints other than the atmospheric demand (Feddema, 1999; Lu *et al.*, 2005). Note that in the CTRL experiments the vegetated surface is mostly a reference crop with particular crop height, a fixed surface resistance and a fixed albedo. Therefore, PET is a representation of the maximum water loss to the atmosphere from a reference crop without restrictions other than the atmospheric demand.

In this study, PET is calculated by the diurnally varying Penman-based energy balance approach of Mahrt and Ek (1984), which reduces the influence of stability by using a stability-dependent aerodynamic resistance. Mahrt and Ek (1984) used the Penman-Monteith equation (equation 2.21) in which the aerodynamic resistance is sensitive to atmospheric stability with the following relationship: $r_a = 1/c_q u$, where c_q is the exchange coefficient for moisture and u is the atmospheric wind speed. The exchange coefficient for moisture has a different form for stable and unstable cases and is expressed in terms of a bulk Richardson (Ri) number (Mahrt and Ek, 1984). The influence of vegetation properties is included through a plant coefficient (usually is a unitless fraction receiving values between 0 and 1), which is estimated using a canopy resistance factor and a surface exchange coefficient for heat and moisture. It is worth noting that the Mahrt and Ek (1984) PET approach has great dependence on net radiation.

Although it is known that temperature, wind speed, radiation and moisture can increase evapotranspiration by plants, these variables need to be quantified in order to estimate the atmospheric demand for evapotranspiration from the Nile Delta region. In this study, the measure of PET shows the maximum possible water loss to the atmosphere from the present-day and pre-historic Nile Delta. Figure 6.12(c) and Figure 6.13(c) map the seasonal wintertime (DJF) and summertime (JJA) PET, respectively. As evident from the Figures 6.12(c) and 6.13(c), PET is greater in the vegetated and built-up areas of the Nile Delta than in the surrounding deserts. Vegetation (cropland) and built-up areas have a lower albedo than that of the surrounding deserts (see Table 6.3) and so absorb more solar radiation. The agricultural and urban areas can also affect other biophysical parameters, including the roughness length, which affects the exchange of mass and energy between the land surface and the boundary layer, and the amount of water recycled to the atmosphere through evaporation and transpiration. We can assume that the urban and vegetated regions increase PET because of the changes in the surface albedo, LAI and roughness length. These changes in the land surface parameters alter the net radiation which can directly affect PET. Also, some level of relationship is found to exist between land surface parameters, heat island and urban/vegetated land difference in PET; more PET is observed in the urban than in the rural areas. This result is in agreement with the findings of Adebayo (1991). In summer, an expected increase in PET (compare with the winter) also is simulated due to the higher levels of solar radiation and the warmer temperatures, which provide the energy for evaporation.

Significant differences between the pre-historic and present-day land-covers are apparent from Figures 6.14 and 6.15. Figure 6.14 (Figure 6.15) maps the seasonal DJF (JJA)

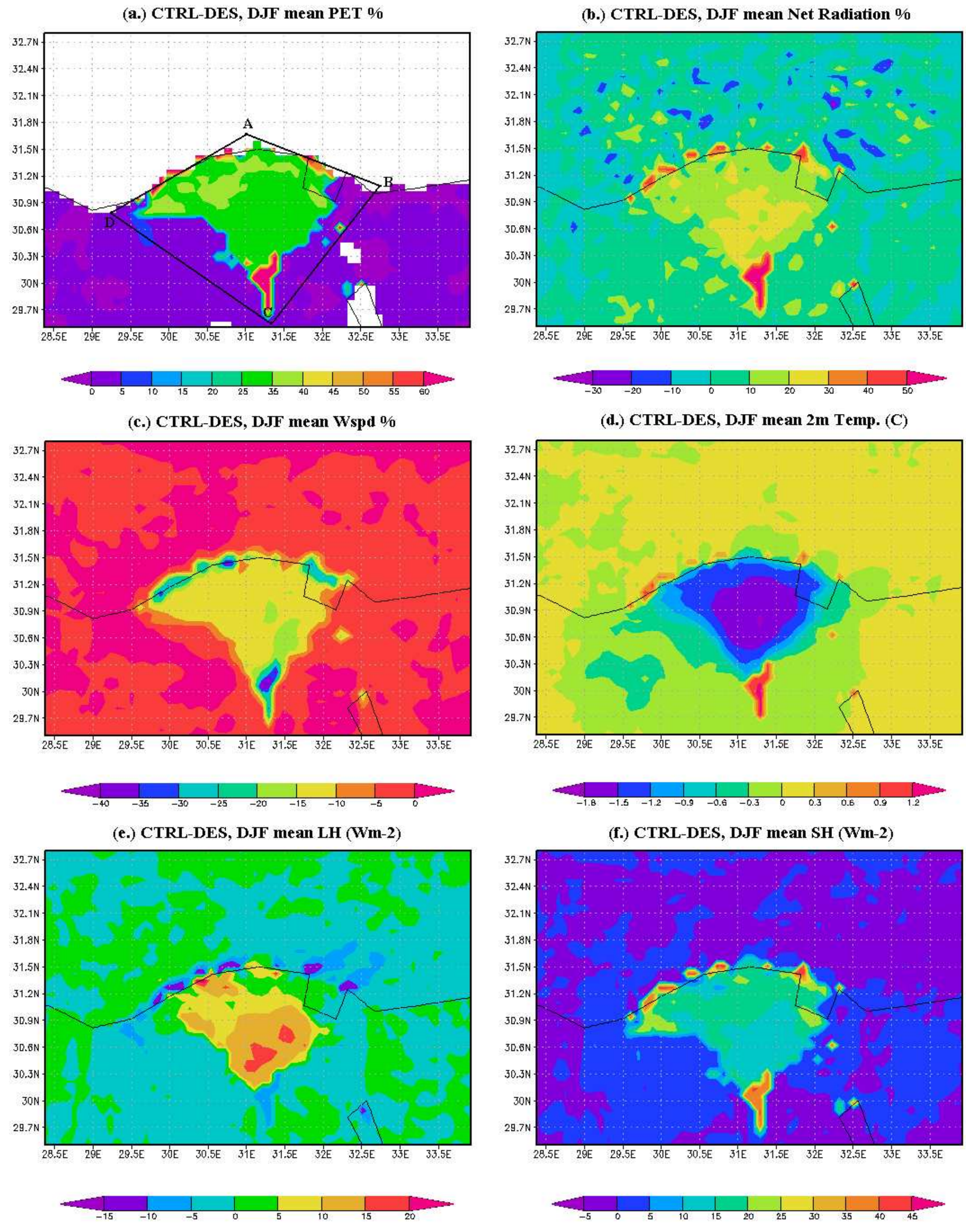

FIGURE 6.14: Mean seasonal DJF differences [present-day minus pre-historic land-cover (CTRL-DES)] for (a) PET (%), (b) net radiation (%), (c) surface wind speed (%), (d) surface temperature (°C), (e) latent and (f) sensible heat fluxes (W m^{-2}). In (a), the box ABCD denotes the region for the spatial averaging of meteorological variables. Taken from Giannakopoulou and Toumi (2012).

present-day minus pre-historic land-cover (CTRL-DES) differences in PET, net radiation, energy fluxes (latent and sensible), surface temperature and wind speed for the 9 km spacing. It is evident from the Figure 6.14 that the Nile Delta greening induces significant local changes for all variables. The present-day Nile Delta land-cover has a lower albedo and increased LAI, roughness length and emissivity compared with the pre-historic desert. The mechanisms that link these parameters to the changes in surface temperature and wind speed are quite straightforward. The present-day vegetation causes local surface cooling (by about 1.8 °C) and decreases the surface wind speeds (by approximately 15 %) compared with the past desert conditions [see Figure 6.14(c, d)]. The decreased wind speeds over the agricultural regions of the Nile Delta are mainly caused by an increase in the roughness length. The increased roughness length reduces the aerodynamic resistance, which in turn increases latent and sensible heat fluxes by approximately 10-20 % (see Figure 6.14(e, f)). Note that the changes in latent heat flux are mainly caused by changes in parameter values, such as the increased surface roughness and LAI and not by changes in precipitation which are negligible. Thus, more heat and moisture are transferred upwards into the air, resulting in lower surface temperatures especially at night. As will be shown later, the local cooling over the agricultural Nile Delta is mainly a result of decreases in the nighttime temperatures and is coincident with the changes in latent and sensible heat fluxes.

According to Han *et al.* (2009), changes in PET can be related to changes in meteorological variables such as air temperature, radiation, wind speed and relative humidity. A decrease in surface temperature and wind speed by itself should decrease PET. However, perhaps surprisingly, PET increases by approximately 25-35 % (Figure 6.14(a)). Therefore, changes in temperature and velocity alone do not explain changes in PET.

During the wet season, the present-day Nile Delta albedo (cropland has low terrestrial albedo, which varies from 0.17 to 0.23) increases the solar radiation absorption by the ground, which in turn increases the net radiation by approximately 15-20 % (Figure 6.14(b)). This net radiation change drives the change in PET. A simple manipulation of the Penman-Monteith equation (partial differentiation, ϑ, of equation 2.21 that is provided in section 2.5) shows the PET to net radiation sensitivity:

$$\frac{\vartheta PET}{\vartheta R_N} = \frac{\Delta}{\lambda(\Delta + \gamma(1 + \frac{r_c}{r_a}))}, \tag{6.1}$$

where PET is in mm d^{-1}; R_N is the net radiation (MJ m^{-2} d^{-1}); Δ is the slope of the saturation vapour pressure-temperature curve (kPa °C-1); γ is the psychometric constant (kPa °C^{-1}); λ is the latent heat of vaporization (MJ kg^{-1}); r_c and r_a are the canopy and aerodynamic resistances (s m^{-1}), respectively. Substituting the above expression (equation 6.1) for our typical values we obtain that:

$$\frac{\vartheta PET}{\vartheta R_N} = 0.067 \frac{mm}{MJm^{-2}} \tag{6.2}$$

and

$$\frac{\Delta PET}{PET} \approx 2 \frac{\Delta R_N}{R_N} \tag{6.3}$$

so that the 33 % increase in PET in the Nile Delta agricultural area is indeed largely due to the 15-20 % increase in net radiation.

The seasonal JJA results are qualitatively similar to those of the DJF simulation studies. During the summer, after greening, PET shows a significant response in terms of an increase, while the local climate is subjected to a slight warming at the surface (see Figure 6.15(a, d)). The changes in surface temperature are associated with a slight increase in latent heat flux and a significant increase in sensible heat flux. The sensible and latent heat fluxes are generally enhanced because of the Nile Delta man-induced greening as the roughness length, LAI, surface albedo, stomatal resistance and depth of root zone are changed. The raise in evaporation, due to the increased Nile Delta vegetation coverage and the changed soil conditions, results in a small increase in latent heat flux. As the surface albedo is decreased at the same time, the input from net solar radiation at the surface is increased. This results in more sensible heat flux and, as a consequence, in a small increase in near surface temperature. In particular, the latent and sensible heat fluxes are increased by approximately 10-20 % and 30-70 %, respectively (see Figure 6.15(e, f)). In the CTRL run, in spite of the general temperature increase (higher temperatures by 0.3 °C in the vegetated Nile Delta and 2.1 °C in Cairo) and decrease in wind speed (up to 30 %), there has been an increasing PET in the agricultural Nile Delta by approximately 35-40 % (see Figure 6.15(a, c, d)). These PET changes are in line with the previously observed and discussed PET results for the wet season; PET has limited dependence on temperature and wind speed changes. As can be seen in Figure 6.15(b), the mean seasonally differences in net radiation suggest that the vegetated landscape has received about 15-20 % more radiation compared with the desertification Nile Delta because of a surface albedo decrease. This change in net radiation is the major climatic factor controlling the PET changes in agreement with the recent findings of Shaw and Riha (2011) and Nizinski *et al.* (2011).

It is worth noting that in both winter and summer months within the present-day Nile Delta region the urbanisation effects are evident. Most of the warming is generally consistent with the expansion of urban surfaces in Cairo and in the coastal areas of the Nile Delta. The built-up areas, with their darker-coloured roof structures and paving materials can absorb more incoming solar radiation compared to the pre-historic desert (and the

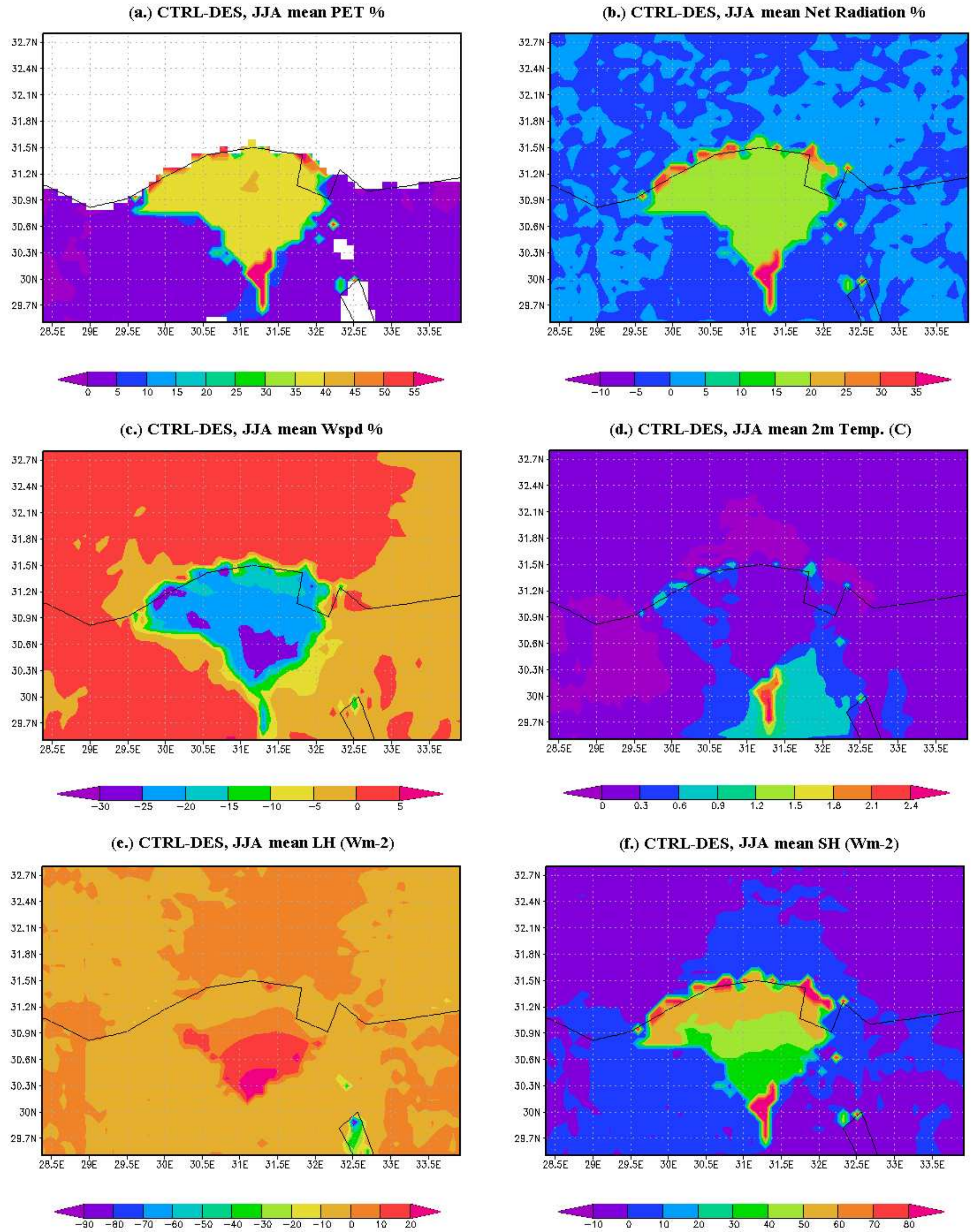

FIGURE 6.15: Mean seasonal JJA differences [present-day minus pre-historic land-cover (CTRL-DES)] for (a) PET (%), (b) net radiation (%), (c) surface wind speed (%), (d) surface temperature (°C), (e) latent and (f) sensible heat fluxes (W m^{-2}).

agricultural areas in the Nile Delta). The increase of urbanisation shifts the surface energy partitioning into less latent (about 10 % for both the DJF and JJA months) and more sensible (35-40 % for the DJF and 70 % for the JJA months) heat flux (see Figures 6.14(e, f) and 6.15(e, f)). Both of these effects contribute to the surface air temperature increase (0.9 °C for DJF and 2.1 °C for JJA months in Cairo). In general, modifications of land-cover that are relevant to the hydrological cycle (e.g. evaporation) are associated with changes of the latent heat flux, while modifications of the surface albedo result in changes of net radiation. Therefore, the significant lower albedo in the present-day built-up areas increases net radiation up to 50 % during winter and by approximately 35 % during summer (see Figures 6.14(b) and 6.15(b)). Subsequently, the increased net radiation enhances PET by approximately 55 % in both seasons over the present-day Cairo (Figures 6.14(a) and 6.15(a)). Note that the results of the desertification experiments are opposite in sign to those found in the greening and urban cases.

6.7.2 Factors influencing the surface energy budget

The mean DJF diurnal cycle of surface temperature, wind speed, energy fluxes, precipitation and PET for each of our experiments are shown in Figure 6.16.

Interestingly, inspection of the spatial average [over the ABCD box in Figure 6.14(a)] surface temperature shows that the variable in the CTRL run is characterised by a faster nighttime cooling rate compared with the rate of cooling simulated in the DES experiment (see Figure 6.16(b)). The larger daytime temperatures and the increased emissivity in the CTRL run contribute to this faster nighttime cooling in the vegetated Nile Delta. The darker-coloured vegetated Nile Delta absorbs more energy, gets warmer and emits more longwave (infrared) radiation than the pre-historic Nile Delta during the day (see Figure 6.16(e)). In order to confirm our assumption that the emissivity affects the rate of cooling, we conducted emissivity sensitivity experiments in which the emissivity values were set equal to 0.95 in the Nile Delta region for both the CTRL and DES experiments. Note that previously in the CTRL run the seasonally averaged emissivity for cropland was equal to 0.95 and in the DES experiment the seasonally averaged emissivity for barren vegetated land was equal to 0.9. Figure 6.17 shows the DJF seasonally averaged surface temperature for the emissivity sensitivity experiments (both CTRL and DES experiments with 0.95 emissivity) and for the DES experiment (emissivity equal to 0.9). By increasing emissivity in the desertification experiment, we expect to observe lower temperatures. As seen in Figure 6.17, the simulated nocturnal temperatures in the emissivity DES run tend to decrease faster than they do in the DES experiment. This result suggests that emissivity affects the nighttime cooling rate.

According to Wichansky *et al.* (2008), boundary layer variables such as surface rough-

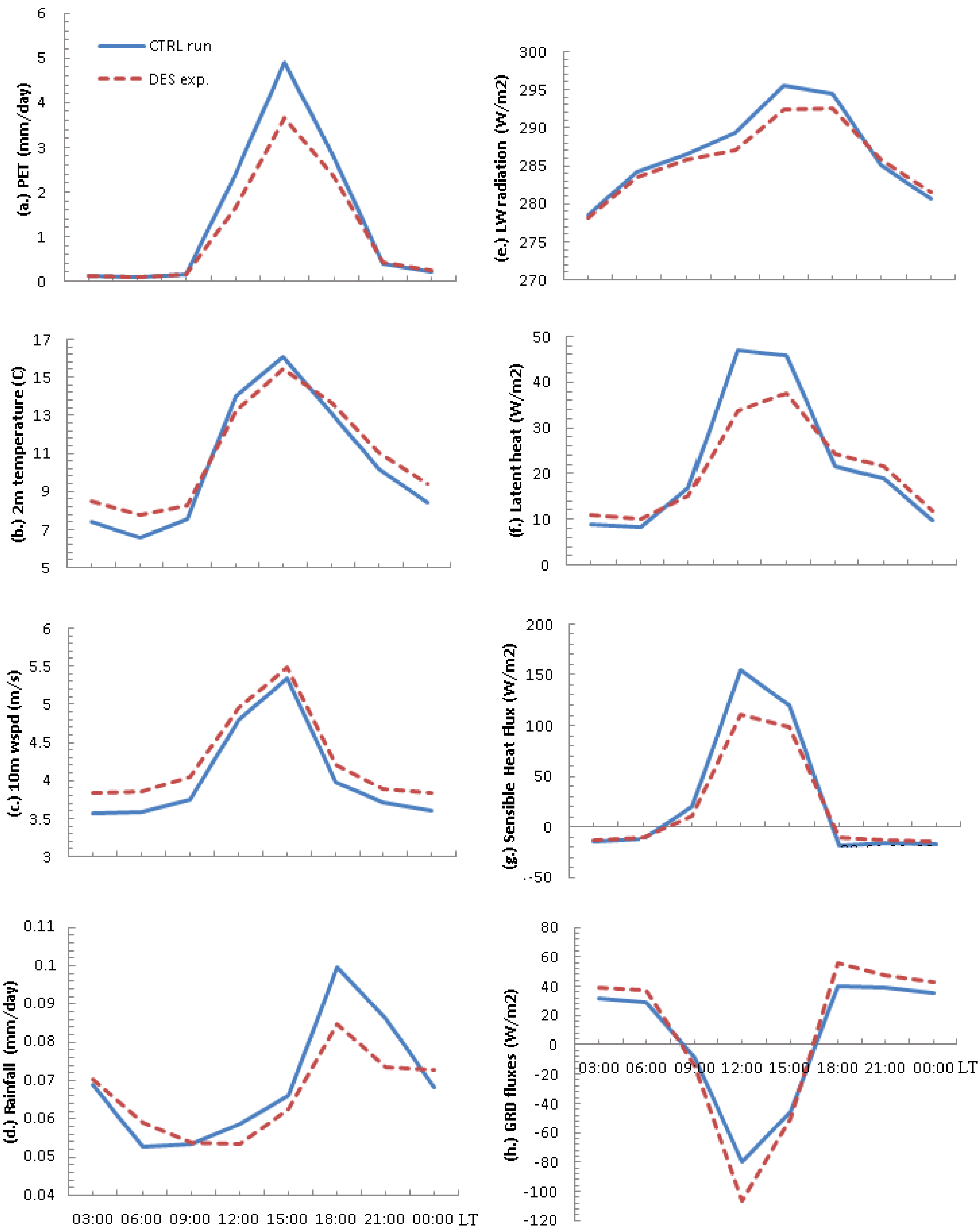

FIGURE 6.16: The diurnally averaged seasonally time series of mean DJF (a.) PET (mm d^{-1}), (b.) surface temperature (°C), (c.) wind speed (m s^{-1}), (d.) rainfall (mm d^{-1}), (e.) longwave radiation (W m^{-2}), (f) latent, (g.) sensible and (h.) ground heat fluxes (W m^{-2}) over the ABCD box in Figure 6.14(a). The solid and dashed curves are for the CTRL and DES experiments, respectively. The x axis represents the hour in local time (LT). Taken from Giannakopoulou and Toumi (2012).

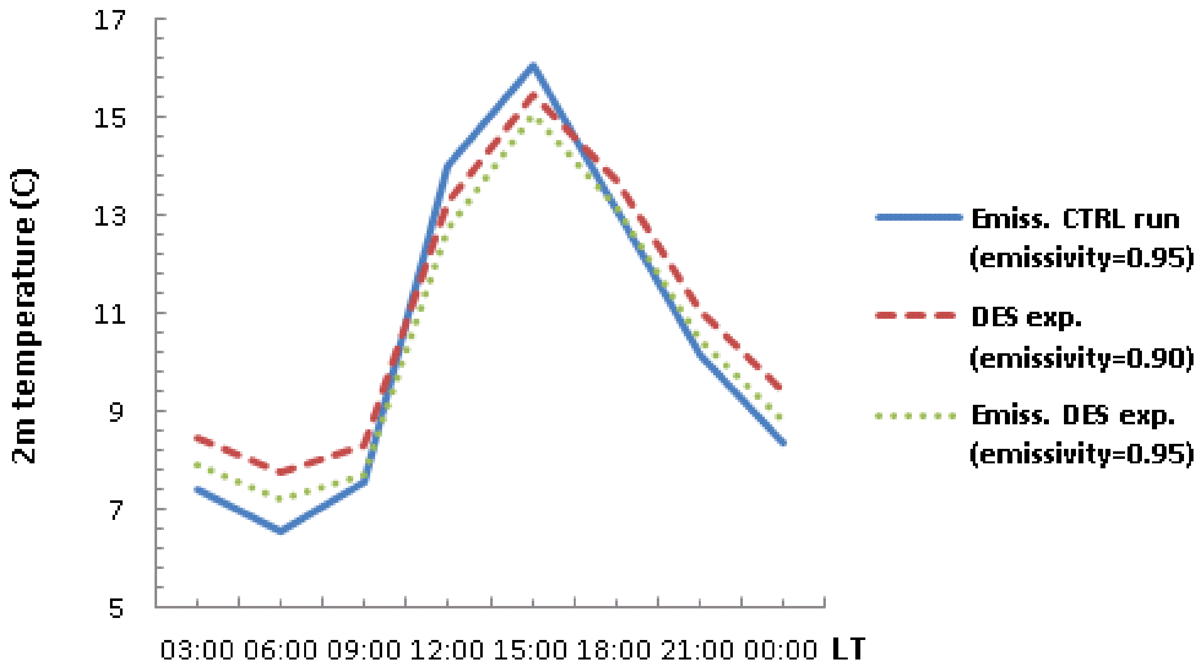

FIGURE 6.17: DJF seasonally averaged surface temperature (°C) over the Nile Delta [ABCD box in Figure 6.14(a)] versus time (LT). The solid and dotted curves are for the emissivity CTRL and DES experiments (emissivity = 0.95), respectively. The dashed line is for the DES experiment (emissivity = 0.90).

ness length, LAI, wind speed and soil heat capacity can also influence the nighttime temperatures. The modelling results indicate that, when the man-induced greening increases LAI, the daytime surface temperature has a slight increase, while the nocturnal surface temperature decreases significantly, which is consistent with the findings of Jin *et al.* (2010). It seems that the increased LAI enhances the upward sensible heat fluxes during daytime and, thus, increases the near-surface temperatures. According to Jin *et al.* (2010), the increased LAI and roughness length due to vegetation result in less stable near-surface boundary layers during the night. We can therefore assume that the evening temperature increase in the desertification Nile Delta results from the more stable PBL that restricts the downward sensible heat flux and keeps more energy near the surface.

During the day, solar radiation heats up the vegetated land more rapidly than the eastern MS (and the pre-historic Nile Delta), causing a horizontal temperature gradient between the land and the sea. The air over the agricultural Nile Delta heats up and, thus, expands more rapidly than the air over the sea. An area of surface low pressure develops over land in response to offshore flow at higher levels. Conversely, an area of high pressure develops over sea in response to the accumulation of air at higher levels. These areas of surface high and low pressure lead to a horizontal pressure gradient which generates a sea breeze. At nighttime the reverse process occurs and a land breeze develops

(Mostafaeipour, 2010). In the CTRL run the vegetated Nile Delta is warmer during the day and cooler at night than it is in the DES experiment (Figure 6.16(b)). These temperature differences between present-day and pre-historic Nile Delta result in stronger north-to-south temperature gradients, which in turn create stronger sea and land breezes that can also affect the rate of cooling.

The changes in the diurnal temperature range are an unexpected result from the sensitivity experiments (Figure 6.16(b)). The greening has influenced the simulated seasonally mean daily maximum and minimum temperatures. The difference between maximum and minimum temperatures in the CTRL run is about 9 °C, which is 3 °C more than those observed in the DES experiment. This result suggests that the man-made greening is associated with a larger diurnal temperature range. Over the Nile Delta the increase in vegetation coverage and the decreased albedo combine to increase evaporation during the day. According to Zhao and Pitman (2002), the high evaporation around noon, when the maximum temperature is reached, should suppress the temperatures, which create a reduction of the maximum temperature and, therefore, a reduction of the diurnal range. However, the Nile Delta greening results in a small increase of the maximum temperature and in a decrease of the minimum temperature, which in turn increase the magnitude of the diurnal range.

Figure 6.16 shows expected diurnal cycle of PET, wind speed and turbulent heat fluxes. During the day the present-day vegetation increases PET by approximately 1.5 mm d^{-1} (Figure 6.16(a)). This change is consistent with the increase in net radiation we have described earlier. In addition, there has been decrease in the surface wind speed over the diurnal cycle (Figure 6.16(c)) because of the increased roughness length and the decreased aerodynamic resistance, which also affect the sensible and latent heat fluxes. At the noontime, the maximum latent and sensible heat fluxes are increased by about 20 W m^{-2} and 50 W m^{-2}, respectively (Figure 6.16(f, g)). Therefore, more heat is transferred upwards into the air and more evaporation is taking place in the CTRL experiment because of the warmer and moister daytime surface.

After Pitman (2003), conceptual diagrams of the effects of greening on the local climate (Figures 2.8 and 2.9) are provided in chapter 2 (section 2.3). The Nile Delta greening causes a reduction in albedo, which in turn increases shortwave absorption by the ground, net radiation, latent and sensible heat fluxes. The increased turbulent fluxes tend to enhance water vapour and boundary layer warming (see Figure 6.18). Although the nighttime cooling is stronger in the CTRL run, the increased sensible heat fluxes result in atmospheric heating above the surface (Figure 6.18(a)); the daytime warmer surface in the control run transfers more heat upwards into the boundary layer. Figure 6.18 shows the vertical cross-section of the seasonal DJF average temperature and wind speed taken for the present-day minus pre-historic land-cover (CTRL-DES). The south-to-north cross-

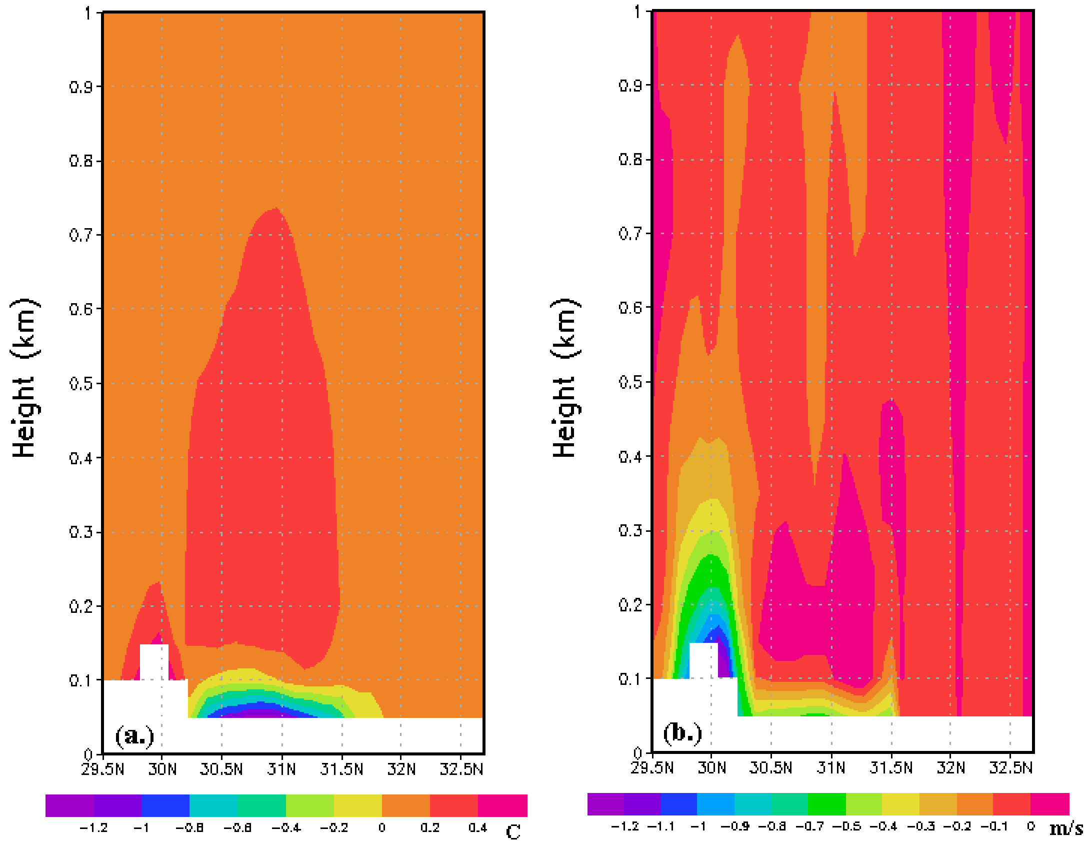

FIGURE 6.18: Vertical cross-section at longitude 31.3 °E extending from latitude 29.5 °N to 32.7 °N showing the mean seasonal (DJF) differences [present-day minus pre-historic land-cover (CTRL-DES)] for (a) air temperature (°C) and (b) wind speed (m s^{-1}) up to 1 km above sea level (9 km spacing). Blank areas appear where the WRF model provides AGL information.

section near 31.3 °E extends from 29.5 °N to 32.7 °N and prominent on this cross-section is the ABL warming and the decreased wind speeds near the surface due to the increased roughness length. The changes in surface temperature and moisture extend well into the atmosphere up to 700 m ASL and affect the boundary layer as well as the atmospheric circulation.

The increased water vapour and boundary layer warming cause an increase of the convective clouds, which in turn enhance the minimal Nile Delta rainfall during the daytime (see Figure 6.16(d)). The processes of evapotranspiration are closely related to the water found in soil moisture, which is dependent on a number of factors in addition to precipitation and evaporation. These factors are the soil type and depth, vegetation coverage and slope. Greening increases soil moisture and that in turn produces high evaporation, especially if the temperatures are significantly high during the day. The surface evaporation is also controlled by the energy fluxes and by the aerodynamic, stomatal and soil resistances. In the CTRL run the high roughness length and LAI and the low stomatal resistance of the present-day Nile Delta increase the evaporation rate during the daytime.

Thus, the atmosphere gains moisture from the underlying surface and, therefore, cause a further increase in rainfall. The latent heat flux differences between the CTRL and DES experiments in Figure 6.16(f) confirm our assumption of increasing evaporation due to the presence of the Nile Delta. However, it is evident that minor changes are observed in the minimal precipitation over the agricultural Nile Delta; during late afternoon, the maximum mean rainfall is approximately 0.1 mm d^{-1} for the CTRL run and 0.08 mm d^{-1} for the DES experiment (Figure 6.16(d)). It is worth noting that this result was not obtained in most of the afforestation/greening studies, which predict enhancement of the upward motions, moisture and, consequently, a large increase in rainfall (e.g. Xue, 1993). The minimal increase in precipitation over the present-day Nile Delta can suggest that there is no simple interaction between the water supply from the ground in the form of evapotranspiration and the return of that water to the land in the form of rain. It seems that large-scale systems have an impact on the amount of precipitation, which is in agreement with the latest study of Angelini *et al.* (2011).

During the day, the net radiation is a positive value allowing the surface to gain energy. As introduced in section 2.3, this energy is distributed over the sensible, latent and ground heat fluxes. During the daytime, the man-induced greening increases sensible and latent heat fluxes and reduces the heat that is conducted down into the subsurface (Figure 6.16(h)). In particular, during the day, more solar radiation is absorbed at the surface, and the ground heats up more rapidly in the agricultural Nile Delta. Initially, most of the heat is conducted down into the soil, but the sensible and latent heat fluxes dominate. Thus, more heat is primarily transferred to the air and more transpiration from the plants and more evaporation from the soil surface is observed. As a consequence, the subsurface is less heated by approximately 40 W m^{-2} in the CTRL run than in the DES experiment. This indicates that the less energy that had been stored in the subsurface during the day is conducted during the night toward the surface as less positive ground heat flux.

We can conclude that changes in the Nile Delta land-cover are not reflected by changes in rainfall, but are more evident in changes in the surface energy budget, temperature, wind speed and most importantly in PET. It is worth noting, that similar conclusions can also be made for the 2008 dry season.

6.7.3 Factors influencing storm events

The eastern Mediterranean is a region of great interest because of its cyclone development, its complex orography, and also its location between mid-latitudes and subtropics. As discussed in subsection 6.1.1, several studies have attempted to explain the origins of Mediterranean cyclones and their development (e.g. Mehta and Yang, 2008; Flocas *et al.*,

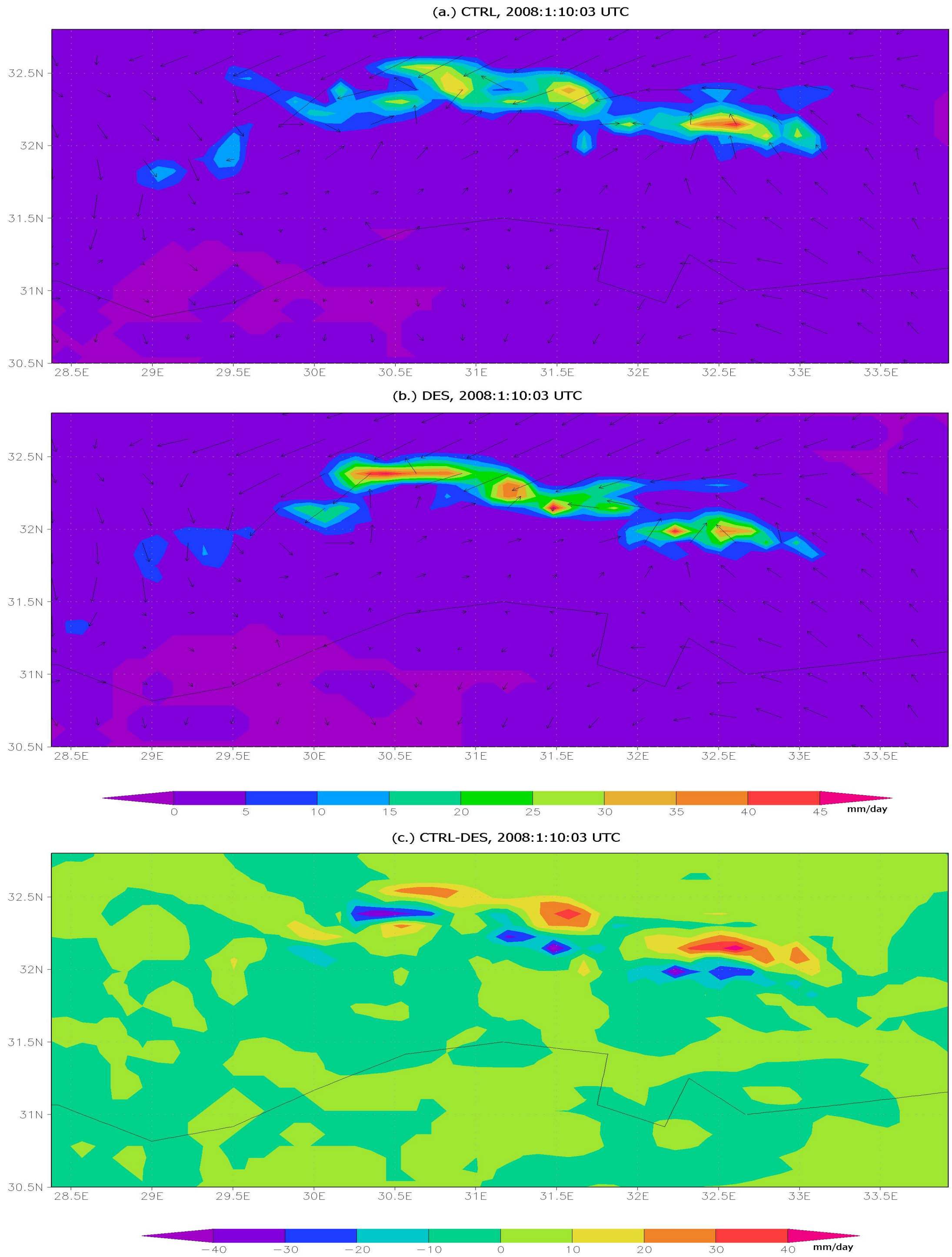

FIGURE 6.19: Storm event at 03:00 UTC on 10 January 2008 over eastern MS for the (a) CTRL run, (b) DES experiment and (c) (CTRL-DES) differences. The shaded contours indicate the amount of rainfall (mm d^{-1}) and the black wind barbs are the surface wind speed (m s^{-1}). Taken from Giannakopoulou and Toumi (2012).

2010; Katsafados *et al.*, 2011), but none of these examined the Nile Delta man-made greening effects on storm strength and position.

The birth, development and intensity of a deep rainy system over the eastern MS is investigated with the WRF model at the 9 km horizontal resolution. A winter storm event of 9-11 January 2008 was selected because of its strength and position (high frequency of severe cyclogenesis over the eastern MS). In order to analyse the synoptic conditions during the cyclone birth and development, the simulation results of the 81 km horizontal resolution modelling domain are also used. It seems that cyclogenesis started at 06:00 UTC on 9 January 2008 near the Libyan city of Benghazi with central mean surface pressure of approximately 986.4 mbar. In agreement with other simulation studies of deep Mediterranean storms (e.g. Katsafados *et al.*, 2011), the maximum absolute vorticity (30×10^{-5} s^{-1}) at 500 mbar was positioned prior to the surface low-pressure in the west/southwest. According to the Katsafados *et al.* (2011) study, this result is a strong indication of rapid baroclinic development. As mentioned in section 6.1, the cyclonic intense precipitation in the southern part of the eastern Mediterranean basin is mostly associated with cyclonic systems that start their development in the south-western regions of the MS, and then migrate to the east (Lionello *et al.*, 2006). Indeed, the rain system moved over the southern part of the eastern MS during an 18-hour period.

The most remarkable feature of this study is the response of this frontal system to the man-made greening. The rain system moves farther away from the Nile Delta coastlines. As an example, Figure 6.19 shows strong northerly/northeasterly winds and the storm event over the eastern MS (centred at latitude 32.3 °N and longitudes 29 °E - 33 °E) at 03:00 UTC on 10 January 2008 for both the CTRL and DES simulations. The maximum precipitation is approximately 40 mm d^{-1} in both experiments, but a clear decrease in rainfall close to the Nile Delta coast is observed with the present-day land-cover, representing shifts of the associated rain system (Figure 6.19(c)).

At night the Nile Delta cools faster than the eastern MS due to the differences in their specific heat capacity, resulting in a cooling of the immediate overlying air. Since the vegetated Nile Delta cools below that of the neighbouring SST, a temperature difference is established and lower pressures over the sea than that of the land are observed, setting up a land breeze. Therefore, winds move offshore along the pressure gradient as long as the north-easterly surface winds captured over the sea are not strong enough to oppose the land breeze (Figure 6.20(a)). The cold air from the land meets the warm air from the sea and enhances the convergence over the sea.

Figure 6.20 shows the vertical cross-section of the wind speed and air temperature taken for the present-day minus pre-historic land-cover (CTRL-DES) at 03:00 UTC on 10 January 2008. The south-to-north cross-section near 31.0 °E extends from 30.0 °N to 32.5 °N and prominent on this cross-section are offshore winds between latitudes 31.5 °N

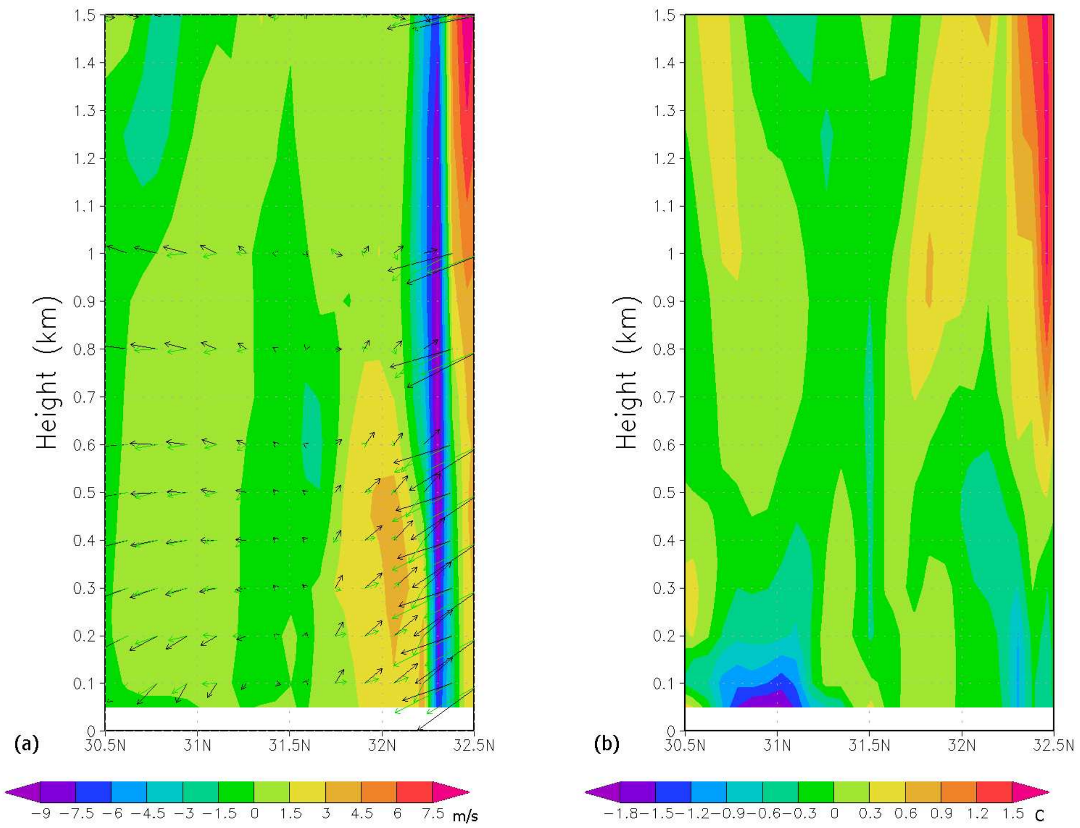

FIGURE 6.20: Vertical cross-section at 31.0 °E extending from 30.0 °N to 32.5 °N showing the differences (CTRL-DES) for (a) wind speed (m s^{-1}) and (b) air temperature (°C) up to 1.5 km above sea level (9 km spacing) at 03:00 UTC on 10 January 2008. In panel (a), the black and green wind barbs indicate the wind direction for the CTRL and DES runs, respectively.

and 32.3 °N, indicating a land breeze circulation (Figure 6.20(a)). A stronger land breeze is simulated in the CTRL run with increased wind speeds of the order of 4 m s^{-1} within the ABL. It seems that the vertical extent of the land breeze circulation cell is about 1.5 km with the stronger winds to be observed below 800 m.

As introduced in section 6.1, the genesis and development of cyclones in the eastern MS usually result from a combination of factors, including the strong land–sea pressure gradients and the large-scale circulations (e.g. Lionello *et al.*, 2006; Mehta and Yang, 2008). It may be reasonable to assume that a possible explanation for the frontal shift in the CTRL run is the land breeze interaction with the large-scale surface wind pattern that is dominant over the eastern MS. The colder vegetated Nile Delta (by about 1.8 °C) affects the movement of the front by creating a stronger land breeze (Figure 6.20(a, b)). The observed northerly/northeasterly winds over the eastern MS are not strong enough to oppose the land breeze and, therefore, contribute to the position of the front. Subsequently, the man-made greening shifts the frontal system farther to the north away from the Nile Delta coast. Over the following 12 hours, minor changes in the weather pattern are observed in both experiments. The land breeze and subsequently the storm event die once the Nile Delta warms up again during the day.

We thus show that the Nile Delta agriculture can affect offshore storms, extending the impact of land-use beyond the immediate local climate.

6.8 Summary of findings

In this study, certain land–atmosphere–water interactions were investigated by means of the Weather Research and Forecasting (WRF) model to identify the sensitivity of the local climate to the Nile Delta man-made greening. Desertification (DES) experiments were conducted for comparison with control (CTRL) simulations, which employ the present-day Nile Delta vegetation coverage for the 2007/2008 winter (December-January-February: DJF) and 2008 (June-July-August: JJA) summer months. For the pre-historic desert land-use, we reclassified the vegetated and urban areas in the Nile Delta as barren vegetated land with sandy soils.

It was found that both DJF and JJA seasonal and diurnal cycles of the surface temperature, wind speed, precipitation, energy fluxes and potential evapotranspiration (PET) are well reproduced by the WRF model. Land-cover changes greatly influenced the surface albedo, roughness length, LAI, aerodynamic, stomatal and soil resistances. In general, land-cover modifications that were relevant to the hydrological cycle (e.g. precipitation, evaporation) were associated with changes of the latent heat flux, while modifications of the surface albedo resulted in changes of net radiation. The agricultural Nile Delta produced a roughness length increase, which acted as a positive radiative forcing on the surface energy budget (latent and sensible heat fluxes). The vegetated Nile Delta compared with the pre-historic desert state has lower albedo which increased the net radiation and strengthened the land and sea breeze circulations. The net radiation increase was found as the principle cause for the increase in PET.

A decrease in albedo led to more solar radiation absorbed by the ground and to a net radiation increase at the top of the atmosphere, which allowed precipitation development. Surface roughness increase positively affected the fluxes of heat, momentum and moisture from the surface to the atmosphere, and therefore convection too. In addition, the soil moisture increase by man-made greening affected evapotranspiration and therefore moisture availability in the atmosphere, which in general also positively affected precipitation. However, the aforementioned three mechanisms slightly increased the minimal precipitation over the Nile Delta.

Interestingly, the agricultural Nile Delta with the lower albedo displaced offshore storms. A frontal system over the eastern Mediterranean Sea was shifted farther away from the Nile Delta coastal areas. This shift was attributed to a stronger land breeze in the present-day Nile Delta. We can conclude that changes in the land surface parameters provided important influence of the man-induced greening on local and non-local scale. Several wider conclusions from this study can now be drawn:

(i) The lower albedo of agricultural land-use tends to increase the net radiation, which in turn enhances the maximum possible water loss to the atmosphere from a vegetated surface. Under these conditions agricultural use increases the water demand by enhancing PET. In effect the vegetation–radiation–PET interaction is a positive feedback on water demand.

(ii) Man-made greening can modify non-local frontal systems associated with storm events.

Chapter 7

Conclusions and Future Work

7.1 Summary of Work

Deeper understanding of the land–boundary layer–sea interactions is needed both in the context of low-level jet (LLJ) development and land-cover/land-use changes. To address this need and hence provide a way to achieve a better understanding of the LLJs' development and characteristics, we chose to study the summertime LLJ over the Persian Gulf, known as the Shamal. This thesis investigated and determined the physical mechanisms that are responsible for the development, intensity, direction and diurnal variation of this summertime LLJ. Motivated by the importance of understanding the land-cover changes–atmosphere coupling, the sensitivity of the Nile Delta local climate to the present-day man-made greening/farming was also investigated and addressed. For the purposes of this research, the Weather Research and Forecasting (WRF) model was used.

Chapter 1 introduced the context of this work and provided the thesis' objectives and outline. Five objectives were related to the study of a summertime Shamal wind event over the Persian Gulf and four objectives were relevant to the study of the present-day Nile Delta greening effects on the local climate. These nine objectives are now reviewed in the light of the work achieved in this thesis.

Chapter 2 provided a broad literature review locating the work presented in the thesis within the different areas of relevant research. This chapter involved a discussion of the basic atmospheric boundary layer (ABL) principles and an overview of LLJ studies. The aspects that have been extensively documented in the LLJ studies were the nocturnal occurrence of the low-level wind maxima and the role of ABL processes (e.g. inertial oscillation and diurnal heating of a sloping terrain) in their development and diurnal variation. A presentation of the most known and well-studied physical mechanisms that are responsible for the development of LLJs in many parts of the world was provided.

The background related to the radiative and turbulent fluxes over land was also presented in chapter 2. Studies of land-cover/land-use changes were reviewed to show that land-cover modifications have attracted widespread interest in fields such as meteorology, climatology and hydrology. In the majority of the studies reviewed in chapter 2, land-use modifications revealed considerable changes in the surface energy budget, precipitation and circulation patterns. Chapter 2 also provided different potential evapotranspiration (PET) definitions and calculation methods. PET studies were additionally reviewed to show its importance in meteorology and hydrology. The need for accurate PET estimates in order to make sustainable regional terrestrial water distributions under changing conditions of land-cover was presented.

Chapter 3 provided an analytic description of the main components of the WRF model, Version 3. We discussed the ability of the WRF model to use different map projections, domain sizes, horizontal and vertical resolutions. We also presented a variety of physics parameterisations (e.g. planetary boundary layer, surface, radiation, cumulus and microphysics schemes) that are available in the WRF model. A description of the global atmospheric re-analyses and the terrestrial data selected for the WRF model initialisation was provided. Limitations and problems of the model and datasets were discussed.

Chapter 4 examined the sensitivity of the performance of the WRF model to the use of different planetary boundary layer (PBL) schemes. Comparison of surface and boundary layer observations with 3-days high resolution WRF simulations with four different (two local closure and two non-local closure) PBL schemes over the Persian Gulf in summer 1982 showed that the Quasi-Normal Scale Elimination (QNSE) PBL scheme satisfactorily simulates the stable boundary layer compared to the other three PBL schemes. Accurately simulating the meteorological processes within the PBL is essential for correctly simulating LLJs' development, vertical structure, intensity and direction. The first objective of this thesis was to **show the ability of the WRF model, Version 3.2, to accurately simulate the vertical structure, wind speed and wind direction of the summertime LLJs observed over the Persian Gulf**. Indeed, the WRF model simulated the LLJs' horizontal and vertical structure, strength, nocturnal features and northerly/northwesterly direction in exceptionally good agreement with the observations.

Chapter 5 presented the study of a typical summertime Shamal wind event observed over the Persian Gulf and southern Iraq. The case study period (0000 UTC, 07 June 1982 – 0000 UTC, 14 June 1982) was divided into a period during which the Shamal wind was spatially extended (strong wind over the Persian Gulf and southern Iraq) and a period during which it was less spatially extended (strong flow only over the Gulf). It is worth noting that the fine structure of the observed Shamal winds was captured, unlike to similar LLJ studies in which the maximum wind speed was underestimated and the height of the LLJ core was overestimated (e.g. Atkinson and Zhu, 2005; Storm *et al.*, 2009). A

LLJ profile was observed when the maximum wind speed occurred between 300 m and 700 m AGL, whilst the wind remained geostrophic at the surface (due to friction) and above the boundary layer top. The height of the wind maxima was related to the height and the magnitude of the temperature inversion in agreement with Membery's (1983) observations. The one-way nested simulation with the highest horizontal resolution of 3 km provided compelling evidence of the strong diurnal variation in both the Shamal wind speed and wind direction.

The second and third aims of this study were to **examine the factors that determine the Shamal wind development, strength, duration and direction** and to **investigate the orographic effects on this LLJ development**. We concluded that several factors contributed to the Shamal formation, intensity, duration and direction. These factors were the semi-permanent synoptic systems, the Persian Gulf topography (gradual up-sloping terrain in Saudi Arabia, the Zagros Mountains with their sharply rising sloping terrain and the land–sea distribution), the frictional decoupling and the daytime heating and nocturnal cooling of the mountainous sloping terrain. In particular, the northwesterly winds appeared to occur as a result of the interaction of two circulating pressure centres: a low-pressure centre over Iran and a semi-permanent high-pressure cell over northwestern Saudi Arabia. The northwesterly flow was enhanced by the strong west-to-east pressure gradients. This was most pronounced whenever a low-pressure centre developed near the Gulf of Oman and over the Lavan Island. The effects of the Persian Gulf orography on the Shamal development were investigated by conducting, in addition to a control run, a number of terrain height sensitivity experiments (zero terrain, 500 m plateau and 50 % reduction in the Zagros Mountain height). The results provided evidence that the Shamal position and wind direction were significantly modulated by the Zagros Mountains topography. The Zagros Mountains in Iran not only channelled the northwesterly winds but also provided a barrier for the easterly monsoon airflow, which maximized the wind speed over the Persian Gulf. Based on the Shamal definition given in chapter 5, in the zero terrain height experiment no Shamal flow was observed since very intense easterly winds were dominant over the Persian Gulf. In the mountain height experiments, a weak and narrow LLJ was created closer to the west coast of the Persian Gulf. This result verified that the orographic height determines the Shamal characteristics. To determine and understand the impact of the land–sea distribution on the Shamal intensity, a land–sea sensitivity experiment was also presented. Based on this experiment, we found that the land breeze and the lower friction over the sea increased the intensity of the nocturnal jet over the Persian Gulf during the less extensive period.

The last objective of this work was to **identify the physical mechanisms that explain the diurnal oscillation of the Shamal winds**. To achieve this, in addition to the terrain height and land-sea experiments, novel mountain slope sensitivity experiments were conducted. Orography, mountain slopes and land/sea breeze circulations were found to be key factors for the strong diurnal variation of the Shamal wind speed and wind direction; the Blackadar's (1957) mechanism appeared to be secondary to the heating in forcing the Shamal. The results from the zero terrain height experiment revealed a flow that was characterised by strong periodic variation in wind speed, indicating the important role of the water–land distribution. However, easterly wind direction with no diurnal cycle was obtained. This suggested that the mountainous terrain was involved in a physical mechanism that caused the Shamal winds to reverse direction twice per day. The daily heating cycle over the sloping terrain appeared to be a possible mechanism. Based on the mountain slope sensitivity experiments, it was concluded that only during the less extensive period the Zagros Mountains' slope significantly affected the Shamal wind intensity and direction. Both novel shallow and steep mountain slope sensitivity studies featured a jet-like flow over the Persian Gulf. The steep slopes caused larger wind speeds; however, the shallow slopes revealed a stronger diurnally varying wind direction due to larger daytime heating and nighttime cooling of the sloping terrain. The land/sea breeze circulations altered the LLJ behaviour in terms of the diurnal zonal geostrophic wind component changes. This was significantly different from the widely-studied Great Plains LLJ (e.g. Parish and Oolman, 2010).

In chapter 6, the effects of the present-day Nile Delta man-made greening on local climate were assessed by conducting desertification experiments which employ the pre-historic Nile Delta landscape. This study focused on how the Nile Delta local climate has changed from a past period where human-induced activity did not exist; this was not a future climate scenario. The WRF model, Version 3.2.1, was integrated for the 2007/2008 winter months (December-January-February: DJF) and the 2008 summer months (June-July-August: JJA) with climatological surface conditions (control runs) and desert conditions (desertification experiments). This study was a one-way nested run with 9 km as the highest horizontal resolution. The desert conditions in the WRF model were prescribed by replacing the land surface over the Nile Delta with barren/sparsely vegetated land with sandy soils. Subsequently, the surface albedo, roughness length and several other land surface parameters in the WRF model were modified too. To the knowledge of the author, the sensitivity experiments in chapter 6 were the first of their kind in the Nile Delta region.

The first two aims of this study were to **determine the impacts of the man-made greening on the local climate** and to **investigate the Nile Delta land-use effects on the surface energy budget, circulation patterns and a storm event**. Significant differences between the pre-historic and present-day land-covers were apparent from the experiments, and these differences agreed reasonably well with our understanding of the man-induced greening. In general, surface albedo, LAI and roughness length were the parameters primarily considered in the assessment of the physical impact of the Nile Delta greening on the surface energy budget, net radiation, surface temperature, wind speed and PET. In particular, the increased roughness length in the agricultural Nile Delta resulted in weaker winds near the surface. During the winter months, faster nighttime cooling rate was observed because of the man-induced greening. The larger daytime surface temperatures and the increased emissivity in the vegetated Nile Delta contributed to this result. The increased LAI and surface roughness resulted in less stable near-surface boundary layers which also appeared to affect the rate of the nighttime cooling. The daytime maximum temperature increase and the nighttime minimum temperature decrease over the green Nile Delta suggested an increased diurnal temperature range.

The present-day Nile Delta vegetation coverage with the lower surface albedo increased the shortwave absorption by the ground and the net radiation. Latent and sensible heat fluxes were also enhanced because of the lower albedo and the increased roughness length. The increase in turbulent fluxes raised evaporation and boundary layer warming. Subsequently, a small increase of the minimal convective rainfall and soil moisture was observed. While the aforementioned process was fairly localised in space, it was also responsible for non-local effects. We identified that a frontal system over the eastern Mediterranean Sea, associated with a storm event, was shifted farther away from the Nile Delta coastline. This shift was attributed to a stronger land breeze in the control run.

The last objective of this study was to **explore the changes in PET and the relationship of these changes to other meteorological parameters such as wind speed, temperature and net radiation**. The Penman-based (radiation-based) energy balance approach of Mahrt and Ek (1984) was used in this study to calculate PET and to evaluate the sensitivity of changes in the Nile Delta land-cover on its value. The changes in surface temperature and wind speed provided compelling evidence that these components were not the key factors for the PET changes. The net radiation increase was found as the principle cause for the increase in PET. This suggested that agricultural use increases the water demand in the Nile Delta region by enhancing PET.

7.2 Future Work

7.2.1 Sensitivity experiments

The sensitivity experiments presented in chapters 5 and 6 in the context of land–boundary layer–sea interactions may also be used to improve the current understanding and modelling capability of LLJs observed worldwide and to investigate the effects of land-cover/land-use changes on local, regional and global climate. Further work directly proposed by the sensitivity experiments of this thesis includes:

Mountain slope sensitivity experiments

The LLJs have practical interest because of their effects on the moisture and dust/sand transport and theoretical and modelling interest because of the large amount of vertical wind shear associated with them. There are several geographic locations worldwide that have been identified as especially favourable for LLJ development. Among these locations are the Persian Gulf, the Great Plains of the United States and the California, in which significant LLJs, in terms of their impact on severe weather, dust mobilisation and precipitation, occur (e.g. Burk and Thompson, 1996; Parish and Oolman, 2010; Giannakopoulou and Toumi, 2011).

A possible limitation of the Shamal study presented in this thesis is that the WRF model was integrated only for a particular summertime LLJ event. Similar experiments should be considered with other summer and winter Shamal wind events and with other LLJs that are observed in areas with meteorological and physiographic features similar to those observed in the Persian Gulf. We also suggest that similar experiments can be carried out using other high-resolution models with different parameterisations of the boundary layer and the land surface processes.

In chapter 5, we presented mountain slope sensitivity experiments for the summertime LLJ observed over the Persian Gulf and southern Iraq. We propose that future modelling studies can use these experiments, since the simulation results are encouraging and can be validated in a wide range of applications. The mountain slope sensitivity experiments provide an insight into the role of mountain slope and width in the LLJs' diurnal variation and intensity and, therefore, can be used for a deeper understanding of the physical processes underlying other LLJs. These experiments also provide the framework for future studies to assess the mountainous sloping terrain effects on orographic, stratiform and convective precipitation. For example, the mesoscale characteristics of fronts may be altered by topographic changes associated with shallow or steep mountainous orography. These experiments have potential in areas such as the Great Plains and California, where LLJs and precipitation events are frequently observed.

In contrast to the many precipitation studies and the accompanying mountain height sensitivity experiments, there are no modelling studies focusing on the influence of the mountainous sloping terrain on precipitation in the Persian Gulf. It will be interesting to perform numerical studies in order to examine the effects of the diurnal variation of the Shamal wind events on the evaporation and subsequently on the precipitation. The experiments presented in chapter 5 can be applied without difficulty to any numerical weather prediction (NWP) model.

Nile Delta land-use sensitivity experiments

The pre-historic Nile Delta assumed a desert-like morphology until its modification by cultivation and irrigation in the late Holocene period. In the absence of human activity much of the Nile Delta would have remained a desert landmass (Holmes, 1993; Hassan, 1997). In chapter 6, we presented desertification experiments in which the landscape conditions in the Nile Delta were quite extreme. The desert conditions were prescribed by replacing the present-day Nile Delta land-cover with barren vegetated land with sandy soils and without irrigation. We made this simplified assumption because our study focused on how the Nile Delta local climate has changed from a past period when human-induced activity did not exist.

It is known that the extensive agricultural area in the Nile Delta relies on the irrigation for crop production. However, irrigation in the Nile Delta is varied and complex and most of the meteorological models do not include irrigation schemes. It is worth noting that the Nile Delta is an area which is characterised by minimal precipitation. Even in some regions in which the average rainfall is sufficient for cultivation, marked annual variations in precipitation often make cultivation without irrigation risky. We suggest that future greening studies should consider the complex interaction between the vegetation coverage and the irrigation. In order to assess the effects of limited or extensive irrigation on the local climate, we propose that future modelling studies can include irrigation methods in the WRF model. We assume that additional water to the soil column can alter the energy and water budget estimations. For example, our assumption is that increased irrigation in the Nile Delta will affect soil moisture which in turn can result in more humid and cooler local conditions.

The Nile Delta has also received considerable attention from researchers because the effects of global warming and the potential increase in sea level make it a vulnerable coastal zone (e.g. Frihy *et al.*, 1991; Yates and Strzepek, 1998; El-Banna and Frihy, 2008; El-Nahry and Doluschitz, 2010). Future work may include sea-level rise sensitivity experiments with the WRF model. These experiments would likely have stronger influences on variables such as convective rainfall and circulation patterns.

More sophisticated land surface categories or schemes with additional urban parameters can be used in future research. In particular, land surface classes that describe increasing levels of the urban hierarchy (e.g. metropolis, city, town), each with different surface albedos and roughness length that would be related to the density of the urban area, can be explored. We believe that all of these enhancements would yield stronger land-cover influences upon the present-day urban atmosphere.

7.2.2 One-dimensional energy balance model

We suggest the development and evaluation of a one-dimensional surface energy balance model (EBM) for comparison with the WRF simulations of chapter 6 for the Nile Delta area. Although there is no a priori guarantee that such a one-dimensional EBM will help us understand the climate system and climatic changes in the Nile Delta since the pre-historic times, someone can adopt the optimistic point of view that solutions to the simplified models can provide some interesting results as well as serve as a guide for experimentation with the more sophisticated EBM that is used in the WRF model. This one-dimensional EBM can be forced by climatological winds, temperature, downward longwave radiation and specific humidity. This simplified model can also take into account changes in land surface parameters such as changes in surface albedo, roughness length and emissivity. The development of a one-dimensional EBM might enable a more quantitative discussion of what is affecting the climatic changes observed in the Nile Delta region because of the present-day greening.

Bibliography

Adebayo YR. 1991. ”Heat island” in a Humid Tropical City and its Relationship with Potential Evaporation. *Theoretical and Applied Climatology* **43**: 137– 147.

Ali AH. 1994. Chapter 3: Wind Regime of the Arabian Gulf. In: *The Gulf War and the Environment.*, Farouk EB, Makharita RM (eds), Gordon and Breach Science Publishers: New York, USA, pp. 31–48.

Alinot C, Masson C. 2005. Model for the Atmospheric Boundary Layer Under Various Thermal Stratifications. *Journal of Solar Energy Engineering* **127**(4): 438–443.

Anderson BT, Roads JO, Chen SC, Juang HMH. 2001. Model dynamics of summertime low-level jets over northwestern Mexico. *Journal of Geophysical Research* **106**(D4): 3401–3413.

Anderson JR, Hardy EE, Roach JT, Witmer RE. 1976. A land use and land cover classification system for use with remote sensor data. *U.S. Geological Survey Professional Paper 964* : 1–41.

Anderson RG, Canadell JG, Randerson JT, Jackson RB, Hungate Ba, Baldocchi DD, Ban-Weiss Ga, Bonan GB, Caldeira K, Cao L, Diffenbaugh NS, Gurney KR, Kueppers LM, Law BE, Luyssaert S, O’Halloran TL. 2011. Biophysical considerations in forestry for climate protection. *Frontiers in Ecology and the Environment* **9**(3): 174–182.

Andrews DG. 2000. *An introduction to atmospheric physics*. Cambridge University Press.

Angelini IM, Garstang M, Davis RE, Hayden B, Fitzjarrald DR, Legates DR, Greco S, Macko S, Connors V. 2011. On the coupling between vegetation and the atmosphere. *Theoretical and Applied Climatology* **105**(1-2): 243–261.

Angevine WM, Jiang H, Mauritsen T. 2010. Performance of an eddy diffusivity-mass flux scheme for shallow cumulus boundary layers. *Monthly Weather Review* **138**: 2895–2912.

Atkinson BW, Zhu M. 2005. Radar-duct and boundary-layer characteristics over the area of The Gulf. *Quarterly Journal of the Royal Meteorological Society* **131**(609): 1923–1953.

Ayyad MA. 1973. Vegetation and Environment of the Western Mediterranean Coastal Land of Egypt: I. The Habitat of Sand Dunes. *Journal of Ecology* **61**(2): 509–523.

Bala G, Caldeira K, Wickett M, Phillips TJ, Lobell DB, Delire C, Mirin A. 2007. Combined climate and carbon-cycle effects of large-scale deforestation. *Proceedings of the National Academy of Sciences of the United States of America* **104**(16): 6550–55.

Blackadar AK. 1957. Boundary layer wind maxima and their significance for the growth of nocturnal inversions. *Bulletin of the American Meteorology Society* **38**(5): 283–290.

Boer B. 1997. An introduction to the climate of the United Arab Emirates. *Journal of Arid Environments* **35**(1): 3–16.

Bollasina M, Nigam S. 2011. Modeling of Regional Hydroclimate Change over the Indian Subcontinent: Impact of the Expanding Thar Desert. *Journal of Climate* **24**(12): 3089–3106.

Bolle HJ. 2003. Chapter 2: Climate, Climate Variability and Impacts in the Mediterranean Area: An overview. In: *Mediterranean climate: variability and trends.*, Bolle HJ (ed), Springer Verlag, Berlin, pp. 5–86.

Bonner WD. 1968. Climatology of the Low Level Jet. *Monthly Weather Review* **96**(12): 833–850.

Bonner WD, Paegle J. 1970. Diurnal variations in boundary layer winds over the south-central United States in summer. *Monthly Weather Review* **98**(10): 735–744.

Borge R, Alexandrov V, Jose del Vas J, Lumbreras J, Rodriguez E. 2008. A comprehensive sensitivity analysis of the WRF model for air quality applications over the Iberian Peninsula. *Atmospheric Environment* **42**: 8560–8574.

Bougeault P, Lacarrere P. 1989. Parameterization of orography-induced turbulence in a mesobeta-scale model. *Monthly Weather Review* **117**: 1872–1890.

Braun SA, Rotunno R, Klemp JB. 1999. Effects of Coastal Orography on Landfalling Cold Fronts. Part I: Dry, Inviscid Dynamics. *Journal of the Atmospheric Sciences* **56**(4): 517–533.

Bretherton CS, Park S. 2009. A new moist turbulence parameterization in the Community Atmosphere Model. *Journal of Climate* **22**(12): 3422–3448.

Broadus J, Milliman S, Edwards D, Aubrey D, Gable F. 1986. Rising sea level and damming of rivers: possible effects in Egypt and Bangladesh. In: *Effects of changes in stratospheric ozone and global climate. Vol 4. Sea level rise*, Titus JG (ed), Washington, DC: United States Environmental Protection Agency, pp. 165–189.

Brooks IM, Goroch AK, Rogers DP. 1999. Observations of Strong Surface Radar Ducts over the Persian Gulf. *Journal of Applied Meteorology* **38**(9): 1293–1310.

Brooks IM, Rogers DP. 2000. Aircraft observations of the mean and turbulent structure of a shallow boundary layer over the Persian Gulf. *Boundary-Layer Meteorology* **95**(2): 189–210.

Burk SD, Thompson WT. 1996. The Summertime Low-Level Jet and Marine Boundary Layer Structure along the California Coast. *Monthly Weather Review* **124**(4): 668–686.

Chagnon FJF, Bras RL, Wang J. 2004. Climatic shift in patterns of shallow clouds over the Amazon. *Geophysical Research Letters* **31**: 1–4.

Changnon SA. 1992. Inadvertent weather modification in urban areas: Lessons for global climate change. *Bulletin of the American Meteorological Society* **73**: 619–627.

Charney JG. 1975. Dynamics of deserts and drought in the Sahel. *Quarterly Journal of the Royal Meteorological Society* **101**: 193–202.

Chattopadhyay N, Hulme M. 1997. Evaporation and potential evapotranspiration in India under conditions of recent and future climate change. *Agricultural and Forest Meteorology* **87**(1): 55–73.

Chen F, Dudhia J. 2001. Coupling an advanced land surface–hydrology model with the Penn State–NCAR MM5 modeling system. Part I: Model implementation and sensitivity. *Monthly Weather Review* **129**: 569–585.

Cohen S, Ianetz a, Stanhill G. 2002. Evaporative climate changes at Bet Dagan, Israel, 1964-1998. *Agricultural and Forest Meteorology* **111**(2): 83–91.

Conway D, Hulme M. 1996. The Impacts of Climate Variability and Future Climate Change in the Nile Basin on Water Resources in Egypt. *International Journal of Water Resources Development* **12**(3): 277–296.

Crawford KC, Hudson HR. 1973. The Diurnal Wind Variation in the Lowest 1500 ft in Central Oklahoma: June 1966-May 1967. *Journal of Applied Meteorology* **12**: 127–132.

Cuxart J, Holtslag AAM, Beare RJ, Bazile E, Beljaars A, Cheng A, Conangla L, Ek M, Freedman F, Hamdi R, Kerstein A, Kitagawa H, Lenderink G, Lewellen D, Mailhot J, Mauritsen T, Perov V, Schayes G, Svensson G, Taylor P, Weng W, Wunsch S. 2006. Single-column model intercomparison for a stably statified atmospheric boundary layer. *Bound.-Layer Meteor.* **118**: 273–303, doi: 10.1007/s10546-005-3780-1.

D' Almeida C, Vorosmarty CJ, Hurtt GC, Marengo JA, Dinigman SL, Keim BD. 2007. The effects of deforestation on the hydrological cycle in Amazonia: a review on scale and resolution. *International Journal of Climatology* **27**: 633–647, doi: 10.1002/joc.

Dayan U. 1986. Climatology of Back Trajectories from Israel Based on Synoptic Analysis. *Journal of Climate and Applied Meteorology* **25**(5): 591–595.

Dee DP, Uppala SM, Simmons AJ, Berrisford P, Poli P, Kobayashi S, Andrae U, Balmaseda MA, Balsamo G, Bauer P, Bechtold P, Beljaars aCM, van de Berg L, Bidlot J, Bormann N, Delsol C, Dragani R, Fuentes M, Geer AJ, Haimberger L, Healy SB, Hersbach H, Hólm EV, Isaksen L, Kå llberg P, Köhler M, Matricardi M, McNally AP, Monge-Sanz BM, Morcrette JJ, Park BK, Peubey C, de Rosnay P, Tavolato C, Thépaut JN, Vitart F. 2011. The ERA-Interim reanalysis: configuration and performance of the data assimilation system. *Quarterly Journal of the Royal Meteorological Society* **137**(656): 553–597.

Doyle JD. 1997. The Influence of Mesoscale Orography on a Coastal Jet and Rainband. *Monthly Weather Review* **125**(7): 1465–1488.

Duda M. 2011. The WRF Preprocessing System: Description of General Functions. Joint NCAR-NCAS WRF Tutorial, Edinburgh, Scotland. URL `http://www.mmm.ucar.edu/wrf/users/tutorial/201001/WPS-general.pdf`.

Dudhia J. 1989. Numerical study of convection observed during the winter monsoon experiment using a mesoscale two-dimensional model. *Journal of Atmospheric Sciences* **46**: 3077–3107.

Dudhia J. 2011a. Overview of WRF Physics. Power Point Slides presented at the November 2011 NCAS Tutorial. URL `http://www.mmm.ucar.edu/wrf/users/tutorial/201111/14_Physics_Dudhia.pdf`.

Dudhia J. 2011b. WRF Four-Dimensional Data Assimilation (FDDA). Power Point Slides presented at the November 2011 NCAS Tutorial. URL `http://www.mmm.ucar.edu/wrf/users/tutorial/201101/WRF_FDDA_Dudhia.pdf`.

Dunn S, Mackay R. 1995. Spatial variation in evapotranspiration and the influence of land use on catchment hydrology. *Journal of Hydrology* **171**(1-2): 49–73.

ECMWF. 2006. European Centre for Medium-Range Weather Forecasts (ECMWF) 40-year re-analysis data (ERA-40). http://badc.nerc.ac.uk/view/badc.nerc.ac.uk__ATOM__dataent_ECMWF-E40.

ECMWF. 2009. European Centre for Medium-Range Weather Forecasts (ECMWF) ERA-Interim Re-Analysis data. URL http://badc.nerc.ac.uk/view/badc.nerc.ac.uk__ATOM__dataent_12458543158227759.

Egger J. 1999. Inertial Oscillations Revisited. *Journal of Atmospheric Sciences* **56**: 2951–2954.

El-Askary H, Farouk R, Ichoku C, Kafatos M. 2009. Transport of dust and anthropogenic aerosols across Alexandria , Egypt. *Annales Geophysicae* **27**: 2869–2879.

El-Banna MM, Frihy OE. 2008. Natural and anthropogenic influences in the northeastern coast of the Nile delta, Egypt. *Environmental Geology* **57**(7): 1593–1602.

El-Banna MM, Frihy OE. 2009. Human-induced changes in the geomorphology of the northeastern coast of the Nile delta, Egypt. *Geomorphology* **107**: 72–78.

El-Nahry AH, Doluschitz R. 2010. Climate change and its impacts on the coastal zone of the Nile Delta, Egypt. *Environmental Earth Sciences* **59**(7): 1497–1506.

El-Raey M, Nasr S, Frihi S, Desouki S, Dewidar K. 1995. Potential impacts of accelerated sea-level rise on Alexandria Governorate, Egypt. *Journal of Coastal Research* **14**: 190–204.

El-Sabh MI, Murty TS. 1989. Storm Surges in the Arabian Gulf. *Natural Hazards* **1**: 371–385.

Esteban JG, Gonzalez C, Curtale F, Muñoz Antoli C, Valero MA, Bargues MD, El-Sayed M, El-Wakeel AAW, Abdel-Wahab Y, Montresor A, Engels D, Savioli L, Mas-Coma S. 2003. Hyperendemic fascioliasis associated with schistosomiasis in villages in the Nile Delta of Egypt. *The American Journal of Tropical Medicine and Hygiene* **69**(4): 429–37.

Evans JP, Smith RB, Oglesby RJ. 2004. Middle East climate simulation and dominant precipitation processes. *International Journal of Climatology* **24**(13): 1671–1694.

Feddema JJ. 1999. Future African water resources: interactions between soil degradation and global warming. *Climatic Change* **42**: 561–596.

Flocas HA, Simmonds I, Kouroutzoglou J, Keay K, Hatzaki M, Bricolas V, Asimakopoulos D. 2010. On Cyclonic Tracks over the Eastern Mediterranean. *Journal of Climate* **23**(19): 5243–5257.

Frenken K (ed). 2005. *Irrigation in Africa in Figures: AQUASTAT Survey - 2005*, vol. Water Reports 29. FAO Land and Water Development Division, Rome.

Friedl MA, McIver DK, Hodges JCF, Zhang XY, Muchoney D, Strahler AH, Woodcock CE, Gopal S, Scheider A, Cooper A, Baccini A, Gao F, Schaaf C. 2002. Global land cover mapping from MODIS: algorithms and early results. *Remote Sensing of Environment* **83**(1-2): 287–302.

Frihy OE, Fanos AM, Khafagy Aa, Komar PD. 1991. Patterns of nearshore sediment transport along the Nile Delta, Egypt. *Coastal Engineering* **15**(5-6): 409–429.

Gallo KP, Easterling DR, Peterson TC. 1996. The Influence of Land Use/Land Cover on Climatological Values of the Diurnal Temperature Range. *Journal of Climate* **9**(11): 2941–2944.

Gao G, Chen D, Ren G, Chen Y, Liao Y. 2006. Spatial and temporal variations and controlling factors of potential evapotranspiration in China: 1956-2000. *Journal of Geographical Sciences* **16**(1): 3–12.

Garcia-Carreras L, Parker DJ. 2011. How does local tropical deforestation affect rainfall? *Geophysical Research Letters* **38**(19): 1–6.

Garcia-Diez M, Fernandez J, Fita L, Yague C. 2012. Seasonal dependence of WRF model biases and sensitivity to PBL schemes over Europe. *Quarterly Journal of the Royal Meteorological Society* doi: 10.1002/qj.1976.

Garratt JR. 1992. *The Atmospheric Boundary Layer*. Cambridge Univ. Press: New York.

Gates LD, Liess S. 2001. Impacts of deforestation and afforestation in the Mediterranean region as simulated by the MPI atmospheric GCM. *Global and Planetary Change* **30**: 309–328.

Giannakopoulou EM, Toumi R. 2011. The Persian Gulf summertime low-level jet over sloping terrain. *Quarterly Journal of the Royal Meteorological Society* **138**(662): 145–157.

Giannakopoulou Em, Toumi R. 2012. Impacts of the Nile Delta land-use on the local climate. *Atmospheric Science Letters* **13**(3): 208–215.

Gill D. 2011. WRF Fundamentals Nesting. Power Point Slides presented at the November 2011 NCAS Tutorial. URL http://www.mmm.ucar.edu/wrf/users/tutorial/201111/09_WRF_Nesting.pdf.

Giri C, Zhu Z, Reed B. 2005. A comparative analysis of the Global Land Cover 2000 and MODIS land cover data sets. *Remote Sensing of Environment* **94**(1): 123–132.

Glickman TS. 2000. *AMS Glossary of Meteorology*. Boston, U.S.A, 2nd edn.

Granger RJ. 1989. An examination of the concept of potential evaporation. *Journal of Hydrology* **111**: 9–19.

Hamon RW. 1963. Computation of direct runoff amounts from storm rainfall. *International Association of Scientific Hydrology* **63**: 52–62.

Han S, Hu H, Yang D, Liu Q. 2009. Differences in changes of potential evaporation in the mountainous and oasis regions of the Tarim basin, northwest China. *Science in China Series E: Technological Sciences* **52**(7): 1981–1989.

Hassan FA. 1997. The Dynamics of a Riverine Civilization: A Geoarchaeological Perspective on the Nile Valley, Egypt. *World Archaeology* **29**(1): 51–74.

Henderson-Sellers A, Dickinson RE, Durbidge TB, Kennedy PJ, Mcguffie K, Pitman AJ. 1993. Tropical Deforestation: Modeling Local- to Regional-Scale Climate Change. *Journal of Geophysical Research* **98**(D4): 7289–7315.

Herron N, Davis R, Jones R. 2002. The effects of large-scale afforestation and climate change on water allocation in the Macquarie River catchment, NSW, Australia. *Journal of Environmental Management* **65**(4): 369–381.

Holmes DL. 1993. Rise of the Nile Delta. *Nature* **363**: 402–403.

Holton JR. 1967. The diurnal boundary layer wind oscillation above sloping terrain. *Tellus* **19**(2): 199–205.

Holz RK. 1969. Man-Made Landforms in the Nile Delta. *Geographical Review* **59**(2): 253–269.

Hong SY, Dudhia J, Chen SH. 2004. A revised approach to ice microphysical processes for the bulk parameterization of clouds and precipitation. *Monthly Weather Review* **132**: 103–120.

Hong SY, Noh Y, Dudhia J. 2006. A new vertical diffusion package with an explicit treatment of entrainment processes. *Monthly Weather Review* **134**: 2318–2341.

Hu XM, Nielsen-Gammon JW, Zhang F. 2010. Evaluation of Three Planetary Boundary Layer Schemes in the WRF Model. *Journal of Applied Meteorology and Climatology* **49**(9): 1831–1844.

Hunt JCR, Orr A, Rottman JW, Capon R. 2004. Coriolis effects in mesoscale flows with sharp changes in surface conditions. *Quarterly Journal of the Royal Meteorological Society* **130**: 2703–2731.

Jiang X, Lau NC, Held IM, Ploshay JJ. 2007. Mechanisms of the Great Plains Low-Level Jet as Simulated in an AGCM. *Journal of the Atmospheric Sciences* **64**(2): 532–547.

Jin J, Lu S, Li S, Miller NL. 2010. Impact of Land Use Change on the Local Climate over the Tibetan Plateau. *Advances in Meteorology* **2010**: 1–6.

Kaimal JC, Finnigan JJ. 1994. *Atmospheric boundary layer flows: their structure and measurement.* Oxford University Press: New York, USA.

Kain JS. 2004. The Kain-Fritsch convective parameterization: An update. *Journal of Applied Meteorology* **43**: 170–181.

Kallos G, Kotroni V, Lagouvardos K, Papadopoulos A. 1998. On the long-range transport of air pollutants from Europe to Africa. *Geophysical Research Letters* **25**(5): 619–622.

Kampf J, Sadrinasab M. 2006. The circulation of the Persian Gulf: a numerical study. *Ocean Science* **2**(1): 27–41.

Kanae S, Oki T, Musiake K. 2001. Impact of Deforestation on Regional Precipitation over the Indochina Peninsula. *Journal of Hydrometeorology* **2**(1): 51–70.

Katsafados P, Mavromatidis E, Papadopoulos a, Pytharoulis I. 2011. Numerical simulation of a deep Mediterranean storm and its sensitivity on sea surface temperature. *Natural Hazards and Earth System Science* **11**(5): 1233–1246.

Laval K, Picon L. 1986. Effect of a Change of the Surface Albedo of the Sahel on Climate. *Journal of the Atmospheric Sciences* **43**(21): 2418–2429.

Lhommel JP. 1997. Towards a rational definition of potential evaporation. *Hydrology and Earth System Sciences* **1**(2): 257–264.

Lionello P, Bhend J, Buzzi A, Della-Marta PM, Krichak SO, Jans A, Maheras P, Sanna A, Trigo IF, Trigo R. 2006. Chapter 6: Cyclones in the Mediterranean region: Climatology and effects on the environment. In: *Mediterranean, Developments in Earth and Environmental Sciences*, vol. 4, Lionello P, Boscolo R (eds), Elsevier, pp. 325–372.

Liu X, Ren L, Yuan F, Singh VP, Fang X, Yu Z, Zhang W. 2008. Quantifying the effect of land use and land cover change on green water and blue water in northern part of China. *Hydrology and Earth System Sciences Discussions* **5**(4): 2425–2457.

Loveland TR, Estes JE, Scepan J. 1999. Global land cover mapping and validation - Foreword. *Photogrammetric Engineering and Remote Sensing* **65**(9): 1011–1012.

Loveland TR, Merchant JW, Ohlen DO, Brown JF. 1991. Development of a land-cover characteristics database for the conterminous U.S. *Photogrammetric Engineering and Remote Sensing* **57**(11): 1453–1463.

Loveland TR, Reed BC, Brown JF, Ohlen DO, Zhu Z, Yang L, Merchant JW. 2000. Development of a global land cover characteristics database and IGBP DISCover from 1 km AVHRR data. *International Journal of Remote Sensing* **21**(6/7): 1303–1330.

Lu J, Sun G, McNulty SG, Amatya M. 2005. A comparison of six potential evapotranspiration methods for regional use in southeastern United States. *Journal of the American Water Resources Association* **41**(3): 621–633.

Maheras P, Flocas HA, Patrikas I. 2001. A 40 year objective climatology of surface cyclones in the Mediterranean region: spatial and temporal distribution. *International Journal of Climatology* **21**: 109–130.

Mahrt L, Ek M. 1984. The Influence of Atmospheric Stability on Potential Evaporation. *Journal of Climate and Applied Meteorology* **23**(2): 222–234.

Mariotti A, Struglia MV, Zeng N, Lau KM. 2002. The Hydrological Cycle in the Mediterranean Region and Implications for the Water Budget of the Mediterranean Sea. *Journal of Climate* **15**(13): 1674–1690.

Marshall J, Plumb R. 2008. *Atmosphere, Ocean and Climate Dynamics: An Introductory Text*. Elsevier Academic Press: USA.

McNider RT, Pielke RA. 1981. Diurnal Boundary-Layer Development over Sloping Terrain. *Journal of the Atmospheric Sciences* **38**(10): 2198–2212.

Mehta AV, Yang S. 2008. Precipitation climatology over Mediterranean Basin from ten years of TRMM measurements. *Advances In Geosciences* **17**: 87–91.

Mellor GL, Yamada T. 1982. Development of a Turbulence Closure Model for Geophysical Fluid Problems. *Reviews of Geophysics and Space Physics* **20**(4): 851–875.

Membery DA. 1983. Low level wind profiles during the Gulf Shamal. *Weather* **38**(1): 18–24.

Michalakes J, Vachharajani M. 2008. GPU Acceleration of Numerical Weather Prediction. *Parallel Processing Letters* **18**(04): 531–548.

Mlawer EJ, Taubman SJ, Brown PD, Iacono MJ, Clough SA. 1997. Radiative transfer for inhomogeneous atmosphere: RRTM, a validated correlated-k model for the longwave. *Journal of Geophysical Research* **102**: 16 663–16 682.

Monteith JL. 1965. Evaporation and environment. The state of movement of water in living organisms. *XIXth Symposium of the society of experimental biology* : 205–234.

Mostafaeipour A. 2010. Feasibility study of offshore wind turbine installation in Iran compared with the world. *Renewable and Sustainable Energy Reviews* **14**(7): 1722–1743.

Nizinski JJ, Galat G, Galat-Luong A. 2011. Water balance and sustainability of eucalyptus plantations in the Kouilou basin (Congo-Brazzaville). *Russian Journal of Ecology* **42**(4): 305–314.

OAS. 1991. Desertification Hazard Assessment. In: *Primer on Natural Hazard Management in Integrated Regional Development Planning*, ch. 9, Organization of American States. Dept. of Regional Development and Environment: Washington, D.C.

Olson JB, Colle BA. 2009. Three-Dimensional Idealized Simulations of Barrier Jets along the Southeast Coast of Alaska. *Monthly Weather Review* **137**(1): 391–413.

Oudin L, Hervieu F, Michel C, Perrin C, Andreassian V, Anctil F, Loumagne C. 2005. Which potential evapotranspiration input for a lumped rainfall-runoff model? Part 2-Towards a simple and efficient potential evapotranspiration model for rainfall-runoff modelling. *Journal of Hydrology* **303**: 290–306.

Oyama MD, Nobre CA. 2004. Climatic Consequences of a Large-Scale Desertification in Northeast Brazil: A GCM Simulation Study. *Journal of Climate* **17**(16): 3203–3213.

Ozdogan M, Gutman G. 2008. A new methodology to map irrigated areas using multi-temporal MODIS and ancillary data: An application example in the continental US. *Remote Sensing of Environment* **112**(9): 3520–3537.

Ozdogan M, Salvucci GD. 2004. Irrigation-induced changes in potential evapotranspiration in southeastern Turkey: Test and application of Bouchet's complementary hypothesis. *Water Resources Research* **40**(4): 1–12.

Pagowski M. 2004. Some Comments on PBL Prameterizations in WRF. *Proc. Joint WRF/MM5 Users' Workshop, Boulder, CO, National Center for Atmospheric Research, 1.13.* : 273–275.

Pan Z, Segal M, Arritt RW. 2004. Role of topography in forcing low-level jets in central U.S. during the 1993 flood-altered terrain simulations. *Monthly Weather Review* **132**: 396–403.

Parish TR, Oolman LD. 2010. On the Role of Sloping Terrain in the Forcing of the Great Plains Low-Level Jet. *Journal of the Atmospheric Sciences* **67**(8): 2690–2699.

Parish TR, Rodi AR, Clark RD. 1988. A Case Study of the Summertime Great Plains Low Level Jet. *Monthly Weather Review* **116**(1): 94–105.

Penman HL. 1948. Natural evaporation from open water, bare soil and grass. *Royal Society of London Proceedings, Series A* **193**: 120–145.

Penman HL. 1956. Evaporation: an introductory survey. *Netherlands Journal of Agricultural Science* **4**: 9–29.

Peppler RA. 1988. A Review of Static Stability Indices and Related Thermodynamic Parameters. *Illinois State Water Survey Miscellaneous Publication* **104**: 87.

Perrone TJ. 1979. Winter shamal in the Persian Gulf. *Technical Report TR-79-06, Naval Environmental Prediction Research Facility, Monterey, USA* .

Petterssen S. 1956. *Weather analysis and forecasting*. Mac Graw Hill: New York, USA.

Pielke RA, Avissar R, Raupach M, Dolman AJ, Zeng X, Denning AS. 1998. Interactions between the atmosphere and terrestrial ecosystems: influence on weather and climate. *Global Change Biology* **4**(5): 461–475.

Pierrehumbert RT. 1984. Linear Results on the Barrier Effects of Mesoscale Mountains. *Journal of the Atmospheric Sciences* **41**(8): 1356–1367.

Pierrehumbert RT, Wyman B. 1985. Upstream Effects of Mesoscale Mountains. *Journal of Atmospheric Sciences* **42**(10): 977–1003.

Piety CA. 2005. Radar Wind Profiler Observations in Maryland: A Preliminary Climatology of the Low Level Jet. Technical report, Department of Atmospheric and Oceanic Science, The University of Maryland.

Pitman AJ. 2003. The evolution of, and revolution in, land surface schemes designed for climate models. *International Journal of Climatology* **23**(5): 479–510.

Pitman AJ, Narisma GT, Pielke Sr RA, Holbrook NJ. 2004. Impact of land cover change on the climate of southwest Western Australia. *Journal of Geophysical Research* **109**: 1–12.

Pleim JE. 2007. A combined local and nonlocal closure model for the atmospheric boundary layer. Part II: application and evaluation in a mesoscale meteorological model. *Journal of Applied Meteorology and Climatology* **46**: 1396–1409.

Priestley CHB, Taylor RJ. 1972. On the assessment of surface heat flux and evaporation using large scale parameters. *Monthly Weather Review* **100**: 81–92.

Purevjav G, Luvsan N. 2004. The impact of desertification on Mongolian climate and its numerical study using regional climate model (RegCM3). In: *Proceedings of the 3rd International Workshop on Terrestrial Change in Mongolia*. Tsukuba, Japan, pp. 112–113.

Radinovic D. 1987. *Mediterranean cyclones and their influence on the weather and climate*. PSMP Rep Series 24, WMO: Geneva, Switzerland.

Rana G, Katerji N. 2000. Measurement and estimation of actual evapotranspiration in the field under Mediterranean climate : a review. *European Journal of Agronomy* **13**: 125 – 153.

Rao PG, Al-Sulaiti M, Al-Mulla AH. 2001. Winter Shamals in Qatar, Arabian Gulf. *Weather* **56**: 444–451.

Rao PG, Hatwar HR, Al-Sulaiti MH, Al-Mulla AH. 2003. Summer shamals over the Arabian Gulf. *Weather* **58**(12): 471–478.

Reiter E. 1963. *Jet-Stream Meteorology*. University of Chicago Press: Chicago, illustrated edn.

Renfrew IA, Moore GWK, Kristjánsson JE, Ólafsson H, Gray SL, Petersen GN, Bovis K, Brown PRA, FI, Haine T, Hay C, Irvine EA, Lawrence A, Ohigashi T, Outten S, Pickart RS, Shapiro M, Sproson D, Swinbank R, Woolley A, Zhang S. 2008. The Greenland Flow Distortion Experiment. *Bulletin of the American Meteorological Society* **89**(9): 1307–1324.

Rife DL, Pinto JO, Monaghan AJ, Davis CA, Hannan JR. 2010. Global Distribution and Characteristics of Diurnally Varying Low-Level Jets. *Journal of Climate* **23**: 5041–5064.

Rind D, Goldberg R, Hansen J, Rosenzweig C, Ruedy R. 1990. Potential Evapotranspiration and the Likelihood of Future Drought. *Journal of Geophysical Research* **95**(D7): 9983–10 004.

Rodwell M, Hoskins B. 2001. Subtropical anticyclones and summer monsoons. *Journal of Climate* **14**: 3192–3211.

Rohling EJ, Hilgen FJ. 1991. The eastern Mediterranean climate at times of sapropel formation : a review. *Geologie En Mijnbouw* **70**: 253–264.

Sestini G. 1989. The implications of climate changes for the Nile Delta. Technical report, WG 2/14. UNEP/OCA, Nairobi, Kenya.

Shapiro A, Fedorovich E. 2010. Analytical description of a nocturnal low-level jet. *Quarterly Journal of the Royal Meteorological Society* **136**(650): 1255–1262.

Shaw SB, Riha SJ. 2011. Assessing temperature-based PET equations under a changing climate in temperate, deciduous forests. *Hydrological Processes* **25**(9): 1466–1478.

Shi JJ, Chang SW, Holt TR, Hogan TF, Westphal DL. 2004. A Meteorological Reanalysis for the 1991 Gulf War. *Monthly Weather Review* **132**(2): 623–640.

Shin HH, Hong SY. 2011. Intercomparison of Planetary Boundary-Layer Parametrizations in the WRF Model for a Single Day from CASES-99. *Boundary-Layer Meteorology* **139**: 261–281.

Shuttleworth WJ. 1993. Evaporation. In: *Handbook of Hydrology*, Maidment D (ed), McGraw-Hill, New York.

Skamarock B, Dudhia J. 2011. The Advanced Research WRF (ARW) Dynamics Solver. Power Point Slides presented at the November 2011 NCAS Tutorial. URL http://www.mmm.ucar.edu/wrf/users/tutorial/201111/07_tut_dyn_arw_201111.pdf.

Skamarock WC, Klemp JB. 2008. A time-split nonhydrostatic atmospheric model for weather research and forecasting applications. *Journal of Computational Physics* **227**(7): 3465–3485.

Skamarock WC, Klemp JB, Dudhia J, Gill DO, Barker DM, Duda MG, X-Y H, Wang W, Powers JG. 2008. A Description of the Advanced Research WRF Version 3. *NCAR Technical Note 475. National Center for Atmospheric Research: Boulder, CO* (June): 1–105.

Smith RB. 1979. The influence of mountains on the atmosphere. *Advances in Geophysics* **21**: 87–230.

Soriano C, Jorba O, Baldasano JM. 2002. One-way nesting versus two-way nesting: Does it really make a difference? In: *Air Pollution Modeling and its Applications XV*, Borrego C, Suyches G (eds), Kluwer Academic/Plenum Publishers: New York, pp. 177–185.

Stanley DJ, Warne AG. 1993. Sea level rise and initiation of Predynastic culture in the Nile Delta. *Nature* **363**: 435–438.

Stanley JD, Bernhardt CE. 2010. Alexandria's Eastern Harbor, Egypt: Pollen, Microscopic Charcoal, and the Transition from Natural to Human-Modified Basin. *Journal of Coastal Research* **26**(1): 67–79.

Stensrud DJ. 1996. Importance of low-level jets to climate: A review. *Journal of Climate* **9**(8): 1698–1711.

Storm B, Dudhia J, Basu S, Swift A, Giammanco I. 2009. Evaluation of the Weather Research and Forecasting Model on Forecasting Low-level Jets: Implications for Wind Energy. *Wind Energy* **12**(1): 81–90.

Strzepek K, Onyeji S, Saleh M, Yates D. 1995. An Assessment of Integrated Climate Change Impacts of Egypt. In: *As climate changes: international impacts and implications*, Strzepek KM, Smith JB (eds), Cambridge, Cambridge University Press, pp. 180–200.

Stull RB. 1988. *An introduction to boundary layer meteorology*. Kluwer Academic.

Sukoriansky S, Galperin B, Perov V. 2005. Application of a new spectral theory of stable stratified turbulence to the atmospheric boundary layer over sea ice. *Boundary-Layer Meteorology* **117**: 231–257.

Sukoriansky S, Galperin B, Perov V. 2006. A quasi-normal scale elimination model of turbulence and its application to stably stratified flows. *Nonlinear Processes in Geophysics* **13**(1): 9–22.

Sun G, Zuo C, Liu S, Liu M, McNulty SG, Vose JM. 2008. Watershed Evapotranspiration Increased due to Changes in Vegetation Composition and Structure Under a Subtropical Climate. *Journal of the American Water Resources Association* **44**(5): 1164–1175.

Thomas A. 2000. Spatial and temporal characteristics of potential evapotranspiration trends over China. *International Journal of Climatology* **20**(4): 381–396.

Thoppil PG, Hogan PJ. 2010. Persian Gulf response to a wintertime shamal wind event. *Deep-Sea Research Part I* **57**(8): 946–955.

Thornthwaite CW. 1948. An Approach toward a Rational Classification of Climate. *Geographical Review* **38**(1): 55–94.

Thornthwaite CW, Mather JR. 1955. The water balance. *Publications in Climatology* **8**(1): 1–86.

Thorpe AJ, Guymer TH. 1977. The nocturnal jet. *Quarterly Journal of the Royal Meteorological Society* **103**(438): 633–653.

Ting M, Wang H. 2006. The Role of the North American Topography on the Maintenance of the Great Plains Summer Low-Level Jet. *Journal of the Atmospheric Sciences* **63**(3): 1056–1068.

Trabucco A, Zomer R, Bossio D, Vanstraaten O, Verchot L. 2008. Climate change mitigation through afforestation/reforestation: A global analysis of hydrologic impacts with four case studies. *Agriculture, Ecosystems & Environment* **126**(1-2): 81–97.

Trigo IF, Davies TD, Bigg GR. 1999. Objective Climatology of Cyclones in the Mediterranean Region. *Journal of Climate* **12**: 1685–1696.

Tsvieli Y, Zangvil A. 2005. Synoptic climatological analysis of 'wet' and 'dry' Red Sea Troughs over Israel. *International Journal of Climatology* **25**(15): 1997–2015.

Uccellini LW, Johnson DR. 1979. The coupling of upper and lower troposphere jet streaks and implications for the development of severe convective storms. *Monthly Weather Review* **107**: 682–703.

Uppala SM, Kallberg PW, Simmons AJ, Andrae U, Bechtold VDC, Fiorino M, Gibson JK, Haseler J, Hernandez A, Kelly GA, Li X, Onogi K, Saarinen S, Sokka N, Allan RP, Andersson E, Arpe K, Balmaseda MA, Beljaars ACM, Berg LVD, Bidlot J, Bormann N, Caires S, Chevallier F, Dethof A, Dragosavac M, Fisher M, Fuentes M, Hagemann S, Holm E, Hoskins BJ, Isaksen L, Janssen PAEM, Jenne R, Mcnally AP, Mahfouf JF, Morcrette JJ, Rayner NA, Saunders RW, Simon P, Sterl A, Trenberth KE, Untch A, Vasiljevic D, Viterbo P, Woollen J. 2005. The ERA-40 re-analysis. *Quarterly Journal of the Royal Meteorological Society* **131**(612): 2961–3012.

Vinukollu RK, Wood EF, Ferguson CR, Fisher JB. 2011. Global estimates of evapotranspiration for climate studies using multi-sensor remote sensing data: Evaluation of three process-based approaches. *Remote Sensing of Environment* **115**(3): 801–823.

Vishkaee FA, Flamant C, Cuesta J, Oolman L, Flamant P, Khalesifard HR. 2012. Dust transport over Iraq and northwest Iran associated with winter Shamal: A case study. *Journal of Geophysical Research* **117**: 1–14.

Wagner A. 1939. Uber die Tageswinde in der freien Atmosphare [Concerning the Daily Wind in the Free Atmosphere]. *Beitrage Zur Physik der freien Atmosphare* **25**: 145–170.

Wallace J. 1995. Calculating evaporation: resistance to factors. *Agricultural and Forest Meteorology* **73**(3–4): 353–366.

Wallace J, Hobbs P. 2006. *Atmospheric Science: An Introductory Survey*. Academic press, second edn.

Walters K, Sjoberg W. 1990. *The Persian Gulf Region. A Climatological Study*. Air Force Environmental Technical Applications Center Scott AFB IL.

Wang Q, Takahashi H. 1999. A Land Surface Water Deficit Model for an Arid and Semi-arid Region: Impact of Desertification on the Water Deficit Status in the Loess Plateau , China. *Journal of Climate* **12**: 244–257.

Wang W, Bruyere C, Duda M, Dudhia J, Gill D, Lin HC, Michalakes J, Rizvi S, Zhang X. 2011. *ARW, Version 3 Modeling System User's Guide November 2011*. Mesoscale & Microscale Meteorology Division and National Center for Atmospheric Research.

Wang X, Jin P. 2006. Water shortage and needs for wastewater re-use in the north China. *Water Science and Technology* **53**(9): 35.

Warner TT, Sheu RS. 2000. Multiscale Local Forcing of the Arabian Desert Daytime Boundary Layer, and Implications for the Dispersion of Surface-Released Contaminants. *Journal of Applied Meteorology* **39**: 686–707.

Wexler H. 1961. A boundary layer interpretation of the low level jet. *Tellus* **13**: 368–378.

Whiteman CD, Bian X, Zhong S. 1997. Low-Level Jet Climatology from Enhanced Rawinsonde Observations at a Site in the Southern Great Plains. *Journal of Applied Meteorology* **36**: 1363–1376.

Wichansky PS. 2008. Evaluating the effects of historical land cover change on summertime weather and climate in New Jersey. PhD thesis, The State University of New Jersey.

Wichansky PS, Steyaert LT, Walko RL, Weaver CP. 2008. Evaluating the effects of historical land cover change on summertime weather and climate in New Jersey: Land cover and surface energy budget changes. *Journal of Geophysical Research* **113**: 1–25.

Xiu A, Adelman Z, Frank B, Adel H, Limei R, Mathur R, Pleim J, Wong D. 2011. Comparison of the CAM and RRTMG Radiation Schemes in WRF and coupled WRF-CMAQ models. UNC Institute for the Environment.

Xue Y. 1993. The influence and mechanisms of biosphere feedback on African climate. *Macroscale Modelling of the Hydrosphere (Proceedings of the Yokohama Symposium)* **214**: 119–124.

Xue Y. 1996. The Impact of Desertification in the Mongolian and the Inner Mongolian Grassland on the Regional Climate. *Journal of Climate* **9**(9): 2173–2189.

Xue Y, Shukla J. 1993. The Influence of Land Surface Properties on Sahel Climate. Part I: Desertification. *Journal of Climate* **6**(12): 2232–2245.

Xue Y, Shukla J. 1996. The Influence of Land Surface Properties on Sahel Climate. Part II. Afforestation. *Journal of Climate* **9**(12): 3260–3275.

Yang D, Shao W, Yeh PJF, Yang H, Kanae S, Oki T. 2009. Impact of vegetation coverage on regional water balance in the nonhumid regions of China. *Water Resources Research* **45**: 1–13.

Yates DN, Strzepek KM. 1998. An Assessment of Integrated Climate Change Impacts on the Agricultural Economy of Egypt. *Climatic Change* **38**(3): 261–287.

Zehnder JA, Bannon PR. 1988. Frontogenesis over a Mountain Ridge. *Journal of the Atmospheric Sciences* **45**(4): 628–644.

Zeng N, Dickinson RE, Zeng X. 1996. Climatic Impact of Amazon Deforestation-Mechanistic Model Study. *Journal of Climate* **9**(4): 859–883.

Zhang DL, Zheng WZ. 2004. Diurnal Cycles of Surface Winds and Temperatures as Simulated by Five Boundary Layer Parameterizations. *Journal of Applied Meteorology* **43**: 157–169.

Zhang L, Dawes WR, Walker GR. 2001. Response of mean annual evapotranspiration to vegetation changes at catchment scale. *Water Resources Research* **37**: 701–708.

Zhao M, Pitman AJ. 2002. The regional scale impact of land cover change simulated with a climate model. *International Journal of Climatology* **22**(3): 271–290.

Zheng W, Ni Y. 1999. A numerical experiment study for effects of the grassland desertification on summer drought in North China. *Advances in Atmospheric Sciences* **16**(2): 251–262.

Zheng X, Eltahir EaB. 1997. The response to deforestation and desertification in a model of West African monsoons. *Geophysical Research Letters* **24**(2): 155–158.

Zhong S, Fast JD, Bian X. 1996. A Case Study of the Great Plains Low-Level Jet Using Wind Profiler Network Data and a High-Resolution Mesoscale Model. *Monthly Weather Review* **124**(5): 785–806.

Zhu M, Atkinson BW. 2004. Observed and modelled climatology of the land-sea breeze circulation over the Persian Gulf. *International Journal of Climatology* **24**(7): 883–905.